Title
Development of Conducting Polymer Hybrid Materials for Advanced Supercapacitive Energy Storage

Author
Chang, Xueying

Publication Date
2023

Peer reviewed|Thesis/dissertation

UNIVERSITY OF CALIFORNIA

Los Angeles

Development of Conducting Polymer Hybrid Materials for Advanced Supercapacitive Energy Storage

A dissertation submitted in partial satisfaction of the requirements for the degree Doctor of Philosophy in Chemistry

by

Xueying Chang

2023

ABSTRACT OF THE DISSERTATION

Development of Conducting Polymer Hybrid Materials

for Advanced Supercapacitive Energy Storage

by

Xueying Chang

Doctor of Philosophy in Chemistry

University of California, Los Angeles, 2023

Professor Richard B. Kaner, Chair

Long cycle life and high energy/power density are imperative to electrochemical energy storage systems. Conducting polymers like polyaniline have shown great potential as electroactive electrode materials but are limited by poor cycling and rate performance. To address these challenges, we have developed molecular engineering approaches to construct advanced conducting polymer hybrid materials for high-performance supercapacitors. One approach is enabled by the formation of covalent linkages between a 3D graphene network and short-chain conducting polymers built through azide click chemistry. An ultralong cycle life can be achieved by the designed electrode material while the capacitance can be further boosted using a redox-active electrolyte. We further seek to develop a scalable, effortless, and cost-efficient approach toward the fabrication of conducting polymer-based electrodes to reduce the time/energy

consumption associated with conventional high-temperature synthetic methods. A simple one-step laser-induced stabilization of aniline oligomers on carbon nanotubes is established through amide covalent coupling. By taking advantage of the short-chain conducting polymers and the covalent connections, the designed electrode exhibits remarkable cycling stability and good rate capability. To further understand the capacitance degradation mechanisms of aniline oligomer-based materials during long-term cycling, two composite electrodes based on aniline trimers and carbon nanotubes are studied as model systems and are systematically investigated at both pre-cycling and post-cycling states through physicochemical and electrochemical characterizations. Furthermore, a promising nanocomposite based on an interpenetrating network of polyaniline and lignosulfonate has been designed as a waste-to-wealth approach to improve the supercapacitive performance of polyaniline. Additionally, a facile and green electrosynthesis approach is presented to fabricate a polydopamine nanofilm supported on oxygen-functionalized carbon cloth, which delivers high energy density and outstanding cycling stability. These studies present effective molecular design and facile fabrication approaches toward next-generation flexible, robust, and sustainable energy storage devices.

The dissertation of Xueying Chang is approved.

Xiangfeng Duan

Chong Liu

Qibing Pei

Richard B. Kaner, Committee Chair

University of California, Los Angeles

2023

Dedicated to my family.

TABLE OF CONTENTS

LIST OF FIGURES

LIST OF TABLES

LIST OF SCHEMES

ACKNOWLEDGEMENT

I take great pleasure in expressing my gratitude to those who contributed to making this dissertation possible. First, I would like to convey my utmost gratitude to my advisor, Professor Richard B. Kaner, for being an incredibly supportive and amazing advisor. Ric has been giving me the freedom to pursue the research directions that I am passionate about and always providing support and guidance when I am in need, which has been so important for me to enjoy my journey and grow as a research scientist. My sincere gratitude also goes to my dissertation committee members, Professor Richard B. Kaner, Professor Xiangfeng Duan, Professor Chong Liu, and Professor Qibing Pei, for their constant support and invaluable guidance for both my research and professional growth.

I would like to convey my genuine appreciation to Dr. Maher F. El-Kady, Dr. Cheng-Wei Lin, and Ailun Huang for all the insightful discussions, precious comments, and unwavering help that have enriched my research considerably. In addition, I have had a series of amazing collaborations and the privilege of working with these incredibly smart and amazing people, including Professor Mir F. Mousavi, Professor Yuzhang Li, Dr. Haosen Wang, Dr. Mackenzie Anderson, Dr. Stephanie Aguilar, Yuto Katsuyama, Zhiyin Yang, Chenxiang Wang, Jason Zi Jie Zhu, Bo Liu, Xinyue Zhang, Grace Vasiknanonte, Neda Dianat, Masumeh Moloudi, and Navid Khodayar. I would also like to extend my heartfelt thanks to past and present members of the Kaner lab for their help and encouragement: Dr. Chris Turner, Dr. Brian McVerry, Dr. Mit Muni, Dr. Lisa Pangilinan, Dr. Shuangmei Xue, Dr. Chenhao Ji, Dr. Wai H. Mak, Dr. Shanlin Hu, Na He, Ethan Rao, Sophia Uemura, Markus Thiel, Bradley Kroes, Spencer Hamilton, and Jasmine Keane. Moreover, my genuine gratefulness goes to the hardworking staff in the department for always

being helpful and supportive: Dr. Ignacio Martini, Dr. Ta-Chung Ong, Dr. Saeed Khan, and Dr. Greg Khitrov.

I have received tremendous support, strength, and encouragement from my friends, including Na He, Ailun Huang, Cheng-Wei Lin, Jiaxin Ning, Yiran Cheng, Tianyang Yan, etc. I cherish all the beautiful memories we shared and the wonderful trips we took together. I feel incredibly fortunate to have such friends to share happiness with during good times and support each other during difficult times.

Last but not least, I would like to thank my affectionate family for their continuous support and encouragement in all my endeavors. My utmost loving gratitude goes to my parents for their unconditional love and unwavering support throughout my life and studies. They are the people that I can always turn to whenever I need help and support. I know they always have my back and I love them so much.

Chapter 2 is reprinted (adapted) with permission from (Chang, X.; El-Kady, M. F.; Huang, A.; Lin, C.-W.; Aguilar, S.; Anderson, M.; Zhu, J. Z. J.; Kaner, R. B. "3D Graphene Network with Covalently-Grafted Aniline Tetramer for Ultralong-Life Supercapacitors" *Adv. Funct. Mater.* 2021, 31, 2102397 DOI: 10.1002/adfm.202102397). Copyright (2021) John Wiley and Sons. Prof. Richard B. Kaner was the PI and supervised the project. All authors were involved in data collection, results discussion, and manuscript review.

Chapter 3 is reprinted (adapted) with permission from (Chang, X.; Lin, C.-W.; Huang, A.; El-Kady, M. F.; Kaner, R. B. "Molecular Engineering of Hierarchical Conducting Polymer Composites for Highly Stable Supercapacitors" *Nano Lett.* 2023, 23, 3317–3325 DOI: 10.1021/acs.nanolett.3c00284). Copyright (2023) American Chemical Society. Prof. Richard B.

Kaner was the PI and supervised the project. All authors were involved in data collection, results discussion, and manuscript review.

Chapter 4 is reprinted (adapted) with permission from (Chang, X.; Yang, Z.; Huang, A.; Katsuyama, Y.; Lin, C.-W.; El-Kady, M. F.; Wang, C.; Kaner, R. B. "Understanding the Degradation Mechanisms of Conducting Polymer Supercapacitors" *In press*.). Copyright (2023) John Wiley and Sons. Prof. Richard B. Kaner was the PI and supervised the project. All authors were involved in data collection, results discussion, and manuscript review.

Chapter 5 is reprinted (adapted) with permission from (Dianat, N.; Rahmanifar M. S.; Noori, A.; El-Kady, M. F.; Chang, X.; Kaner, R. B.; Mousavi, M. F. "Polyaniline-Lignin Interpenetrating Network for Supercapacitive Energy Storage" *Nano Lett.* 2021, 21, 9485–9493 DOI: 10.1021/acs.nanolett.1c02843). Copyright (2021) American Chemical Society. Prof. Richard B. Kaner and Prof. Mir F. Mousavi were the PI. All authors were involved in data collection, results discussion, and manuscript review.

Chapter 6 is reprinted (adapted) with permission from (Moloudi, M.; Rahmanifar M. S.; Noori, A.; Chang, X.; Kaner, R. B.; Mousavi, M. F. "Bioinspired Polydopamine Supported on Oxygen-Functionalized Carbon Cloth as a High-Performance 1.2 V Aqueous Symmetric Metal-Free Supercapacitor" *J. Mater. Chem. A* 2021, 9, 7712–7725 DOI: 10.1039/D0TA12624A). Copyright (2021) Royal Society of Chemistry. Prof. Richard B. Kaner and Prof. Mir F. Mousavi were the PI. All authors were involved in data collection, results discussion, and manuscript review.

The research presented in this dissertation was supported by: Dr. Myung Ki Hong, Endowed Chair in Materials Innovation at University of California, Los Angeles; California NanoSystems Institute (CNSI); and Graduate Division at University of California, Los Angeles.

VITA

2018 – 2023	Graduate Student Researcher with Prof. Richard B. Kaner University of California, Los Angeles Los Angeles, California
2018 – 2022	Teaching Assistant University of California, Los Angeles Los Angeles, California
2020	Master of Science in Chemistry University of California, Los Angeles Los Angeles, California
2018	Bachelor of Science in Chemistry Nankai University Tianjin, China
2014 – 2018	Undergraduate Researcher Nankai University Tianjin, China

LIST OF PUBLICATIONS AND PRESENTATIONS

1. **Xueying Chang***, Ailun Huang*, Richard B. Kaner, "Electrochemical and Physicochemical Characterizations of Pseudocapacitive Composite Electrodes" *Manuscript in preparation*. (*Both authors contributed equally)

2. Ailun Huang, Zhiyin Yang, **Xueying Chang**, Cheng-Wei Lin, Richard B. Kaner, "Nanoengineered Vanadium Oxide Composite as High-Performance Anode for Aqueous Li-ion Hybrid Battery" *Submitted*.

3. **Xueying Chang**, Zhiyin Yang, Ailun Huang, Yuto Katsuyama, Cheng-Wei Lin, Maher F. El-Kady, Chenxiang Wang, Richard B. Kaner, "Understanding the Degradation Mechanisms of Conducting Polymer Supercapacitors" *In press*.

4. **Xueying Chang**, Cheng-Wei Lin, Ailun Huang, Maher F. El-Kady, Richard B. Kaner, "Molecular Engineering of Hierarchical Conducting Polymer Composites for Highly Stable Supercapacitors" *Nano Letters* **2023**, 23, 3317–3325.

5. Navid Khodayar, Abolhassan Noori, Mohammad S. Rahmanifar, Yasin Shabangoli, Afshin Baghervand, Maher F. El-Kady, Nasim Hassani, **Xueying Chang**, Mehdi Neek-Amal, Richard B. Kaner, Mir F. Mousavi, "Super-Fast and Super-Long-Life Rechargeable Zinc Battery" *Advanced Energy Materials* **2022**, 12, 2202784.

6. Neda Dianat, Mohammad S. Rahmanifar, Abolhassan Noori, Maher F. El-Kady, **Xueying Chang**, Richard B. Kaner*, and Mir F. Mousavi, "Polyaniline-Lignin Interpenetrating Network for Supercapacitive Energy Storage" *Nano Letters* **2021**, 21, 9485–9493.

7. **Xueying Chang**, Maher F. El-Kady, Ailun Huang, Cheng-Wei Lin, Stephanie Aguilar, Mackenzie Anderson, Jason Zi Jie Zhu, Richard B. Kaner, "3D Graphene Network with Covalently-Grafted Aniline Tetramer for Ultralong-Life Supercapacitors" *Advanced Functional Materials* **2021**, 31, 2102397.

8. Ailun Huang, Maher F. El-Kady, **Xueying Chang**, Mackenzie Anderson, Cheng-Wei Lin, Christopher L. Turner, Richard B. Kaner, "Facile Fabrication of Multivalent VO_x/Graphene Nanocomposite Electrodes for High-Energy-Density Symmetric Supercapacitors" *Advanced Energy Materials* **2021**, 11, 2100768.

9. Chenxiang Wang, Mit Muni, Volker Strauss, Arie Borenstein, **Xueying Chang**, Ailun Huang, Sheng Qu, Kimberly Sung, Tera Gilham, Richard B. Kaner, "Graphene's Role in Emerging Trends of Capacitive Energy Storage" *Small*, **2021**, 17, 2006875.

10. Masumeh Moloudi, Mohammad S. Rahmanifar, Abolhassan Noori, **Xueying Chang**, Richard B. Kaner, Mir F. Mousavi, "Bioinspired Polydopamine Supported on Oxygen-Functionalized Carbon Cloth as a High-Performance 1.2 V Aqueous Symmetric Metal-Free Supercapacitor" *Journal of Materials Chemistry A*, **2021**, 9, 7712–7725.

11. Shengli Chen, **Xueying Chang**, Pingchuan Sun, Wangqing Zhang, "Versatile Multicompartment Nanoparticles Constructed with Two Thermo-Responsive, pH-Responsive and Hydrolytic Diblock Copolymers" *Polymer Chemistry*, **2017**, 8, 5593–5602.

12. Yaqing Qu, **Xueying Chang**, Shengli Chen, Wangqing Zhang, "In situ Synthesis of Thermoresponsive 4-Arm Star Block Copolymer Nano-Assemblies by Dispersion RAFT Polymerization" *Polymer Chemistry*, **2017**, 8, 3485–3496.

13. **Xueying Chang**, Ailun Huang, Cheng-Wei Lin, Stephanie Aguilar, Mackenzie Anderson, Jason Zi Jie Zhu, Maher F. El-Kady, Richard B. Kaner, "Design of Conducting Polymer-Based Supercapacitors Towards Ultralong Lifespan" *Poster presentation at MRS Spring Meeting*, Honolulu, HI, May 2022.

14. **Xueying Chang**, Ailun Huang, Maher F. El-Kady, Cheng-Wei Lin, Stephanie Aguilar, Mackenzie Anderson, Jason Zi Jie Zhu, Richard B. Kaner, "Covalent Coupling-Stabilized Conducting Polymers for High-Performance Supercapacitors" *Poster presentation at ACS Spring Meeting*, San Diego, CA, March 2022.

CHAPTER 1. INTRODUCTION

1.1 Electrochemical Energy Storage Technologies

The exhaustion of fossil fuels and the resulting environmental pollution and climate change necessitates the development of eco-friendly and sustainable energy sources.[1] However, reliable and uninterrupted utilization of sustainable energy harvesting including solar, wind, tidal, and geothermal requires the integration of an energy storage system to ensure consistent power output. Electrochemical energy storage systems, such as rechargeable batteries and supercapacitors, are currently the most popular and practical solutions for storing and delivering electrical energy. They are used in a wide range of applications, from small portable devices such as cell phones and laptops to larger systems such as electric vehicles and grid-scale energy storage.[2, 3]

Batteries and supercapacitors represent the two leading electrochemical energy storage technologies. Rechargeable batteries have seen a gradual rise in energy density from several tens of watt-hours per kilogram (such as lead-acid, nickel-cadmium, and nickel metal hydride) to hundreds of watt-hours per kilogram (including lithium-ion, lithium-sulfur, and lithium-air batteries).[4, 5] Nonetheless, batteries face the challenges of low power density and limited cycle life, caused by the charge storage mechanism, which involves the transformation of chemical bonds *via* electrochemical redox reactions in the bulk of active materials.[3, 6] Additionally, when operated at high power, batteries are susceptible to resistive losses caused by slow electron and ion transport, which can result in heat generation and dendrite formation, posing a significant safety risk.[3]

On the other hand, supercapacitors store charges through rapid, surface-controlled processes, including electrostatic or Faradaic electrochemical processes.[6, 7] Supercapacitors are used in applications that require high power density and fast charging/discharging capabilities, such as hybrid electric vehicles, regenerative braking, and uninterruptible power supply systems.[6] They also exhibit advantages including high operating safety, high efficiency, and high performance stability compared to batteries.[7] Unfortunately, the energy density of supercapacitors is generally in the range of several to tens of watt-hours per kilogram, significantly lower than batteries and fuel cells, which hinders their widespread applications.[4]

A Ragone plot (**Figure 1.1**) shows the power versus the energy density of several electrochemical energy storage devices currently available.[6] Power density describes the energy delivery rate, while energy density refers to the energy storage capacity of a device. The research and development of electrochemical energy storage systems aims to achieve both high energy and power densities, specifically high-energy supercapacitors and high-power batteries, with extended cycle life and reduced cost.

1.2 Basic Background and Charge Storage Mechanisms of Supercapacitors

Supercapacitors are constituted by a positive and a negative electrode soaked in an electrolyte, while physically and electrically separated by an ion-permeable, electronically insulating separator. During operation, the charges are mainly stored at the interface between the electrolyte and electrode active materials, such as porous carbon materials, transition metal oxides, and conducting polymers. Capacitance is an evaluation of the charge storage capability of a capacitive electrode, which can be calculated using **Equation 1.1**:

$$C = \frac{\Delta Q}{\Delta U} \tag{1.1}$$

where ΔQ is the amount of electric charge stored (in the unit of Coulombs), ΔU is the electric potential applied on the electrode (in the unit of volts), and the capacitance C is given by the unit of Farads (F).

In general, the charge storage mechanism of capacitive electrodes can be categorized into two main groups: electric double-layer capacitors (EDLCs) and pseudocapacitors (**Figure 1.2**).[7] Conventional supercapacitor electrodes utilize porous carbon materials, adopting electric double-layer capacitance, where the charge is physically stored by electrostatic charge adsorption at the electrode–electrolyte interfaces.[8] Carbon-based materials ranging from commercial activated carbons to carbon nanomaterials, such as graphene and carbon nanotubes, have been widely used and studied for EDLCs mainly due to their large surface area and good electrical conductivity.[8] Since the specific capacitance of EDLCs is strongly dependent on the accessible surface area and surface properties of the electrode materials, they practically generate relatively low energy density compared to batteries.

To increase their energy density, pseudocapacitance has been introduced by adding electroactive materials, including transition metal oxides (such as RuO_2, MnO_2, and V_2O_5) as well as conducting polymers (such as polyaniline, polypyrrole, and poly(3,4-ethylenedioxythiophene)). The pseudocapacitance involves fast, reversible electron transfer at the surface or near-surface of the electrode active materials, which associates with a valence state change of the electrode material.[9] Pseudocapacitive charge storage mechanisms can be further divided into three categories based on different electrochemical interfacial processes: redox pseudocapacitance, underpotential deposition, and intercalation pseudocapacitance (**Figure 1.2**).[7] Redox pseudocapacitance uses electron transfer between an oxidized species and a reduced species. The commonly used electroactive materials including conducting polymers and transition metal oxides

exhibit redox pseudocapacitance, contributed by their intrinsically reversible surface redox couples. Underpotential deposition occurs when ions deposit on a 2D metal–electrolyte interface at potentials positive to their reversible redox potential. Intercalation pseudocapacitance occurs when ions intercalate into a redox-active material with no crystallographic phase change and in a time scale close to that of an EDLC.

To achieve both high energy density and power density in supercapacitors, hybrid electrode materials as well as hybrid supercapacitor devices have been developed by incorporating materials using different types of charge storage mechanisms. Hybrid electrode materials integrating porous carbon and pseudocapacitive materials within a single electrode with favorable architectures allow synergistic effects through the combination of electric double-layer capacitance and pseudocapacitance, contributing to high energy/power densities. In addition, since pseudocapacitive (or battery-type) materials generally suffer from either low electrical conductivity (such as MnO_2) or poor cycling stability (such as conducting polymers), carbonaceous materials can provide high electrical conductivity and mechanical support through hybridization, leading to an overall improved electrochemical performance of the electrode materials. On the other hand, a typical hybrid supercapacitor device consists of a capacitive negative electrode (such as porous carbon) and a pseudocapacitive or battery-type positive electrode (such as MnO_2 or $Ni(OH)_2$). This asymmetric configuration can extend the operating voltage window of aqueous electrolytes beyond the thermodynamic limit of water (1.23 V) and increase the energy density of the device.[7] Furthermore, by replacing the inert electrolyte with a redox-active electrolyte, redox-active electrolyte hybrid capacitors can be achieved, where extra capacity can be contributed by high-speed solution-phase Faradaic reactions while maintaining high rate capability and cycling stability. Therefore, the rational design of hybrid electrode

materials with favorable structures and architectures as well as the development of hybrid supercapacitor devices with optimized electrochemical performance can be expected to continue to be a hot research topic with the goal of increasing energy density without compromising the high power density of supercapacitors.

1.3 Dissertation Overview

This research focuses on designing advanced conducting polymer hybrid materials and developing facile fabrication techniques in pursuit of broader practical applications for conducting polymers in high-performance supercapacitors. This study showcases diverse techniques for incorporating innovative molecular designs into conventional materials to achieve improved electrochemical performance, which also serves as a foundation for comprehending the underlying mechanisms and chemistry. The relationship between structures and properties is methodically sought in these systems through the combination of physicochemical and electrochemical characterizations.

Conducting polymers such as polyaniline are considered promising pseudocapacitive materials, owing to their tunable intrinsic electrical conductivity, high theoretical capacitance, ease of synthesis, sustainability, high flexibility, and low cost relative to their existing inorganic counterparts.[10, 11] Unfortunately, the applications of conducting polymers have been plagued by their instability problem of continued capacitance loss during long-term cycling.[12-14] This has been ascribed mainly to structural pulverization, including repeated swelling and shrinking of polymer chains as a consequence of the doping/de-doping process (counterion insertion/extraction).[15-17] Significant attempts have been undertaken to improve the electrochemical performance of conducting polymers as electrode materials for supercapacitors. One strategy is to incorporate conducting polymers with carbon materials such as carbon nanotubes,[18-20] reduced graphene

oxide,[21, 22] or other buffering substrates. The carbon materials with high electrical conductivity, large surface area, and high mechanical strength have been employed to enhance the overall electrochemical performance of the electrode materials. Another strategy comprises the utilization of short-chain oligomers in substitution of long-chain polymers.[23-25] The oligomers provide electrochemical properties comparable to conducting polymers, while with much shorter chain lengths, the oligomers have shown greater resilience to the extension, contraction, and scission of polymer chains. Intending to further improve the electrochemical performance of conducting polymer-based supercapacitors, several studies have introduced covalent bonds between conducting polymers (or oligomers) and buffering substrates to establish strong and enduring conjugated interactions for faster electron/charge transfer and higher cycling stability.[26-29]

In Chapter 2, a facile synthetic method is demonstrated for covalently grafting aniline tetramers, the basic building block of polyaniline, onto 3D graphene networks *via* a single-step perfluorophenylazide coupling reaction to create a hybrid electrode material for ultralong-life supercapacitors.[28] The molecular design incorporates the substitution of long-chain polyaniline with short-chain aniline tetramers and the introduction of covalent linkages between aniline tetramers and 3D graphene networks, which greatly enhances the charge–discharge cycling stability of polyaniline-based supercapacitors. The designed electrode material exhibits superior cycling stability (85% capacitance retention after 30,000 cycles) compared to noncovalently grafted, long-chain polyaniline-based hybrid materials (70% capacitance retention after 10,000 cycles) in a three-electrode setup. The capacitance can be further boosted through fast and reversible redox reactions on the electrode surface using a redox-active electrolyte while maintaining outstanding cycling stability (82% capacitance retention after 100,000 cycles for a symmetric quasi-solid-state device).

In previous literature reports, the synthesis of conducting polymer hybrid materials normally requires multistep processes,[26, 30, 31] while the formation of covalent linkages typically requires high-temperature treatments such as hydrothermal processing.[28, 32] Consequently, we further seek to develop a simple, scalable, and cost-efficient approach toward the fabrication of conducting polymer-based electrodes to reduce the time/energy consumption associated with conventional synthetic methods, as demonstrated in Chapter 3. A molecular design approach of binding short-chain aniline trimers and carbon nanotubes through the formation of amide covalent linkages enabled by a simple laser scribing technique is presented.[29] The covalently coupled aniline trimer/carbon nanotubes composite retains 80% of its original capacitance after 20,000 charge/discharge cycles, which readily outperforms long-chain polyaniline-based composites without covalent connections. The compact aniline trimer/carbon nanotubes heterointerfaces produce fast charge/discharge kinetics and excellent rate capability.

Although tremendous efforts have been devoted to overcoming the instability problem of conducting polymers, there is limited research on the factors leading to the degradation of cycling stability and the mechanisms behind capacitance fading in conducting polymer or oligomer materials. Chapter 4 aims to further understand the capacitance degradation mechanisms of aniline oligomer-based materials during long-term cycling. Two composite electrodes based on aniline trimers and carbon nanotubes are studied as model systems and are systematically investigated at both pre-cycling and post-cycling states through physicochemical and electrochemical characterizations. The study affirms that the beneficial impact of covalent bonding between aniline trimers and carbon nanotubes leads to enhanced cycling stability by preventing the detachment of aniline trimer and maintaining the electrode microstructure during the charge/discharge cycling

process. In addition, higher porosity positively affects electron/ion transfer and the adaptation to volumetric changes, resulting in higher conductivity and extended cycle life.

The increasing environmental concerns necessitate the creation of energy storage systems that are highly efficient, inexpensive, reliable, sustainable, and eco-friendly. Chapter 5 demonstrates a promising nanocomposite based on an interpenetrating network of polyaniline and sulfonated lignin.[33] Lignin is a redox-active biopolymer that constitutes 20 to 30% of the solid weight of trees and other lignocellulosic biomasses.[34, 35] The direct use of lignin or its derivatives as a pseudocapacitive material presents new opportunities for creating sustainable active materials for value-added applications.[35, 36] The designed nanocomposite exhibits a specific capacitance of 1200 F g^{-1} at 1 A g^{-1}, surpassing the best-known conducting polymer-lignin supercapacitors. This is attributed to the fast H^+ insertion/de-insertion kinetics rate, rather than the slow SO_4^{2-} doping/de-doping process. The fabricated symmetric devices can deliver a high specific energy of 21.2 W h kg^{-1}, an outstanding specific power of 26.0 kW kg^{-1}, along with superb flexibility and excellent cycling stability.

Aligning with the objective of developing sustainable energy storage systems, Chapter 6 further describes a facile and green electrosynthesis approach to fabricate a bioinspired polydopamine nanofilm supported on oxygen-functionalized carbon cloth.[37] Polydopamine exhibits pseudocapacitive properties, which can be attributed to its chemical structure that contains catechol, amine, and imine functionalities. The fabricated binder-free and flexible electrode delivers a high specific capacitance of 626 F g^{-1} at a current density of 1.0 A g^{-1}. The symmetric all-solid-state flexible device covers almost the entire thermodynamic stability window of aqueous electrolytes (1.2 V), delivers a high specific energy of 11.7 Wh kg^{-1}, superb specific power of up to 6.4 kW kg^{-1}, and excellent flexibility along with outstanding cycling stability.

Chapter 7 provides conclusions from the work presented in this thesis and suggestions for possible future work. These research studies together present effective molecular design and facile fabrication approaches toward conducting polymer hybrid materials and provide insights into building next-generation flexible, robust, and sustainable energy storage devices.

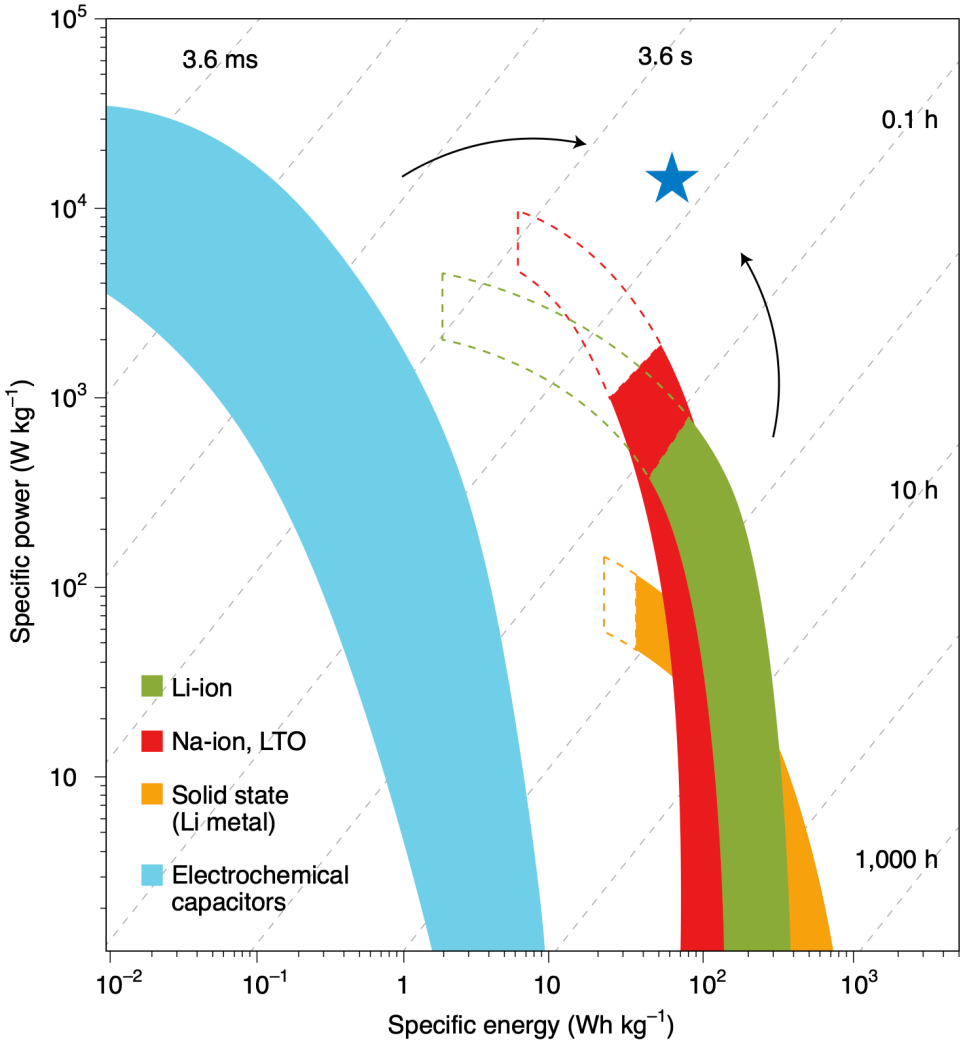

Figure 1.1. Ragone plot of several electrochemical energy storage systems currently available.[6]

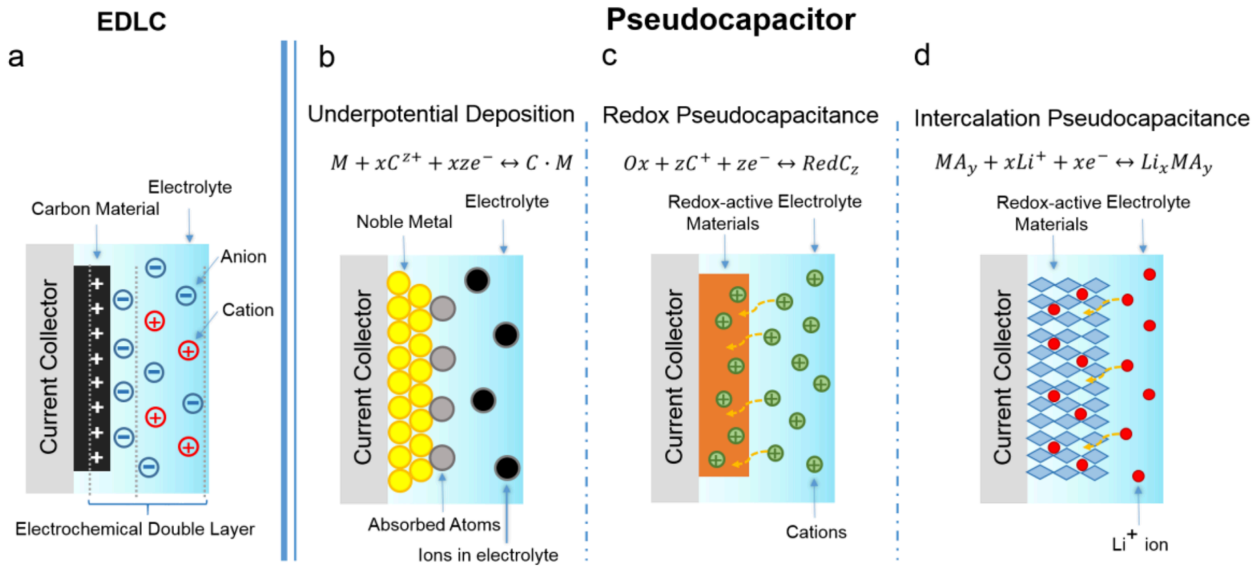

Figure 1.2. Schematics of charge-storage mechanisms for (a) an EDLC and (b–d) different types of pseudocapacitive electrodes.[7]

1.4 References

(1) Chu, S.; Cui, Y.; Liu, N. The path towards sustainable energy. *Nat. Mater.* **2017**, *16*, 16–22.

(2) Dunn, B.; Kamath, H.; Tarascon, J. M. Electrical energy storage for the grid: a battery of choices. *Science* **2011**, *334*, 928–935.

(3) Choi, N.-S.; Chen, Z.; Freunberger, S. A.; Ji, X.; Sun, Y.-K.; Amine, K.; Yushin, G.; Nazar, L. F.; Cho, J.; Bruce, P. G. Challenges Facing Lithium Batteries and Electrical Double-Layer Capacitors. *Angew. Chem. Int. Ed.* **2012**, *51*, 9994–10024.

(4) Zhou, G.; Xu, L.; Hu, G.; Mai, L.; Cui, Y. Nanowires for Electrochemical Energy Storage. *Chem. Rev.* **2019**, *119*, 11042–11109.

(5) Liu, C.; Li, F.; Ma, L.-P.; Cheng, H.-M. Advanced Materials for Energy Storage. *Adv. Mater.* **2010**, *22*, E28–E62.

(6) Simon, P.; Gogotsi, Y. Perspectives for electrochemical capacitors and related devices. *Nat. Mater.* **2020**, *19*, 1151–1163.

(7) Shao, Y.; El-Kady, M. F.; Sun, J.; Li, Y.; Zhang, Q.; Zhu, M.; Wang, H.; Dunn, B.; Kaner, R. B. Design and Mechanisms of Asymmetric Supercapacitors. *Chem. Rev.* **2018**, *118*, 9233–9280.

(8) Zhang, L. L.; Zhao, X. S. Carbon-based materials as supercapacitor electrodes. *Chem. Soc. Rev.* **2009**, *38*, 2520–2531.

(9) Augustyn, V.; Simon, P.; Dunn, B. Pseudocapacitive oxide materials for high-rate electrochemical energy storage. *Energy Environ. Sci.* **2014**, *7*, 1597–1614.

(10) Han, Y.; Dai, L. Conducting Polymers for Flexible Supercapacitors. *Macromol. Chem. Phys.* **2019**, *220*, 1800355.

(11) Li, Z.; Gong, L. Research Progress on Applications of Polyaniline (PANI) for Electrochemical Energy Storage and Conversion. *Materials* **2020**, *13*, 548.

(12) Liu, T.; Finn, L.; Yu, M.; Wang, H.; Zhai, T.; Lu, X.; Tong, Y.; Li, Y. Polyaniline and Polypyrrole Pseudocapacitor Electrodes with Excellent Cycling Stability. *Nano Lett.* **2014**, *14*, 2522–2527.

(13) Song, Y.; Liu, T.-Y.; Xu, X.-X.; Feng, D.-Y.; Li, Y.; Liu, X.-X. Pushing the Cycling Stability Limit of Polypyrrole for Supercapacitors. *Adv. Funct. Mater.* **2015**, *25*, 4626–4632.

(14) Eftekhari, A.; Li, L.; Yang, Y. Polyaniline supercapacitors. *J. Power Sources* **2017**, *347*, 86–107.

(15) Zhao, Y.; Liu, B.; Pan, L.; Yu, G. 3D nanostructured conductive polymer hydrogels for high-performance electrochemical devices. *Energy Environ. Sci.* **2013**, *6*, 2856–2870.

(16) Heinze, J.; Frontana-Uribe, B. A.; Ludwigs, S. Electrochemistry of Conducting Polymers—Persistent Models and New Concepts. *Chem. Rev.* **2010**, *110*, 4724−4771.

(17) Otero, T. F.; Alfaro, M.; Martinez, V.; Perez, M. A.; Martinez, J. G. Biomimetic Structural Electrochemistry from Conducting Polymers: Processes, Charges, and Energies. Coulovoltammetric Results from Films on Metals Revisited. *Adv. Funct. Mater.* **2013**, *23*, 3929–3940.

(18) Huang, F.; Chen, D. Towards the upper bound of electrochemical performance of ACNT@polyaniline arrays as supercapacitors. *Energy Environ. Sci.* **2012**, *5*, 5833–5841.

(19) Niu, Z.; Zhou, W.; Chen, X.; Chen, J.; Xie, S. Highly Compressible and All-Solid-State Supercapacitors Based on Nanostructured Composite Sponge. *Adv. Mater.* **2015**, *27*, 6002–6008.

(20) Simotwo, S. K.; Delre, C.; Kalra, V. Supercapacitor Electrodes Based on High-Purity Electrospun Polyaniline and Polyaniline–Carbon Nanotube Nanofibers. *ACS Appl. Mater. Interfaces* **2016**, *8*, 21261–21269.

(21) Meng, Y.; Wang, K.; Zhang, Y.; Wei, Z. Hierarchical Porous Graphene/Polyaniline Composite Film with Superior Rate Performance for Flexible Supercapacitors. *Adv. Mater.* **2013**, *25*, 6985–6990.

(22) Liu, L.; Niu, Z.; Zhang, L.; Zhou, W.; Chen, X.; Xie, S. Nanostructured Graphene Composite Papers for Highly Flexible and Foldable Supercapacitors. *Adv. Mater.* **2014**, *26*, 4855–4862.

(23) Yan, J.; Yang, L.; Cui, M.; Wang, X.; Chee, K. J.; Nguyen, V. C.; Kumar, V.; Sumboja, A.; Wang, M.; Lee, P. S. Aniline Tetramer-Graphene Oxide Composites for High Performance Supercapacitors. *Adv. Energy Mater.* **2014**, *4*, 1400781.

(24) Wang, H.; Yu, Z.; El-Kady, M. F.; Anderson, M.; Kowal, M. D.; Li, M.; Kaner, R. B. Graphene/oligoaniline based supercapacitors: Towards conducting polymer materials with high rate charge storage. *Energy Storage Mater.* **2019**, *19*, 137–147.

(25) Han, H.; Lee, S. W.; Moon, K. H.; Cho, S. Fabrication of Solid-State Asymmetric Supercapacitors Based on Aniline Oligomers and Graphene Electrodes with Enhanced Electrochemical Performances. *ACS Omega* **2019**, *4*, 1244–1253.

(26) Kumar, N. A.; Choi, H.-J.; Shin, Y. R.; Chang, D. W.; Dai, L.; Baek, J.-B. Polyaniline-Grafted Reduced Graphene Oxide for Efficient Electrochemical Supercapacitors. *ACS Nano* **2012**, *6*, 1715–1723.

(27) Liu, X.; Shang, P.; Zhang, Y.; Wang, X.; Fan, Z.; Wang, B.; Zheng, Y. Three-dimensional and stable polyaniline-grafted graphene hybrid materials for supercapacitor electrodes. *J. Mater. Chem. A* **2014**, *2*, 15273–15278.

(28) Chang, X.; El-Kady, M. F.; Huang, A.; Lin, C.-W.; Aguilar, S.; Anderson, M.; Zhu, J. Z. J.; Kaner, R. B. 3D Graphene Network with Covalently-Grafted Aniline Tetramer for Ultralong-Life Supercapacitors. *Adv. Funct. Mater.* **2021**, *31*, 2102397.

(29) Chang, X.; Lin, C.-W.; Huang, A.; El-Kady, M. F.; Kaner, R. B. Molecular Engineering of Hierarchical Conducting Polymer Composites for Highly Stable Supercapacitors. *Nano Lett.* **2023**, *23*, 3317–3325.

(30) Li, J.; Qiu, S.; Liu, B.; Chen, H.; Xiao, D.; Li, H. Strong interaction between polyaniline and carbon fibers for flexible supercapacitor electrode materials. *J. Power Sources* **2021**, *483*, 229219.

(31) Zhao, B.; Hu, H.; Yu, A.; Perea, D.; Haddon, R. C. Synthesis and Characterization of Water Soluble Single-Walled Carbon Nanotube Graft Copolymers. *J. Am. Chem. Soc.* **2005**, *127*, 8197−8203.

(32) Hou, T.; Liu, B.; Sun, X.; Fan, A.; Xu, Z.; Cai, S.; Zheng, C.; Yu, G.; Tricoli, A. Covalent Coupling-Stabilized Transition-Metal Sulfide/Carbon Nanotube Composites for Lithium/Sodium-Ion Batteries. *ACS Nano* **2021**, *15*, 6735−6746.

(33) Dianat, N.; Rahmanifar, M. S.; Noori, A.; El-Kady, M. F.; Chang, X.; Kaner, R. B.; Mousavi, M. F. Polyaniline-Lignin Interpenetrating Network for Supercapacitive Energy Storage. *Nano Lett.* **2021**, *21*, 9485–9493.

(34) Espinoza-Acosta, J. L.; Torres-Chavez, P. I.; Olmedo-Martinez, J. L.; Vega-Rios, A.; Flores-Gallardo, S.; Zaragoza-Contreras, E. A. Lignin in storage and renewable energy applications: A review. *J. Energy Chem.* **2018**, *27*, 1422–1438.

(35) Wu, X.; Jiang, J.; Wang, C.; Liu, J.; Pu, Y.; Ragauskas, A.; Li, S.; Yang, B. Lignin-derived electrochemical energy materials and systems. *Biofuels, Bioprod. Biorefin.* **2020**, *14*, 650–672.

(36) Gan, D.; Xing, W.; Jiang, L.; Fang, J.; Zhao, C.; Ren, F.; Fang, L.; Wang, K.; Lu, X. Plant-inspired adhesive and tough hydrogel based on Ag-Lignin nanoparticles-triggered dynamic redox catechol chemistry. *Nat. Commun.* **2019**, *10*, 1487.

(37) Moloudi, M.; Rahmanifar, M. S.; Noori, A.; Chang, X.; Kaner, R. B.; Mousavi, M. F. Bioinspired polydopamine supported on oxygen-functionalized carbon cloth as a high-performance 1.2 V aqueous symmetric metal-free supercapacitor. *J. Mater. Chem. A* **2021**, *9*, 7712–7725.

CHAPTER 2. 3D GRAPHENE NETWORK WITH COVALENTLY-GRAFTED ANILINE TETRAMER FOR ULTRALONG-LIFE SUPERCAPACITORS

2.1 Abstract

The conducting polymer polyaniline (PANI) has been considered as a promising pseudocapacitive electrode material for supercapacitors due to its high specific capacitance, low cost, and environmental friendliness. However, the poor cycling stability of PANI during charge–discharge processes limits its widespread practical applications. Herein, a facile synthetic method is demonstrated for covalently grafting aniline tetramer (TANI), the basic building block of PANI, onto 3D graphene networks *via* perfluorophenylazide coupling chemistry to create a hybrid electrode material for ultralong-life supercapacitors. The design, which substitutes long-chain PANI with short-chain TANI and introduces covalent linkages between TANI and 3D graphene, greatly enhances the charge–discharge cycling stability of PANI-based supercapacitors. The electrode material as well as the fabricated symmetric all-solid-state supercapacitors exhibit extraordinary long cycle life (>85% capacitance retention after 30,000 charge–discharge cycles). The capacitance can be further boosted through fast and reversible redox reactions on the electrode surface using a redox-active electrolyte while maintaining outstanding cycling stability (82%

capacitance retention after 100,000 cycles for a symmetric all-solid-state device). While conducting polymers are known to be limited by their poor cycling stability, this work provides an effective strategy to achieve enhanced cycle life for conducting polymer-based energy storage devices.

2.2 Introduction

Polyaniline (PANI), as a typical conducting polymer, is considered as a promising pseudocapacitive electrode material for supercapacitors, owing to its good electrochemical activity, high theoretical pseudocapacitance, ease of synthesis, and environmental friendliness.[1] However, one of the main challenges for the widespread practical application of PANI is its poor cycling stability due to the volumetric changes that occur during repeated charge–discharge processes (insertion/de-insertion of counter ions).[2, 3] The swelling and shrinking of PANI chains may lead to structural instability and mechanical degradation, thereby degenerating its capacitive performance with cycling.[4]

One way to address this problem comprises the substitution of PANI with short-chain aniline tetramer (TANI). TANI (also known as tetra-aniline) is the basic building block of PANI, exhibiting very similar doping and redox chemistry to those of polyaniline. However, TANI is less susceptible to volumetric degradation compared to PANI during repeated charge–discharge processes due to its shorter chain length.[5, 6] For example, Yan *et al.* reported good cycling stability with 93% to 96% capacitance retention after 2000 cycles in a three-electrode test by loading aniline tetramers on graphene oxide (GO) to prevent chain breaking and raise the tolerance to volume change.[5] Recently, Wang *et al.* reported a reduced graphene oxide (rGO)/oligoaniline composite, which exhibits good cycling stability of 91% capacitance retention after 2000 cycles in a three-electrode cell setup.[7]

On the other hand, combining PANI/TANI with carbon-based materials, such as carbon nanotubes,[8-10] GO,[5] and rGO,[7, 11-13] is another effective approach to enhance the cycling stability of PANI-based supercapacitors while simultaneously achieving better electrochemical performance. These carbon-based materials not only reinforce the conducting polymer structures mechanically, reducing the volumetric degradation of PANI, but also provide greater electrical conductivity and larger surface area. Among all carbon-based materials, graphene manifests high electrical conductivity, great mechanical strength, and large theoretical surface area ($2630\ m^2\ g^{-1}$),[14] making it one of the most promising candidates for PANI/TANI-carbon composites. Furthermore, 3D graphene networks (GN) with little restacking of the 2D graphene layers are favorable to develop conducting polymer-graphene hybrid electrode materials due to their extremely low density as well as highly interconnected hierarchical porous structure enabling fast ion transport and electron transfer.[15] Tremendous efforts have been devoted to the development of PANI-3D graphene composites using various synthetic methods, including the self-assembly of GO with PANI followed by the reduction of GO,[16-19] the sacrificial porous template method followed by polymerization of aniline,[11, 20] the two-step consecutive electrochemical deposition[21] or electrochemical co-deposition method,[22] and the 3D printing method.[23] However, among most of the present synthetic routes, PANI was bound to graphene by noncovalent interactions, such as Van der Waals forces, π–π stacking interactions, electrostatic interactions, and hydrogen bonding. Accordingly, PANI chains suffer from the risk of detachment from the surface of graphene, which may deteriorate the cycling stability and can be exacerbated by long-term utilization or in a large-scale application. In addition, the absence of conjugated bonds between PANI and graphene may also reduce charge mobility across interphases.[24]

In order to further enhance the cycling stability of PANI-based supercapacitors, a variety of studies have introduced covalent linkages between PANI and graphene to provide conjugated, strong, permanent interactions.[24-34] The covalent connections between PANI and graphene have been suggested to be beneficial for ensuring synergistic effects as well as enhancing the mechanical stability of the PANI structure, which may lead to extended cycle life of PANI-based supercapacitors.[34] However, most of the reported covalently linked PANI/TANI-graphene composites have been synthesized through complicated chemical routes with multiple steps, which can be rather arduous and time-consuming. The typical approach involves covalent functionalization of the GO surfaces through acyl chlorination,[25-27, 33] diazotization[24, 28-30] or an azide crosslinking reaction[31] followed by the reduction of GO, which is subsequently polymerized in the presence of aniline monomers. Moreover, covalently linked TANI-3D graphene composites have not been well studied. Therefore, it is an important challenge to develop a facile synthetic strategy to construct highly durable electrode materials for ultralong-life PANI-based supercapacitors.

In this work, a single-step solvothermal self-assembly method was developed capable of producing a covalently connected TANI-3D graphene composite as the electrode material for PANI-based supercapacitors to achieve ultralong cycle life. Starting from GO and 4-azidotetrafluorobenzoyl tetra-aniline (ATFB-TANI), the reduction of GO to form a 3D GN and the covalent attachment of TANI to the surface of rGO took place simultaneously during a one-step-one-pot solvothermal treatment. Following this intriguing surface functionalization process, the synthesized ATFB-TANI-*grafted*-3D GN (AT*g*GN) composite was fabricated into a binder-free electrode, which exhibits greatly improved electrochemical performance. Especially notable is its exceptional cycling stability (85% capacitance retention after 30,000 cycles) compared to

noncovalently grafted, long-chain PANI-based hybrid materials (70% capacitance retention after 10,000 cycles) in a three-electrode setup. Additionally, the assembled all-solid-state supercapacitors derived from AT*g*GN are capable of delivering remarkable cycling stability with 87% capacitance retention after 30,000 cycles, outperforming the vast majority of PANI-based supercapacitors reported previously. Furthermore, a redox additive hydroquinone (HQ) providing additional Faradaic capacitance with direct redox reactions on the electrode surfaces can be introduced into the electrolyte to further boost the capacitance of the supercapacitor, while maintaining excellent cycling stability.

2.3 Results and Discussion

An ATFB-TANI-*grafted*-3D GN (AT*g*GN) composite was prepared by a simple one-step-one-pot solvothermal reaction (**Figure 2.1a**). In order to graft TANI onto large-scale rGO surfaces, perfluorophenylazide was applied due to its fast and nondestructive photochemistry. Upon thermal or photo activation, the perfluorophenylazides on 4-azidotetrafluorobenzoyl tetra-aniline (ATFB-TANI) can undergo decomposition releasing nitrogen (N_2) to form highly reactive singlet perfluorophenylnitrene radicals, which can further undergo C=C addition or C–H insertion reactions.[35, 36] A solution of ATFB-TANI was first uniformly mixed with a GO suspension, followed by a solvothermal self-assembly process at 180 °C for 24 h to obtain AT*g*GN. During the solvothermal treatment, GO was reduced forming a 3D GN, while simultaneously TANI was covalently grafted onto the rGO surfaces *via* perfluorophenylazide coupling chemistry. The simultaneous formation of 3D GNs and grafting of TANI not only helps to prevent the aggregation of TANI, but also reduces the restacking of graphene layers. The AT*g*GN composites with different TANI contents in the following mass ratios – R_m (TANI:GO) = 1:1, 3:1, 5:1, and 7:1 – were prepared and are denoted as AT*g*GN1, AT*g*GN3, AT*g*GN5, and AT*g*GN7, respectively. For

further comparison, a 3D GN was also prepared by the same procedure with only the presence of the GO suspension.

The morphological structure of the pure 3D GN and the AT*g*GN was characterized by scanning electron microscopy (SEM), transmission electron microscopy (TEM), and energy dispersive X-ray spectroscopy (EDS). In a typical SEM image of AT*g*GN (**Figure 2.1c**), the covalently grafted TANI can be observed residing on the rGO surfaces, while the SEM image of the pure 3D GN (**Figure 2.1b**) reveals only the existence of crumpled rGO sheets. In addition, the inset SEM images within **Figure 2.1b,c** demonstrate the 3D nature of the pure GN and AT*g*GN, whose interconnected 3D porous network structure facilitates rapid electron and ion transport for charge storage. The TEM images of AT*g*GN (**Figure 2.1d,e**) are in good agreement with the SEM image, indicating that the TANI molecules are well dispersed across the 3D GN. The EDS spectrum of AT*g*GN (**Figure 2.1g**) displays peaks for carbon, oxygen, nitrogen, and fluorine, revealing the existence of both rGO and TANI. From the EDS elemental mapping of AT*g*GN (**Figure 2.1h–k**), a homogeneous distribution of C, N, O, and F elements indicates the atomic-scale uniform dispersion of TANI across the surface of the 3D GN.

The formation of covalent connections between TANI and the 3D GN was verified by Fourier-transform infrared (FT-IR) spectroscopy (**Figure 2.2a**). The N=N=N stretching vibration of azido groups at 2120 cm^{-1} is observed in ATFB-TANI, but disappears in AT*g*GN, suggesting the successful covalent grafting of ATFB-TANI onto the 3D GN. In the spectra of ATFB-TANI and AT*g*GN, the bands at 1575 cm^{-1} can be attributed to the stretching vibrations of the C=C bonds on the quinoid rings. The ATFB-TANI exhibits C=C stretching vibrations of benzenoid rings at 1488 cm^{-1}. In the AT*g*GN spectrum, this band blue shifts to 1499 cm^{-1}, indicating that there exists a charge transfer between TANI and the GN.[29] The merger of signals corresponding to C=C

vibrations of the GN and the quinonoid rings of TANI occurs to generate a relatively sharp signal at 1575 cm^{-1} in AT*g*GN compared to ATFB-TANI. Apart from this, the bands at 1295 cm^{-1} and 1258 cm^{-1} can be ascribed to the aromatic amine C–N stretching of TANI. The GO peaks due to alkoxy (C–O stretching at 1055 cm^{-1}) and hydroxyl groups (C–O–H bending at 1399 cm^{-1})[37] disappear from the spectra of AT*g*GN and the pure GN, suggesting the removal of alkoxy and hydroxyl groups during the solvothermal reduction process. The decrease in relative intensity for the C–O (epoxy groups) stretching at 1240 cm^{-1} in the spectra of the pure GN and AT*g*GN also indicates successful deoxygenation of GO. The AT*g*GN samples with different TANI contents as well as the pure GN were further characterized by FT-IR (**Figure S2.1a**) and Raman (**Figure S2.1b**) spectroscopy.

X-ray photoelectron spectroscopy (XPS) was adopted to obtain deeper insights into the elemental composition of the AT*g*GN composite (**Figure 2.2b–d**). The survey scan of AT*g*GN (**Figure 2.2b**) clearly shows the coexistence of carbon (C 1s), oxygen (O 1s), nitrogen (N 1s), and fluorine (F 1s). The curve-fit core level XPS spectrum of C 1s (**Figure 2.2c**) can be deconvoluted into five components. The peaks at 284.6 eV and 285.1 eV correspond to C=C and C–C bonds in the aromatic rings, and the peaks located at 285.9 eV, 286.7 eV, and 288.0 eV can be ascribed to C–N, C–O, and C=O/C–F bonds, respectively. **Figure 2.2d** displays the deconvolution of the curve-fit core level N 1s spectrum. The peaks located at 399.9 eV, 398.7 eV, and 400.9 eV can be attributed to benzenoid amine, quinoid amine, and nitrogen in the covalent structure formed between rGO and perfluorophenylazides.[38] The XPS spectrum of perfluorophenylazide exhibits two N 1s peaks located at 402.1 eV and 405.6 eV, corresponding to the outer and the middle nitrogens of the azide.[39] The disappearance of these two N 1s peaks of azide in AT*g*GN results from the loss of nitrogen (N_2) when the azide decomposed upon thermal activation. Both the results

from XPS and FT-IR analyses confirm the formation of covalent connections between TANI and the 3D GN through perfluorophenylazide-mediated coupling chemistry. The XPS survey scans of other AT*g*GN composites with different TANI contents are presented in **Figure S2.2**. From the survey scans, the nitrogen content (at%) of the AT*g*GN7 composite was determined to be 7.92%. Since GO is nitrogen-free and the only nitrogen-containing species is ATFB-TANI, the nitrogen content can be converted to the weight ratio of TANI to the GN, which was calculated to be 1.4:1 for AT*g*GN7. Similarly, the weight ratios of TANI to GN for other AT*g*GN composites with different TANI contents were calculated and are presented in **Table S2.1**.

To investigate the electrochemical properties of AT*g*GN, the weight ratio of TANI to the GN was first tuned to find the optimal TANI content with regard to the electrochemical performance in a three-electrode cell setup using 1.0 M H_2SO_4 as the electrolyte. The cyclic voltammetry (CV) curves of AT*g*GN with different TANI contents (AT*g*GN1, AT*g*GN3, AT*g*GN5, and AT*g*GN7) at a scan rate of 20 mV s^{-1} are presented in **Figure S2.5a**. All CV curves exhibit a distorted rectangular shape with a pair of broad redox peaks, indicating pseudocapacitive behavior due to the redox transition from TANI. **Figure S2.5b** summarizes the galvanostatic charge–discharge (GCD) plots of all AT*g*GN composites at a current density of 0.5 mA cm^{-2}. With increasing TANI content from AT*g*GN1 to AT*g*GN7, the discharge time becomes longer, which is indicative of better energy storage performance. As demonstrated in **Figure S2.5c**, all samples exhibit exceptional cycling stability, with a specific capacitance retention above 90% after 10,000 charge–discharge cycles, thanks to the utilization of the short-chain TANI as well as the covalent connections between TANI and the 3D GN. Among the four AT*g*GN composites with different TANI contents, AT*g*GN7 shows the highest specific capacitance (278 F g^{-1} at 1 A g^{-1} in 1.0 M

H_2SO_4) and excellent rate performance (**Figure S2.5d**). Therefore, AT*g*GN7 was picked out to conduct further electrochemical studies.

To better understand the merits of the covalent connections between TANI and the 3D GN in AT*g*GN, two control experiments were performed: a physical mixture of TANI with a pure 3D GN (TANI/GN) and a physical mixture of PANI nanofibers with a pure 3D GN (PANI/GN) (**Figure 2.3a**). These two physical mixtures were prepared by a traditional physical mixing method in which TANI or PANI was mixed with the GN in deionized water with the same TANI content as the AT*g*GN composite (the weight ratio of TANI to GN was calculated as 1.4:1 from XPS analysis). Note that in the two physical mixtures, TANI/PANI and GN were held together *via* noncovalent interactions such as Van der Waals forces, electrostatic interactions, and π-π stacking interactions.

The CV curve of PANI/GN in **Figure 2.3b** shows two pairs of PANI redox peaks at 0.21 and 0.48 V (oxidation, vs. Ag/AgCl) due to the transitions from the semiconducting leucoemeraldine to the conducting emeraldine state of PANI and from the emeraldine to the pernigraniline state, respectively. TANI, as the basic building block of PANI, exhibits similar redox and doping chemistry to those of PANI. Thus, TANI/GN displays two pairs of peaks at 0.29 and 0.49 V (oxidation, vs. Ag/AgCl) due to the redox transitions from TANI. The AT*g*GN exhibits a broad peak at 0.48 V (oxidation, vs. Ag/AgCl) originating from the redox transition from the emeraldine state to the pernigraniline state. Compared to the two physical mixtures TANI/GN and PANI/GN, AT*g*GN shows much better capacitive behavior with almost-vertical current switches at the potential extremes. This indicates a fast charge transport within the AT*g*GN sample, which can be ascribed to the efficient electronic coupling originating from the covalent connections between TANI and the 3D GN. The GCD profiles of the AT*g*GN electrode at different current densities

ranging from 0.2 to 20 mA cm^{-2} in a potential window from −0.2 to 0.9 V are shown in **Figure 2.3c**. The nonlinearity of the GCD profiles indicates the operation of pseudocapacitance. The intermediate region (0.4−0.6 V) with a mild slope can be ascribed to reversible Faradaic processes that occur on the AT*g*GN electrode, which is consistent with the CV curves.

As can be seen from **Figure 2.3d**, the AT*g*GN exhibits a capacitance retention above 90% after 10,000 charge–discharge cycles, which is much higher than that of TANI/GN (74% capacitance retention) and PANI/GN (70% capacitance retention). This demonstrates that the substitution of PANI with TANI and the formation of covalent connections between TANI and the 3D GN both contribute to the enhancement of the cycling stability of the PANI-based electrode materials. The inset to **Figure 2.3d** shows that the AT*g*GN electrode retains above 85% of its initial capacitance even after 30,000 charge–discharge cycles, further confirming that the AT*g*GN displays extraordinary long cycle life. **Figure 2.3e** displays the Nyquist plots of the AT*g*GN, TANI/GN, and PANI/GN over a frequency range from 200 kHz to 10 mHz collected by electrochemical impedance spectroscopy (EIS). The AT*g*GN electrode shows a low uncompensated resistance value of around 1.2 Ω, which comprises the electronic resistance of the electrode and the ionic resistance of the electrolyte, suggesting a high conductivity for the AT*g*GN electrode. The near-vertical line in the low-frequency region indicates excellent capacitive behavior. In addition, the relatively small semicircle of the AT*g*GN electrode observed in the high-frequency region (shown in the inset to **Figure 2.3e**) is indicative of a low charge transfer resistance due to the covalent connection between TANI and the 3D GN. The TANI/GN and PANI/GN composites show very similar Nyquist plots to that of AT*g*GN, but with a relatively lower gradient in the low-frequency region and a relatively larger semicircle in the high-frequency region, which account for their inferior capacitive performance.

The rate capability studies of the AT*g*GN, TANI/GN, and PANI/GN composites in the 1.0 M H_2SO_4 aqueous electrolyte are displayed in **Figure 2.3f**. The AT*g*GN electrode displays a specific capacitance of 278 F g^{-1} at 1 A g^{-1} and an areal capacitance of 135 mF cm^{-2} at 1 mA cm^{-2}. It retains a specific capacitance of 204 F g^{-1} at 39 A g^{-1} and an areal capacitance of 104 mF cm^{-2} at 20 mA cm^{-2}. The high-rate capability can be attributed to the efficient interaction of TANI with rGO *via* the covalent connections. In comparison, the TANI/GN exhibits a specific capacitance of 212 F g^{-1} at 1 A g^{-1} and an areal capacitance of 110 mF cm^{-2} at 1 mA cm^{-2}, while the PANI/GN shows a specific capacitance of 154 F g^{-1} at 1 A g^{-1} and an areal capacitance of 78 mF cm^{-2} at 1 mA cm^{-2}. As can be seen, the specific capacitance of the prepared electrodes increases from PANI/GN to TANI/GN to AT*g*GN, demonstrating that the utilization of TANI instead of PANI and the covalent connections between TANI and rGO both contribute to the enhancement of the energy storage performance. The charge storage process of the AT*g*GN electrode can be interpreted based on the power law dependency of the current response on the scan rate in a cyclic voltammetry test using the equation $i(v) = av^b$, where b = 0.5 indicates a diffusion dominated charge storage while b = 1 represents a capacitor-like charge storage mechanism.[40] The b-values for AT*g*GN determined from the slope of the *log(i)* versus *log(v)* plots display a value of 0.89 at the current maxima (**Figure S2.6**), suggesting a combination of the two kinds of charge storage processes, in which the dominant charge storage mechanism is capacitor-like. The integrated surface-controlled charge storage accounts for 82% of the total charge at a scan rate of 5 mV s^{-1} (**Figure 2.3g**), which corroborates the fast kinetics and high rate capability of the AT*g*GN system.

To further differentiate between the unbonded and covalently bonded TANI, we prepared a GN/unbonded TANI analogue (GN/TANI) by using TANI (without the perfluorophenylazide group) instead of ATFB-TANI as the starting material through the same AT*g*GN preparation

procedure. The morphological and compositional analyses are shown in **Figure S2.4**. The GN/unbonded TANI analogue exhibits lower specific capacitance, larger equivalent series resistance (ESR), greater ion diffusion resistance as well as much poorer rate capability in comparison with AT*g*GN (**Figure S2.7**). These results suggest that the covalently attached TANI in AT*g*GN remarkably contributes to the superior electrochemical performance. In addition, the graphene conductive network also plays an imperative role in AT*g*GN, which significantly improves the capacitance and greatly reduces the resistance of the electrode material (**Figure S2.8**).

To evaluate the suitability of AT*g*GN as a promising electrode material for practical energy storage applications, an all-solid-state symmetric AT*g*GN||AT*g*GN device was fabricated by employing AT*g*GN as both the negative and positive electrodes. A traditional PVA/1.0 M H_2SO_4 gel electrolyte was first used in the evaluation of the device. The CV curves of the symmetric AT*g*GN||AT*g*GN device within a voltage window of 0.8 V at various scan rates from 5 to 200 mV s^{-1} are provided in **Figure 2.4a**. The CV curves display a distorted rectangular shape with a pair of redox peaks at 0.46 V (oxidation) due to redox transitions, indicating the operation of both electric double-layer capacitance and pseudocapacitance by the electrode material. In addition, the CV curves retain their pseudo-rectangular shape even at a high scan rate of 200 mV s^{-1}, signifying good rate capability and fast charge−discharge kinetics of the symmetric AT*g*GN||AT*g*GN device. The GCD profiles with negligible *iR* drops also demonstrate fast charge transfer and ion transport within the device (**Figure 2.4b**). The Nyquist plot in **Figure 2.4c** shows essentially no semicircle in the high-frequency region, indicating virtually no charge transfer resistance. The nearly vertical line at low frequency confirms fast electron transport during the redox reactions.

The long-term cycling stability of a supercapacitor is an essential parameter to meet the requirements for practical applications. The cycling stability of a symmetric AT*g*GN||AT*g*GN device was investigated by recording 30,000 charge–discharge cycles at a current density of 2.5 mA cm^{-2} (**Figure 2.4d**). The device lost about 5% of its initial capacitance over the first 200 cycles and its capacitance decreased very slowly thereafter. Thus, the capacitance retention of the device was found to be 93% after 10,000 cycles, 90% after 20,000 cycles, and 87% after 30,000 cycles. The inset to **Figure 2.4d** shows the CV curves before and after 1000, 20,000, and 30,000 charge–discharge cycles. The area under the CV curve decreased relatively fast during the first 1000 cycles, but slowed down significantly thereafter and the shape of the CV curve remained essentially the same with increased cycling. This demonstrates that the symmetric AT*g*GN||AT*g*GN device exhibits remarkable cycling stability, thanks to the short-chain TANI and the formation of covalent connections between TANI and the 3D GN. The cycling stability of AT*g*GN was further compared with that of other carbon- and PANI-based hybrid materials in both conventional three-electrode cells and two-electrode symmetric supercapacitor devices. **Figure 2.4e** demonstrates the comparison of the cycling stability of AT*g*GN in a three-electrode cell setup with other carbon- and PANI-based hybrid materials. As can be seen, the AT*g*GN composite shows exceptionally long cycle life with a capacitance retention of 85% after 30,000 charge–discharge cycles. In comparison, the number of cycles of other carbon- and PANI-based composites[7, 18, 32, 34, 41-53] is generally below 3000 cycles with a capacitance retention of ~85%. Similarly, as depicted in the inset to **Figure 2.4e**, the symmetric AT*g*GN||AT*g*GN device shows superior cycling stability compared to other carbon- and PANI-based symmetric devices.[4, 9, 11, 29, 34, 41, 46, 54-57] The symmetric AT*g*GN||AT*g*GN device retains 87% of its initial capacitance after

30,000 charge–discharge cycles, while the number of cycles of other carbon- and PANI-based symmetric devices is generally below 10,000 cycles with a capacitance retention of ~90%.

Supercapacitor research involving Faradaic processes has traditionally focused on the electrode materials, such as employing conducting polymers or metal oxides, but improvements in pseudocapacitance may be limited if we only depend on the electrode materials. Another strategy to improve the capacitance is to utilize a redox-active electrolyte. Therefore, we further explored the enhancement of capacitance by introducing a redox additive, hydroquinone (HQ), into the original electrolyte in both the three-electrode cells and the symmetric AT*g*GN||AT*g*GN devices. In order to understand the mechanism, we first investigated the electrochemical performance of the AT*g*GN electrode in the presence of HQ in a 1.0 M H_2SO_4 aqueous electrolyte in a three-electrode cell setup. The enhanced capacitance of the HQ-containing system can be explained as illustrated in **Figure 2.5a**. In the absence of the redox additive, only the active materials in the electrode give rise to the Faradaic processes. However, in the presence of a redox additive HQ, the active materials in both electrode and electrolyte get oxidized and reduced simultaneously, leading to higher pseudocapacitance. Additionally, the ion adsorption and desorption at the interface of the electrode and electrolyte leads to electric double-layer capacitance. The HQ contributes to additional pseudocapacitance *via* the Faradaic reactions of the hydroquinone–quinone (HQ–Q) couples:[58-60]

$$HQ \overset{2H^+,2e^-}{\Longleftrightarrow} Q \tag{2.1}$$

Figure 2.5b shows the CV curves of AT*g*GN with different concentrations of HQ (0, 0.01, and 0.02 M) in 1.0 M H_2SO_4 at a scan rate of 50 mV s^{-1} (see **Figure S2.9** for the comparison of CV curves of TANI/GN and PANI/GN in the absence and presence of 0.01 M HQ). The anodic oxidation wave of HQ→Q overlaps well with the electrochemical potential of the redox transition

in TANI from the AT*g*GN electrode around 0.45–0.6 V. As can be seen from **Figure 2.5b**, the intensity of the pair of redox peaks increases significantly as the concentration of HQ is elevated in the electrolyte, which can be explained by the fact that more HQ takes part in the Faradaic reactions and extra electrons work as electron shuttles to the electrode enhancing the electron-transfer processes of the AT*g*GN electrode.[55, 61] **Figure 2.5c** displays the GCD profiles with various concentrations of HQ in 1.0 M H_2SO_4 collected at a current density of 8 mA cm^{-2}. The discharge time becomes longer as the concentration of HQ increases, which is consistent with the CV curves. The areal capacitance of the AT*g*GN electrode was further calculated at various current densities based on the discharge time from the GCD profiles (**Figure 2.5d**). The AT*g*GN electrode shows an areal capacitance of 211 mF cm^{-2} at 3 mA cm^{-2} with 0.02 M HQ, which is about 1.7 times higher than that obtained in the pristine 1.0 M H_2SO_4 (126 mF cm^{-2} at 3 mA cm^{-2}). The areal capacitance of the AT*g*GN electrode shows a 30% increase even in the electrolyte with only 0.01 M HQ (164 mF cm^{-2} at 3 mA cm^{-2}) compared to the pristine 1.0 M H_2SO_4. This promising result indicates that the capacitance of the AT*g*GN supercapacitors can be remarkably enhanced by the introduction of the redox additive HQ into the electrolyte.

As demonstrated in **Figure 2.5e,f**, the areal capacitance and specific capacitance of all three composites (AT*g*GN, TANI/GN, and PANI/GN) increases in the presence of 0.01 M HQ compared to pristine 1.0 M H_2SO_4, indicating additional pseudocapacitance originating from HQ. For the AT*g*GN electrode, the areal capacitance increases from 135 mF cm^{-2} to 184 mF cm^{-2} at 1 mA cm^{-2} and the specific capacitance increases from 263 F g^{-1} to 401 F g^{-1} at 1 mA cm^{-2} in the presence of 0.01 M HQ. In the presence of 0.01 M HQ, the AT*g*GN electrode retains an areal capacitance of 128 mF cm^{-2} and a specific capacitance of 279 F g^{-1} at 20 mA cm^{-2}, suggesting that the AT*g*GN electrode still retains high rate capability in the HQ-containing redox-active

electrolyte. Similarly, the rate capability of the two physical mixtures TANI/GN and PANI/GN remains relatively constant in the presence of 0.01 M HQ. Note that the specific capacitances in **Figure 2.5f** were calculated based only on the mass of the electrode materials. In addition, the AT*g*GN electrode exhibits greater enhancement in the areal capacitance in the presence of 0.01 M HQ compared to the two physical mixtures − TANI/GN and PANI/GN, implying that more HQ contributes to the Faradaic capacitance on the surface of the AT*g*GN electrode than with the physical mixtures. The simultaneous formation of 3D GN and grafting of TANI during the synthesis of AT*g*GN not only helps to prevent the aggregation of TANI, but also reduces the restacking of graphene layers, leading to a larger internal surface area[58] compared to the physical mixtures. The 3D porous nature of AT*g*GN offers efficient electron and ion transport pathways and allows easy access of the electrolyte ions to the surface of the electrode for fast and reversible redox reactions (pseudocapacitance) as well as ion adsorption and desorption (electric double-layer capacitance). Therefore, an HQ-containing redox-active electrolyte is suitable for use with the AT*g*GN composite to boost the capacitance.

For the pursuit of practical applications, the symmetric AT*g*GN||AT*g*GN devices in a redox-active PVA/H_2SO_4/HQ gel electrolyte were further assessed. The concentration of H_2SO_4 and HQ in the gel electrolyte was 1.0 M and 0.01 M, respectively. A schematic illustration of the symmetric AT*g*GN||AT*g*GN device configuration and a zoom-in view of the 3D microstructure within an AT*g*GN electrode are depicted in **Figure 2.6a**. An all-solid-state symmetric AT*g*GN||AT*g*GN supercapacitor was fabricated from two identical AT*g*GN electrodes, separated by an ion-porous membrane and a PVA/H_2SO_4/HQ gel electrolyte. Within the 3D graphene porous structure, the covalently grafted TANI as well as the HQ molecules from the electrolyte both contribute to the pseudocapacitance of the device.

Figure 2.6b,c show the CV curves and the GCD profiles of the symmetric AT*g*GN||AT*g*GN device with the redox-active gel electrolyte at various scan rates and current densities, respectively. A comparison of the CV and GCD curves of the symmetric AT*g*GN||AT*g*GN device in the absence and presence of 0.01 M HQ is displayed in **Figure S2.10**. Both the CV and GCD plots with the HQ-containing electrolyte exhibit similar shapes to those using a normal PVA/H_2SO_4 gel electrolyte, but with enhanced charge storage performance. As demonstrated in **Figure 2.6b**, the CV curves with the HQ containing electrolyte display a larger area under each CV curve compared to those with the normal electrolyte. Similarly, the GCD profiles with the HQ containing electrolyte (**Figure 2.6c**) exhibit greater discharge time compared to those without HQ. These results indicate that the introduction of the redox additive HQ into the normal PVA/H_2SO_4 gel electrolyte boosts the capacitance of the symmetric AT*g*GN||AT*g*GN device. It should be noted that the CV curves of the symmetric AT*g*GN||AT*g*GN device in the presence of 0.01 M HQ (**Figure 2.6b**) exhibit a slight deviation from the rectangular shape at high scan rates compared to those in the absence of HQ. This is a consequence of the slower kinetics of the hydroquinone–quinone (HQ–Q) Faradaic process pertaining to the time needed to form the double layer, which leads to a contribution of additional pseudocapacitance from this redox reaction at lower scan rates.[59]

The long-term cycling stability of the symmetric AT*g*GN||AT*g*GN device in the HQ containing gel electrolyte was evaluated over 100,000 charge–discharge cycles at a current density of 2.5 mA cm^{-2}. As demonstrated in **Figure S2.11**, the symmetric AT*g*GN||AT*g*GN device shows outstanding cycling stability in an HQ containing gel electrolyte, which retains 82% of its initial capacitance even after 100,000 charge–discharge cycles. The device lost about 12% of its initial capacitance over the first 1000 cycles and its capacitance decreased very slowly thereafter.

Figure 2.6d presents a comparison of the cycling stability of the symmetric AT*g*GN||AT*g*GN devices in the absence and presence of 0.01 M HQ during 30,000 charge–discharge cycles. As can be seen, the cycling performance of the symmetric AT*g*GN||AT*g*GN device in the presence of 0.01 M HQ shows capacitance retention of 78% after 30,000 cycles, which is not as good as that with a normal PVA/H_2SO_4 gel electrolyte (87% capacitance retention over 30,000 cycles), which could be ascribed to the lack of completion of the HQ redox reaction within the operating voltage window of the device.[58] It should be noted that although the cycling stability of the HQ-containing device is slightly lower than that without HQ, the overall capacitance has been elevated to a higher level compared to the normal electrolyte. Even after 30,000 cycles, the specific capacitance of the HQ-containing cell is still 28% higher than that obtained in the normal PVA/H_2SO_4 gel electrolyte. The inset to **Figure 2.6d** displays the CV curves of the device before and after 1000, 10,000, 30,000, and 90,000 charge−discharge cycles at 50 mV s^{-1}. The area under the CV curve decreased relatively fast during the first 1000 cycles, but slowed down considerably thereafter. The CV curves retained essentially the same rectangular shape during the cycling process.

Figure 2.6e demonstrates the rate capability studies of the symmetric AT*g*GN||AT*g*GN devices in the absence and presence of 0.01 M HQ. Note that the values of specific capacitance and current density of the device containing 0.01 M HQ in **Figure 2.6e** were calculated based on the mass of the AT*g*GN electrode active materials. As illustrated in **Figure 2.6e**, the HQ-containing cell exhibits a higher specific capacitance of 188 F g^{-1} at 1 mA cm^{-2} compared to the normal cell without HQ (148 F g^{-1} at 1 mA cm^{-2}). The areal capacitance of the HQ-containing cell also shows a higher value of 94 mF cm^{-2} at 0.5 mA cm^{-2} compared to the normal PVA/H_2SO_4 cell (81 mF cm^{-2} at 0.5 mA cm^{-2}). Even at a high current density of 10 mA cm^{-2}, the specific capacitance of the device with 0.01 M HQ (57 F g^{-1}) is three times higher than that of the normal

PVA/H_2SO_4 cell (19 F g^{-1}), further verifying that the addition of HQ into the electrolyte boosts the capacitance of the symmetric AT*g*GN||AT*g*GN device.

2.4 Conclusions

This work deals with one of the fundamental problems of PANI-based supercapacitors: poor charge−discharge cycling stability. A facile "grafting to" approach *via* perfluorophenylazide coupling chemistry has been successfully demonstrated for the synthesis of covalently grafted TANI to a 3D GN. Through a one-step solvothermal reaction, the simultaneous covalent grafting of TANI and the reduction of GO to form a 3D GN has been realized. The resulting AT*g*GN composite can exhibit much improved electrochemical performance. Remarkably, it can achieve superior cycling stability with 85% capacitance retention after 30,000 charge−discharge cycles in a three-electrode setup, which far exceeds that of noncovalently grafted, long-chain PANI-based hybrid materials with an equivalent PANI/TANI content. Both the utilization of short-chain TANI and the formation of covalent connections between the two components lead to remarkable cycling stability. The subsequently fabricated all-solid-state symmetric devices can still demonstrate outstanding cycling stability with capacitance retention above 87% after 30,000 charge−discharge cycles, placing it among the best long-cycle-life PANI-based supercapacitors. Furthermore, a redox additive − hydroquinone (HQ) − was introduced into the electrolyte, leading to an enhancement in the specific capacitance of the supercapacitor, while the symmetric devices were still capable of delivering an ultralong cycle life (82% capacitance retention after 100,000 cycles). This investigation provides a facile and effective approach to achieving ultralong cycle life for conducting polymer-based energy storage devices.

2.5 Experimental Section

Synthesis of ATFB-TANI-grafted-3D GN (ATgGN) Composites: Graphene oxide (GO) was synthesized through a modified Hummer's method.[62] 4-azidotetrafluorobenzoyl tetra-aniline (ATFB-TANI) was prepared by a previous method reported elsewhere.[36] Briefly, ATFB-TANI ethanol solution (5 mL, with different concentrations) was added into a GO dispersion in ethanol (5 mL, 4 mg mL^{-1}) dropwise using a syringe pump under continuous stirring, followed by further vigorous stirring for 3 h at room temperature. The final concentration of GO was 2 mg mL^{-1} and the total volume of the mixture was 10 mL. The uniform mixture was then sealed in a 25 mL Teflon-lined autoclave and maintained at 180 °C for 24 h. The autoclave was then cooled naturally to room temperature. The as-prepared AT*g*GN composite was thoroughly washed with ethanol until the supernatant turned colorless in order to remove any residual unreacted ATFB-TANI molecules followed by repeated washing with deionized water. The final AT*g*GN composite was freeze-dried using liquid nitrogen. A pure 3D GN was also prepared by the same procedure with only the presence of the GO suspension (2 mg mL^{-1}).

Fabrication of ATgGN Electrodes and All-solid-state Symmetric ATgGN||ATgGN Supercapacitors: The AT*g*GN working electrodes were made by drop-casting the homogeneous sample solution (no binder) on graphite paper current collectors (1 cm × 1 cm), which were then dried under ambient conditions overnight. The mass loading of each electrode was calculated from the weight difference before and after drop-casting (measured by a Mettler Toledo MX5 microbalance ±1 μg error). Typical loadings of the materials were ~0.3–0.5 mg cm^{-2}. An all-solid-state symmetric AT*g*GN||AT*g*GN supercapacitor was fabricated from two identical pieces (1 cm × 1 cm) of AT*g*GN electrodes, separated by an ion-porous membrane (cellulose separator, NKK TF4030). Two kinds of gel electrolyte were used in fabricating the symmetric devices:

PVA/1.0 M H_2SO_4 and PVA/1.0 M H_2SO_4/0.01 M HQ. Briefly, PVA (1.0 g) was dissolved in water (10 mL) and stirred vigorously for 30 min at 90 °C. Next, stock H_2SO_4 (0.56 mL, 1.84 g mL^{-1}) was added to make a PVA/1.0 M H_2SO_4 gel electrolyte. For preparing the PVA/1.0 M H_2SO_4/0.01 M HQ gel electrolyte, HQ (11.0 mg, 0.1 mmol) was further added into the as-prepared PVA/1.0 M H_2SO_4 (10 mL). The resulting gel electrolytes were applied to the electrodes and left for 30 min in order to ensure complete wetting of the electrode surfaces. The two electrolyte-filled electrodes and the separator were then assembled and dried for 12 h at room temperature until fully solidified.

Characterization: The morphological and structural characterizations of the materials were carried out by scanning electron microscopy (SEM) using a JEOL JSM-6700F FE-SEM and transmission electron microscope (TEM, Tecnai G TF20 TEM, FEI Inc.). Elemental analyses of the samples were obtained using an energy dispersive X-ray spectrometer (EDS, as an attachment to an SEM instrument). Fourier-transform infrared (FT-IR) spectroscopy by attenuated total reflectance was performed on a JASCO FT/IR-6300. X-ray photoelectron spectroscopy (XPS) measurements were obtained using a Kratos Axis Ultra DLD spectrometer with a monochromatic Al K_α X-ray source (λ = 1486.6 eV).

Electrochemical Measurements: The electrochemical measurements including CV, GCD, EIS, and cycling stability measurements were conducted using a Biologic VMP3 electrochemical workstation (VMP3b-10, USA Science Instrument). In all three-electrode studies, graphite sheet was used as the counter electrode and Ag/AgCl was used as the reference electrode. The EIS measurements were performed at 0.2 V relative to the reference electrode over a frequency range from 200 kHz to 10 mHz with an amplitude of 10 mV. In the two-electrode tests of the ATgGN

symmetric devices, the EIS measurements were performed at open circuit voltage over a frequency range from 1 kHz to 10 mHz with an amplitude of 10 mV.

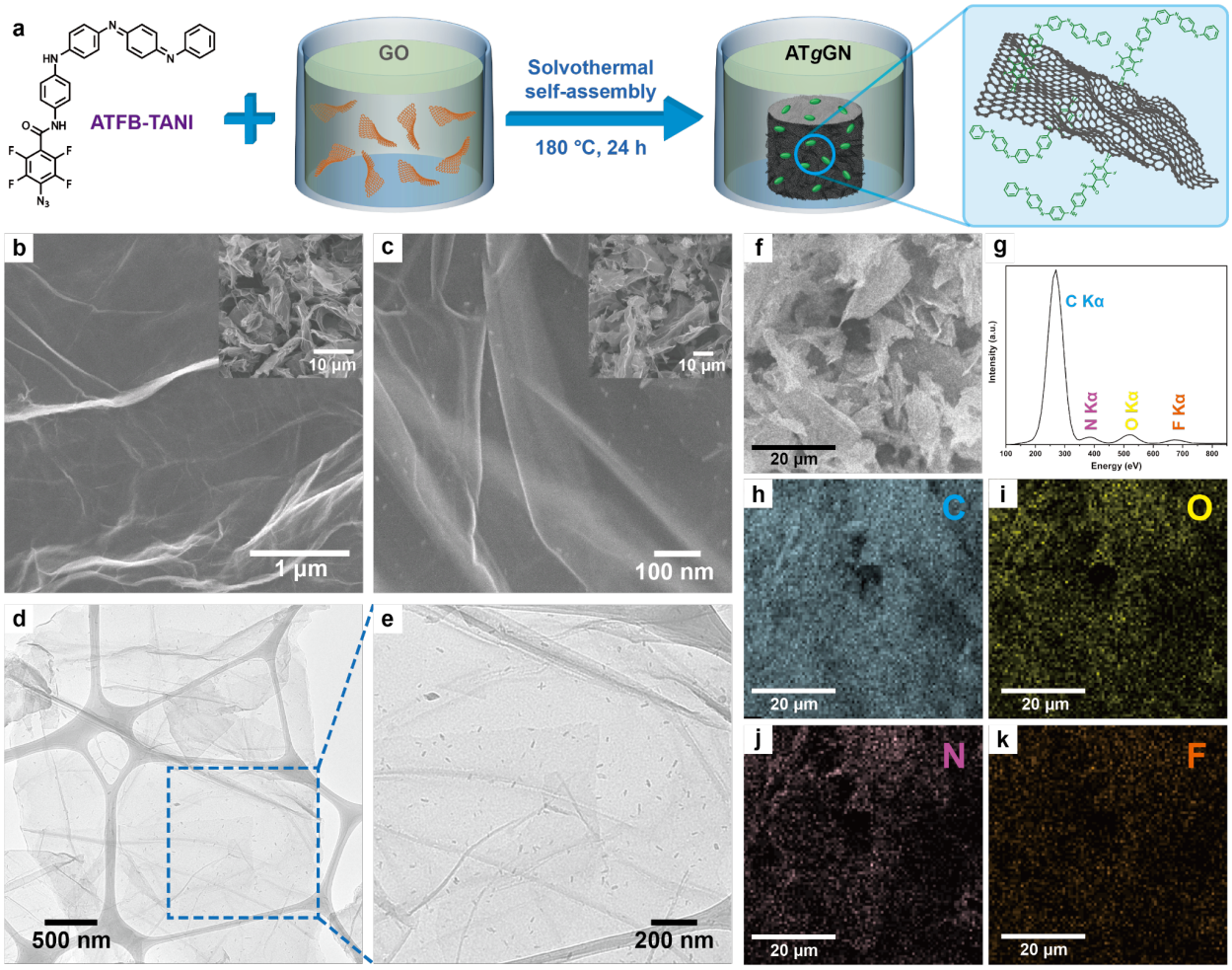

Figure 2.1. (a) Schematic illustration of the fabrication process for an ATFB-TANI-*grafted*-3D GN (ATgGN). SEM images of (b) a pure GN and (c) ATgGN, with the insets showing the images at lower magnifications. (d,e) TEM images of ATgGN at different magnifications. (f) The SEM image, (g) EDS spectrum, and (h–k) EDS elemental mapping of carbon, oxygen, nitrogen, and fluorine of ATgGN.

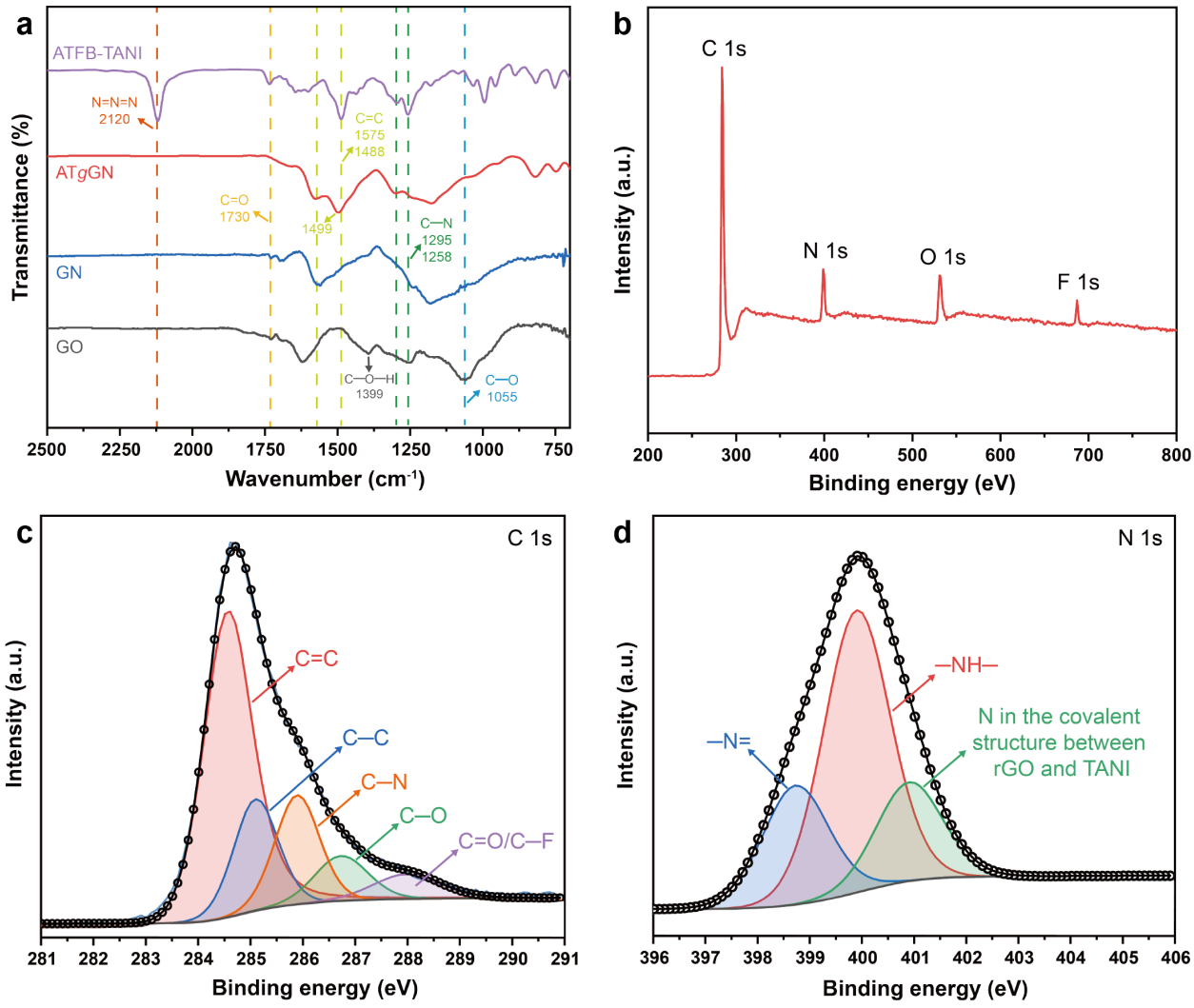

Figure 2.2. (a) FT-IR spectra of the ATgGN, pure GN as well as starting materials GO and ATFB-TANI. (b) The survey XPS spectrum of the ATgGN. Deconvoluted core level XPS spectra of ATgGN, (c) C 1s and (d) N 1s.

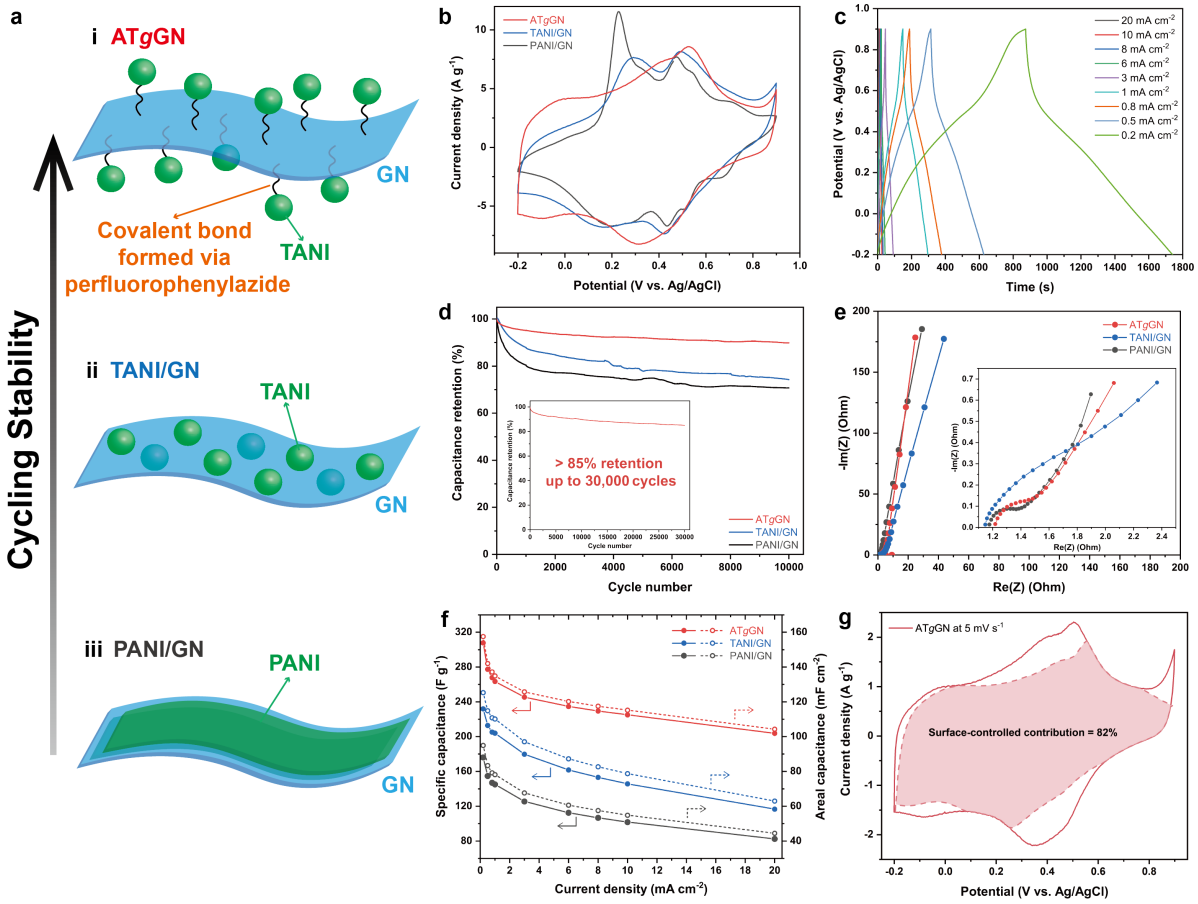

Figure 2.3. Investigation and comparison of the electrochemical performance of the ATgGN, TANI/GN, and PANI/GN electrodes in 1.0 M H_2SO_4 in a three-electrode cell setup. (a) Schematic illustration of the structure of (i) ATgGN, (ii) TANI/GN, and (iii) PANI/GN. The cycling stability of each composite exhibits an increasing trend from (iii) to (ii) to (i). (b) The CV curve of each sample at a scan rate of 20 mV s^{-1}. (c) GCD profiles of the ATgGN electrode at different current densities ranging from 0.2 to 20 mA cm^{-2}. (d) Cycling stability study during 10,000 charge–discharge cycles. The inset shows the cycling stability of the ATgGN electrode during 30,000 charge–discharge cycles. (e) The Nyquist plots over a frequency range from 200 kHz to 10 mHz. The inset shows a magnified high-frequency region. (f) Rate capability studies, specific capacitance, and areal capacitance as a function of current density. (g) Quantification of the surface-controlled and diffusion-controlled charge storage in ATgGN electrode at 5 mV s^{-1}.

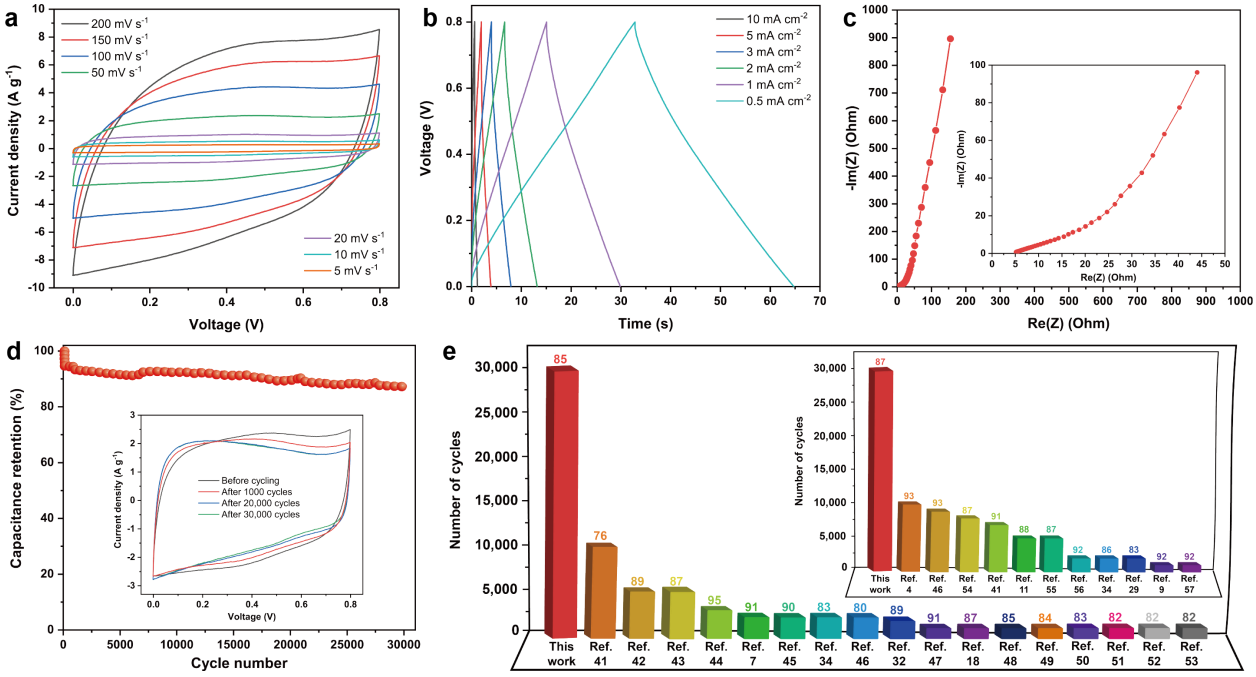

Figure 2.4. Electrochemical evaluation of the symmetric ATgGN||ATgGN devices in a PVA/H_2SO_4 gel electrolyte. (a) CV curves at various scan rates from 5 to 200 mV s^{-1}. (b) GCD profiles at different current densities from 0.5 to 10 mA cm^{-2}. (c) The Nyquist plot over a frequency range from 1 kHz to 10 mHz. The inset shows a magnified high-frequency region. (d) Cycling stability study during 30,000 charge–discharge cycles. The inset displays the CV diagrams before and after 1000, 20,000, and 30,000 charge–discharge cycles at 50 mV s^{-1}. (e) A comparison of the cycling stability of ATgGN in a three-electrode cell setup with other carbon- and PANI-based hybrid materials (the height of each bar represents the number of cycles and the label on each bar represents the corresponding capacitance retention in percentage). The inset shows a comparison of the cycling stability of the ATgGN||ATgGN symmetric device with other carbon- and PANI-based symmetric devices.

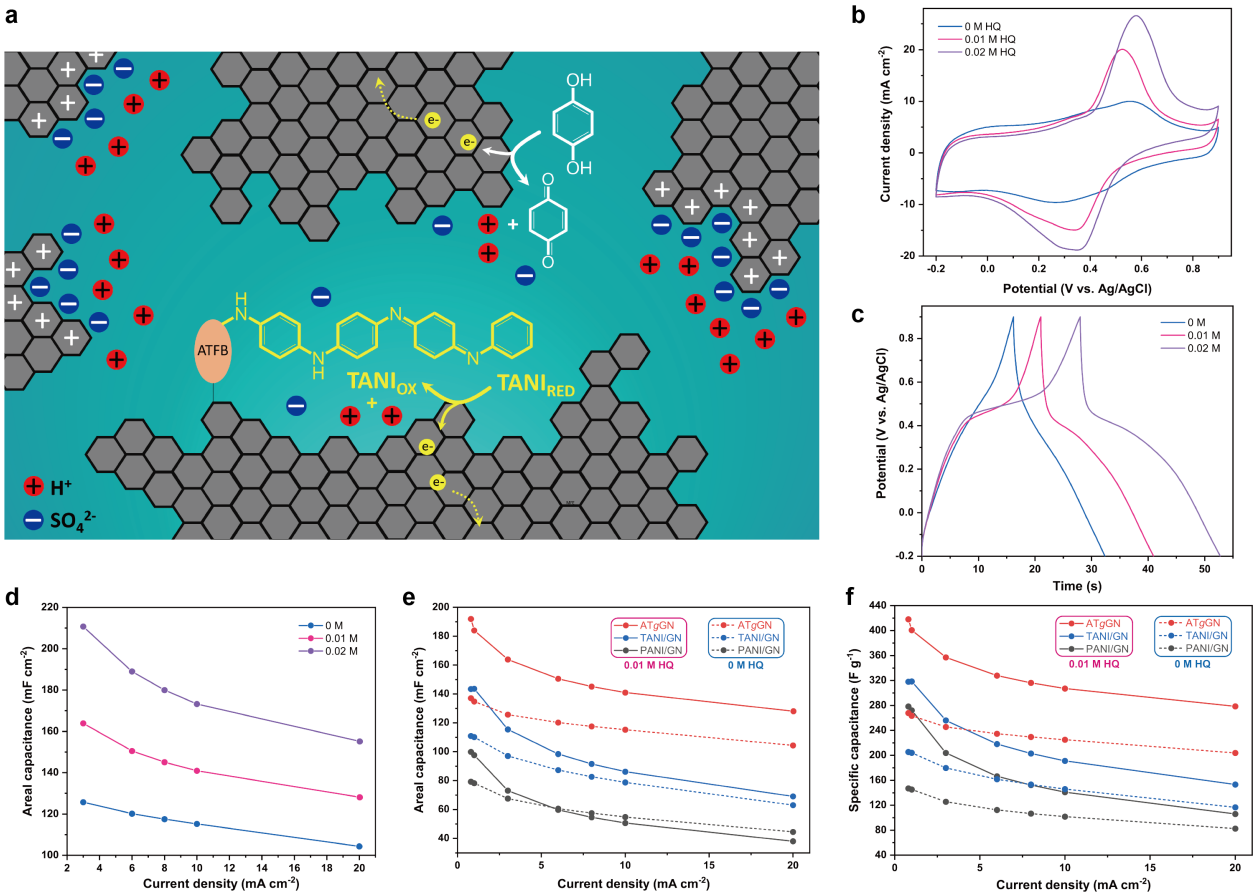

Figure 2.5. Electrochemical evaluation of the prepared electrodes in an HQ containing redox-active electrolyte in a three-electrode cell setup. (a) Schematic illustration of the charge storage mechanism in ATgGN supercapacitors in the presence of a redox additive HQ in 1.0 M H_2SO_4 electrolyte. (b) CV curves of ATgGN collected at an increasing concentration of HQ, tested at a scan rate of 50 mV s^{-1}. (c) GCD plots of ATgGN collected at a current density of 8 mA cm^{-2}. (d) Areal capacitance vs. current density for ATgGN in 1.0 M H_2SO_4 containing different concentrations of HQ (0, 0.01, and 0.02 M). (e) Areal capacitances and (f) specific capacitances of the ATgGN, TANI/GN, and PANI/GN electrodes at different current densities in 1.0 M H_2SO_4 in the absence and presence of 0.01 M HQ.

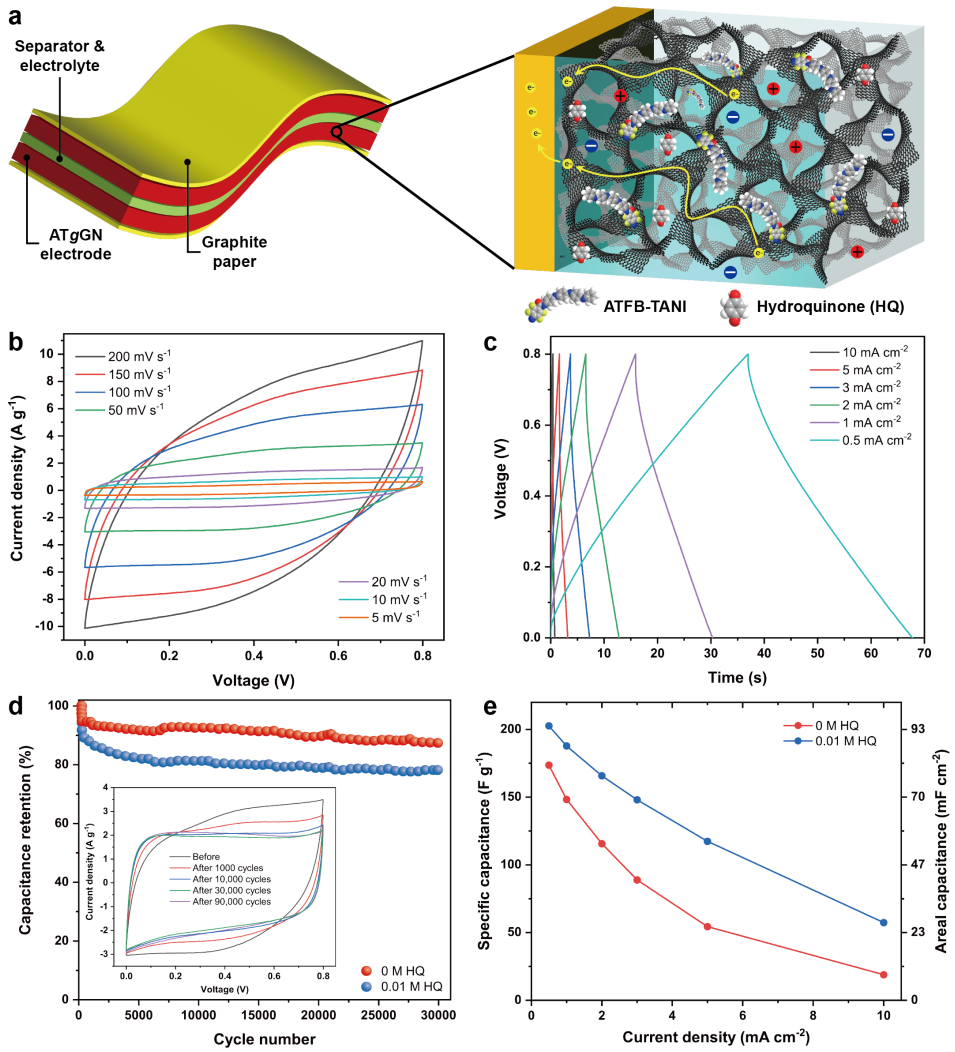

Figure 2.6. Electrochemical evaluation of the symmetric ATgGN||ATgGN devices in a redox-active PVA/H_2SO_4/HQ gel electrolyte. (a) Schematic illustration of the configuration of an all-solid-state symmetric ATgGN||ATgGN device and a zoom-in view of the 3D microstructure within an ATgGN electrode. (b) CV curves at various scan rates from 5 to 200 mV s^{-1}. (c) GCD profiles at different current densities from 0.5 to 10 mA cm^{-2}. (d) Comparison of the cycling stability in the absence and presence of 0.01 M HQ during 30,000 charge–discharge cycles. The inset displays the CV curves of the HQ-containing device before and after 1000, 10,000, 30,000, and 90,000 charge−discharge cycles at 50 mV s^{-1}. (e) Specific capacitances and areal capacitances of the symmetric devices in the absence and presence of 0.01 M HQ at different current densities.

2.6 Supporting Information

2.6.1 Experimental Section

Materials: Graphite paper used as a current collector was purchased from Digi-Key Electronics (manufactured by Panasonic Electronic Components, part number: P13689-ND). Polyvinyl alcohol (PVA, M_w = 31,000–50,000, 98–99% hydrolyzed) and hydroquinone (HQ, ≥99%) were purchased from Sigma-Aldrich. Sulfuric acid (H_2SO_4) and ethanol (EtOH) were purchased from Fisher Scientific. All chemicals were reagent grade and used without further purification.

Preparation of TANI: Aniline tetramer (TANI) was prepared using a modified method reported elsewhere.[36] Briefly, N-phenyl-1,4-phenylenediamine (aniline dimer, 0.92 g, 5 mmol, 1 equiv.) was dissolved in ethanol (10 mL) followed by a gentle ultrasonication. Then, hydrochloric acid (HCl, 50 mL, 0.1 M) was added to a round bottom flask (250 mL) and stirred for 30 min. A solution of ferric chloride hexahydrate (0.81 g, 5 mmol, 1 equiv.) dissolved in HCl (100 mL, 0.1 M) was quickly poured into the round bottom flask. The mixture was stirred at room temperature for ~2 h. After the reaction, the precipitate was washed with 0.1 M HCl at least three times (50 mL per wash) in order to fully remove the iron ions. The solid was then stirred with 2.0 M ammonium hydroxide (~50 mL) for 60 min, followed by cycles of centrifugation and washing with deionized water until the supernatant became pH neutral. The final product was collected after air dried overnight.

Preparation of PANI: Polyaniline (PANI) nanofibers were synthesized through a previously reported method.[63] Briefly, aniline monomer (0.3 mL) and ammonium peroxydisulfate (APS, 0.18 g) were dissolved in HCl (10 mL, 1.0 M), respectively. The two newly prepared solutions were mixed together, shaken vigorously for ~20 s, and left still overnight. Then, the precipitate

was thoroughly washed with 1.0 M HCl for several times and air-dried for a few days. The SEM images of the obtained PANI nanofibers are presented in **Figure S2.3**.

Preparation of TANI/GN and PANI/GN: The two physical mixtures – TANI/GN and PANI/GN – were prepared by a traditional physical mixing method. Briefly, the 3D graphene network (GN) was prepared by the same solvothermal reaction as AT*g*GN with only the presence of the GO suspension (2 mg mL^{-1}). The TANI or PANI was mixed with the GN in deionized water with the same TANI content as the AT*g*GN7 composite (the weight ratio of TANI to GN was calculated as 1.4:1 from XPS analysis). The uniform mixtures were obtained after vigorous stirring at room temperature overnight. The TANI/GN and PANI/GN electrodes were made by directly drop-casting the as-synthesized mixtures (no binder) on graphite paper current collectors (1 cm × 1 cm), which were then dried under ambient conditions overnight.

Calculation methods of electrochemical data: The gravimetric specific capacitance (C_s) and areal capacitance (C_a) of the electrodes tested in a three-electrode cell setup were calculated from the GCD profiles using the following equations[40],

$$C_s = \frac{I \times \Delta t}{m \times \Delta V} \ (F\ g^{-1}) \qquad \text{(S2.1) (Three-electrode)}$$

$$C_a = \frac{I \times \Delta t}{a \times \Delta V} \ (mF\ cm^{-2}) \qquad \text{(S2.2) (Three-electrode)}$$

where I is the discharge current (mA), Δt is the discharge time (s), ΔV is the potential window (V), m is the mass of the active electrode materials (mg) and a represents the surface area of the electrode (cm^2). The specific capacitance ($C_{S,electrode}$) and areal capacitance ($C_{A,electrode}$) of each of the positive and negative electrodes can be derived from the capacitance of the symmetric two-electrode device calculated from GCD profiles according to the following equations[40],

$$C_{S,electrode} = 4 \times C_{S,device} = 4 \times \frac{I \times \Delta t}{M \times \Delta V} \ (F\ g^{-1}) \qquad \text{(S2.3) (Two-electrode)}$$

$$C_{A,electrode} = 2 \times C_{A,device} = 2 \times \frac{I \times \Delta t}{A \times \Delta V} \, (mF \, cm^{-2})$$ (S2.4) (Two-electrode)

where I is the discharge current (mA), Δt is the discharge time (s), ΔV is the potential window (V), M is the total mass of the active materials used in the two electrodes (mg) and A represents the geometric area of the device (cm^2).

2.6.2 Materials Characterizations

When taking a close look at the FT-IR spectra (**Figure S2.1a**), the intensities of the bands at 1488 and 1295 cm^{-1} increase from AT*g*GN1 to AT*g*GN7. These two bands can be attributed to the stretching vibrations of the C=C bonds on the benzenoid rings and the aromatic amine C–N stretching of TANI, respectively. The slightly increasing peak intensities demonstrate a higher TANI presence in the final AT*g*GN network with more initial ATFB-TANI. The Raman spectrum of a pure graphene network (GN) (**Figure S2.1b**) displays two prominent peaks at 1331 and 1595 cm^{-1}, which correspond to the D mode (or the phonon mode related to the conversion of an sp^2-hybridized carbon to an sp^3-hybridized carbon) and the G mode (related to the vibration of an sp^2-hybridized carbon), respectively. In the spectra of the AT*g*GN composites, the bands at 1339 and 1595 cm^{-1} can be attributed to the merger of signals of TANI and the graphene network structure. Note that the D band of AT*g*GN blue shifts from 1331 to 1339 cm^{-1} compared to GN, indicating strong interactions between TANI and the graphene network.[30, 64] In addition, the bands at 1162–1192, 1222, 1263, 1391, 1469, 1499, 1565, and 1629 cm^{-1} demonstrate the existence of TANI. Furthermore, the increasing intensity of these peaks from AT*g*GN1 to AT*g*GN7 also suggests a trend of the more the initial TANI used, the higher the resulting presence of TANI in the final AT*g*GN product. Therefore, the Raman analysis together with the FT-IR and XPS analysis supports the covalent attachment of TANI to the graphene network.

From the survey scans (**Figure S2.2**), the nitrogen content (in at%) of the AT*g*GN1, AT*g*GN3, AT*g*GN5 and AT*g*GN7 was determined to be 4.79%, 6.26%, 7.39% and 7.92%, respectively. Since GO is nitrogen-free and the only nitrogen containing species is ATFB-TANI, the nitrogen contents can be converted to the weight ratios of TANI to GN, which were calculated and are presented in **Table S2.1**. The detailed calculations for AT*g*GN7 are as follows:

The molecular mass (without H) of ATFB-TANI after thermal activation (loss of N_2, $C_{31}N_5OF_4$):

$$M(ATFB-TANI) = 31 \times 12\,u + 5 \times 14\,u + 1 \times 16\,u + 4 \times 19\,u = 534\,u$$

The molecular mass (without H) of TANI ($C_{24}N_4$):

$$M(TANI) = 24 \times 12\,u + 4 \times 14\,u = 344\,u$$

Conversion of N in at% to N in wt% within the composite:

$$\frac{M(N)}{M(Total)} = \frac{7.92 \times 14\,u}{87.3 \times 12\,u + 7.92 \times 14\,u + 3.83 \times 16\,u + 0.95 \times 19\,u} = 0.0896$$

The weight percentage of ATFB-TANI in the composite:

$$\frac{M(ATFB-TANI)}{M(Total)} = \frac{M(ATFB-TANI)}{M(N)} \times \frac{M(N)}{M(Total)} = \frac{534\,u}{5 \times 14\,u} \times 0.0896 = 0.683$$

The weight ratio of TANI to rGO:

$$\frac{M(TANI)}{M(rGO)} = \frac{M(TANI)}{M(ATFB-TANI)} \times \frac{M(ATFB-TANI)}{M(rGO)} = \frac{344\,u}{534\,u} \times \frac{0.683}{(1-0.683)} = 1.39$$

A GN/unbonded TANI analogue (GN/TANI) was prepared by using phenyl/amine end-capped TANI (without the perfluorophenylazide group) instead of ATFB-TANI as the starting material through the same AT*g*GN preparation procedure. The SEM images of the GN/unbonded TANI analogue (**Figure S2.4a,b**) reveal severe aggregation of unbonded TANI. In contrast, the TANI observed in the AT*g*GN made using the perfluorophenylazide chemistry is much more uniformly distributed on the surface of the rGO sheets (**Figure S2.4c,d**). This indicates that the covalent bond

formation is capable of alleviating the aggregation of TANI. The XPS analysis (**Figure S2.4e**) shows that ~93% of the unbonded TANI in the GN/TANI was removed during the rinsing process. The existence of a small amount of TANI can be explained by the physical interactions between TANI and rGO, including π–π stacking interactions, Van der Waals forces, hydrogen bonding, etc.

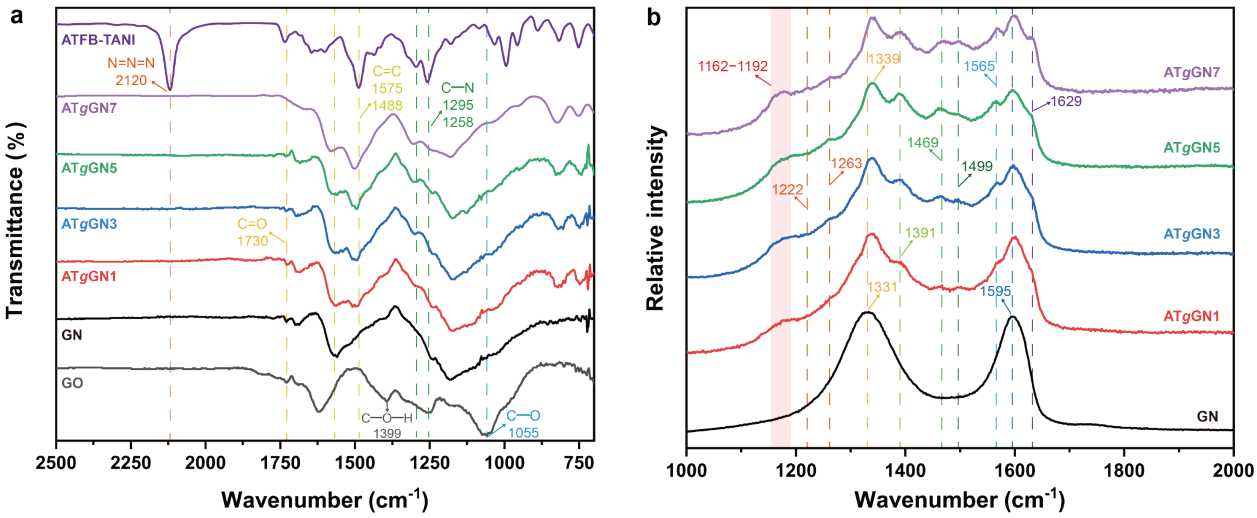

Figure S2.1. (a) FT-IR spectra and (b) Raman spectra of ATgGN with different TANI contents.

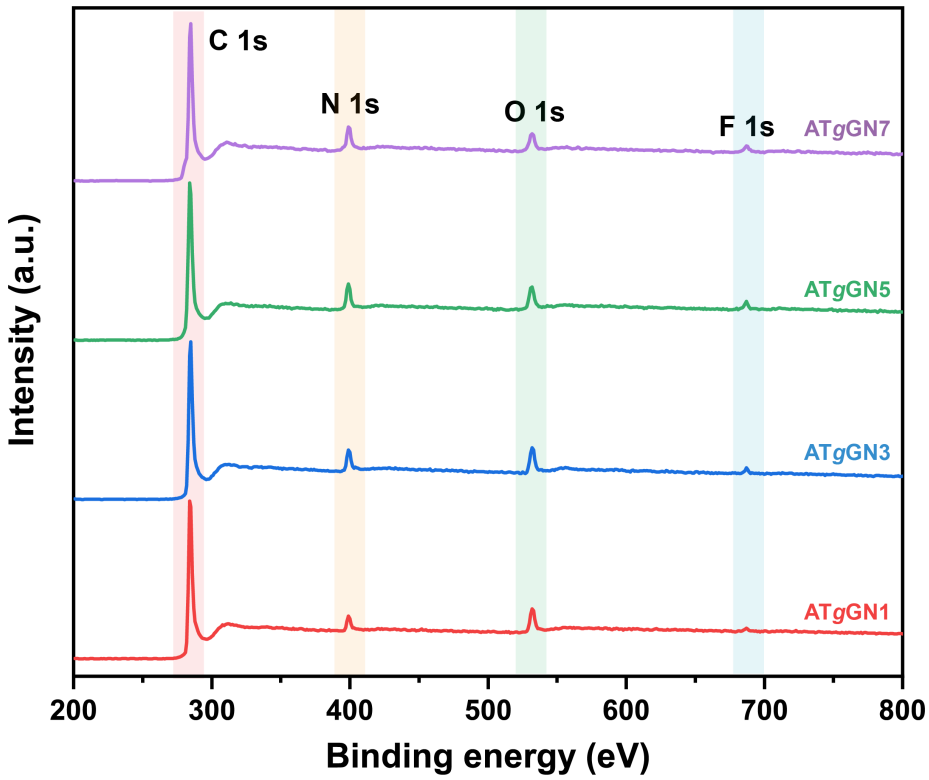

Figure S2.2. XPS survey scans of ATgGN with different TANI contents.

Table S2.1. The Weight Ratios of TANI to rGO in ATgGN with Different TANI Contents

ATgGN	C 1s %	N 1s %	O 1s %	F 1s %	Weight ratio of TANI to rGO[a)]
1	91.48	4.79	3.42	0.31	0.46 : 1
3	90.55	6.26	2.75	0.43	0.77 : 1
5	88.10	7.39	3.59	0.93	1.14 : 1
7	87.30	7.92	3.83	0.95	1.39 : 1

a) Calculated from N 1s %.

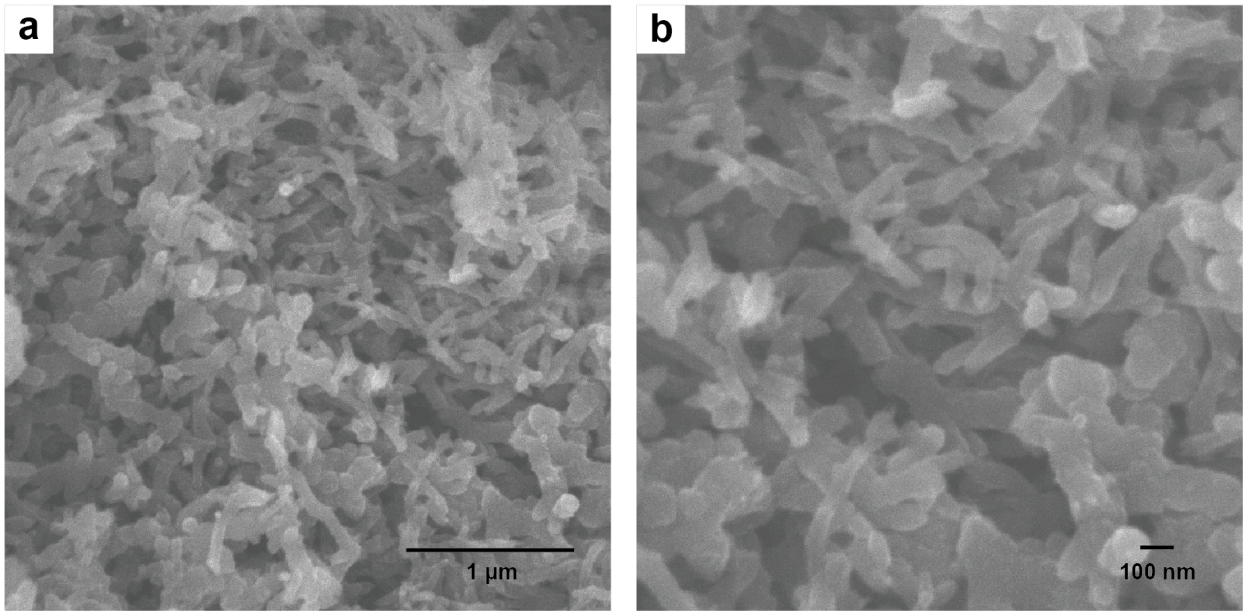

Figure S2.3. SEM images of PANI nanofibers at different magnifications.

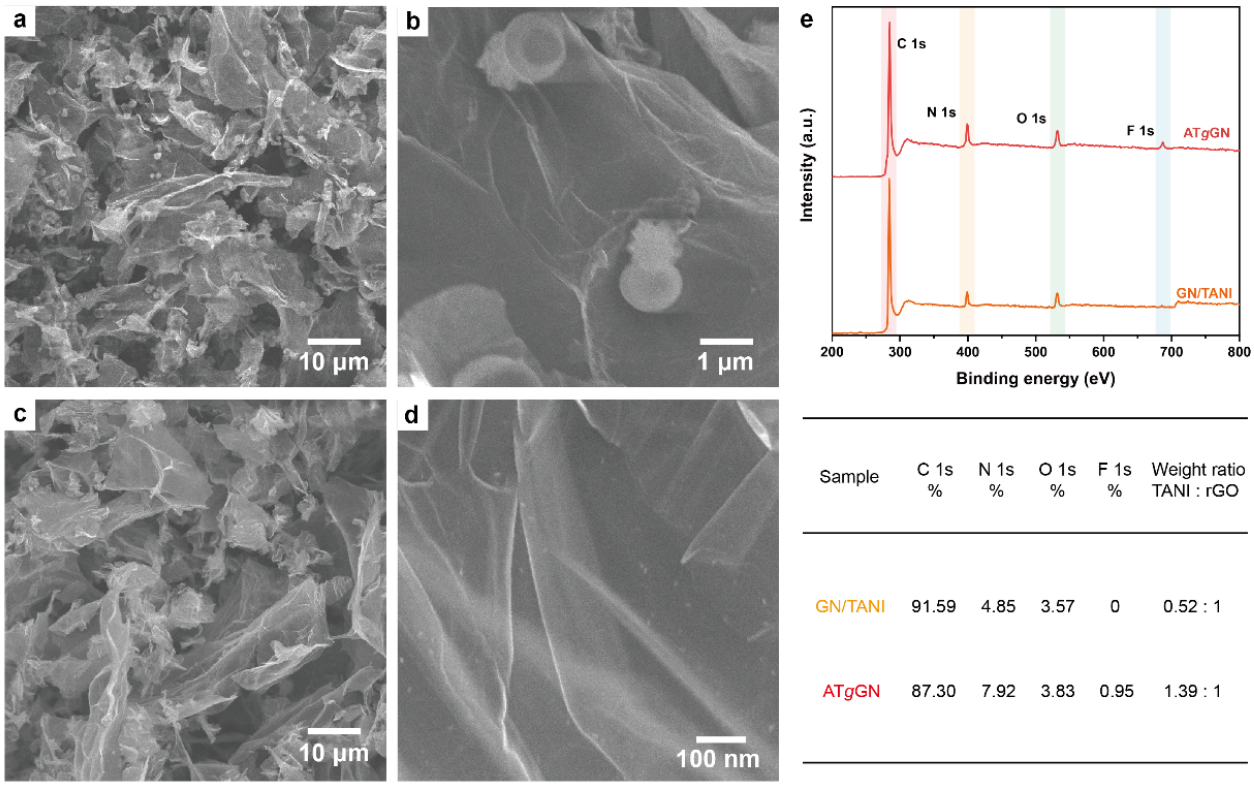

Sample	C 1s %	N 1s %	O 1s %	F 1s %	Weight ratio TANI : rGO
GN/TANI	91.59	4.85	3.57	0	0.52 : 1
ATgGN	87.30	7.92	3.83	0.95	1.39 : 1

Figure S2.4. (a,b) SEM images of GN/TANI at low and high magnification. (c,d) SEM images of ATgGN at low and high magnification. (e) XPS survey scans of GN/TANI and ATgGN, with a table providing the quantitative analysis.

2.6.3 Electrochemical Measurements and Analysis

The charge storage process can be interpreted based on the dependency of the current response on the scan rate in a cyclic voltammetry test according to **Equation S2.5**,[40, 65]

$$i(v) = av^b \quad \text{(S2.5)}$$

where the current *i* is fit to a power law with the potential scan rate *v*, and the exponential term *b* is indicative of the charge storage mechanism. The *b*-value can be determined from the slope of the *log(i)* versus *log(v)* plots as shown in **Equation S2.6**.

$$log\, i(v) = log\, a + b\, log\, v \quad \text{(S2.6)}$$

For $b = 0.5$, the charge storage process is diffusion-controlled including Faradaic redox reactions, while $b = 1$ represents a capacitive or surface-contolled charge storage mechanism. The calculated *b*-value of ATgGN7 is 0.89 at the current maxima (**Figure S2.6**), indicating a combination of the two kinds of charge storage processes, in which the dominant charge storage mechanism is capacitor-like.

The diffusion contribution and capacitive contribution to the charge storage processes can be quantitatively analyzed according to **Equation S2.7**, where k_1v and $k_2v^{1/2}$ corresponds to surface- and diffusion-cotrolled processes, respectively.[66]

$$i(V) = k_1v + k_2v^{1/2} \quad \text{(S2.7)}$$

Equation S2.7 can be rearranged as **Equation S2.8** by dividing both sides by $v^{1/2}$.

$$i(V)/v^{1/2} = k_1v^{1/2} + k_2 \quad \text{(S2.8)}$$

By plotting $i(V)/v^{1/2}$ against $v^{1/2}$, the slope of the curve corresponds to k_1 and the y-intercept corresponds to k_2. Note that the maximum contribution from the diffusion-controlled processes is obtained at slow scan rates. Thereby, this analysis was conducted at slow scan rates in the range from 1 to 5 mV s^{-1}. **Figure 2.3g** shows that the surface-controlled contribution accounts for 82%

of the total charge storage, which demonstrates the fast kinetics and high rate capability of the AT*g*GN electrode.

To further differentiate between the unbonded and covalently bonded TANI, the electrochemical performance of the GN/unbonded TANI analogue (GN/TANI) was tested and compared to that of AT*g*GN. As can be seen from **Figure S2.7**, the neat GN sample exhibits almost pure electric double-layer capacitance with a specific capacitance of 135 F g^{-1} at 0.2 mA cm^{-2}. In comparison, the GN/unbonded TANI analogue shows additional pseudocapacitance from TANI, resulting in a specific capacitance of 224 F g^{-1} at 0.2 mA cm^{-2}. However, the GN/unbonded TANI analogue demonstrates much poorer rate capability (with only 20% capacitance retention at 20 mA cm^{-2}) (**Figure S2.7d**), greater ion diffusion resistance as well as higher equivalent series resistance (ESR) (**Figure S2.7c**) compared to GN and AT*g*GN. This can be ascribed to the severe aggregation of TANI in the GN/unbonded TANI sample. The AT*g*GN shows much better capacitive behavior with almost-vertical current switches at the potential extremes compared to the GN/unbonded TANI analogue (**Figure S2.7a**), which indicates faster charge transport within the electrode material. These results suggest that the covalent bonding in AT*g*GN significantly contributes to the excellent electrochemical performance.

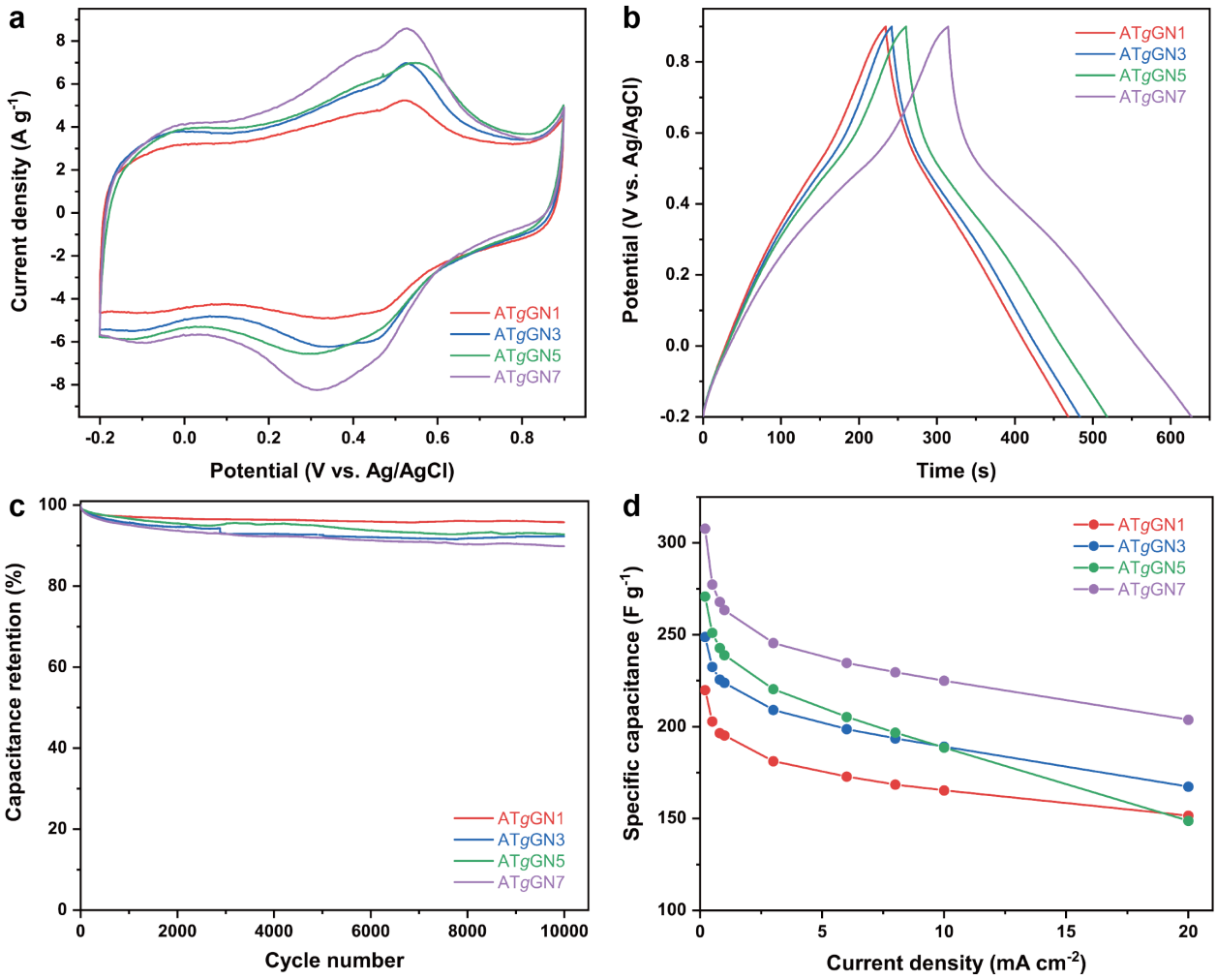

Figure S2.5. Electrochemical performance of ATgGN with different TANI contents in 1.0 M H_2SO_4 in a three-electrode cell setup. (a) CV curves at a scan rate of 20 mV s^{-1}. (b) GCD plots at a current density of 0.5 mA cm^{-2}. (c) Cycling stability study during 10,000 charge–discharge cycles; and (d) Rate performance (specific capacitance as a function of current density) of ATgGN with different TANI contents.

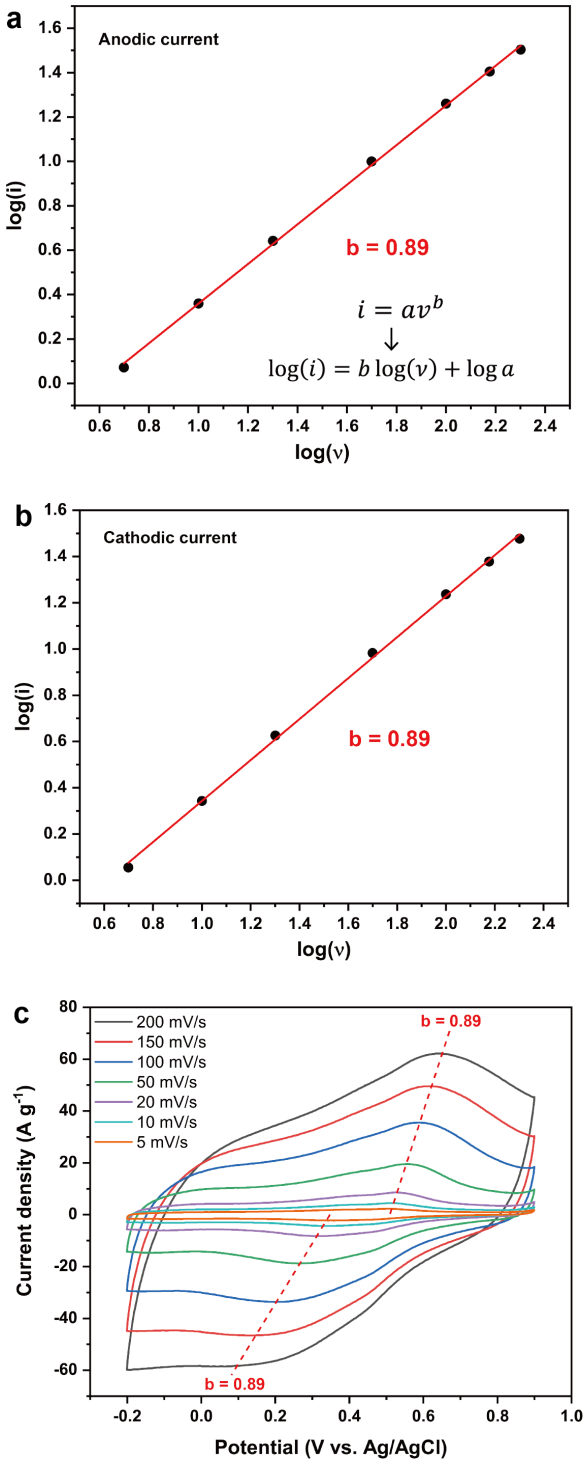

Figure S2.6. Analysis of the charge storage mechanism of ATgGN7. The *log (i)* versus *log (v)* plot of the (a) anodic and (b) cathodic peak currents. (c) The *b*-values that are calculated at the current maxima for ATgGN7 are labeled on the CV plots next to the corresponding peaks.

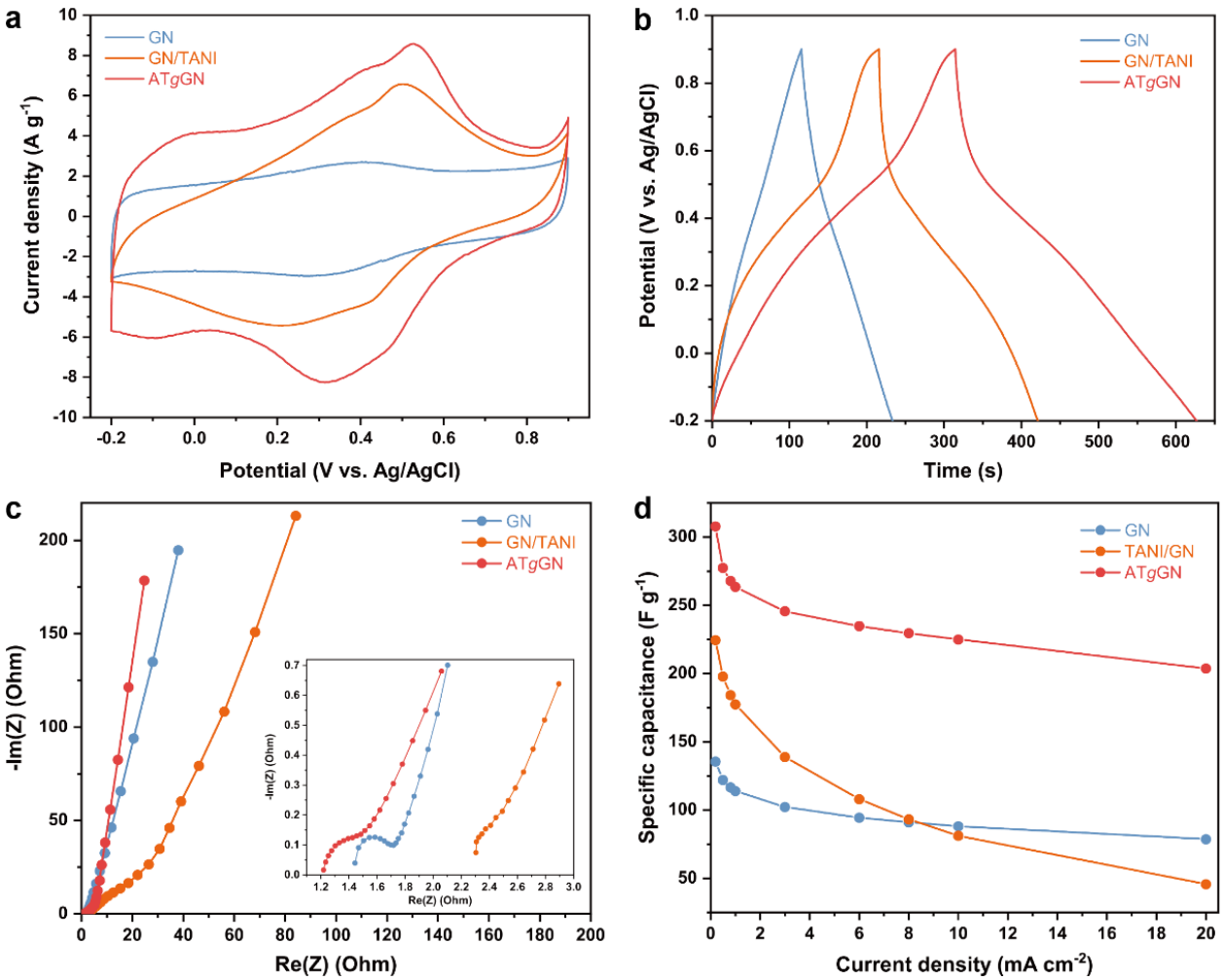

Figure S2.7. Comparison of the electrochemical performance of GN, GN/TANI, and AT*g*GN in 1.0 M H_2SO_4 in a three-electrode cell setup. (a) CV curves at a scan rate of 20 mV s^{-1}. (b) GCD plots at a current density of 0.5 mA cm^{-2}. (c) Nyquist plots over a frequency range from 200 kHz to 10 mHz with an inset showing magnified high-frequency region and (d) a rate capability study (specific capacitance vs. current density).

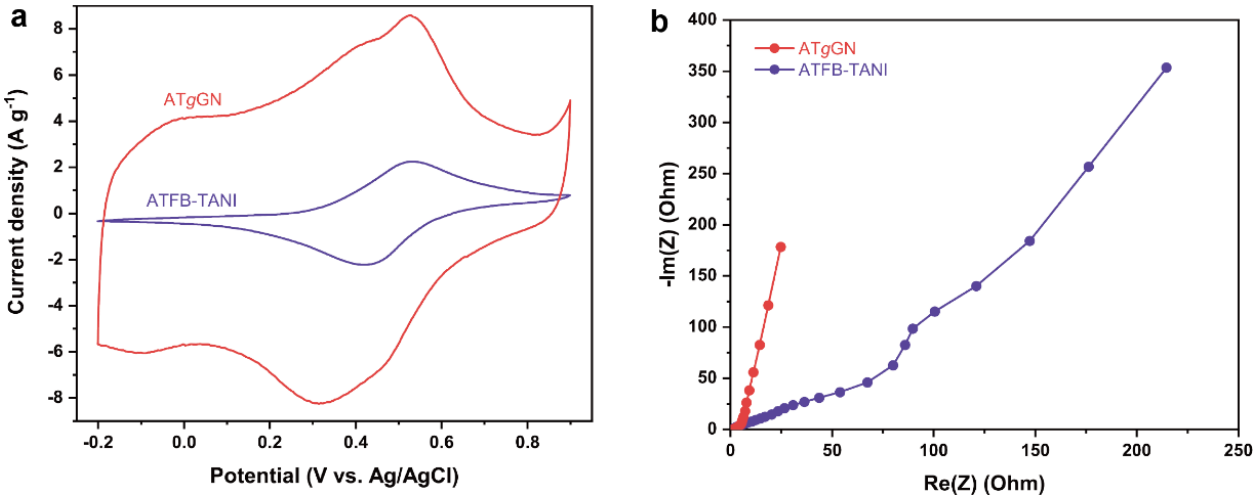

Figure S2.8. Electrochemical performance of ATFB-TANI and AT*g*GN in 1.0 M H_2SO_4 in a three-electrode cell setup. (a) CV curves at a scan rate of 20 mV s^{-1}. (b) Nyquist plots over a frequency range from 200 kHz to 10 mHz.

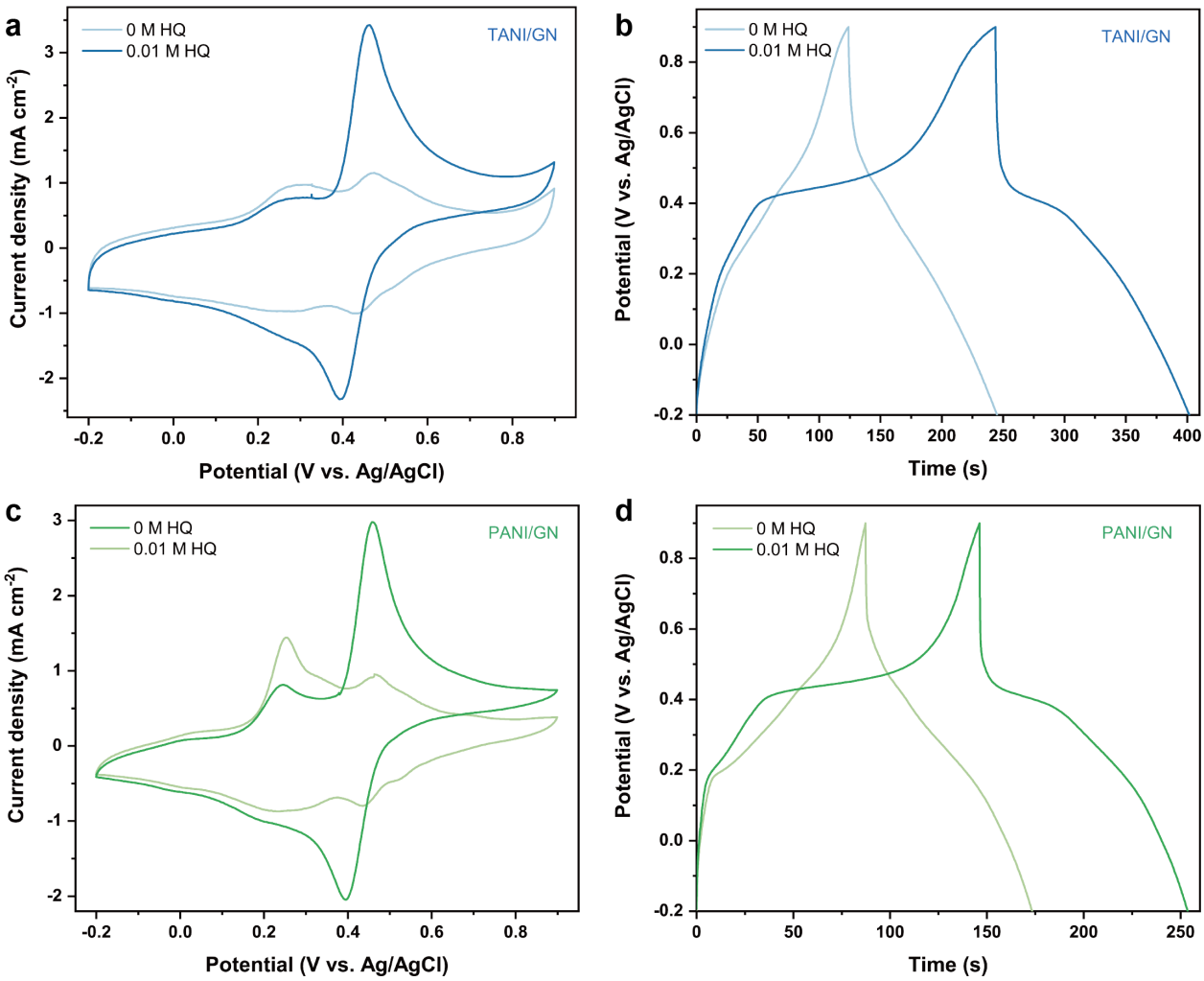

Figure S2.9. Comparison of the electrochemical performance of the two physical mixtures, TANI/GN and PANI/GN, in the absence and presence of 0.01 M HQ in 1.0 M H_2SO_4 in a three-electrode cell setup. (a) CV curves of TANI/GN at a scan rate of 5 mV s^{-1}. (b) GCD plots of TANI/GN at a current density of 1 mA cm^{-2}. (c) CV curves of PANI/GN at a scan rate of 5 mV s^{-1}. (d) GCD plots of PANI/GN at a current density of 1 mA cm^{-2}.

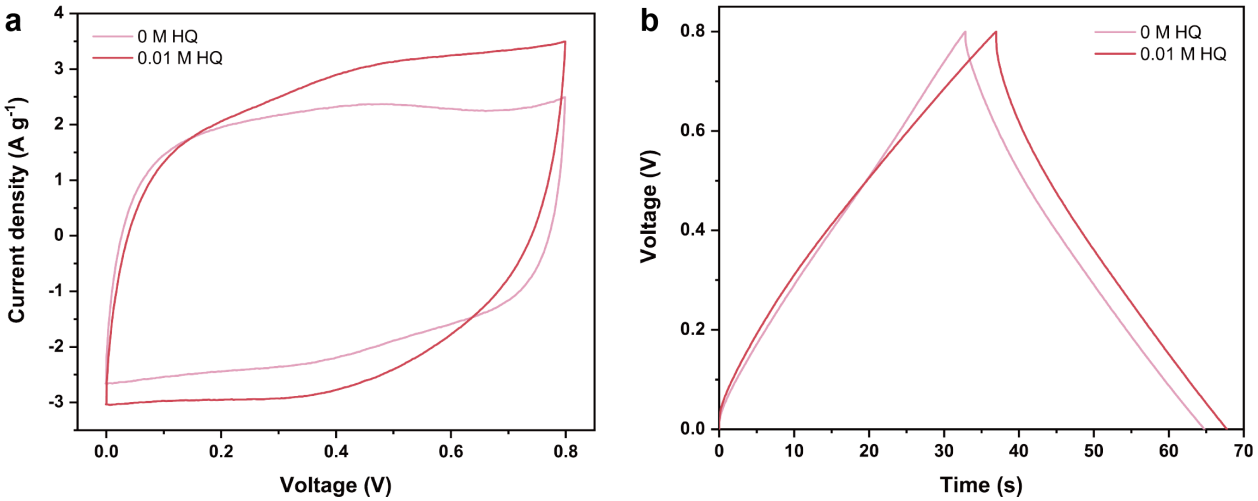

Figure S2.10. Electrochemical performance of the symmetric AT*g*GN||AT*g*GN device in the absence and presence of 0.01 M HQ. (a) CV curves at a scan rate of 50 mV s^{-1}. (b) GCD plots at a current density of 0.5 mA cm^{-2}.

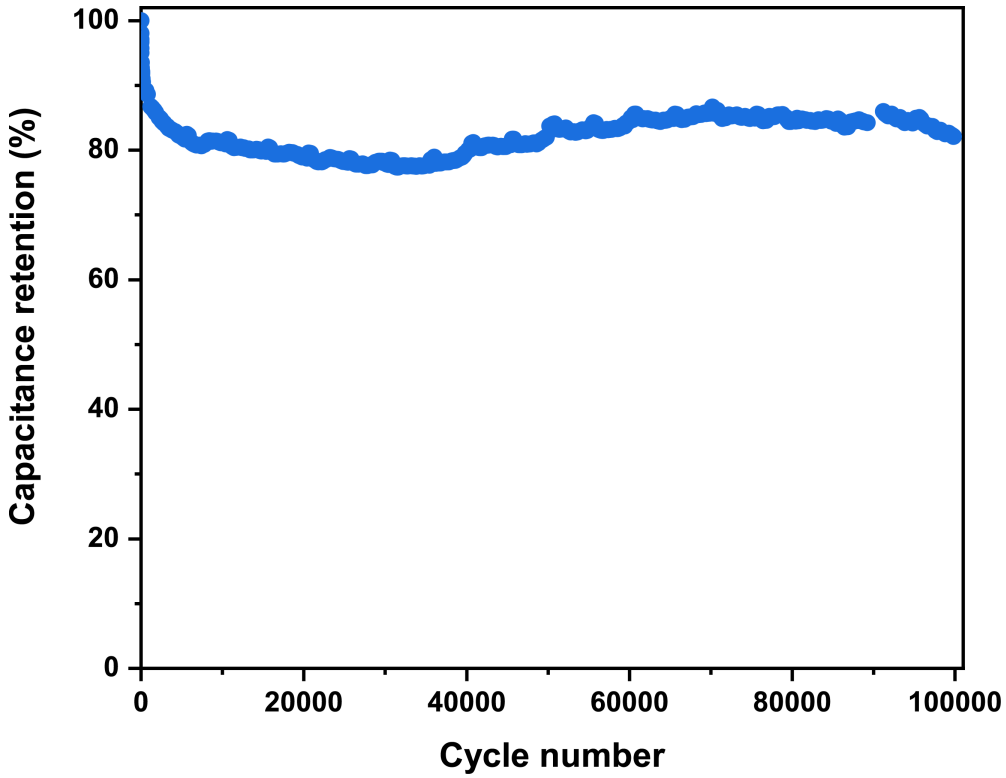

Figure S2.11. Long-term cycling stability of the symmetric ATgGN||ATgGN device in the HQ containing gel electrolyte (PVA/H_2SO_4/HQ) over 100,000 charge–discharge cycles at a current density of 2.5 mA cm^{-2}.

2.6.4 Comparison with Literature Reports

Table S2.2. Comparison of the Electrochemical Performance Including the Cycling Stability of AT*g*GN with Other Carbon- and PANI-based Composites in a Three-electrode Cell Setup

Materials	Specific capacitance (current density or scan rate)	Cycle number	Cycle stability (current density or scan rate)	Ref.
AT*g*GN7	**278 F g^{-1} (1 A g^{-1}) (406 F g^{-1} (2 A g^{-1}) with 0.01 M HQ)**	**20,000**	**87% (25 A g^{-1})**	**This work**
		30,000	**85% (25 A g^{-1})**	
3D-G/PANI	777 F g^{-1} (1 A g^{-1})	60,000	85% (5 A g^{-1})	[19]
fCC-PANI array-rGO	471 mF cm^{-2} (0.5 mA cm^{-2})	10,000	75.5% (100 mV s^{-1})	[41]
GCS@PANI@RGO	446.19 F g^{-1} (5 mV s^{-1})	5000	87.7% (2 A g^{-1})	[42]
PANI/3D graphene	1002 F g^{-1} (1 mA cm^{-2})	5000	86.5% (4 mA cm^{-2})	[43]
Whiskerlike PANI/ mesoporous carbon	900 F g^{-1} (0.5 A g^{-1})	3000	95% (5 A g^{-1})	[44]
Graphene/OANI	640 F g^{-1} (0.2 mA cm^{-2})	2000	91%	[7]
Reduced CND-g-PANI	972 F g^{-1} (1 A g^{-1})	2000	90% (10 A g^{-1})	[45]
GO-g-PANI	965 F g^{-1} (1 A g^{-1})	2000	83%	[34]
Self-healing PANI-GO	757 F g^{-1} (1 A g^{-1})	2000	80% (100 mV s^{-1})	[46]
PANI-ATRGO	1510 F g^{-1} (1 A g^{-1})	1500	89% (100 mV s^{-1})	[32]
PANI-frGO	590 F g^{-1} (0.1 A g^{-1})	1000	91% (2 A g^{-1})	[47]
N-doped graphene/PANI hydrogels (GMPH7)	514.3 F g^{-1} (1 A g^{-1})	1000	87.1% (10 A g^{-1})	[18]
rGO-PANI (50%) hydrogel	921 F g^{-1} (1 A g^{-1})	1000	85.2% (10 A g^{-1})	[48]
Graphene/PANI (GEP)	1126 F g^{-1} (1 mV s^{-1})	1000	84% (0.2 A g^{-1})	[49]
PANI NFs/FrGO	692 F g^{-1} (1 A g^{-1})	1000	83.3% (10 A g^{-1})	[50]
Graphene/PANI hydrogel (GPH)	865.6 F g^{-1} (1 A g^{-1})	1000	82% (5 A g^{-1})	[51]
BC/GE/PANI	645 F g^{-1} (1 A g^{-1})	1000	82.2% (5 mV s^{-1})	[52]
Graphene/PANI	763 F g^{-1} (1 A g^{-1})	1000	82% (5 A g^{-1})	[53]

Table S2.3. Comparison of the Electrochemical Performance Including the Cycling Stability of the Symmetric AT*g*GN||AT*g*GN Device with Other Carbon- and PANI-based Symmetric Devices

Materials	Specific capacitance (current density or scan rate)	Cycle number	Cycle stability (current density or scan rate)	Ref.
AT*g*GN7	**148 F g^{-1} (1 A g^{-1})**	**20,000**	**90% (2.5 mA cm^{-2})**	**This work**
		30,000	**87% (2.5 mA cm^{-2})**	
AT*g*GN7	**188 F g^{-1} (1 A g^{-1}) (with 0.01 M HQ)**	**30,000**	**78% (2.5 mA cm^{-2})**	
		100,000	**82% (2.5 mA cm^{-2})**	
3D-G/PANI	665 F g^{-1} (1 A g^{-1})	10,000	100% (5 A g^{-1})	19
PU/CNT/PAni	51.2 F g^{-1} (50 mA, device)	10,000	93% (50 mA)	4
Self-healing PANI-GO	134.7 F g^{-1} (1 A g^{-1})	9000	93.2% (2 A g^{-1})	46
Self-healing AT-GO	130 F g^{-1} (1 A g^{-1})	9000	97.5% (2 A g^{-1})	46
PVA/G/PAni-4C/G	90 F g^{-1} at 3 mA	20,000	90% at 50 mA	67
		70,000	77.9% at 50 mA	
PANI nanorod arrays/graphene	230 mF cm^{-2} (0.1 mA cm^{-2})	8000	86.9%	54
fCC-PANI array-rGO	197 mF cm^{-2} (0.1 mA cm^{-2})	7000	91.3% (5 mA cm^{-2})	41
3D-RGO/PANI	362 F g^{-1} (1 A g^{-1})	5000	88% (5 A g^{-1})	11
PANI-FCC	484 F g^{-1} (1 A g^{-1})	5000	87% at 1, 2, 5, 10, and 20 A g^{-1} (1000 cycles for each current density)	55
PANI-GO	555 F g^{-1} (0.2 A g^{-1})	2000	92% (1 A g^{-1})	56
GO-g-PANI	517 F g^{-1} (1 A g^{-1})	2000	86% (10 A g^{-1})	34
Covalently grafted PANI/GO	422 F g^{-1} (1 A g^{-1})	2000	83% (2 A g^{-1})	29
PANI-SWCNTs-sponge	216 F g^{-1} (0.64 A g^{-1})	1000	92%	9
Carbon nanotubes/PANI	350 F g^{-1} (0.1 A g^{-1})	1000	92% (1 A g^{-1})	57

2.7 References

(1) Li, Z.; Gong, L. Research Progress on Applications of Polyaniline (PANI) for Electrochemical Energy Storage and Conversion. *Materials* **2020**, *13*, 548.

(2) Park, J. H.; Park, O. O. Hybrid electrochemical capacitors based on polyaniline and activated carbon electrodes. *J. Power Sources* **2002**, *111*, 185–190.

(3) Kovalenko, I.; Bucknall, D. G.; Yushin, G. Detonation Nanodiamond and Onion-Like-Carbon-Embedded Polyaniline for Supercapacitors. *Adv. Funct. Mater.* **2010**, *20*, 3979–3986.

(4) Khosrozadeh, A.; Darabi, M. A.; Wang, Q.; Xing, M. Polyaniline nanoflowers grown on vibration-isolator-mimetic polyurethane nanofibers for flexible supercapacitors with prolonged cycle life. *J. Mater. Chem. A* **2017**, *5*, 7933–7943.

(5) Yan, J.; Yang, L.; Cui, M.; Wang, X.; Chee, K. J.; Nguyen, V. C.; Kumar, V.; Sumboja, A.; Wang, M.; Lee, P. S. Aniline Tetramer-Graphene Oxide Composites for High Performance Supercapacitors. *Adv. Energy Mater.* **2014**, *4*, 1400781.

(6) Li, R.; Lin, C.-W.; Shao, Y.; Chang, C. W.; Yao, F.-K.; Kowal, M. D.; Wang, H.; Yeung, M.; Huang, S.-C.; Kaner, R. B. Characterization of Aniline Tetramer by MALDI TOF Mass Spectrometry upon Oxidative and Reductive Cycling. *Polymers* **2016**, *8*, 401.

(7) Wang, H.; Yu, Z.; El-Kady, M. F.; Anderson, M.; Kowal, M. D.; Li, M.; Kaner, R. B. Graphene/oligoaniline based supercapacitors: Towards conducting polymer materials with high rate charge storage. *Energy Storage Mater.* **2019**, *19*, 137–147.

(8) Huang, F.; Chen, D. Towards the upper bound of electrochemical performance of ACNT@polyaniline arrays as supercapacitors. *Energy Environ. Sci.* **2012**, *5*, 5833–5841.

(9) Niu, Z.; Zhou, W.; Chen, X.; Chen, J.; Xie, S. Highly Compressible and All-Solid-State Supercapacitors Based on Nanostructured Composite Sponge. *Adv. Mater.* **2015**, *27*, 6002–6008.

(10) Yu, J.; Lu, W.; Pei, S.; Gong, K.; Wang, L.; Meng, L.; Huang, Y.; Smith, J. P.; Booksh, K. S.; Li, Q.; et al. Omnidirectionally Stretchable High-Performance Supercapacitor Based on Isotropic Buckled Carbon Nanotube Films. *ACS Nano* **2016**, *10*, 5204–5211.

(11) Meng, Y.; Wang, K.; Zhang, Y.; Wei, Z. Hierarchical Porous Graphene/Polyaniline Composite Film with Superior Rate Performance for Flexible Supercapacitors. *Adv. Mater.* **2013**, *25*, 6985–6990.

(12) Liu, L.; Niu, Z.; Zhang, L.; Zhou, W.; Chen, X.; Xie, S. Nanostructured Graphene Composite Papers for Highly Flexible and Foldable Supercapacitors. *Adv. Mater.* **2014**, *26*, 4855–4862.

(13) Ashok Kumar, N.; Baek, J.-B. Electrochemical supercapacitors from conducting polyaniline–graphene platforms. *Chem. Commun.* **2014**, *50*, 6298–6308.

(14) Novoselov, K. S.; Fal′ko, V. I.; Colombo, L.; Gellert, P. R.; Schwab, M. G.; Kim, K. A roadmap for graphene. *Nature* **2012**, *490*, 192–200.

(15) Wang, M.; Duan, X.; Xu, Y.; Duan, X. Functional Three-Dimensional Graphene/Polymer Composites. *ACS Nano* **2016**, *10*, 7231–7247.

(16) Li, P.; Jin, Z.; Peng, L.; Zhao, F.; Xiao, D.; Jin, Y.; Yu, G. Stretchable All-Gel-State Fiber-Shaped Supercapacitors Enabled by Macromolecularly Interconnected 3D Graphene/Nanostructured Conductive Polymer Hydrogels. *Adv. Mater.* **2018**, *30*, 1800124.

(17) Wu, J.; Zhang, Q. E.; Wang, J.; Huang, X.; Bai, H. A self-assembly route to porous polyaniline/reduced graphene oxide composite materials with molecular-level uniformity for high-performance supercapacitors. *Energy Environ. Sci.* **2018**, *11*, 1280–1286.

(18) Zou, Y.; Zhang, Z.; Zhong, W.; Yang, W. Hydrothermal direct synthesis of polyaniline, graphene/polyaniline and N-doped graphene/polyaniline hydrogels for high performance flexible supercapacitors. *J. Mater. Chem. A* **2018**, *6*, 9245–9256.

(19) Li, K.; Liu, J.; Huang, Y.; Bu, F.; Xu, Y. Integration of ultrathin graphene/polyaniline composite nanosheets with a robust 3D graphene framework for highly flexible all-solid-state supercapacitors with superior energy density and exceptional cycling stability. *J. Mater. Chem. A* **2017**, *5*, 5466–5474.

(20) Yu, P.; Zhao, X.; Huang, Z.; Li, Y.; Zhang, Q. Free-standing three-dimensional graphene and polyaniline nanowire arrays hybrid foams for high-performance flexible and lightweight supercapacitors. *J. Mater. Chem. A* **2014**, *2*, 14413–14420.

(21) Chen, K.; Chen, L.; Chen, Y.; Bai, H.; Li, L. Three-dimensional porous graphene-based composite materials: electrochemical synthesis and application. *J. Mater. Chem.* **2012**, *22*, 20968–20976.

(22) Zhou, Q.; Li, Y.; Huang, L.; Li, C.; Shi, G. Three-dimensional porous graphene/polyaniline composites for high-rate electrochemical capacitors. *J. Mater. Chem. A* **2014**, *2*, 17489–17494.

(23) Wang, Z.; Zhang, Q. E.; Long, S.; Luo, Y.; Yu, P.; Tan, Z.; Bai, J.; Qu, B.; Yang, Y.; Shi, J.; et al. Three-Dimensional Printing of Polyaniline/Reduced Graphene Oxide Composite for High-Performance Planar Supercapacitor. *ACS Appl. Mater. Interfaces* **2018**, *10*, 10437–10444.

(24) Liu, Y.; Ma, Y.; Guang, S.; Ke, F.; Xu, H. Polyaniline-graphene composites with a three-dimensional array-based nanostructure for high-performance supercapacitors. *Carbon* **2015**, *83*, 79–89.

(25) Kumar, N. A.; Choi, H.-J.; Shin, Y. R.; Chang, D. W.; Dai, L.; Baek, J.-B. Polyaniline-Grafted Reduced Graphene Oxide for Efficient Electrochemical Supercapacitors. *ACS Nano* **2012**, *6*, 1715–1723.

(26) An, J.; Liu, J.; Zhou, Y.; Zhao, H.; Ma, Y.; Li, M.; Yu, M.; Li, S. Polyaniline-Grafted Graphene Hybrid with Amide Groups and Its Use in Supercapacitors. *J. Phys. Chem. C.* **2012**, *116*, 19699–19708.

(27) Liu, J.; An, J.; Zhou, Y.; Ma, Y.; Li, M.; Yu, M.; Li, S. Preparation of an Amide Group-Connected Graphene–Polyaniline Nanofiber Hybrid and Its Application in Supercapacitors. *ACS Appl. Mater. Interfaces* **2012**, *4*, 2870–2876.

(28) Kumar, M.; Singh, K.; Dhawan, S. K.; Tharanikkarasu, K.; Chung, J. S.; Kong, B.-S.; Kim, E. J.; Hur, S. H. Synthesis and characterization of covalently-grafted graphene–polyaniline nanocomposites and its use in a supercapacitor. *Chem. Eng. J.* **2013**, *231*, 397–405.

(29) Li, Z.-F.; Zhang, H.; Liu, Q.; Liu, Y.; Stanciu, L.; Xie, J. Covalently-grafted polyaniline on graphene oxide sheets for high performance electrochemical supercapacitors. *Carbon* **2014**, *71*, 257–267.

(30) Liu, X.; Shang, P.; Zhang, Y.; Wang, X.; Fan, Z.; Wang, B.; Zheng, Y. Three-dimensional and stable polyaniline-grafted graphene hybrid materials for supercapacitor electrodes. *J. Mater. Chem. A* **2014**, *2*, 15273–15278.

(31) Ramasamy, M. S.; Mahapatra, S. S.; Yi, D. H.; Yoo, H. J.; Cho, J. W. Synthesis and electrochemical properties of conducting polyaniline/graphene hybrids by click chemistry. *RSC Adv.* **2014**, *4*, 23936–23942.

(32) Ke, F.; Liu, Y.; Xu, H.; Ma, Y.; Guang, S.; Zhang, F.; Lin, N.; Ye, M.; Lin, Y.; Liu, X. Flower-like polyaniline/graphene hybrids for high-performance supercapacitor. *Compos. Sci. Technol.* **2017**, *142*, 286–293.

(33) Wang, S.; Li, L.; Wang, Q.; Fan, Y.; Shen, J.; Zhang, K.; Yang, L.; Zhang, W. Aniline oligomer-modified graphene for enhanced electrochemical performances. *Synth. Met.* **2018**, *243*, 107–114.

(34) Ghosh, T.; Basak, U.; Bairi, P.; Ghosh, R.; Pakhira, M.; Ball, R.; Biswas, B.; Chatterjee, D. P. Hierarchical Nanocomposites by Oligomer-Initiated Controlled Polymerization of Aniline on Graphene Oxide Sheets for Energy Storage. *ACS Appl. Nano Mater.* **2020**, *3*, 1693–1705.

(35) Liu, L.-H.; Yan, M. Functionalization of pristine graphene with perfluorophenyl azides. *J. Mater. Chem.* **2011**, *21*, 3273–3276.

(36) Lin, C.-W.; Aguilar, S.; Rao, E.; Mak, W. H.; Huang, X.; He, N.; Chen, D.; Jun, D.; Curson, P. A.; McVerry, B. T.; et al. Direct grafting of tetraaniline via perfluorophenylazide photochemistry to create antifouling, low bio-adhesion surfaces. *Chem. Sci.* **2019**, *10*, 4445–4457.

(37) Guo, H.-L.; Wang, X.-F.; Qian, Q.-Y.; Wang, F.-B.; Xia, X.-H. A Green Approach to the Synthesis of Graphene Nanosheets. *ACS Nano* **2009**, *3*, 2653–2659.

(38) Park, J.; Jayawardena, H. S. N.; Chen, X.; Jayawardana, K. W.; Sundhoro, M.; Ada, E.; Yan, M. A general method for the fabrication of graphene–nanoparticle hybrid material. *Chem. Commun.* **2015**, *51*, 2882–2885.

(39) Zorn, G.; Liu, L.-H.; Árnadóttir, L.; Wang, H.; Gamble, L. J.; Castner, D. G.; Yan, M. X-ray Photoelectron Spectroscopy Investigation of the Nitrogen Species in Photoactive Perfluorophenylazide-Modified Surfaces. *J. Phys. Chem. C.* **2014**, *118*, 376–383.

(40) Noori, A.; El-Kady, M. F.; Rahmanifar, M. S.; Kaner, R. B.; Mousavi, M. F. Towards establishing standard performance metrics for batteries, supercapacitors and beyond. *Chem. Soc. Rev.* **2019**, *48*, 1272–1341.

(41) Du, P.; Dong, Y.; Kang, H.; Yang, X.; Wang, Q.; Niu, J.; Wang, S.; Liu, P. Graphene-Wrapped Polyaniline Nanowire Array Modified Functionalized of Carbon Cloth for High-Performance Flexible Solid-State Supercapacitor. *ACS Sustain. Chem. Eng.* **2018**, *6*, 14723–14733.

(42) Liu, L.; Wang, Y.; Meng, Q.; Cao, B. A novel hierarchical graphene/polyaniline hollow microsphere as electrode material for supercapacitor applications. *J. Mater. Sci.* **2017**, *52*, 7969–7983.

(43) Kulkarni, S. B.; Patil, U. M.; Shackery, I.; Sohn, J. S.; Lee, S.; Park, B.; Jun, S. High-performance supercapacitor electrode based on a polyaniline nanofibers/3D graphene framework as an efficient charge transporter. *J. Mater. Chem. A* **2014**, *2*, 4989–4998.

(44) Wang, Y. G.; Li, H. Q.; Xia, Y. Y. Ordered Whiskerlike Polyaniline Grown on the Surface of Mesoporous Carbon and Its Electrochemical Capacitance Performance. *Adv. Mater.* **2006**, *18*, 2619–2623.

(45) Ghosh, T.; Ghosh, R.; Basak, U.; Majumdar, S.; Ball, R.; Mandal, D.; Nandi, A. K.; Chatterjee, D. P. Candle soot derived carbon nanodot/polyaniline hybrid materials through controlled grafting of polyaniline chains for supercapacitors. *J. Mater. Chem. A* **2018**, *6*, 6476–6492.

(46) Wang, W.; Yan, J.; Liu, J.; Ou, D.; Qin, Q.; Lan, B.; Ning, Y.; Zhou, D.; Wu, Y. Self-healing polyaniline-graphene oxides based electrodes with enhanced cycling stability. *Electrochim. Acta* **2018**, *282*, 835–844.

(47) Wang, L.; Ye, Y.; Lu, X.; Wen, Z.; Li, Z.; Hou, H.; Song, Y. Hierarchical Nanocomposites of Polyaniline Nanowire Arrays on Reduced Graphene Oxide Sheets for Supercapacitors. *Sci. Rep.* **2013**, *3*, 1–9.

(48) Hu, N.; Zhang, L.; Yang, C.; Zhao, J.; Yang, Z.; Wei, H.; Liao, H.; Feng, Z.; Fisher, A.; Zhang, Y.; et al. Three-dimensional skeleton networks of graphene wrapped polyaniline nanofibers: an excellent structure for high-performance flexible solid-state supercapacitors. *Sci. Rep.* **2016**, *6*, 19777.

(49) Wang, H.; Hao, Q.; Yang, X.; Lu, L.; Wang, X. A nanostructured graphene/polyaniline hybrid material for supercapacitors. *Nanoscale* **2010**, *2*, 2164–2170.

(50) Jin, K.; Zhang, W.; Wang, Y.; Guo, X.; Chen, Z.; Li, L.; Zhang, Y.; Wang, Z.; Chen, J.; Sun, L.; et al. In–situ hybridization of polyaniline nanofibers on functionalized reduced graphene oxide films for high-performance supercapacitor. *Electrochim. Acta* **2018**, *285*, 221–229.

(51) Ji, J.; Li, R.; Li, H.; Shu, Y.; Li, Y.; Qiu, S.; He, C.; Yang, Y. Phytic acid assisted fabrication of graphene/polyaniline composite hydrogels for high-capacitance supercapacitors. *Compos. B. Eng* **2018**, *155*, 132–137.

(52) Luo, H.; Dong, J.; Zhang, Y.; Li, G.; Guo, R.; Zuo, G.; Ye, M.; Wang, Z.; Yang, Z.; Wan, Y. Constructing 3D bacterial cellulose/graphene/polyaniline nanocomposites by novel layer-by-layer in situ culture toward mechanically robust and highly flexible freestanding electrodes for supercapacitors. *Chem. Eng. J.* **2018**, *334*, 1148-1158.

(53) Cong, H.-P.; Ren, X.-C.; Wang, P.; Yu, S.-H. Flexible graphene–polyaniline composite paper for high-performance supercapacitor. *Energy Environ. Sci.* **2013**, *6*, 1185–1191.

(54) Wu, X.; Wu, G.; Tan, P.; Cheng, H.; Hong, R.; Wang, F.; Chen, S. Construction of microfluidic-oriented polyaniline nanorod arrays/graphene composite fibers for application in wearable micro-supercapacitors. *J. Mater. Chem. A* **2018**, *6*, 8940–8946.

(55) Hashemi, M.; Rahmanifar, M. S.; El-Kady, M. F.; Noori, A.; Mousavi, M. F.; Kaner, R. B. The use of an electrocatalytic redox electrolyte for pushing the energy density boundary of a flexible polyaniline electrode to a new limit. *Nano Energy* **2018**, *44*, 489–498.

(56) Xu, J.; Wang, K.; Zu, S.-Z.; Han, B.-H.; Wei, Z. Hierarchical Nanocomposites of Polyaniline Nanowire Arrays on Graphene Oxide Sheets with Synergistic Effect for Energy Storage. *ACS Nano* **2010**, *4*, 5019–5026.

(57) Meng, C.; Liu, C.; Chen, L.; Hu, C.; Fan, S. Highly Flexible and All-Solid-State Paperlike Polymer Supercapacitors. *Nano Lett.* **2010**, *10*, 4025–4031.

(58) Roldán, S.; Blanco, C.; Granda, M.; Menéndez, R.; Santamaría, R. Towards a Further Generation of High-Energy Carbon-Based Capacitors by Using Redox-Active Electrolytes. *Angew. Chem. Int. Ed.* **2011**, *50*, 1699–1701.

(59) Roldán, S.; Granda, M.; Menéndez, R.; Santamaría, R.; Blanco, C. Mechanisms of Energy Storage in Carbon-Based Supercapacitors Modified with a Quinoid Redox-Active Electrolyte. *J. Phys. Chem. C.* **2011**, *115*, 17606–17611.

(60) Chen, W.; Rakhi, R. B.; Alshareef, H. N. Capacitance enhancement of polyaniline coated curved-graphene supercapacitors in a redox-active electrolyte. *Nanoscale* **2013**, *5*, 4134–4138.

(61) Hwang, J. Y.; El-Kady, M. F.; Li, M.; Lin, C.-W.; Kowal, M.; Han, X.; Kaner, R. B. Boosting the capacitance and voltage of aqueous supercapacitors via redox charge contribution from both electrode and electrolyte. *Nano Today* **2017**, *15*, 15–25.

(62) Hummers, W. S.; Offeman, R. E. Preparation of Graphitic Oxide. *J. Am. Chem. Soc.* **1958**, *80*, 1339–1339.

(63) Li, D.; Kaner, R. B. Shape and Aggregation Control of Nanoparticles: Not Shaken, Not Stirred. *J. Am. Chem. Soc.* **2006**, *128*, 968–975.

(64) Tseng, R. J.; Baker, C. O.; Shedd, B.; Huang, J.; Kaner, R. B.; Ouyang, J.; Yang, Y. Charge transfer effect in the polyaniline-gold nanoparticle memory system. *Appl. Phys. Lett.* **2007**, *90*, 053101.

(65) Cook, J. B.; Kim, H.-S.; Lin, T. C.; Lai, C.-H.; Dunn, B.; Tolbert, S. H. Pseudocapacitive Charge Storage in Thick Composite MoS2 Nanocrystal-Based Electrodes. *Adv. Energy Mater.* **2017**, *7*, 1601283.

(66) Wang, J.; Polleux, J.; Lim, J.; Dunn, B. Pseudocapacitive Contributions to Electrochemical Energy Storage in TiO2(Anatase) Nanoparticles. *J. Phys. Chem. C.* **2007**, *111*, 14925-14931.

(67) Khosrozadeh, A.; Singh, G.; Wang, Q.; Luo, G.; Xing, M. Supercapacitor with extraordinary cycling stability and high rate from nano-architectured polyaniline/graphene on Janus nanofibrous film with shape memory. *J. Mater. Chem. A* **2018**, *6*, 21064–21077.

CHAPTER 3. MOLECULAR ENGINEERING OF HIERARCHICAL CONDUCTING POLYMER COMPOSITES FOR HIGHLY STABLE SUPERCAPACITORS

3.1 Abstract

Long cycle life and high energy/power density are imperative to energy storage systems. Polyaniline (PANI) has shown great potential as an electrode material but is limited by poor cycling and rate performance. We present a molecular design approach of binding short-chain aniline trimers (AT) and carbon nanotubes (CNTs) through the formation of amide covalent linkages enabled by a simple laser scribing technique. The covalently coupled AT/CNT (cc-AT/CNT) composite retains 80% of its original capacitance after 20,000 charge/discharge cycles, which readily outperforms long-chain PANI/CNT composites without covalent connections. The compact AT/CNT heterointerfaces produce fast charge/discharge kinetics and excellent rate capability. The flexible symmetric quasi-solid-state devices can be stably cycled beyond 50,000 cycles, at least 5 times longer than most PANI/CNT-based symmetric supercapacitors reported to date. This molecular design of durable conducting polymer-based electrode materials enabled by laser irradiation presents a feasible approach toward robust advanced energy storage devices.

3.2 Introduction

Supercapacitors have been broadly exploited in light of their fast charging capabilities and high power density.[1, 2] Conducting polymers, such as polyaniline (PANI), provide advantages of intrinsic electrical conductivity and good electrochemical activity, thus being valued as promising sustainable organic electrode materials for supercapacitors.[3] However, PANI has an instability problem of continued capacitance loss during long-term cycling, which is mainly due to deprotonation and structural degradation resulting from large volumetric swelling and shrinking as a consequence of the repeated doping and de-doping processes.[4, 5] In addition, the utilization efficiency of bulk PANI is low due to its minimal available surface area leading to poor accessibility of electrolyte.[6]

To address these issues, aniline oligomers, such as aniline trimer (AT), have been explored as a favorable substitute for PANI.[7, 8] Owing to its short chain length, AT is expected to exhibit less volumetric changes during repeated charge/discharge processes.[7, 9] Combining conducting polymers with carbonaceous materials[10-14] or MXenes[15] as buffering substrates has been recognized as another effective approach. The carbonaceous materials can facilitate electron transfer, provide mechanical reinforcement to the conducting polymer chains, and accommodate volumetric degradation during repeated processes of charging and discharging. Nevertheless, conducting polymers still suffer from the risk of detachment or disconnection from the carbonaceous buffering substrates due to inefficient contact through physical binding. Recently, a potent strategy has been proposed to build covalent connections between conducting polymers and carbonaceous materials.[8, 16] The robust covalent binding has been found to sustain persistent electrical contact between the two components and to minimize mechanical degradation, thus giving rise to an elevated rate capability and extended cycling life.[17]

From another perspective, the synthesis of PANI-carbon composites normally requires multistep processes,[18-20] while the formation of covalent linkages typically requires high-temperature treatments such as hydrothermal processing.[8, 17] Therefore, it is essential to develop scalable, effortless, and cost-efficient approaches toward the synthesis of PANI-based electrode materials. Compared to the traditional high-temperature synthetic methods that are either time- or energy-consuming, the laser scribing technique[21-25] operating under ambient conditions can minimize particle aggregation, reduce time and energy consumption, and improve manufacturability.

In this work, we have developed a simple one-step laser-induced stabilization of aniline trimer on carbon nanotubes through amide covalent coupling. The fabricated covalently coupled AT/CNT (cc-AT/CNT) composite as well as the fabricated flexible symmetric quasi-solid-state devices exhibit remarkable cycling stability. The compact AT/CNT heterointerfaces contribute to efficient electron transfer and good rate capability.

3.3 Results and Discussion

A covalently coupled AT/CNT (cc-AT/CNT) composite was synthesized through a facile laser scribing process as illustrated in **Figure 3.1**. Briefly, an NH_2/NH_2 AT (NH_2/NH_2 end-caped aniline trimer) solution was uniformly mixed with a P3 SWNT (carboxylic acid-functionalized single-walled carbon nanotubes) suspension using a syringe pump while being stirred continuously under ambient conditions. Due to the attraction between the carboxyl groups (–COOH) on P3 SWNT and the amino groups ($–NH_2$) on AT, the AT molecules can be anchored to the carbon nanotubes directly. The mixture was then drop-cast onto a graphite paper current collector. After drying, the AT/CNT thin film was irradiated by a focused 10.6 μm CO_2 laser to prepare the cc-AT/CNT composite within seconds. During the laser scribing process, the high local heating generated at

the surface of the AT/CNT film enabled a condensation reaction between the carboxyl groups (–COOH) on P3 SWNT and the amino groups (–NH_2) on AT to occur by driving off H_2O, leading to the establishment of amide covalent linkages between AT and P3 SWNT. To investigate the structural effects of the cc-AT/CNT composite, three other composites were also evaluated as control experiments: AT/CNT (before laser irradiation), cc-AT/CNT (hydrothermal), and PANI/CNT. AT/CNT (before laser irradiation) can be considered a physical mixture of short-chain AT and P3 SWNT without any amide covalent connections. cc-AT/CNT (hydrothermal) was prepared by a hydrothermal method, where a uniform mixture of NH_2/NH_2 AT and P3 SWNT was maintained at 140 °C for 4 h, during which process amide covalent linkages can form between the two components. PANI/CNT is a physical mixture of long-chain PANI and P3 SWNT.

As shown in **Figure 3.2a**, a scanning electron microscopy (SEM) image demonstrates the morphology of the composite film before (top) and after (bottom) laser irradiation. The cc-AT/CNT composite formed after laser irradiation exhibited a more porous structure, with rougher surfaces, and a darker color compared to an AT/CNT composite before laser irradiation. The structural expansion can be ascribed to the laser-induced local heating that expels gaseous byproducts such as CO_2 and H_2O. In the SEM images of the cc-AT/CNT composite shown in **Figure 3.2b,c** at higher magnifications, it is possible to observe the uniform distribution of AT nanoparticles on the CNTs. The morphology evaluation through transmission electron microscopy (TEM) as illustrated in **Figure 3.2d,e** and **Figure S3.1** provides clear evidence for the even dispersion of AT nanoparticles with an average size of ~5 nm that are tightly bonded to the surface of the CNTs. From the elemental mapping of the cc-AT/CNT composite (**Figure 3.2f–i**) measured by energy dispersive spectroscopy (EDS), an atomic-scale uniformity of the AT/CNT interfaces is reflected by the evidence of homogeneous distribution of C, N, and O elements.

The physical properties and bonding states of the cc-AT/CNT composite were first analyzed by Fourier-transform infrared (FT-IR) spectroscopy. **Figure 3.3a** shows the FT-IR spectra of cc-AT/CNT (after laser irradiation), AT/CNT (before laser irradiation), as well as the starting materials NH_2/NH_2 AT and P3 SWNT. The band at 3376 cm^{-1} corresponding to O–H stretching vibrations in the carboxyl groups (–COOH) was observed in P3 SWNT but essentially disappeared in cc-AT/CNT. Similarly, regarding the amine N–H stretching vibrations at 3309 and 3198 cm^{-1}, the peak intensity decreased from NH_2/NH_2 AT to AT/CNT to cc-AT/CNT. These observations suggest that amide covalent bonds formed between CNTs and AT in the cc-AT/CNT composite after laser irradiation. It is noteworthy that in the FT-IR spectrum of AT/CNT before laser irradiation, there was also a peak intensity decrease in the O–H stretching vibrations and the N–H stretching vibrations, which can be attributed to the formation of ammonium carboxylate salt due to the deprotonation of carboxylic acid by the basic amine. Heating above 100 °C drives water from ammonium carboxylate salt and forms amide covalent bonds. As can be seen, the C=O stretching vibrations at 1736 cm^{-1} in the spectrum of AT/CNT before laser irradiation red-shifted to 1687 cm^{-1} in the spectrum of cc-AT/CNT after laser irradiation, which corresponds to the transition from carboxyl C=O to amide N–C=O. Additionally, the band combination corresponding to the C=C stretching vibrations in P3 SWNT (1581 cm^{-1}) and the quinoid rings of NH_2/NH_2 AT (1595 cm^{-1}) generated a band at 1578 cm^{-1} in the cc-AT/CNT composite. In the spectra of NH_2/NH_2 AT, AT/CNT, and cc-AT/CNT, the band at 1496 cm^{-1} can be assigned to the C=C stretching vibrations on the benzenoid rings of AT. The bands at 1312 cm^{-1} and 1157 cm^{-1} can be ascribed to the aromatic amine C–N stretching vibrations and the in-plane C–H bending vibrations of AT, respectively. From the Raman spectra (**Figure S3.2**), a red shift of ~12 cm^{-1} of

the disorder-induced D band and the graphitic G band was found in the cc-AT/CNT composite after laser irradiation, which can be attributed to the formation of amide covalent linkages.[15]

To further understand the changes in surface composition and chemical states that occurred during the laser scribing process, the cc-AT/CNT composite after laser irradiation and the AT/CNT composite before laser irradiation were analyzed by X-ray photoelectron spectroscopy (XPS). The survey spectra of both composites (**Figure 3.3b**) show the coexistence of carbon (C 1s), nitrogen (N 1s), and oxygen (O 1s). They also indicate lower oxygen content in the composite after laser irradiation, which suggests the formation of amide covalent linkages and the partial reduction of P3 SWNT. For the AT/CNT composite before laser irradiation, the N 1s core level spectrum can be deconvoluted into three components: benzenoid amine nitrogen (–NH–) at 399.8 eV, quinoid imine nitrogen (–N=) at 398.7 eV and positively charged nitrogen (N^+) at 400.9 eV (**Figure 3.3c**). After laser irradiation, a new deconvoluted peak at 401.8 eV became present in the cc-AT/CNT composite (**Figure 3.3d**), which can be assigned to amide nitrogen (N–C=O). Additionally, **Figure 3.3e** displays the O 1s spectrum of AT/CNT, which can be deconvoluted into three components: C–O at 532.7 eV, C=O at 531.6 eV, and O=C–O* at 533.7 eV. After laser irradiation, a new deconvoluted peak at 530.6 eV was observed in the cc-AT/CNT composite (**Figure 3f**), which can be attributed to oxygen in the amide bonds (N–C=O). The new deconvoluted peaks that emerged in the N 1s and O 1s spectra after laser irradiation indicate the formation of amide covalent linkages between AT and CNTs, which align with the N 1s and O 1s spectra in a cc-AT/CNT composite that we prepared using a hydrothermal method (**Figure S3.3**). The C 1s spectra of AT/CNT before laser irradiation (**Figure 3.3g**) and cc-AT/CNT after laser irradiation (**Figure 3.3h**) can be deconvoluted into seven components. The signals at 284.4 and 284.9 eV correlating to C=C and C–C bonds in the aromatic rings, respectively, are observed. The signals

at 285.3, 286.0, 286.9 and 288.1 eV can be assigned to C–N, C–O, C=N, and C=O bonds, respectively. The peaks at 289.8 eV in AT/CNT and 290.5 eV in cc-AT/CNT can be assigned to COOH and (O,N)–C=O, respectively. The XPS spectra of P3 SWNT, NH_2/NH_2 AT, and PANI/CNT are displayed in **Figures S3.4–S3.6** for reference. Additionally, cc-AT/CNT (after laser irradiation) presented higher thermal stability than AT/CNT (before laser irradiation) (**Figure S3.7**), corroborating the establishment of strong covalent coupling after laser irradiation.

The electrochemical properties of the cc-AT/CNT composite were first investigated in a typical three-electrode cell configuration, which takes the active material as the working electrode, graphite sheet as the counter electrode, and Ag/AgCl as the reference electrode in 1.0 M H_2SO_4 electrolyte within a potential window of –0.2–0.8 V (vs. Ag/AgCl). The cyclic voltammetry (CV) curves of cc-AT/CNT in **Figure 3.4a** at different scan rates exhibit two pairs of redox peaks from the redox and doping chemistry in AT, corresponding to the transition from the semiconducting leucoemeraldine state to the conducting emeraldine state and emeraldine to the pernigraniline state, respectively.[8, 16] The electrode kinetics of cc-AT/CNT were further interpreted based on a power-law relationship between the measured current (i) and the scan rate (v):[26]

$$i(v) = av^b \tag{3.1}$$

where a and b are adjustable parameters. In particular, b = 0.5 suggests a diffusion-dominated battery-like charge storage mechanism, while b = 1 reveals a surface-controlled capacitive process. **Figure 3.4b** demonstrates the log(i) vs. log(v) plots, where the b-values of the cathodic and anodic redox peaks were fit to 0.92, 0.94, 0.90, and 0.87 for O1, R1, O2, and R2, respectively, indicating the coexistence of the two types of charge storage mechanisms, where the surface-controlled capacitive process predominates. To distinguish and quantify the capacitive contribution of cc-

AT/CNT, the measured current can be described as a combination of two parts: the diffusion-controlled insertion ($k_1v^{1/2}$) and the surface-controlled pseudocapacitance (k_2v):[27]

$$i(v) = k_1v^{1/2} + k_2v \quad (3.2)$$

Consequently, by determining k_1 and k_2, the fraction of the current due to each charge storage mechanism can be quantified at a specific potential. In **Figure 3.4c**, the shaded region accounts for an 86% capacitive contribution at 5 mV s^{-1}, representing the good rate capability of cc-AT/CNT as an electrode material. The galvanostatic charge–discharge (GCD) profiles of the cc-AT/CNT electrode (**Figure 3.4d**) adopted triangular shapes with negligible *iR* drops and demonstrate that the three-electrode system can be steadily charged from –0.2 to 0.8 V (vs. Ag/AgCl) even at a low current density of 0.2 mA cm^{-2}, confirming fast surface-controlled pseudocapacitive characteristics. The noticeable slope changes around 0.4–0.5 V (vs. Ag/AgCl) are due to the electrochemical redox reactions of AT.

Unlike most of the known conducting polymer-based supercapacitors that suffer from severe capacitance loss and can only retain their peak performance for the first few thousand cycles, superior cycling stability was realized by cc-AT/CNT. As presented in **Figure 3.4e**, the cc-AT/CNT electrode can deliver an 80% capacitance retention after being continuously charged and discharged for 20,000 cycles, while maintaining a stable essentially 100% Coulombic efficiency in a three-electrode setup.

To gain deeper insights into the covalently coupled AT-CNT heterointerfaces, the electrochemical properties of cc-AT/CNT (after laser irradiation) were compared with several control experiments including AT/CNT (before laser irradiation), cc-AT/CNT (hydrothermal), PANI/CNT, and P3 SWNT, which were also characterized by SEM (**Figures S3.8–S3.11**). **Figure 3.4f,g** summarizes the specific capacitance that was calculated based on GCD profiles at a

range of current densities (0.2–20 mA cm^{-2}). The cc-AT/CNT (after laser irradiation) electrode exhibited a specific capacitance of 284 F g^{-1} at 0.2 mA cm^{-2} and retained a specific capacitance of 213 F g^{-1} (75% capacitance retention) when the current density was increased by 100 times (to 20 mA cm^{-2}). This excellent rate performance was comparable to P3 SWNT only, suggesting that the compact AT-CNT heterointerfaces within cc-AT/CNT (after laser irradiation) were greatly beneficial to facilitating electron/ion transfer. In contrast, the cc-AT/CNT (hydrothermal) exhibited much poorer rate capability with only 49% capacitance retention at 20 mA cm^{-2} providing a specific capacitance of 302 F g^{-1} at 0.2 mA cm^{-2}. Although amide covalent linkages were also supposed to be present in the cc-AT/CNT (hydrothermal) composite, this poor rate performance can be attributed to AT aggregation during the hydrothermal process, which is supported by the SEM images (**Figure S3.9**). In addition, at 0.2 mA cm^{-2}, cc-AT/CNT (after laser irradiation) delivered a specific capacitance that was nearly 1.2 times higher than AT/CNT (before laser irradiation) (233 F g^{-1}), 1.3 times higher than PANI/CNT (225 F g^{-1}), and 2.4 times higher than P3 SWNT (119 F g^{-1}). The CV diagrams of AT/CNT (before laser irradiation), cc-AT/CNT (hydrothermal), PANI/CNT, and P3 SWNT (**Figure S3.13** and **S3.14**) also revealed that cc-AT/CNT (after laser irradiation) presented higher specific capacitance and superior rate capability compared to the control experiments.

As illustrated in **Figure 3.4h**, the cc-AT/CNT (after laser irradiation) electrode demonstrated long-term cycling stability with a capacitance retention of 80% after being continuously charged and discharged for 20,000 cycles. In contrast, with the same 80% capacitance retention, the cycle life was 1000, 5000, and 16,000 charge/discharge cycles for PANI/CNT, AT/CNT (before laser irradiation), and cc-AT/CNT (hydrothermal), respectively. This study indicates that by employing short-chain AT and building covalent linkages between AT and CNTs, the long-term cycling

stability of the conducting polymer-based electrode materials can be greatly improved. Furthermore, compared to the traditional high-temperature synthetic methods such as hydrothermal, which generally takes hours to complete, the laser scribing technique can be accomplished within seconds and the as-prepared electrodes can achieve even better electrochemical performance.

To assess the electrochemical performance of cc-AT/CNT (after laser irradiation) for practical applications, symmetric quasi-solid-state supercapacitors with cc-AT/CNT as the electrodes in a PVA/1.0 M H_2SO_4 gel electrolyte were fabricated. The symmetric cc-AT/CNT||cc-AT/CNT device demonstrated nearly rectangular shapes with a set of redox peaks in the CV curves at different scan rates (**Figure 3.5a**), signifying good rate capability and ideal pseudocapacitive energy storage behaviors. The GCD profiles (**Figure 3.5b**) adopted triangular shapes with negligible *iR* drops and demonstrated that the symmetric device can be steadily charged to 0.8 V even at a low current density of 0.5 mA cm^{-2}, suggesting an efficient charge transfer process.

The long-term cycling stability and impedance of the symmetric cc-AT/CNT||cc-AT/CNT device were further evaluated and compared with the symmetric AT/CNT||AT/CNT device (**Figure 3.5c** and **Figure S3.15**). The symmetric cc-AT/CNT||cc-AT/CNT device retained 70% of its initial capacitance after 50,000 charge/discharge cycles. Even after 100,000 cycles of charging and discharging, the symmetric cc-AT/CNT||cc-AT/CNT device can deliver a specific capacitance retention of 63%. In contrast, the symmetric AT/CNT||AT/CNT device already lost 35% of its highest capacitance in the first 1000 cycles and only exhibited specific capacitance retention below 50% after 5000 cycles.

As demonstrated in **Figure 3.5d**, the cc-AT/CNT composite can reach an ultralong cycle life of 20,000 cycles with 80% capacitance retention, which significantly outperformed many reported

electrode materials based on PANI and CNTs hybrid materials such as PANI/CNT/papers,[28] PANI/CNTs,[29] HPC/PANI,[12] HA/CNT/PANI,[30] P-MWNT-PANI,[31] PANI@CNT-CNC/PVA-PAA,[32] PANI-CNT,[33] PANI/MWNT,[34] PANI-RGO/MWCNT,[35] PANI/MWCNT[36] tested in a three-electrode cell setup (details shown in **Table S3.1**). In addition, as shown in **Figure 3.5e**, the fabricated symmetric quasi-solid-state devices based on cc-AT/CNT presented an ultralong cycle life of >50,000 cycles, something that has been difficult to achieve in other PANI- and CNT-based symmetric supercapacitors such as PANI/CNTs/CFP,[37] P@CNTF5,[38] PANI/CNT,[39] CNT/graphene/PANI,[40] PANI/CNTs,[41] CNT/PANI,[42] SFS,[43] S-CPNf,[44] SWCNT/PANI,[45] IR-CNT@PANI,[46] MWCNT-PANI,[47] CNT@PANI,[48] PANI/CNT fiber-shaped supercapacitor[49] (details shown in **Table S3.2**).

3.4 Conclusions

To summarize, we have demonstrated that a facile and potentially scalable laser scribing method can be employed to fabricate durable AT/CNT electrode materials for ultralong cycling supercapacitors. The molecular design approach strongly binds AT and CNTs through amide covalent linkages, which is beneficial for preserving good electrical connections and minimizing mechanical degradation during long-term cycling. The cc-AT/CNT composite, as a proof-of-concept, exhibited remarkable cycling stability, with 80% capacitance retention and Coulombic efficiency close to 100% after 20,000 cycles of repeated charging and discharging, which outperformed the non-covalently coupled, long-chain PANI/CNT composite whose capacitance degraded to 80% after only 1000 cycles. In addition, the compact AT/CNT heterointerfaces in the cc-AT/CNT composite are advantageous for facilitating electron/ion transfer, leading to fast charge/discharge kinetics and good rate capability. Furthermore, the flexible symmetric quasi-solid-state devices based on cc-AT/CNT can deliver superior cycling stability with 70% and 63%

capacitance retention after 50,000 and 100,000 cycles, respectively. This work not only inspires the molecular-level design of high-performance electrode materials but also provides a scalable fabrication strategy for supercapacitors toward flexible electronics.

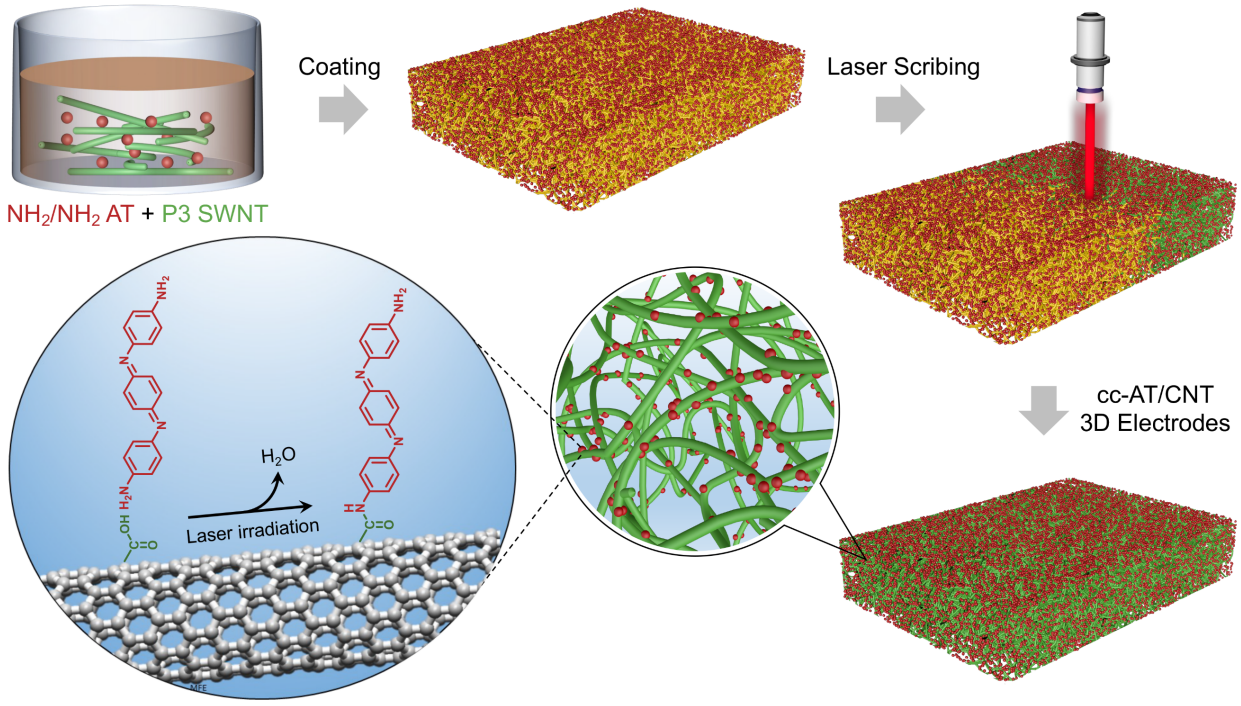

Figure 3.1. Schematic illustration of the fabrication process for the cc-AT/CNT composite.

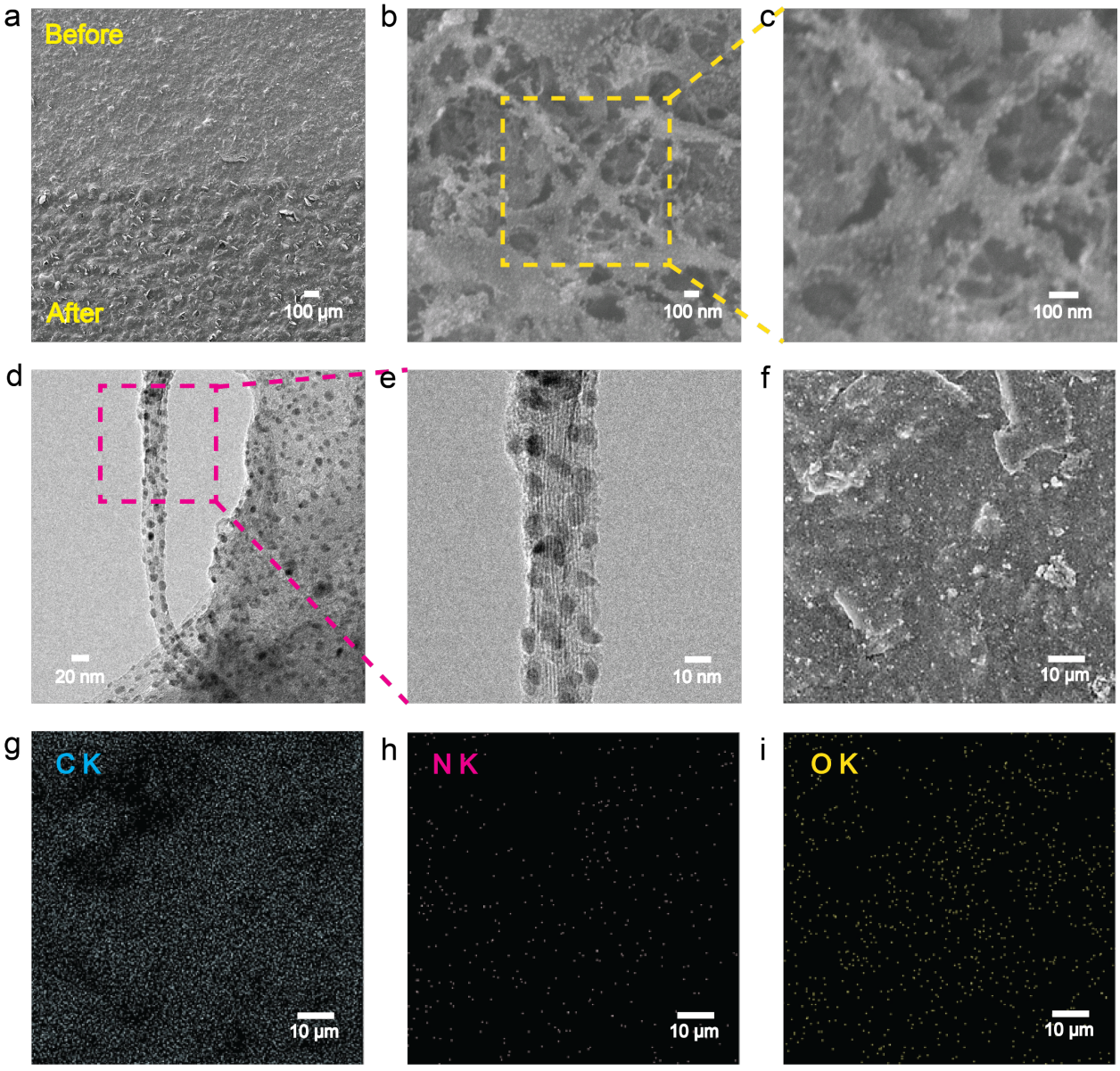

Figure 3.2. Morphological characterizations of the cc-AT/CNT composite. a) SEM image of a composite film showing the composite before (top) and after (bottom) laser irradiation. b,c) SEM images, and d,e) TEM images of the cc-AT/CNT composite at different magnifications. f) Surface morphology of a cc-AT/CNT composite and EDS elemental mapping of g) carbon, h) nitrogen, and i) oxygen in a cc-AT/CNT composite.

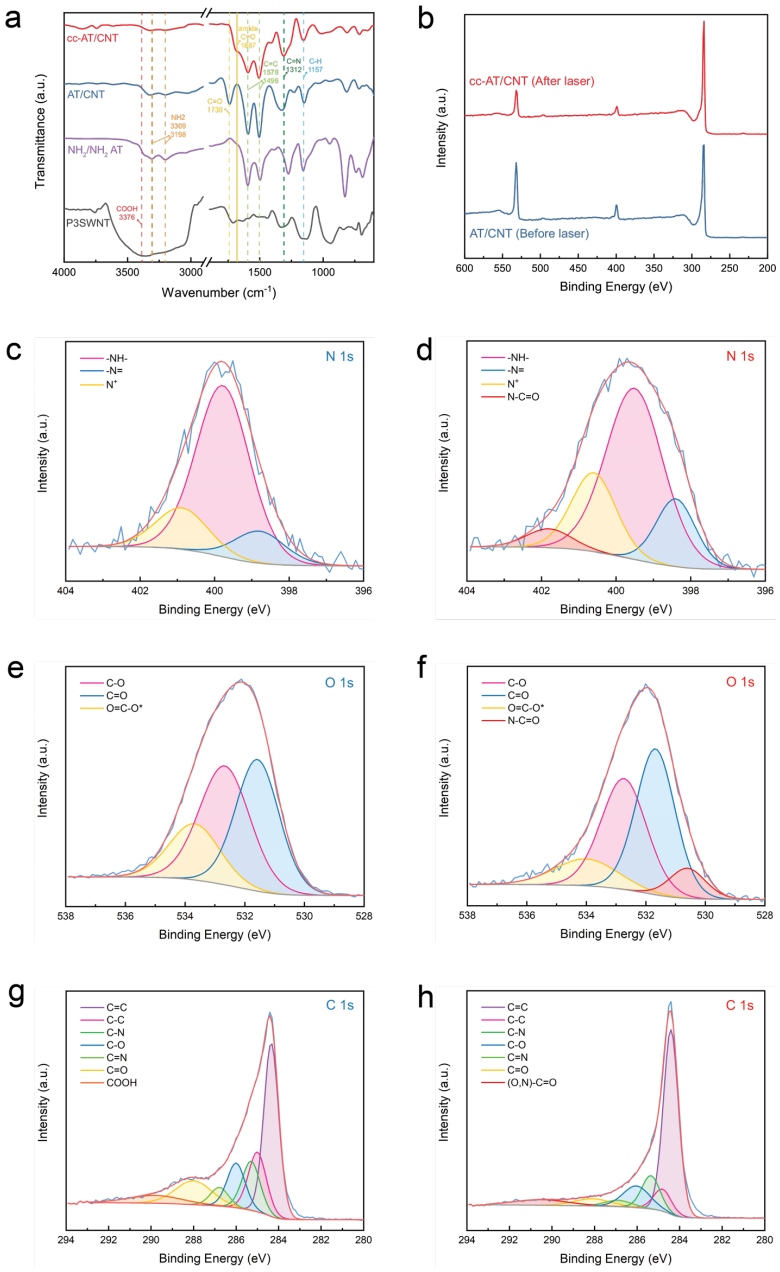

Figure 3.3. Spectroscopic characterizations of the cc-AT/CNT composite. a) FT-IR spectra of cc-AT/CNT (after laser irradiation), AT/CNT (before laser irradiation), as well as the starting materials NH_2/NH_2 AT and P3 SWNT. b) XPS survey spectra of cc-AT/CNT (after laser irradiation), and AT/CNT (before laser irradiation). Deconvoluted N 1s core level XPS spectra of c) AT/CNT and d) cc-AT/CNT. Deconvoluted O 1s core level XPS spectra of e) AT/CNT and f) cc-AT/CNT. Deconvoluted C 1s core level XPS spectra of g) AT/CNT and h) cc-AT/CNT.

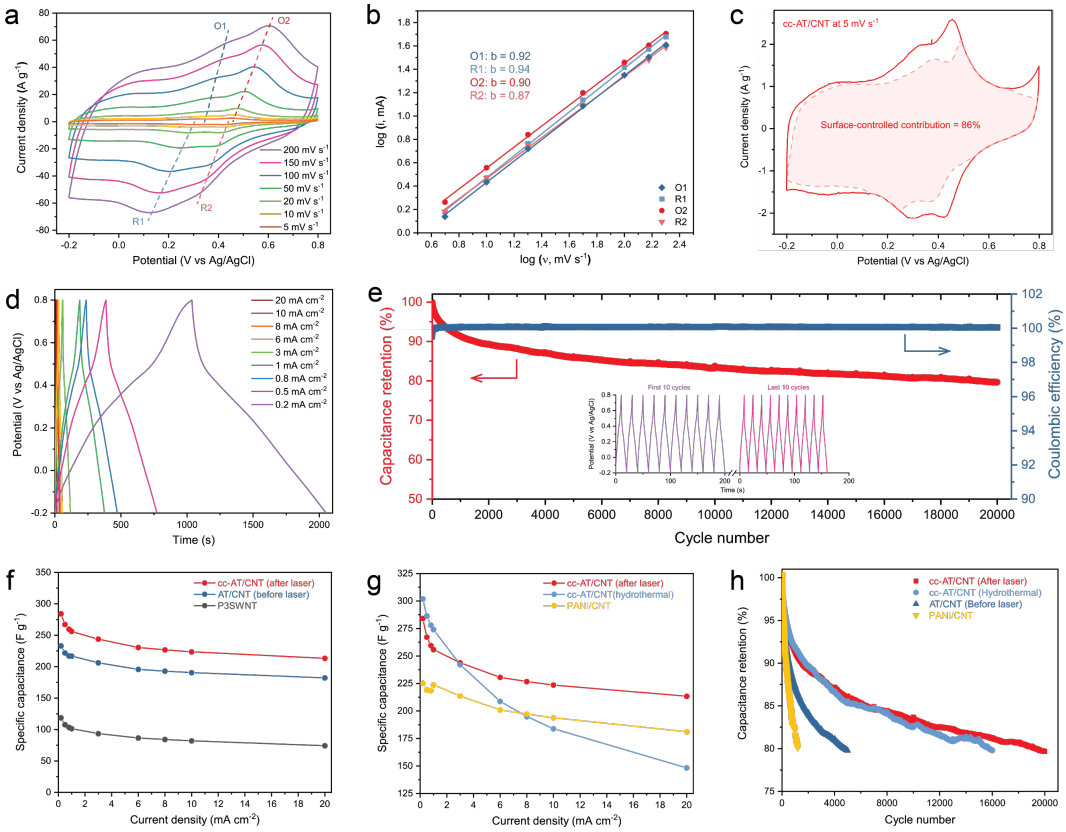

Figure 3.4. Electrochemical performance study in 1.0 M H_2SO_4 in a three-electrode cell setup. a) CV curves at various scan rates from 5 to 200 mV s^{-1} and b) determination of *b*-values at each redox peak in log(*i*) vs. log(*v*) plots. c) Quantification of the surface-controlled and diffusion-controlled charge storage in a cc-AT/CNT electrode at 5 mV s^{-1}. d) GCD profiles of a cc-AT/CNT electrode at different current densities ranging from 0.2 to 20 mA cm^{-2}. e) Long-term cycling performance of a cc-AT/CNT during 20,000 charge/discharge cycles at a current density of 21 A g^{-1}, with the inset showing the initial (1^{st}–10^{th}) and the last ($19{,}990^{th}$–$20{,}000^{th}$) ten GCD cycles of the electrode. f) The rate performance study of cc-AT/CNT (after laser irradiation), AT/CNT (before laser irradiation), P3 SWNT, as well as g) cc-AT/CNT (hydrothermal), and PANI/CNT composite. h) Cycling stability study of cc-AT/CNT (after laser irradiation), cc-AT/CNT (hydrothermal), AT/CNT (before laser irradiation), and PANI/CNT until 80% capacitance retention.

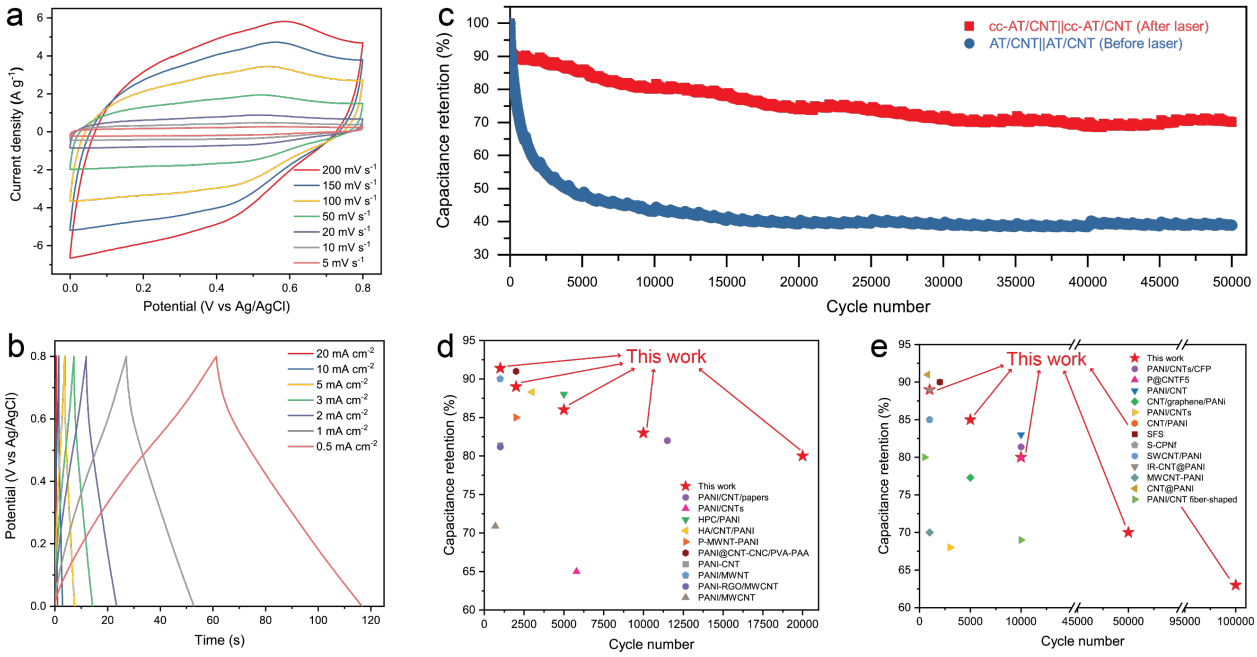

Figure 3.5. Electrochemical evaluation of the symmetric quasi-solid-state devices in a PVA/H_2SO_4 gel electrolyte. a) CV curves of a symmetric cc-AT/CNT||cc-AT/CNT device at various scan rates from 5 to 200 mV s^{-1}. b) GCD profiles of a symmetric cc-AT/CNT||cc-AT/CNT device at different current densities from 0.5 to 10 mA cm^{-2}. c) Cycling stability study of the two symmetric quasi-solid-state devices during 50,000 charge/discharge cycles at 4 A g^{-1}. Comparison of the cycling stability performance of d) other PANI/CNT nanocomposites as electrodes[12, 28-36] and e) other symmetric supercapacitors based on PANI/CNT nanocomposites[37-49] with this work.

3.5 Supporting Information

3.5.1 Experimental Section

Materials: Carboxylic acid-functionalized single-walled carbon nanotubes (P3 SWNT) were purchased from Carbon Solutions, Inc. (CSI). Polyvinyl alcohol (PVA, M_w = 89,000–98,000, 98–99% hydrolyzed), aniline (≥ 99.5%)， and p-phenylenediamine were purchased from Sigma-Aldrich. Ammonium persulfate (98+%) was purchased from Acros. Ammonium hydroxide (28–30%) was purchased from VWR. Sulfuric acid (H_2SO_4), hydrochloric acid (HCl), and ethanol were purchased from Fisher Scientific. Graphite paper used as current collectors was purchased from Digi-Key Electronics (manufactured by Panasonic Electronic Components, part number: P13689-ND). All reagents were used without further purification.

Synthesis of Amine/Amine End-capped Aniline Trimer (NH_2/NH_2 AT): Amine/amine end-capped aniline trimer (NH_2/NH_2 AT) was prepared by a modified reported method.[50] In brief, 0.86 g of p-phenylenediamine was dissolved in a solution of 100 mL of 1.0 M HCl and 40 mL of ethanol, with the assistance of gentle ultrasonication. The solution in a round bottom flask was then chilled in a salty ice bath. Later on, 1.8 g of ammonium persulfate was added in quickly, and the solution was stirred for around 2.5 min. Once the color of the solution started showing grey, 1.5 mL of aniline was added in and kept stirring for 40 min. The resulting solution was vacuum filtered and washed with deionized water. After treating with 1.0 M ammonium hydroxide solution for 2 hours, the solution was again vacuum filtered and washed with deionized water until the filtrate became pH neutral. A blue powder with approximately 30% yield was collected after air drying for a few days. The nuclear magnetic resonance (NMR) spectrum of the synthesized NH_2/NH_2 AT is shown in **Figure S3.12**.

Preparation of Covalently Coupled Aniline Trimer/Carbon Nanotubes (cc-AT/CNT) Composite upon Laser Irradiation: In a typical synthesis, NH_2/NH_2 AT was dissolved in deionized water (10 mL, 5 mg mL^{-1}) through bath sonication, and P3 SWNT was uniformly dispersed in deionized water (10 mL, 5 mg mL^{-1}) through ultrasonication. Next, the NH_2/NH_2 AT solution was slowly added into the P3 SWNT suspension at a controlled rate while stirring using a syringe pump, followed by vigorous stirring for 3 h at room temperature. The uniform mixture was then drop-cast on graphite paper current collectors (1 cm × 1 cm), which were then left to dry under ambient conditions. Typical loadings of the materials were about 0.5–0.8 mg cm^{-2}. Finally, the dried film was laser-scribed using a 40 W full spectrum laser muse 2D vision desktop CO_2 laser cutter under ambient conditions. The geometric patterns for laser scribing were generated in RetinaEngrave. We set 10% laser power, 1000 dpi resolution and 100% speed (~90 s for a 1×1 cm^2 area) to prepare cc-AT/CNT electrodes. The as-made cc-AT/CNT electrodes were directly used for electrochemical testing and characterization.

Preparation of Covalently Coupled Aniline Trimer/Carbon Nanotubes (cc-AT/CNT) Composite Using a Hydrothermal Method: In a typical synthesis, 8 mg of P3 SWNT was dispersed in 14 mL of deionized water, which was further ultrasonicated until a uniform dispersion was obtained. Then 8 mg of NH_2/NH_2 AT was slowly added to the P3 SWNT uniform dispersion under vigorous stirring, followed by continuous stirring for 2 h at room temperature. The uniform mixture was then sealed in a 25 mL Teflon-lined autoclave and maintained at 140 ℃ for 4 h. The autoclave was then cooled naturally to room temperature. The final cc-AT/CNT composite formed by the hydrothermal method was freeze-dried using liquid nitrogen.

Preparation of a Physical Mixture of Polyaniline/Carbon Nanotubes (PANI/CNT): The physical mixture – PANI/CNT – was prepared by a traditional physical mixing method. Briefly,

the PANI nanofibers were mixed with P3 SWNT in deionized water. The weight ratio of PANI to P3 SWNT was 1:1, which was the same as the weight ratio of AT to P3 SWNT in the cc-AT/CNT (after laser irradiation) composite. The uniform mixture was obtained after vigorous stirring at room temperature overnight. The PANI/CNT electrodes were made by directly drop-casting the as-synthesized mixture (no binder) on graphite paper current collectors (1 cm × 1 cm), which were then dried under ambient conditions overnight.

Materials Characterization: The morphological and structural characterizations of the materials were carried out by scanning electron microscopy (SEM) using a JEOL JSM-6700F FE-SEM and transmission electron microscope (TEM, T20 iCorr (FEI) High-Res CryoEM and CryoET). Elemental analyses of the samples were obtained using an energy dispersive X-ray spectrometer (EDS, as an attachment to an SEM instrument). Fourier-transform infrared (FT-IR) spectroscopy by attenuated total reflectance was performed on a JASCO FT/IR-6300. X-ray photoelectron spectroscopy (XPS) measurements were obtained using a Kratos Axis Ultra DLD spectrometer with a monochromatic Al K_α X-ray source (λ = 1486.6 eV). Thermal gravimetric analysis (TGA) was carried out on a Perkin Elmer TGA 8000 at a heating rate of 10 °C min^{-1} in air.

Electrochemical Characterization: The electrochemical performances of the prepared electrodes were characterized by cyclic voltammetry (CV), galvanostatic charge–discharge (GCD), electrochemical impedance spectroscopy (EIS), and cycling stability measurements with various electrolytes at room temperature. In all three-electrode studies, graphite sheets were used as the counter electrode, and Ag/AgCl was used as the reference electrode. The EIS measurements were performed at 0.2 V relative to the reference electrode over a frequency range from 200 kHz to 10 mHz with an amplitude of 10 mV. In the two-electrode tests of the symmetric devices, the

EIS measurements were performed at open circuit voltage over a frequency range from 1 kHz to 10 mHz with an amplitude of 10 mV. All electrochemical data were collected using a Biologic VMP3 electrochemical workstation (VMP3b-10, USA Science Instrument). The mass loading of each electrode was calculated from the weight difference before and after drop-casting (measured by a Mettler Toledo MX5 microbalance ±1 μg error). An all-solid-state symmetric supercapacitor was fabricated from two identical pieces (1 cm × 1 cm) of cc-AT/CNT electrodes, separated by an ion-porous membrane (cellulose separator, NKK TF4030). A PVA/1.0 M H_2SO_4 gel electrolyte was used in fabricating the symmetric devices. Briefly, 1.0 g of PVA was dissolved in 10 mL of water and stirred vigorously for 30 min at 90 ℃. Then, 0.56 mL of stock H_2SO_4 was added to prepare a PVA/1.0 M H_2SO_4 gel electrolyte. The resulting gel electrolyte was applied to the electrodes and left for 60 min to ensure complete wetting of the electrode surfaces. The two electrolyte-filled electrodes and the separator were then assembled and dried for 12 h at room temperature until fully solidified.

Calculation Methods for Electrochemical Data: The gravimetric specific capacitance (C_s) and areal capacitance (C_a) of the electrodes tested in a three-electrode cell setup were calculated from the GCD profiles using the following equations:[51]

$$C_s = \frac{I \times \Delta t}{m \times \Delta V}\ (F\,g^{-1}) \qquad \text{(S3.1) (Three-electrode)}$$

$$C_a = \frac{I \times \Delta t}{a \times \Delta V}\ (mF\,cm^{-2}) \qquad \text{(S3.2) (Three-electrode)}$$

where I is the discharge current (mA), Δt is the discharge time (s), ΔV is the potential window (V), m is the mass of the active electrode materials (mg) and a represents the surface area of the electrode (cm^2).

The specific capacitance ($C_{S,electrode}$) and areal capacitance ($C_{A,electrode}$) of each of the positive and negative electrodes can be derived from the capacitance of the symmetric two-electrode device calculated from GCD profiles according to the following equations:[51]

$$C_{S,electrode} = 4 \times C_{S,device} = 4 \times \frac{I \times \Delta t}{M \times \Delta V} \ (F\,g^{-1}) \quad \text{(S3.3) (Two-electrode)}$$

$$C_{A,electrode} = 2 \times C_{A,device} = 2 \times \frac{I \times \Delta t}{A \times \Delta V} \ (mF\,cm^{-2}) \quad \text{(S3.4) (Two-electrode)}$$

where I is the discharge current (mA), Δt is the discharge time (s), ΔV is the potential window (V), M is the total mass of the active materials used in the two electrodes (mg) and A represents the geometric area of the device (cm^2).

3.5.2 Materials Characterization

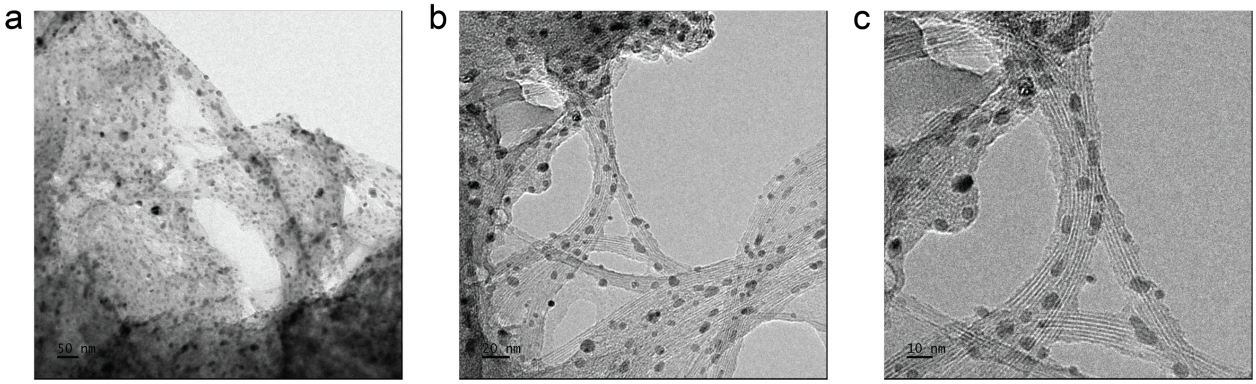

Figure S3.1. TEM images of cc-AT/CNT (after laser irradiation).

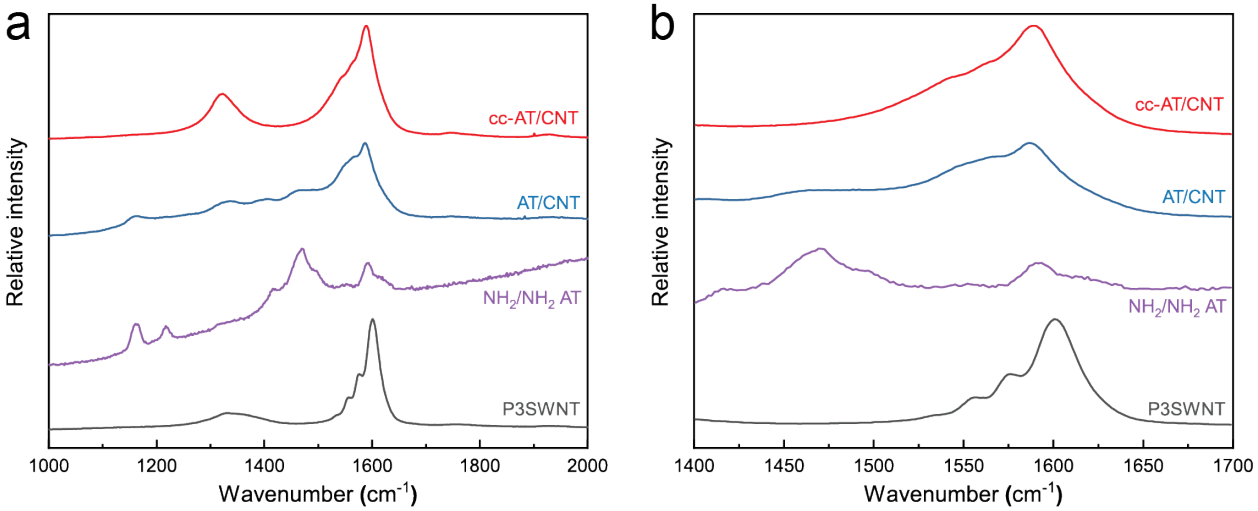

Figure S3.2. Raman spectra of cc-AT/CNT (after laser irradiation), AT/CNT (before laser irradiation) as well as the starting materials NH_2/NH_2 AT and P3 SWNT at a) a zoom-out view and b) a zoom-in view.

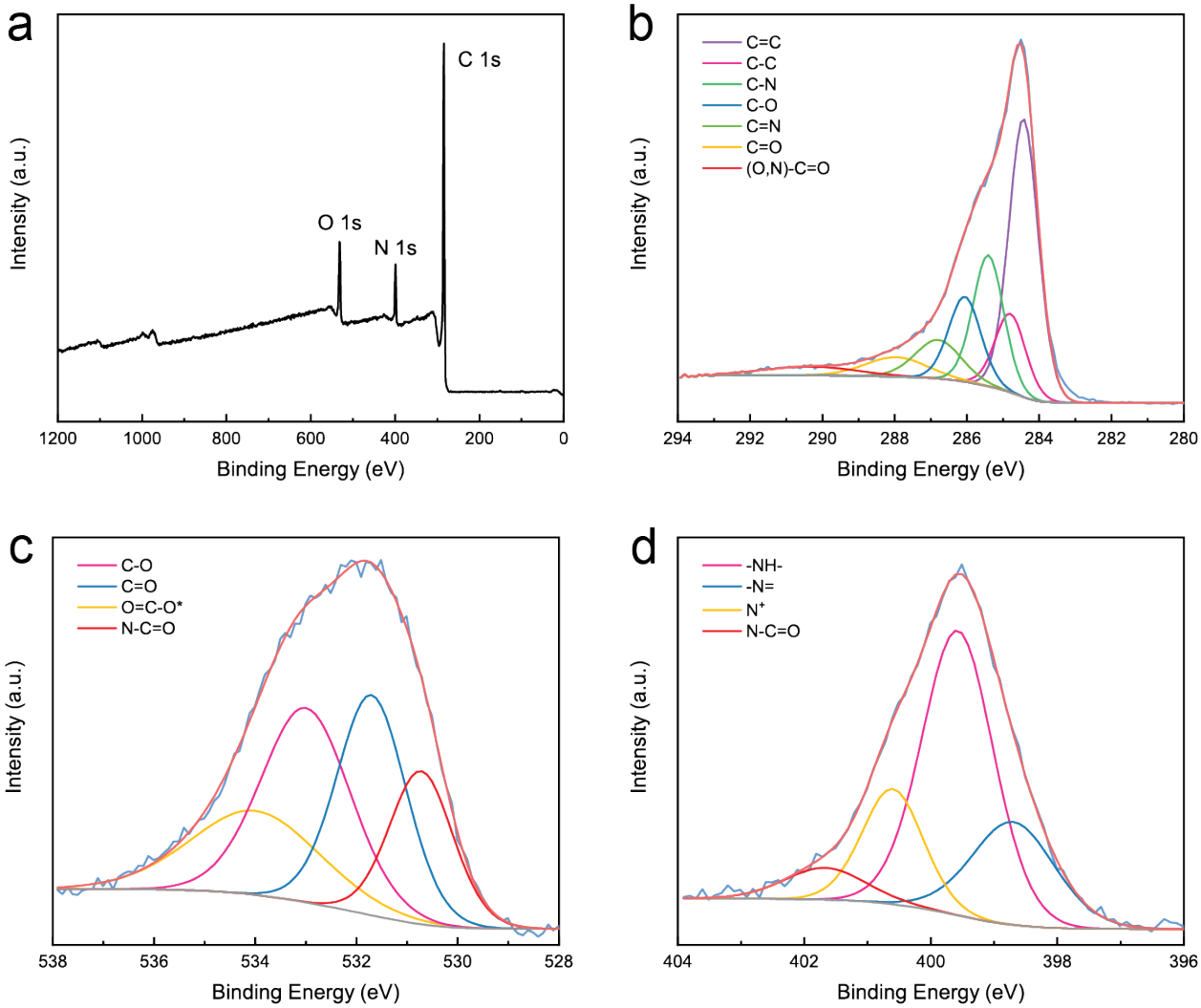

Figure S3.3. a) XPS survey spectra, b) deconvoluted C 1s, c) O 1s, and d) N 1s core level XPS spectra of cc-AT/CNT (hydrothermal).

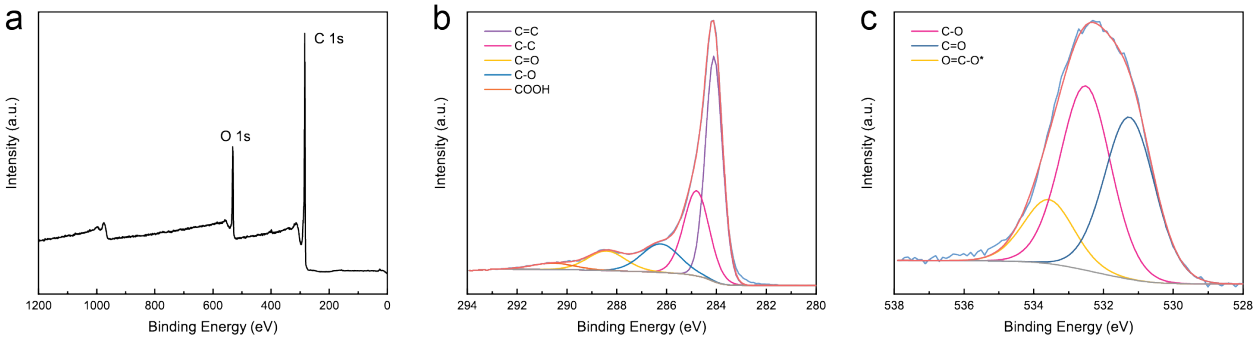

Figure S3.4. a) XPS survey spectra, b) deconvoluted C 1s, and c) O 1s core level XPS spectra of P3 SWNT.

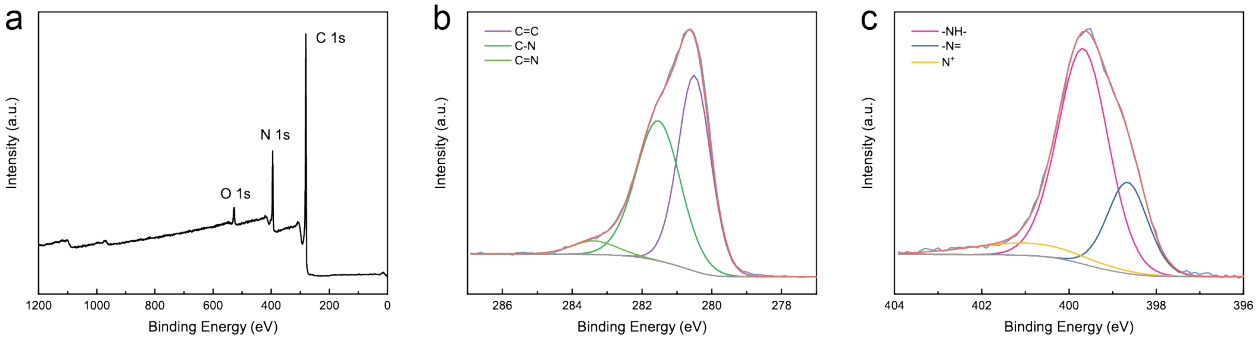

Figure S3.5. a) XPS survey spectra, b) deconvoluted C 1s, and c) N 1s core level XPS spectra of NH_2/NH_2 AT.

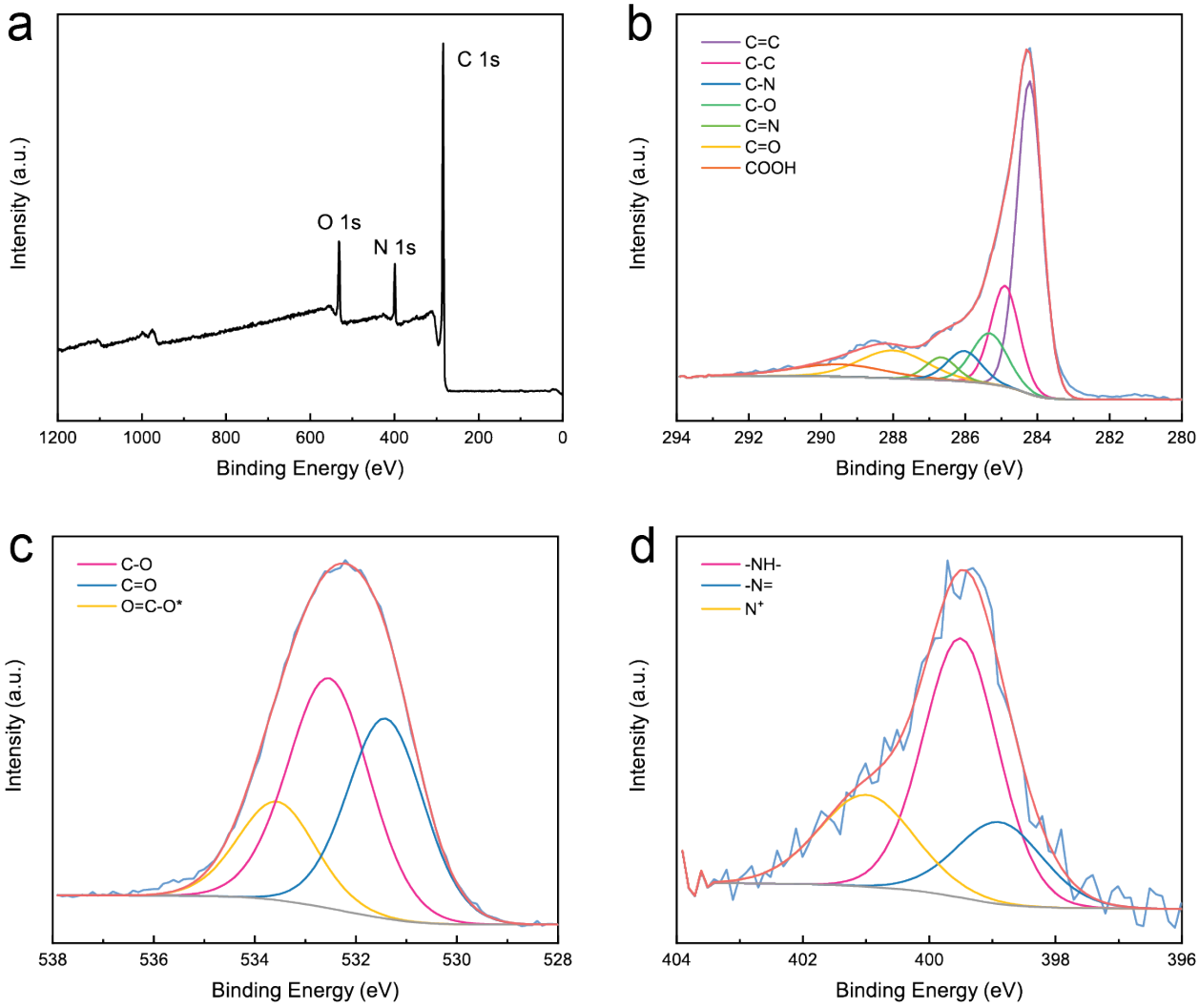

Figure S3.6. a) XPS survey spectra, b) deconvoluted C 1s, c) O 1s, and d) N 1s core level XPS spectra of PANI/CNT.

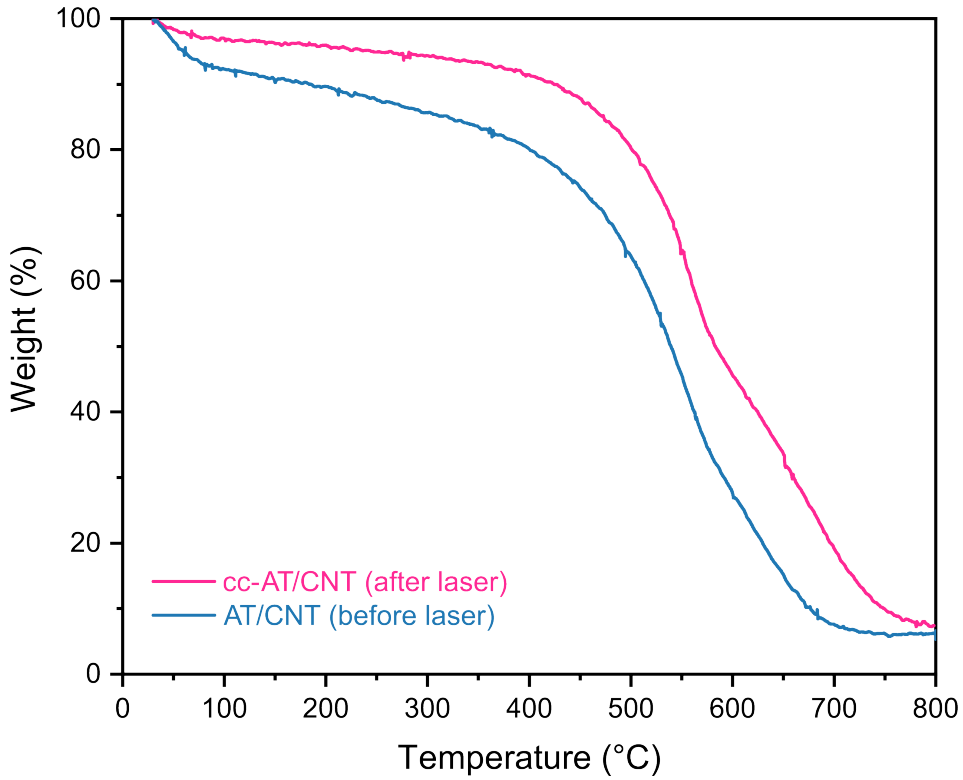

Figure S3.7. TGA of cc-AT/CNT after laser irradiation, AT/CNT before laser irradiation as well as the starting materials NH_2/NH_2 AT and P3 SWNT.

As depicted in **Figure S3.7**, cc-AT/CNT (after laser irradiation) exhibits comparatively higher thermal stability than AT/CNT (before laser irradiation). Both composites present two steps of weight loss. The first phase of weight loss occurring at less than 100 °C is due to the evaporation or expulsion of the absorbed water, where AT/CNT (before laser irradiation) shows a weight loss of 7.2% while cc-AT/CNT (after laser irradiation) exhibits a weight loss of 3.0%. The second step involves the degradation of AT and CNT. The onset of the decomposition of AT/CNT (before laser irradiation) occurs at ~400 °C, while that of cc-AT/CNT (after laser irradiation) occurs at ~450 °C. The enhancement in thermal stability of cc-AT/CNT (after laser irradiation) can be explained by the strong interactions between AT and CNT due to the formation of amide covalent connections.

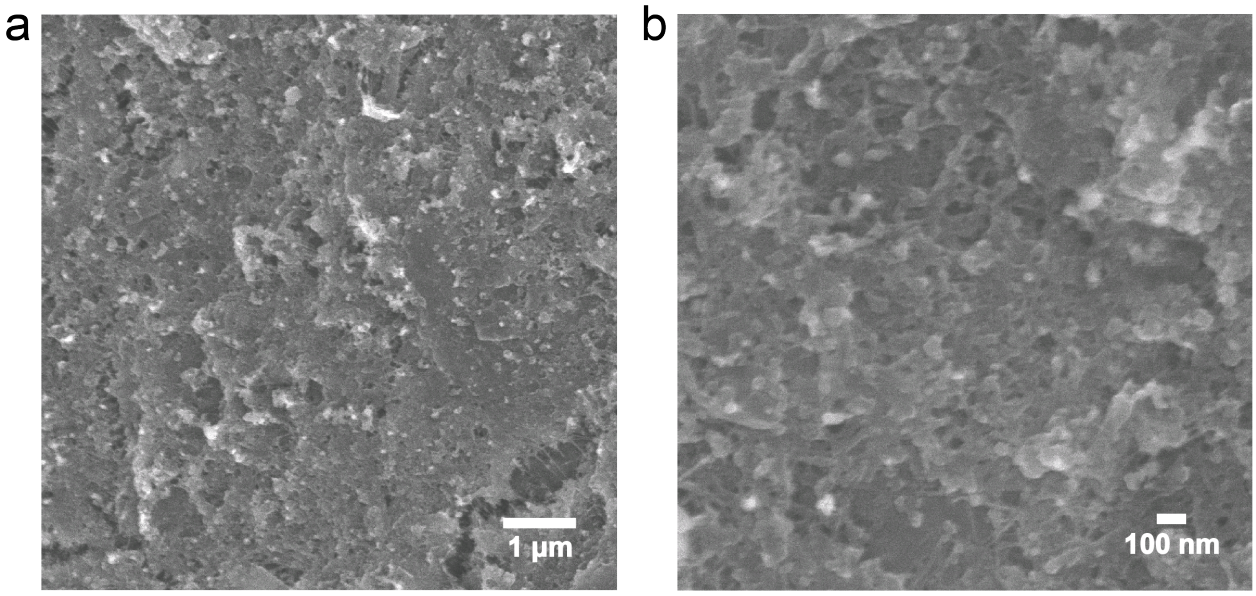

Figure S3.8. SEM images of AT/CNT (before laser irradiation).

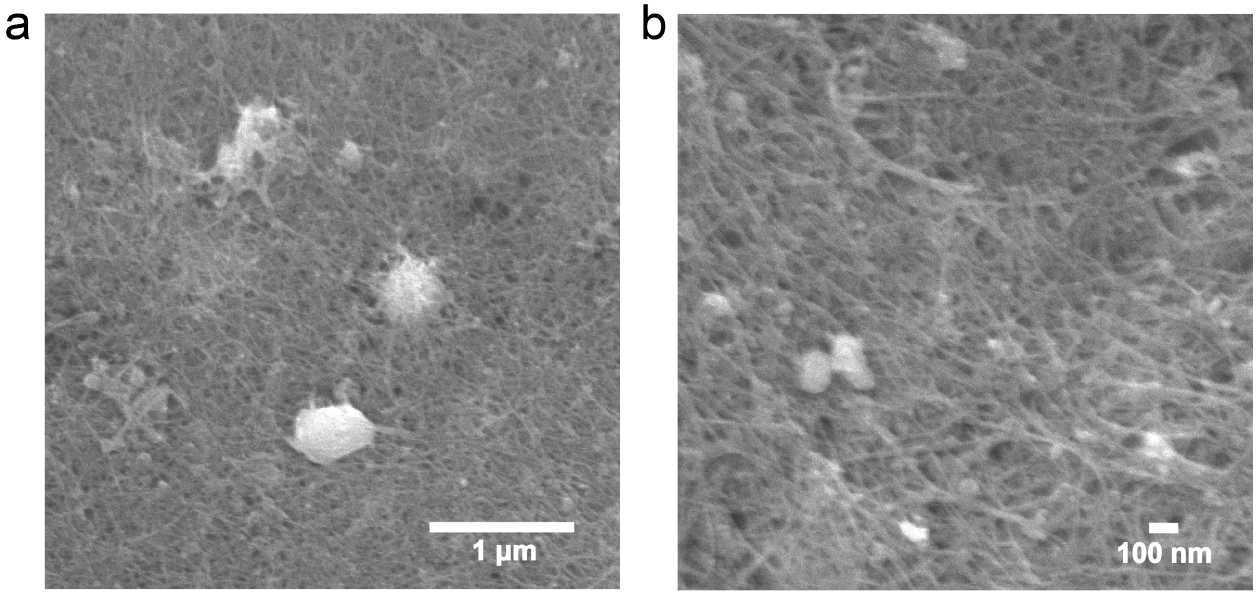

Figure S3.9. SEM images of cc-AT/CNT (hydrothermal).

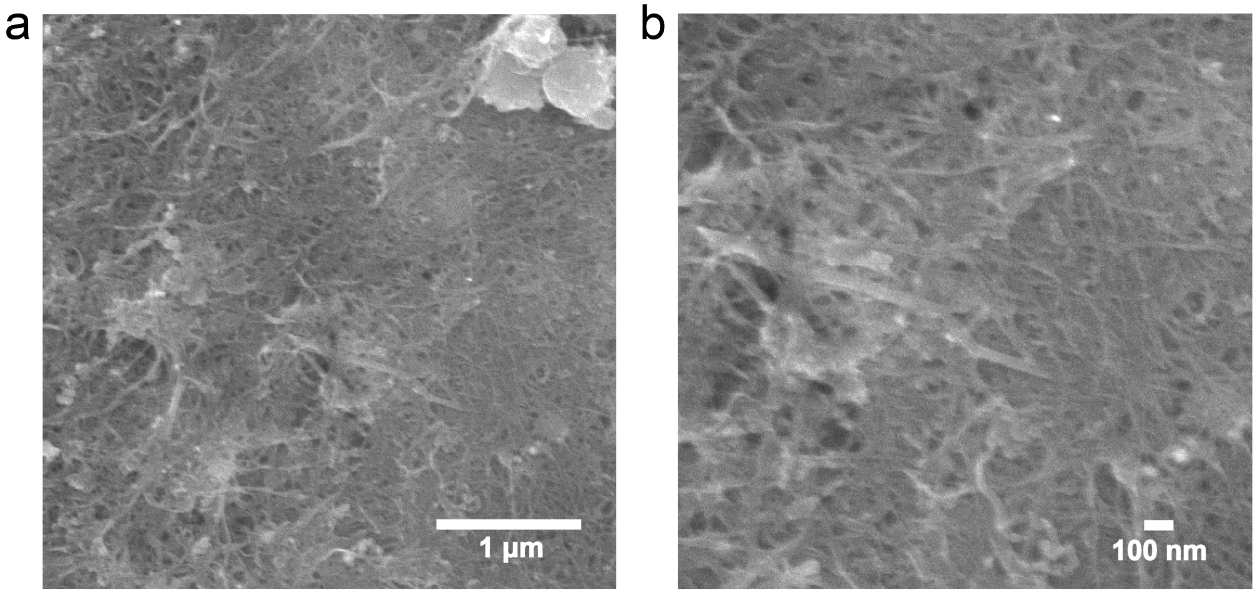

Figure S3.10. SEM images of PANI/CNT.

The P3 SWNT was first fully dispersed in DI H_2O, which was then drop-cast on a graphite paper substrate (without any additives). Half of the dried P3 SWNT film was laser scribed using a 40 W full spectrum laser muse 2D vision desktop CO_2 laser cutter under ambient conditions. The SEM image in **Figure S3.11a** shows the P3 SWNT film before (bottom) and after (top) laser irradiation. After laser irradiation, the CNT film demonstrates a more porous structure, with rougher surfaces, and a darker color compared to it before laser irradiation. At a higher magnification, the P3 SWNT film before laser irradiation (**Figure S3.11b**) shows a dense and compact structure of highly overlapping CNTs. In contrast, the P3 SWNT film after laser irradiation (**Figure S3.11c**) presents a more porous structure with less stacking of the CNTs. The likely mechanism is that the flux of the laser-induced chemically released gases (CO_2, H_2O, etc.) enables the formation of a hierarchical porous structure.[52] It is noteworthy that the electrochemical performance data of the control experiment P3 SWNT mentioned in the manuscript were collected on the original P3 SWNT without any laser irradiation.

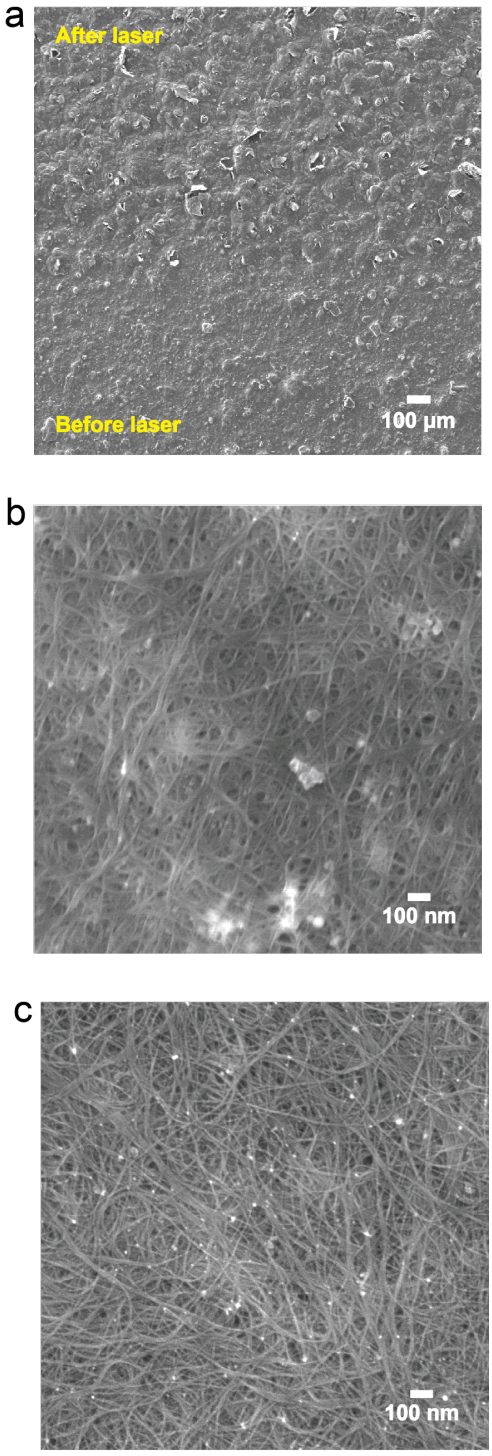

Figure S3.11. a) SEM image of a P3 SWNT film before (bottom) and after (top) laser irradiation; SEM images at a higher magnification of P3 SWNT b) before and c) after laser irradiation.

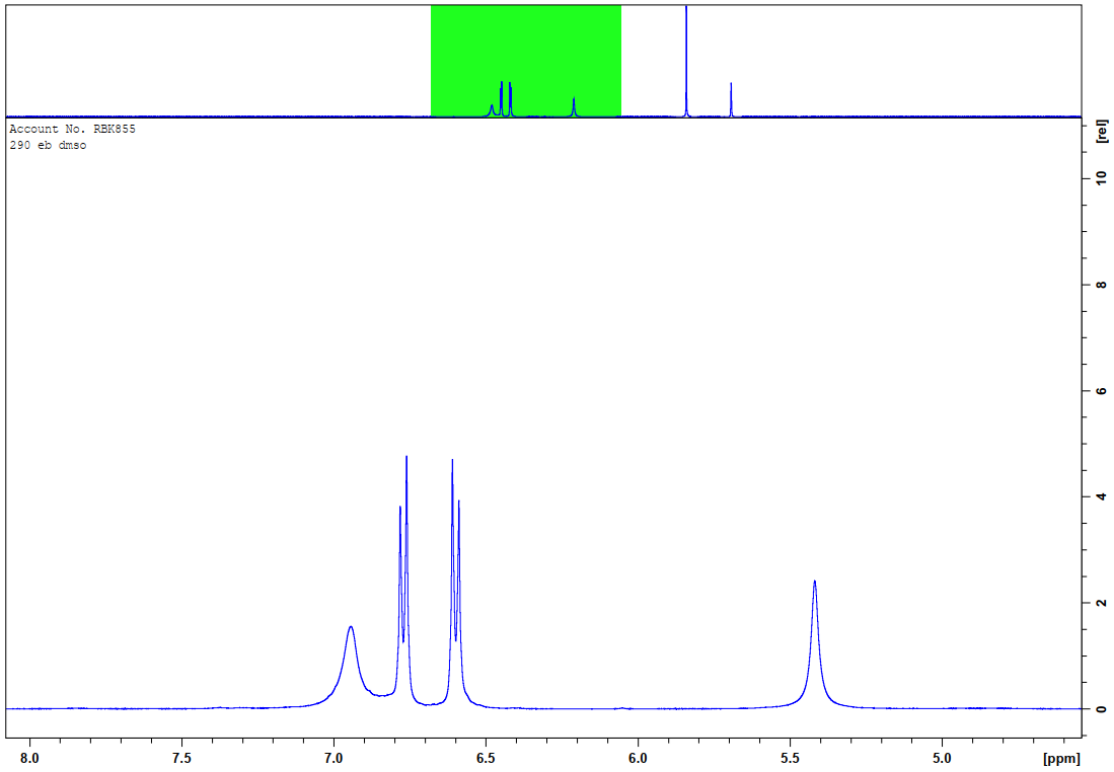

Figure S3.12. NMR spectrum of amine/amine end-capped aniline trimer (NH_2/NH_2 AT) in deuterated DMSO.

3.5.3 Electrochemical Performance

As shown in **Figure S3.13**, at 5 mV s^{-1}, the CV curve of cc-AT/CNT (after laser irradiation) showed a larger integrated area compared to the AT/CNT (before laser irradiation), P3 SWNT, and PANI/CNT, indicating higher specific capacitance. The cc-AT/CNT (after laser irradiation) along with AT/CNT (before laser irradiation), cc-AT/CNT (hydrothermal), and PANI/CNT exhibited two sets of redox peaks, corresponding to the near-surface Faradaic processes of redox transitions in AT or PANI.

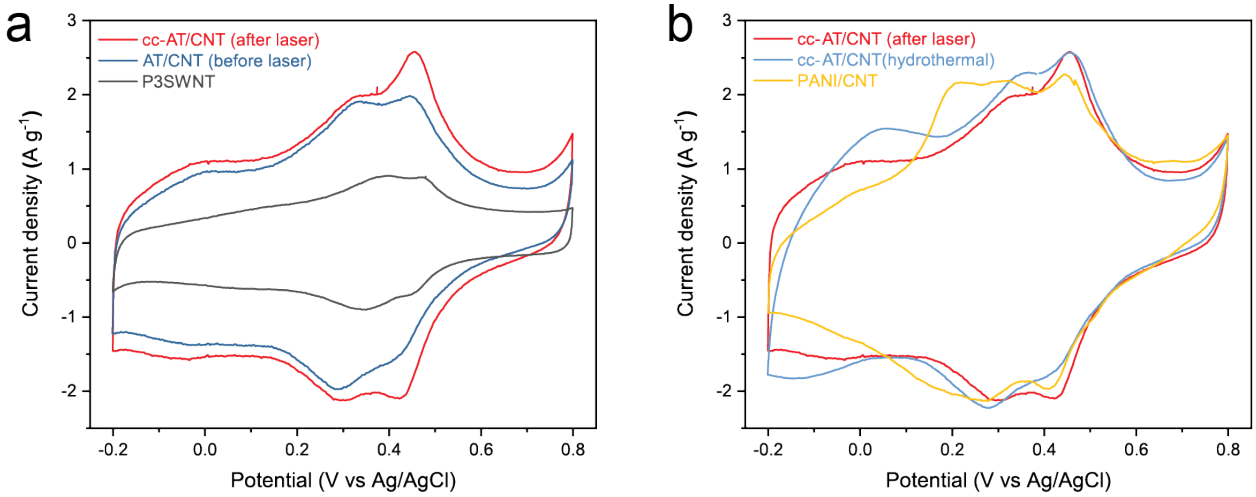

Figure S3.13. a) The CV curves of cc-AT/CNT (after laser irradiation), AT/CNT (before laser irradiation), P3 SWNT, b) cc-AT/CNT (hydrothermal), and PANI/CNT composite at a scan rate of 5 mV s^{-1}.

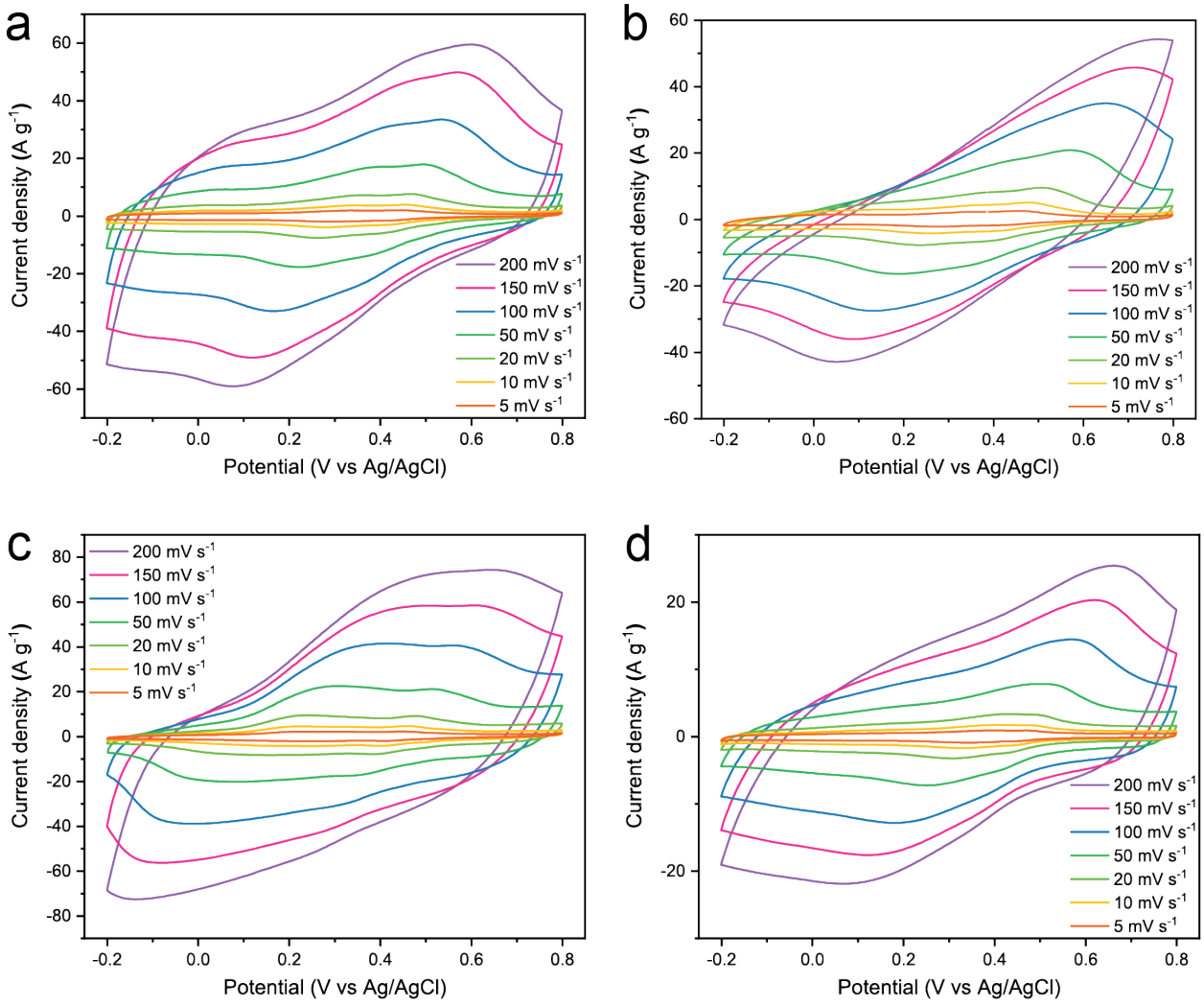

Figure S3.14. CV curves of a) AT/CNT (before laser irradiation), b) cc-AT/CNT (hydrothermal), c) PANI/CNT, and d) P3 SWNT at various scan rates from 5 to 200 mV s^{-1}.

In the Nyquist plot of the symmetric cc-AT/CNT||cc-AT/CNT device (**Figure S3.15a**), barely any semicircle can be observed at high frequency, implying almost no charge transfer resistance. At low frequency, the Nyquist plot of the symmetric cc-AT/CNT||cc-AT/CNT device (red) showed a near-vertical line with a higher gradient than the symmetric AT/CNT||AT/CNT device (blue), confirming faster electron transport during the redox reactions. Moreover, as shown in the inset to **Figure S3.15a**, the Nyquist plot of the symmetric cc-AT/CNT||cc-AT/CNT device (red) presented a lower uncompensated resistance value (~1.99 Ω) than the symmetric AT/CNT||AT/CNT device (blue), suggesting a higher electrical conductivity of the cc-AT/CNT electrode after the laser irradiation process. **Figure S3.15b** displays the CV diagrams of the symmetric cc-AT/CNT||cc-AT/CNT device after 1000, 5000, 10,000, 20,000, 30,000, and 40,000 charge/discharge cycles, where the capacitance faded steadily in the first 20,000 cycles and the capacitance fade was negligible thereafter.

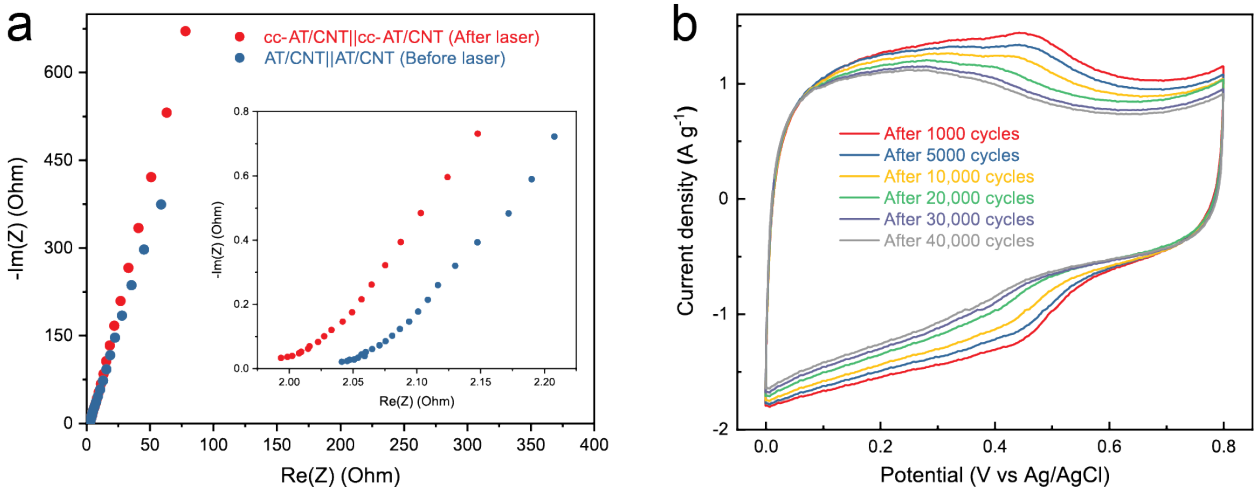

Figure S3.15. a) Nyquist plots of a cc-AT/CNT||cc-AT/CNT device and an AT/CNT||AT/CNT device over a frequency range from 1 kHz to 10 mHz, with the inset showing a magnified high-frequency region. b) The CV diagrams of the symmetric cc-AT/CNT||cc-AT/CNT device after 1000, 5000, 10,000, 20,000, 30,000 and 40,000 charge/discharge cycles at 50 mV s^{-1}.

3.5.4 Comparison with Literature Reports

Table S3.1. Comparison of the Cycling Stability of cc-AT/CNT with Other PANI- and CNT-based Composites in a Three-electrode Cell Setup

Materials	Cycle number	Capacitance retention	Current density or scan rate	Ref.
cc-AT/CNT	**10000**	**83%**	**21 A g^{-1}**	**This work**
	20000	**80%**	**21 A g^{-1}**	
PANI/MWCNT	11500	82%	50 mA cm^{-2}	[28]
PANI/CNTs	5800	65%	15 A g^{-1}	[29]
HPC/PANI	5000	88%	1 A g^{-1}	[12]
HA/CNT/PANI	3000	88.3%	100 mV s^{-1}	[30]
P-MWNT-PANI	2000	85%	2 A g^{-1}	[31]
PANI@CNT-CNC/PVA-PAA	2000	91%	1 A g^{-1}	[32]
PANI-CNT	1000	81.4%	2 A g^{-1}	[33]
PANI/MWNT	1000	90%	1 A g^{-1}	[34]
PANI-RGO/MWCNT	1000	81.2%	10 A g^{-1}	[35]
PANI/MWCNT	700	70.9%	5 mV s^{-1}	[36]

Table S3.2. Comparison of the Cycling Stability of the Symmetric Quasi-solid-state cc-AT/CNT||cc-AT/CNT Device with Other PANI- and CNT-based Symmetric Devices

Materials	Cycle number	Capacitance retention	Current density or scan rate	Ref.
cc-AT/CNT	**5000**	**85%**	**4 A g^{-1}**	**This work**
	10000	**80%**	**4 A g^{-1}**	
	50000	**70%**	**4 A g^{-1}**	
	100000	**63%**	**4 A g^{-1}**	
PANI/CNTs/CFP	10000	81.4%	1.8 A·g^{-1}	[37]
P@CNTF5	10000	79.9%	50 A·g^{-1}	[38]
PANI/CNT	10000	83%	16 A g^{-1}	[39]
CNT/graphene/PANi	5000	77.3%	1 A g^{-1} (with 800% strain)	[40]
PANI/CNTs	3000	68%	0.5 A g^{-1}	[41]
CNT/PANI	2000	90%	1 A·g^{-1}	[42]
SFS	2000	90%	1 A·g^{-1}	[43]
S-CPNf	1000	85%	0.25 A·g^{-1}	[44]
SWCNT/PANI	1000	85%	N/A	[45]
IR-CNT@PANI	1000	89%	1 A·g^{-1}	[46]
MWCNT-PANI	1000	70%	N/A	[47]
CNT@PANI	800	91%	N/A	[48]
PANI/CNT fiber-shaped supercapacitor	10000	69%	1 A·g^{-1}	[49]
	500	80%	1 A·g^{-1}	

3.6 References

(1) Liu, L.; Taberna, P.-L.; Dunn, B.; Simon, P. Future Directions for Electrochemical Capacitors. *ACS Energy Lett.* **2021**, *6*, 4311−4316.

(2) Evanko, B.; Boettcher, S. W.; Yoo, S. J.; Stucky, G. D. Redox-Enhanced Electrochemical Capacitors: Status, Opportunity, and Best Practices for Performance Evaluation. *ACS Energy Lett.* **2017**, *2*, 2581−2590.

(3) Jia, X.; Ge, Y.; Shao, L.; Wang, C.; Wallace, G. G. Tunable Conducting Polymers: Toward Sustainable and Versatile Batteries. *ACS Sustain. Chem. Eng.* **2019**, *7*, 14321−14340.

(4) Liu, T.; Finn, L.; Yu, M.; Wang, H.; Zhai, T.; Lu, X.; Tong, Y.; Li, Y. Polyaniline and Polypyrrole Pseudocapacitor Electrodes with Excellent Cycling Stability. *Nano Lett.* **2014**, *14*, 2522−2527.

(5) Song, Y.; Liu, T.-Y.; Xu, X.-X.; Feng, D.-Y.; Li, Y.; Liu, X.-X. Pushing the Cycling Stability Limit of Polypyrrole for Supercapacitors. *Adv. Funct. Mater.* **2015**, *25*, 4626−4632.

(6) Soni, R.; Kashyap, V.; Nagaraju, D.; Kurungot, S. Realizing High Capacitance and Rate Capability in Polyaniline by Enhancing the Electrochemical Surface Area through Induction of Superhydrophilicity. *ACS Appl. Mater. Interfaces* **2018**, *10*, 676−686.

(7) Yan, J.; Yang, L.; Cui, M.; Wang, X.; Chee, K. J.; Nguyen, V. C.; Kumar, V.; Sumboja, A.; Wang, M.; Lee, P. S. Aniline Tetramer-Graphene Oxide Composites for High Performance Supercapacitors. *Adv. Energy Mater.* **2014**, *4*, 1400781.

(8) Chang, X.; El-Kady, M. F.; Huang, A.; Lin, C.-W.; Aguilar, S.; Anderson, M.; Zhu, J. Z. J.; Kaner, R. B. 3D Graphene Network with Covalently-Grafted Aniline Tetramer for Ultralong-Life Supercapacitors. *Adv. Funct. Mater.* **2021**, *31*, 2102397.

(9) Li, R.; Lin, C.-W.; Shao, Y.; Chang, C. W.; Yao, F.-K.; Kowal, M. D.; Wang, H.; Yeung, M.; Huang, S.-C.; Kaner, R. B. Characterization of Aniline Tetramer by MALDI TOF Mass Spectrometry upon Oxidative and Reductive Cycling. *Polymers* **2016**, *8*, 401.

(10) Niu, Z.; Zhou, W.; Chen, X.; Chen, J.; Xie, S. Highly Compressible and All-Solid-State Supercapacitors Based on Nanostructured Composite Sponge. *Adv. Mater.* **2015**, *27*, 6002−6008.

(11) Yu, J.; Lu, W.; Pei, S.; Gong, K.; Wang, L.; Meng, L.; Huang, Y.; Smith, J. P.; Booksh, K. S.; Li, Q.; et al. Omnidirectionally Stretchable High-Performance Supercapacitor Based on Isotropic Buckled Carbon Nanotube Films. *ACS Nano* **2016**, *10*, 5204−5211.

(12) Yu, P.; Zhang, Z.; Zheng, L.; Teng, F.; Hu, L.; Fang, X. A Novel Sustainable Flour Derived Hierarchical Nitrogen-Doped Porous Carbon/Polyaniline Electrode for Advanced Asymmetric Supercapacitors. *Adv. Energy Mater.* **2016**, *6*, 1601111.

(13) Liu, F.; Luo, S.; Liu, D.; Chen, W.; Huang, Y.; Dong, L.; Wang, L. Facile Processing of Free-Standing Polyaniline/SWCNT Film as an Integrated Electrode for Flexible Supercapacitor Application. *ACS Appl. Mater. Interfaces* **2017**, *9*, 33791−33801.

(14) Li, P.; Jin, Z.; Peng, L.; Zhao, F.; Xiao, D.; Jin, Y.; Yu, G. Stretchable All-Gel-State Fiber-Shaped Supercapacitors Enabled by Macromolecularly Interconnected 3D Graphene/Nanostructured Conductive Polymer Hydrogels. *Adv. Mater.* **2018**, *30*, 1800124.

(15) Liu, Y.; Dai, Z.; Zhang, W.; Jiang, Y.; Peng, J.; Wu, D.; Chen, B.; Wei, W.; Chen, X.; Liu, Z.; et al. Sulfonic-Group-Grafted $Ti_3C_2T_x$ MXene: A Silver Bullet to Settle the Instability of Polyaniline toward High-Performance Zn-Ion Batteries. *ACS Nano* **2021**, *15*, 9065−9075.

(16) Ghosh, T.; Basak, U.; Bairi, P.; Ghosh, R.; Pakhira, M.; Ball, R.; Biswas, B.; Chatterjee, D. P. Hierarchical Nanocomposites by Oligomer-Initiated Controlled Polymerization of Aniline on Graphene Oxide Sheets for Energy Storage. *ACS Appl. Nano Mater.* **2020**, *3*, 1693−1705.

(17) Hou, T.; Liu, B.; Sun, X.; Fan, A.; Xu, Z.; Cai, S.; Zheng, C.; Yu, G.; Tricoli, A. Covalent Coupling-Stabilized Transition-Metal Sulfide/Carbon Nanotube Composites for Lithium/Sodium-Ion Batteries. *ACS Nano* **2021**, *15*, 6735−6746.

(18) Li, J.; Qiu, S.; Liu, B.; Chen, H.; Xiao, D.; Li, H. Strong interaction between polyaniline and carbon fibers for flexible supercapacitor electrode materials. *J. Power Sources* **2021**, *483*, 229219.

(19) Kumar, N. A.; Choi, H.-J.; Shin, Y. R.; Chang, D. W.; Dai, L.; Baek, J.-B. Polyaniline-Grafted Reduced Graphene Oxide for Efficient Electrochemical Supercapacitors. *ACS Nano* **2012**, *6*, 1715−1723.

(20) Zhao, B.; Hu, H.; Yu, A.; Perea, D.; Haddon, R. C. Synthesis and Characterization of Water Soluble Single-Walled Carbon Nanotube Graft Copolymers. *J. Am. Chem. Soc.* **2005**, *127*, 8197−8203.

(21) Khodabandehlo, A.; Noori, A.; Rahmanifar, M. S.; El-Kady, M. F.; Kaner, R. B.; Mousavi, M. F. Laser-Scribed Graphene-Polyaniline Microsupercapacitor for the Internet-of-Things Applications. *Adv. Funct. Mater.* **2022**, *32*, 2204555.

(22) Tang, Y. J.; Zheng, H.; Wang, Y.; Zhang, W.; Zhou, K. Laser-Induced Annealing of Metal–Organic Frameworks on Conductive Substrates for Electrochemical Water Splitting. *Adv. Funct. Mater.* **2021**, *31*, 2102648.

(23) Hu, H.; Li, Q.; Li, L.; Teng, X.; Feng, Z.; Zhang, Y.; Wu, M.; Qiu, J. Laser Irradiation of Electrode Materials for Energy Storage and Conversion. *Matter* **2020**, *3*, 95−126.

(24) Huang, A.; El-Kady, M. F.; Chang, X.; Anderson, M.; Lin, C.-W.; Turner, C. L.; Kaner, R. B. Facile Fabrication of Multivalent VO_x/Graphene Nanocomposite Electrodes for High-Energy-Density Symmetric Supercapacitors. *Adv. Energy Mater.* **2021**, *11*, 2100768.

(25) El-Kady, M. F.; Ihns, M.; Li, M.; Hwang, J. Y.; Mousavi, M. F.; Chaney, L.; Lech, A. T.; Kaner, R. B. Engineering three-dimensional hybrid supercapacitors and microsupercapacitors for high-performance integrated energy storage. *Proc. Natl. Acad. Sci. U.S.A.* **2015**, *112*, 4233−4238.

(26) Augustyn, V.; Come, J.; Lowe, M. A.; Kim, J. W.; Taberna, P.-L.; Tolbert, S. H.; Abruña, H. D.; Simon, P.; Dunn, B. High-rate electrochemical energy storage through Li^+ intercalation pseudocapacitance. *Nat. Mater.* **2013**, *12*, 518−522.

(27) Wang, J.; Polleux, J.; Lim, J.; Dunn, B. Pseudocapacitive Contributions to Electrochemical Energy Storage in TiO_2 (Anatase) Nanoparticles. *J. Phys. Chem. C* **2007**, *111*, 14925−14931.

(28) Dong, L.; Liang, G.; Xu, C.; Ren, D.; Wang, J.; Pan, Z.-Z.; Li, B.; Kang, F.; Yang, Q.-H. Stacking up layers of polyaniline/carbon nanotube networks inside papers as highly flexible electrodes with large areal capacitance and superior rate capability. *J. Mater. Chem. A* **2017**, *5*, 19934−19942.

(29) Hussain, S.; Kovacevic, E.; Amade, R.; Berndt, J.; Pattyn, C.; Dias, A.; Boulmer-Leborgne, C.; Ammar, M.-R.; Bertran-Serra, E. Plasma synthesis of polyaniline enrobed carbon nanotubes for electrochemical applications. *Electrochim. Acta* **2018**, *268*, 218−225.

(30) Zheng, T.; Wang, X.; Liu, Y.; Bayaniahangar, R.; Li, H.; Lu, C.; Xu, N.; Yao, Z.; Qiao, Y.; Zhang, D.; et al. Polyaniline-decorated hyaluronic acid-carbon nanotube hybrid microfiber as a flexible supercapacitor electrode material. *Carbon* **2020**, *159*, 65−73.

(31) Jin, L.; Jiang, Y.; Zhang, M.; Li, H.; Xiao, L.; Li, M.; Ao, Y. Oriented Polyaniline Nanowire Arrays Grown on Dendrimer (PAMAM) Functionalized Multiwalled Carbon Nanotubes as Supercapacitor Electrode Materials. *Sci. Rep.* **2018**, *8*, 6268.

(32) Han, J.; Wang, S.; Zhu, S.; Huang, C.; Yue, Y.; Mei, C.; Xu, X.; Xia, C. Electrospun Core–Shell Nanofibrous Membranes with Nanocellulose-Stabilized Carbon Nanotubes for Use as High-

Performance Flexible Supercapacitor Electrodes with Enhanced Water Resistance, Thermal Stability, and Mechanical Toughness. *ACS Appl. Mater. Interfaces* **2019**, *11*, 44624−44635.

(33) Simotwo, S. K.; Delre, C.; Kalra, V. Supercapacitor Electrodes Based on High-Purity Electrospun Polyaniline and Polyaniline–Carbon Nanotube Nanofibers. *ACS Appl. Mater. Interfaces* **2016**, *8*, 21261−21269.

(34) Chang, C.-M.; Weng, C.-J.; Chien, C.-M.; Chuang, T.-L.; Lee, T.-Y.; Yeh, J.-M.; Wei, Y. Polyaniline/carbon nanotube nanocomposite electrodes with biomimetic hierarchical structure for supercapacitors. *J. Mater. Chem. A* **2013**, *1*, 14719.

(35) Wang, C.; Yang, Y.; Li, R.; Wu, D.; Qin, Y.; Kong, Y. Polyaniline functionalized reduced graphene oxide/carbon nanotube ternary nanocomposite as a supercapacitor electrode. *Chem. Commun.* **2020**, *56*, 4003−4006.

(36) Zhou, Y.; Qin, Z.-Y.; Li, L.; Zhang, Y.; Wei, Y.-L.; Wang, L.-F.; Zhu, M.-F. Polyaniline/multi-walled carbon nanotube composites with core–shell structures as supercapacitor electrode materials. *Electrochim. Acta* **2010**, *55*, 3904−3908.

(37) Du, J.; Li, Y.; Zhong, Q.; Yang, J.; Xiao, J.; Chen, D.; Wang, F.; Luo, Y.; Chen, K.; Li, W. Boosting the Utilization and Electrochemical Performances of Polyaniline by Forming a Binder-Free Nanoscale Coaxially Coated Polyaniline/Carbon Nanotube/Carbon Fiber Paper Hierarchical 3D Microstructure Composite as a Supercapacitor Electrode. *ACS Omega* **2020**, *5*, 22119−22130.

(38) Kim, J.-G.; Lee, D.-M.; Jung, J. Y.; Kim, M. J.; Khil, M.-S.; Jeong, H. S.; Kim, N. D. Hybrid Polyaniline/Liquid Crystalline CNT Fiber Composite for Ultimate Flexible Supercapacitors. *ACS Appl. Energy Mater.* **2021**, *4*, 1130−1142.

(39) Che, B.; Li, H.; Zhou, D.; Zhang, Y.; Zeng, Z.; Zhao, C.; He, C.; Liu, E.; Lu, X. Porous polyaniline/carbon nanotube composite electrode for supercapacitors with outstanding rate capability and cyclic stability. *Compos. B: Eng.* **2019**, *165*, 671−678.

(40) Lu, Z.; Foroughi, J.; Wang, C.; Long, H.; Wallace, G. G. Superelastic Hybrid CNT/Graphene Fibers for Wearable Energy Storage. *Adv. Energy Mater.* **2018**, *8*, 1702047.

(41) Zheng, L.; Wang, X.; An, H.; Wang, X.; Yi, L.; Bai, L. The preparation and performance of flocculent polyaniline/carbon nanotubes composite electrode material for supercapacitors. *J. Solid State Electrochem.* **2011**, *15*, 675−681.

(42) Pan, S.; Lin, H.; Deng, J.; Chen, P.; Chen, X.; Yang, Z.; Peng, H. Novel Wearable Energy Devices Based on Aligned Carbon Nanotube Fiber Textiles. *Adv. Energy Mater.* **2015**, *5*, 1401438.

(43) Zhang, Z.; Deng, J.; Li, X.; Yang, Z.; He, S.; Chen, X.; Guan, G.; Ren, J.; Peng, H. Superelastic Supercapacitors with High Performances during Stretching. *Adv. Mater.* **2015**, *27*, 356−362.

(44) Bavio, M. A.; Acosta, G. G.; Kessler, T.; Visintin, A. Flexible symmetric and asymmetric supercapacitors based in nanocomposites of carbon cloth/polyaniline - carbon nanotubes. *Energy* **2017**, *130*, 22−28.

(45) Niu, Z.; Luan, P.; Shao, Q.; Dong, H.; Li, J.; Chen, J.; Zhao, D.; Cai, L.; Zhou, W.; Chen, X.; et al. A “skeleton/skin” strategy for preparing ultrathin free-standing single-walled carbon nanotube/polyaniline films for high performance supercapacitor electrodes. *Energy Environ. Sci.* **2012**, *5*, 8726.

(46) Su, F.; Miao, M.; Niu, H.; Wei, Z. Gamma-Irradiated Carbon Nanotube Yarn As Substrate for High-Performance Fiber Supercapacitors. *ACS Appl. Mater. Interfaces* **2014**, *6*, 2553−2560.

(47) Cai, Z.; Li, L.; Ren, J.; Qiu, L.; Lin, H.; Peng, H. Flexible, weavable and efficient microsupercapacitor wires based on polyaniline composite fibers incorporated with aligned carbon nanotubes. *J. Mater. Chem. A* **2013**, *1*, 258−261.

(48) Wang, K.; Meng, Q.; Zhang, Y.; Wei, Z.; Miao, M. High-Performance Two-Ply Yarn Supercapacitors Based on Carbon Nanotubes and Polyaniline Nanowire Arrays. *Adv. Mater.* **2013**, *25*, 1494−1498.

(49) Chen, X.; Lin, H.; Deng, J.; Zhang, Y.; Sun, X.; Chen, P.; Fang, X.; Zhang, Z.; Guan, G.; Peng, H. Electrochromic Fiber-Shaped Supercapacitors. *Adv. Mater.* **2014**, *26*, 8126−8132.

(50) Wei, Y.; Yang, C. C.; Ding, T. Z. A one-step method to synthesize N,N'-bis(4'-aminophenyl)-1,4-quinonenediimine and its derivatives. *Tetrahedron Lett.* **1996**, *37*, 731−734.

(51) Noori, A.; El-Kady, M. F.; Rahmanifar, M. S.; Kaner, R. B.; Mousavi, M. F. Towards establishing standard performance metrics for batteries, supercapacitors and beyond. *Chem. Soc. Rev.* **2019**, *48*, 1272−1341.

(52) Strauss, V.; Marsh, K.; Kowal, M. D.; El-Kady, M.; Kaner, R. B. A Simple Route to Porous Graphene from Carbon Nanodots for Supercapacitor Applications. *Adv. Mater.* **2018**, *30*, 1704449.

CHAPTER 4. UNDERSTANDING THE DEGRADATION MECHANISMS OF CONDUCTING POLYMER SUPERCAPACITORS

4.1 Abstract

Conducting polymers like polyaniline (PANI) are promising pseudocapacitive electrode materials, yet experience instability in cycling performance. Since polymers often degrade into oligomers, short chain length anilines have been developed to improve the cycling stability of PANI-based supercapacitors. However, the capacitance degradation mechanisms of aniline oligomer-based materials have not been systematically investigated and are little understood. Herein, two composite electrodes based on aniline trimers (AT) and carbon nanotubes (CNTs) are studied as model systems and evaluated at both pre-cycling and post-cycling states through physicochemical and electrochemical characterizations. The favorable effect of covalent bonding between AT and CNTs is confirmed to enhance cycling stability by preventing the detachment of aniline trimer and preserving the electrode microstructure throughout the charge/discharge cycling process. In addition, higher porosity has a positive effect on electron/ion transfer and the adaptation to volumetric changes, resulting in higher conductivity and extended cycle life. This work provides insights into the mechanism of enhanced cycling stability of aniline oligomers, indicating design features for aniline oligomer electrode materials to improve their electrochemical performance.

4.2 Introduction

The proliferation of electrochemical energy storage technologies has led to the widespread use of portable electronics and the increased adoption of renewable energy harvesting. Supercapacitors are a promising energy storage option due to their rapid charging and high power density.[1, 2] Conventional supercapacitor electrodes utilize porous carbon materials, generating relatively low energy density compared to batteries. To increase their energy density, reversible Faradaic processes (pseudocapacitance) have been introduced by adding electroactive materials, such as transition metal oxides and conducting polymers.[3, 4] However, many commonly used transition metal-based electrode materials like manganese oxide suffer from insufficient electrical conductivity, concerns about resource sustainability, and high energy consumption during synthesis and recycling.[5] Conducting polymers such as polyaniline (PANI) offer a viable and sustainable option due to their good environmental stability, inherent electrical conductivity, and high pseudocapacitance.[6] Unfortunately, the application of conducting polymers has been plagued by their rapid capacitance degradation during the charging/discharging cycling process.[6-8] The poor cycling stability of conducting polymers has been ascribed mainly to structural pulverization, including repeated swelling and shrinking of polymer chains as a consequence of the doping/de-doping process (counterion insertion/extraction).[9-13]

Significant attempts have been undertaken to stabilize PANI as an electrode material for supercapacitors. One strategy is to incorporate conducting polymers with carbon materials such as carbon nanotubes (CNTs)[14-16] and reduced graphene oxide (rGO).[17-19] These carbon materials with high electrical conductivity, large surface area, and high mechanical strength can accommodate volumetric changes during the cycling process and facilitate electron transfer. Another strategy comprises the utilization of short-chain aniline oligomers in substitution of long-chain PANI.[20-22]

The aniline oligomers provide electrochemical properties comparable to PANI, while with much shorter chain lengths, aniline oligomers have shown greater resilience to the extension, contraction, and scission of polymer chains. Intending to further improve the cycling stability of PANI-based supercapacitors, several studies have introduced covalent bonds between PANI (or aniline oligomers) and buffering substrates to establish strong and enduring conjugated interactions.[23-28] Our previous work showed that aniline tetramers covalently grafted on 3D graphene networks retained 85% of the initial capacitance after 30,000 charge/discharge cycles in 1.0 M H_2SO_4 aqueous electrolyte.[27]

Although many efforts have been devoted to overcoming the instability problem of PANI, there is limited research on the factors leading to the degradation of cycling stability and the mechanism behind capacitance fading in PANI materials. A few investigations on capacitance fading mechanisms revealed that the poor cycling stability of PANI can be attributed to the volumetric degradation as well as the hydrolysis and over-oxidation degradation of PANI leading to polymer chain decomposition and conductivity decline.[29-32] Moreover, to the best of our knowledge, there are no reported systematic studies on the degradation mechanism of cycling stability based on aniline oligomer electrode materials.

In this work, we demonstrate a systematic investigation of the mechanisms behind the cycling stability of two aniline trimer-based electrode materials: 1) a covalently coupled aniline trimer/carbon nanotube (cc-AT/CNT) composite,[28] and 2) a physical mixture of aniline trimer/carbon nanotube (AT/CNT). The cc-AT/CNT and AT/CNT electrodes were examined at both pre-cycling and post-cycling states through systematic physicochemical and electrochemical characterizations. The results demonstrate that the covalent linkages between AT and CNT greatly contribute to the improvement of cycling stability by alleviating the loss/detachment of aniline

trimer and maintaining the electrode microstructure during the cycling process. In addition, the porous structure of cc-AT/CNT facilitates electrolyte ion transport, leading to faster kinetics and higher cycling stability.

4.3 Results and Discussion

A covalently coupled aniline trimer/carbon nanotube (cc-AT/CNT) composite electrode was prepared from an aniline trimer/carbon nanotube (AT/CNT) composite film through a laser scribing technique.[28] As illustrated in **Scheme 4.1**, amide covalent connections were established under laser irradiation to form cc-AT/CNT, while AT/CNT is a physical mixture of amine/amine-capped aniline trimer (NH_2/NH_2 AT) and carboxylic acid-functionalized single-walled carbon nanotubes (P3 SWNT). Under the high local heating generated at the surface of the AT/CNT film from laser irradiation, a condensation reaction between the carboxyl groups (−COOH) on P3 SWNT and the amino groups ($-NH_2$) on AT was enabled by driving off H_2O to build amide linkages between AT and P3 SWNT.[28] As previously reported, cc-AT/CNT exhibited superior long-term cycling stability (20,000 charge/discharge cycles to reach 80% capacitance retention) compared to AT/CNT (5000 charge/discharge cycles to reach 80% capacitance retention) in 1.0 M H_2SO_4 aqueous electrolyte in a three-electrode cell setup.[28]

To investigate the differences in cycling stability between cc-AT/CNT (after laser irradiation) and AT/CNT (before laser irradiation) electrodes, X-ray photoelectron spectroscopy (XPS) was first carried out to examine the surface elemental composition and chemical states. The N 1s core level XPS spectrum of the post-cycling cc-AT/CNT (**Figure 4.1a**) can be deconvoluted into four components: benzenoid amine nitrogen (–NH–) at 399.6 eV, quinoid imine nitrogen (–N=) at 398.5 eV, positively charged nitrogen (N^+) at 400.5 eV and amide nitrogen (N–C=O) at 401.8 eV.[28, 33-35] After being charged and discharged for 20,000 cycles, the amide nitrogen (N–

C=O) is still evident at 401.8 eV, indicating that the amide covalent connections built from laser irradiation and the chemical structure of cc-AT/CNT were maintained during the cycling process. Likewise, the O 1s core level XPS spectrum of cc-AT/CNT after cycling (**Figure 4.1b**) still retains the amide oxygen (N–C=O) at 530.6 eV,[28] suggesting that the chemical structure of cc-AT/CNT (after laser irradiation) is highly stable upon cycling. The other three components in the O 1s deconvoluted spectrum of cc-AT/CNT can be ascribed to: C–O at 532.7 eV, C=O at 531.5 eV, and O=C–O* at 533.7 eV.[28, 36] For AT/CNT (before laser irradiation) at the post-cycling state, both the N 1s and O 1s core level XPS spectra (**Figure S4.1**) exhibit three deconvolution peaks without any amide nitrogen or oxygen (N–C=O), which are similar to the patterns of AT/CNT at the pre-cycling state. The curve-fit C 1s spectra of cc-AT/CNT (after laser irradiation) and AT/CNT (before laser irradiation) (**Figure S4.2**) can be deconvoluted into seven components: sp^2 carbon (C=C) at 284.1 eV, sp^3 carbon (C−C) at 284.8 eV, C−N at 285.3 eV, C−O at 286.0 eV, C=N at 286.7 eV, and C=O at 288.0 eV. The peaks at 290.0 eV in cc-AT/CNT and 289.7 eV in AT/CNT can be assigned to (O,N)−C=O and COOH, respectively.[28]

Furthermore, as presented in **Table 4.1**, the atomic percentages of cc-AT/CNT (after laser irradiation) and AT/CNT (before laser irradiation) were quantitatively measured at the pre-cycling and post-cycling states, respectively, from the XPS survey scans (**Figure 4.1c**). For AT/CNT (before laser irradiation), the N 1s at% decreased more than 50% (from 6.65% to 3.10%), indicating that a large amount of aniline trimer detached from the electrode during the 20,000 charge/discharge cycles, since AT is highly soluble in the sulfuric acid electrolyte.[31] The capacitance degradation for AT/CNT (72% capacitance retention after 20,000 cycles) can therefore be mainly attributed to the detachment of aniline trimers from CNTs because all the interactions between the two components are essentially physical interactions without strong and

permanent covalent bonds. In contrast, for cc-AT/CNT (after laser irradiation), the N 1s at% decreased by only 15% (from 4.03% to 3.40%) after 20,000 cycles (with 82% capacitance retention). Thus, cc-AT/CNT demonstrated much better preservation of N compared to AT/CNT after cycling (**Figure 4.1d**), suggesting that the existence of amide covalent connections between aniline trimers and CNTs are beneficial to the improvement of cycling stability by alleviating the loss/detachment of aniline trimer during the cycling process. From another perspective, the oxygen content of the cc-AT/CNT film (after laser irradiation) increased, and the C/O ratio decreased after cycling (**Table 4.1**), which can be caused by the hydrolysis of certain ATs into the electrolyte.[29, 30] The water molecules could attack part of the electropositive carbon, resulting in the introduction of carbonyl or hydroxyl terminating groups by intramolecular electron transfer,[29-31] as shown in **Scheme 4.2**. For AT/CNT (before laser irradiation), the oxygen content and the C/O ratio remained almost unchanged after cycling, indicating the detachment and dissolution of AT into the electrolyte due to the lack of strong connections to the CNT matrix.

To further understand the possible mechanisms leading to the excellent cycling stability of the cc-AT/CNT (after laser irradiation) electrodes, scanning electron microscopy (SEM) and transmission electron microscopy (TEM) images were collected for the cc-AT/CNT electrodes before and after the cycling test. Comparing the morphology of the cc-AT/CNT (after laser irradiation) electrode at the pre-cycling (**Figure 4.2a**) and post-cycling (**Figure 4.2b**) state, it is evident that the electrode surface became denser and less porous after 20,000 charge/discharge cycles. During the charging/discharging cycling processes, the aniline trimers are doped/de-doped, where counterions are inserted into and then extracted out of the electrode to balance the charge.[8, 37] When counterions diffuse back into the electrolyte during the discharging process, some of the ion channels will collapse thus compromising the porous structure.[8-10, 12] This could impede

electrolyte ion transport and diminish its access to the surface of the electrode material, resulting in capacitance degradation during long-term cycling. As can be seen in the SEM images at higher magnifications (**Figure 4.2c,d** and **Figures S4.3–4.4**), the cc-AT/CNT electrode still presented a uniform distribution of AT nanoparticles on the CNTs after 20,000 charge/discharge cycles (**Figure 4.2d** and **Figure S4.4**) and retained similar nanostructures compared to the pre-cycling cc-AT/CNT electrode (**Figure 4.2c** and **Figure S4.3**). This observation was also confirmed by the TEM images (**Figure 4.2e,f**), where AT nanoparticles with an average size of ~5–10 nm are still evenly dispersed and strongly attached to the surface of the CNTs after the cycling test. These results corroborate that the amide covalent linkages are advantageous to preserve AT nanoparticles within the electrode material while minimizing capacitance degradation during long-term cycling. **Figure S4.5** displays two small mechanical cracks detected on the electrode after 20,000 charge/discharge cycles, which could result in some capacitance fading.

In contrast, as can be seen in the SEM images (**Figure 4.3a**), the AT/CNT (before laser irradiation) electrodes demonstrated more compact and less porous structures compared to cc-AT/CNT (after laser irradiation) before cycling. After being continuously charged and discharged for 20,000 cycles, a small degree of volume expansion can be observed in the AT/CNT electrodes (**Figure 4.3b**), which can be attributed to the lack of porosity to sufficiently accommodate the diffusion of electrolyte ions during the repeated charge/discharge processes.[8, 38] In addition, at both the pre-cycling and post-cycling states, the AT/CNT electrodes exhibited agglomeration of AT molecules as shown in the SEM images at higher magnification (**Figure 4.3c,d**). The AT agglomerations became slightly larger after cycling, which can be ascribed to the volumetric changes due to the repeated doping/de-doping of AT (insertion/extraction of counterions).[8, 37] The morphology evaluation of the pre-cycling AT/CNT electrode through TEM (**Figure 4.3e**) also

showed the uneven distribution of AT nanoparticles across the CNTs. After 20,000 charge/discharge cycles, the TEM image in **Figure 4.3f** illustrated cleaner carbon nanotubes with less occupation of aniline trimers, indicating the detachment and dissolution of aniline trimers into the electrolyte during the consecutive cycling process.

To gain deeper insights into the difference in cycling stability between cc-AT/CNT (after laser irradiation) and AT/CNT (before laser irradiation) electrodes, the evolution of the electrochemical properties of cc-AT/CNT and AT/CNT during the charge/discharge cycling process was examined by electrochemical impedance spectroscopy (EIS). EIS was carried out during the galvanostatic charge–discharge (GCD) cycling process every 1000 cycles. As demonstrated in the Nyquist plots, the pre-cycling cc-AT/CNT electrode exhibited an internal resistance of 1.88 Ω and a small semicircle in the high-frequency region, generating an equivalent series resistance (ESR)[39] of ~1.90 Ω (**Figure 4.4a**). In comparison, the pre-cycling AT/CNT electrode displayed an internal resistance of 2.50 Ω and a relatively large semicircle at high frequency, yielding an ESR of ~2.53 Ω (**Figure 4.4b**). **Figure S4.6** demonstrated the equivalent circuit for impedance analysis and the curve-fit Nyquist plots. In the low-frequency region, AT/CNT showed a lower gradient of the near-vertical line compared to cc-AT/CNT. Hence, at the pre-cycling state, the cc-AT/CNT electrode demonstrated better capacitive behavior and electrical conductivity compared to AT/CNT, suggesting that the covalent connections between AT and CNTs are beneficial for enhancing the overall electrochemical performance of the electrode material. During the continuous cycling process, the Nyquist plots of cc-AT/CNT (**Figure 4.4a**) illustrate that little change in the internal resistance occurred: from 1.88 Ω (0 cycle), to 1.82 Ω (2000 cycles), to 1.80 Ω (5000 cycles), to 1.80 Ω (10,000 cycles) and then to 1.82 Ω (20,000 cycles), with the charge transfer resistance remaining nearly unchanged (0.01–0.02 Ω). The changes of internal resistance in cc-AT/CNT were

within 0.02 Ω while the low charge transfer resistance was retained from 2000 cycles to 20,000 cycles, revealing that the electronic structures of the electrode and fast ion transport were well maintained throughout the cycling process. It is noteworthy that from the first cycle to the 2000th cycle and beyond, the internal resistance decreased from 1.88 Ω to 1.82 Ω, which could be explained by an electro-activation process, where the accessibility of electrolyte ions in the porous active material gradually increased with cycling.[8, 40-42] In contrast, for AT/CNT with progressive charge/discharge cycling, the internal resistance increased from 2.50 Ω (0 cycle), to 2.61 Ω (2000 cycles), to 2.70 Ω (5000 cycles), to 2.74 Ω (10,000 cycles) and then to 2.73 Ω (20,000 cycles), with a charge transfer resistance of 0.02–0.04 Ω (**Figure 4.4b**). Several components contribute to ESR, such as the electronic resistance of the electrode, contact resistance, and ion transport resistance.[39, 43] However, under the same test conditions in this case, it is reasonable to assume that the volumetric changes and the structural changes due to the detachment of AT from the CNT conductive matrix directly contributed to the ESR increase of ~0.2 Ω after 20,000 cycles. This electrochemical evaluation of the capacitance degradation during the cycling test by EIS elucidated that: 1) the covalent linkages between AT and CNTs benefited the cycling stability of the electrode material by minimizing the loss of AT and maintaining the electronic structure; 2) the porous structure of cc-AT/CNT created by laser irradiation facilitated electrolyte ion transport, leading to faster kinetics and higher cycling stability.

4.4 Conclusions

In summary, the cycling stability improvement of cc-AT/CNT (after laser irradiation) can be explained by the chemical design of amide covalent linkages, which attenuate the loss/detachment of aniline trimers and preserve the microstructure during cycling. The likely capacitance

degradation mechanisms of cc-AT/CNT are the electrode's mechanical degradation such as fewer ion transport pathways and small mechanical cracks that occur after long-term cycling as well as possible hydrolysis of certain AT molecules. For AT/CNT (before laser irradiation), on the other hand, the capacitance fading mechanism can be mainly attributed to the detachment and dissolution of AT into the electrolyte due to the lack of strong connections to the CNT matrix. In addition, compared to the compact electrode structure of AT/CNT, the porous structure of cc-AT/CNT created by laser irradiation is beneficial to facilitating ion transport and accommodating volumetric changes, leading to lower equivalent series resistance and longer cycle life. This investigation provides insights into the cycling stability degradation mechanisms of aniline oligomer-based electrode materials and offers inspiration for the structural design of conducting polymer-based energy storage devices with long cycle life.

4.5 Experimental Section

Preparation of cc-AT/CNT and AT/CNT at both Pre-cycling and Post-cycling States: Covalently coupled aniline trimer/carbon nanotubes (cc-AT/CNT) and a physical mixture of aniline trimer/carbon nanotubes (AT/CNT) were prepared by a previously reported method.[28] In brief, amine/amine end-capped aniline trimer (NH_2/NH_2 AT) solution (10 mL, 5 mg mL^{-1}) was added into carboxylic acid-functionalized single-walled carbon nanotubes (P3 SWNT) suspension (10 mL, 5 mg mL^{-1}) at a controlled rate while stirring at room temperature to form a uniform physical mixture. The uniform mixture was drop-cast on graphite paper current collectors (1 × 1 cm^2) and left to dry under ambient conditions, which was then directly used as an AT/CNT composite electrode. To prepare a cc-AT/CNT electrode, a dried AT/CNT film was laser-scribed using a 40 W full spectrum laser muse 2D vision desktop CO_2 laser cutter under ambient conditions. The laser-scribing parameters were set to 10% laser power, 1000 dpi resolution, and 100% speed.

The as-prepared cc-AT/CNT and AT/CNT electrodes were directly used for electrochemical testing and characterization without any binders or additives. After cycling stability tests, the post-cycling cc-AT/CNT and AT/CNT electrodes were fully rinsed with deionized water to remove any residuals from the electrolyte (1.0 M H_2SO_4) and then freeze-dried using liquid nitrogen.

Materials Characterization: X-ray photoelectron spectroscopy (XPS) measurements were obtained using a Kratos Axis Ultra DLD spectrometer with a monochromatic Al Kα X-ray source (λ = 1486.6 eV). The morphological and structural characterizations of the materials were carried out by scanning electron microscopy (SEM) using a JEOL JSM-6700F FE-SEM and transmission electron microscope (TEM) with a T20 iCorr (FEI) High-Res CryoEM and CryoET.

Electrochemical Characterization: All electrochemical data were collected using a Biologic VMP3 electrochemical workstation (VMP3b-10, USA Science Instrument). In all three-electrode studies, graphite sheets were used as the counter electrode, Ag/AgCl was used as the reference electrode, and 1.0 M H_2SO_4 was used as the aqueous electrolyte. The typical mass loadings of the materials were 0.5–0.8 mg cm^{-2}. The cycling stability tests were conducted by galvanostatic charge–discharge (GCD) from –0.2 V to 0.8 V. The electrochemical impedance spectroscopy (EIS) measurements were performed at 0.5 V relative to the reference electrode over a frequency range from 1 MHz to 10 mHz with a sinusoidal amplitude of 10 mV.

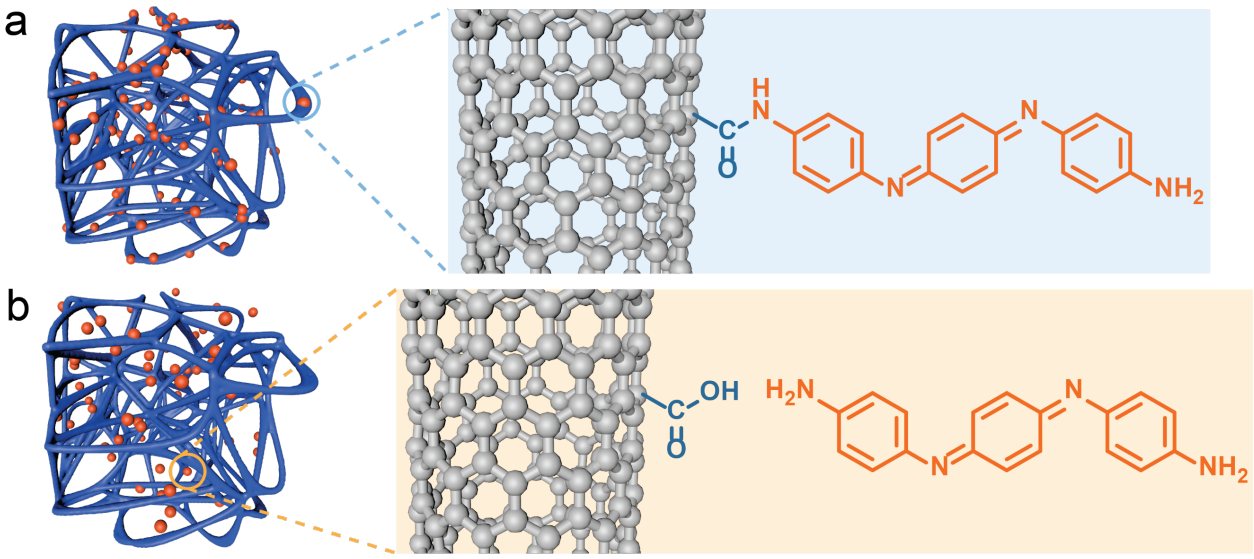

Scheme 4.1. Schematic illustration of a) cc-AT/CNT and b) AT/CNT composite electrode structures.

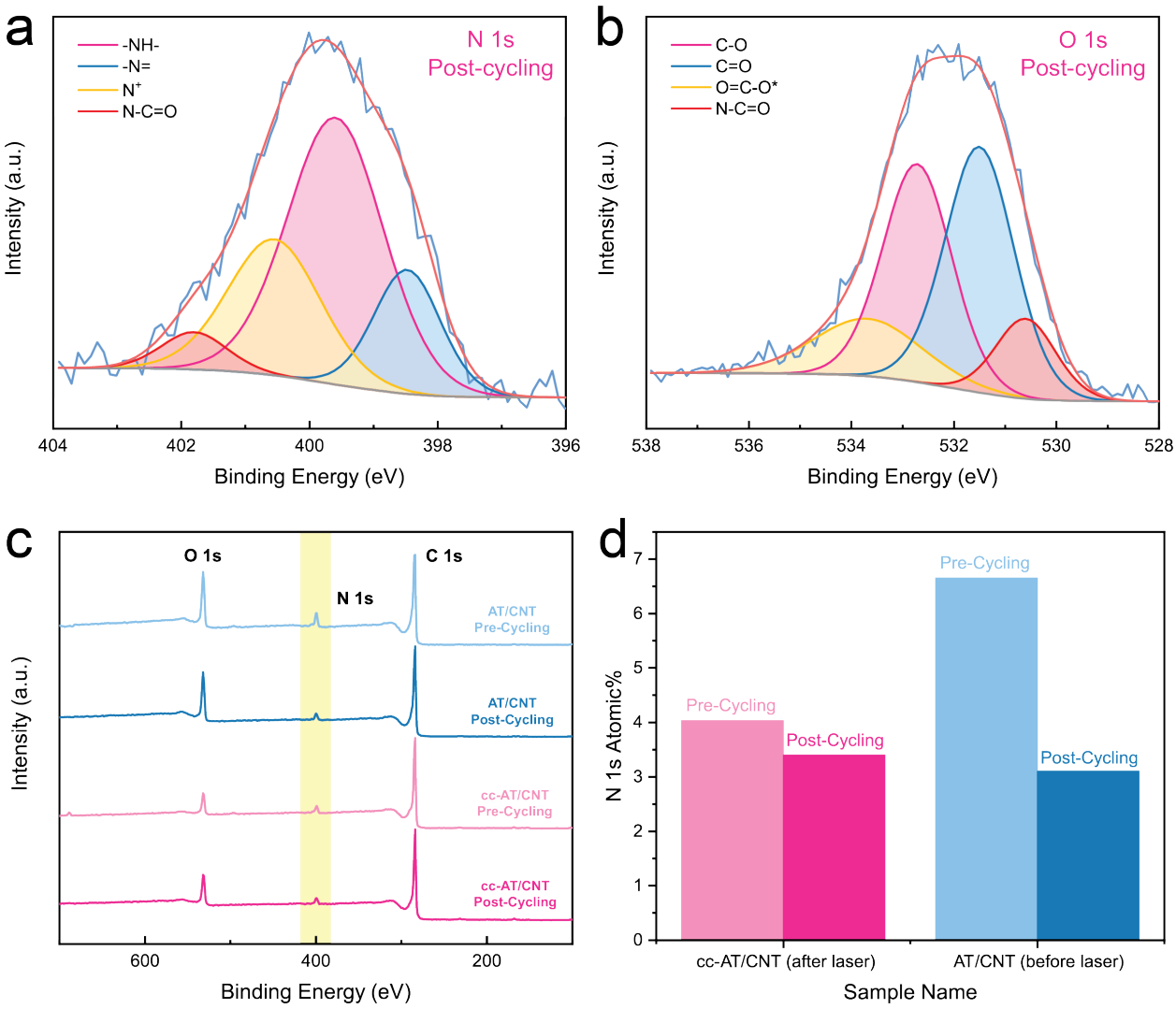

Figure 4.1. a) N 1s and b) O 1s core level XPS spectrum of a cc-AT/CNT electrode after 20,000 charge/discharge cycles. c) XPS survey spectra of cc-AT/CNT and AT/CNT at pre-cycling and post-cycling states. d) Comparison of N 1s at% in cc-AT/CNT and AT/CNT at pre-cycling and post-cycling states from the XPS survey scans.

Table 4.1. Quantitative Analysis of cc-AT/CNT and AT/CNT Composite Electrodes at Pre-cycling and Post-cycling States from XPS Survey Scans

Sample Name	Status	N 1s at%	O 1s at%	C 1s at%	C/O Ratio	Capacitance Retention
cc-AT/CNT	Pre-cycling	4.03	7.73	88.23	11.41	100%
	Post-cycling	3.40	10.82	85.78	7.93	82% (After 20,000 cycles)
AT/CNT	Pre-cycling	6.65	14.46	78.89	5.46	100%
	Post-cycling	3.10	14.73	82.16	5.58	72% (After 20,000 cycles)

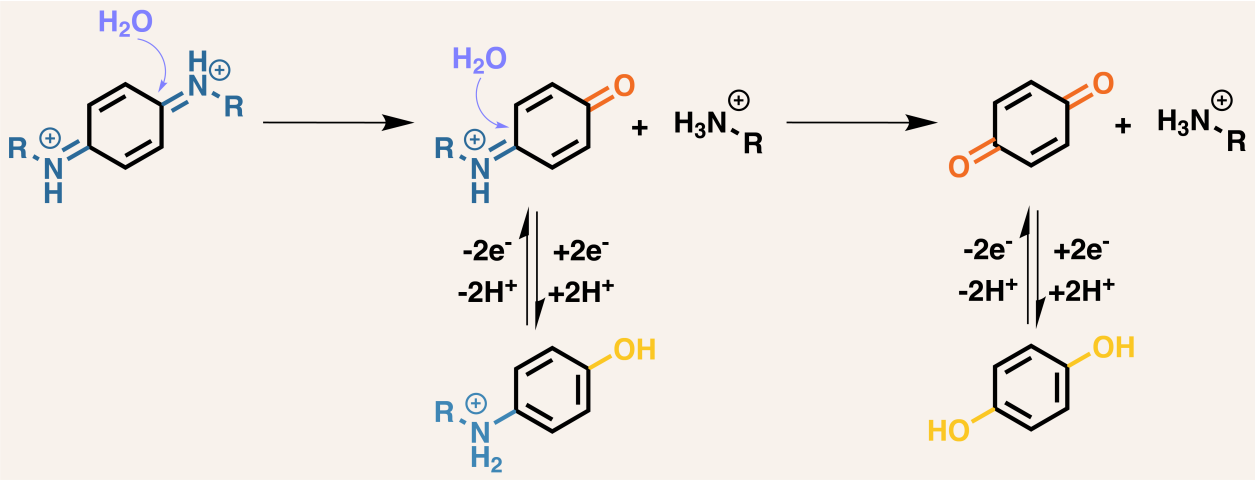

Scheme 4.2. A possible hydrolysis reaction of AT during the electrochemical cycling process, and possible reversible redox reactions involved, where R stands for the rest of the AT chains or CNT structures in the cc-AT/CNT electrodes.

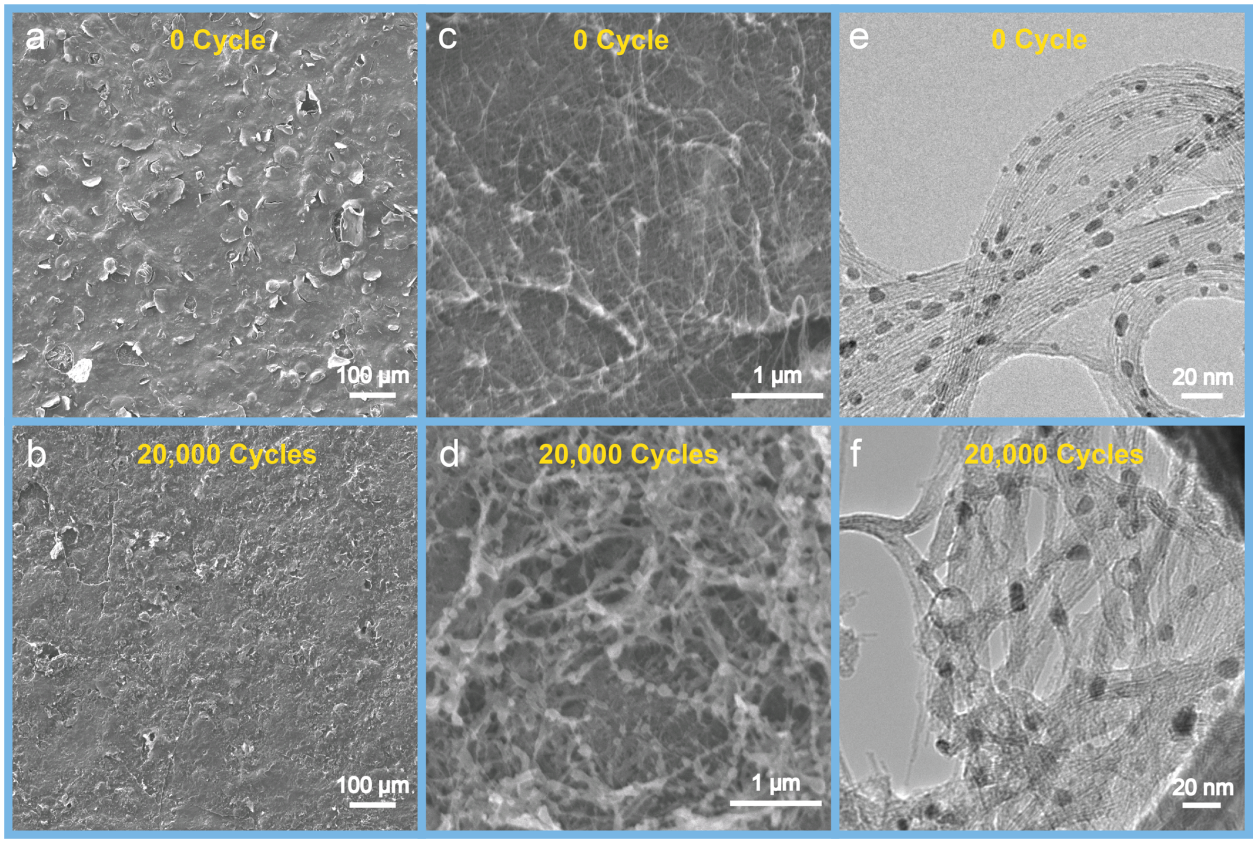

Figure 4.2. SEM images of cc-AT/CNT at the a) pre-cycling and b) post-cycling states. SEM images of cc-AT/CNT at higher magnification at the c) pre-cycling and d) post-cycling states. TEM images of cc-AT/CNT at the e) pre-cycling and f) post-cycling states.

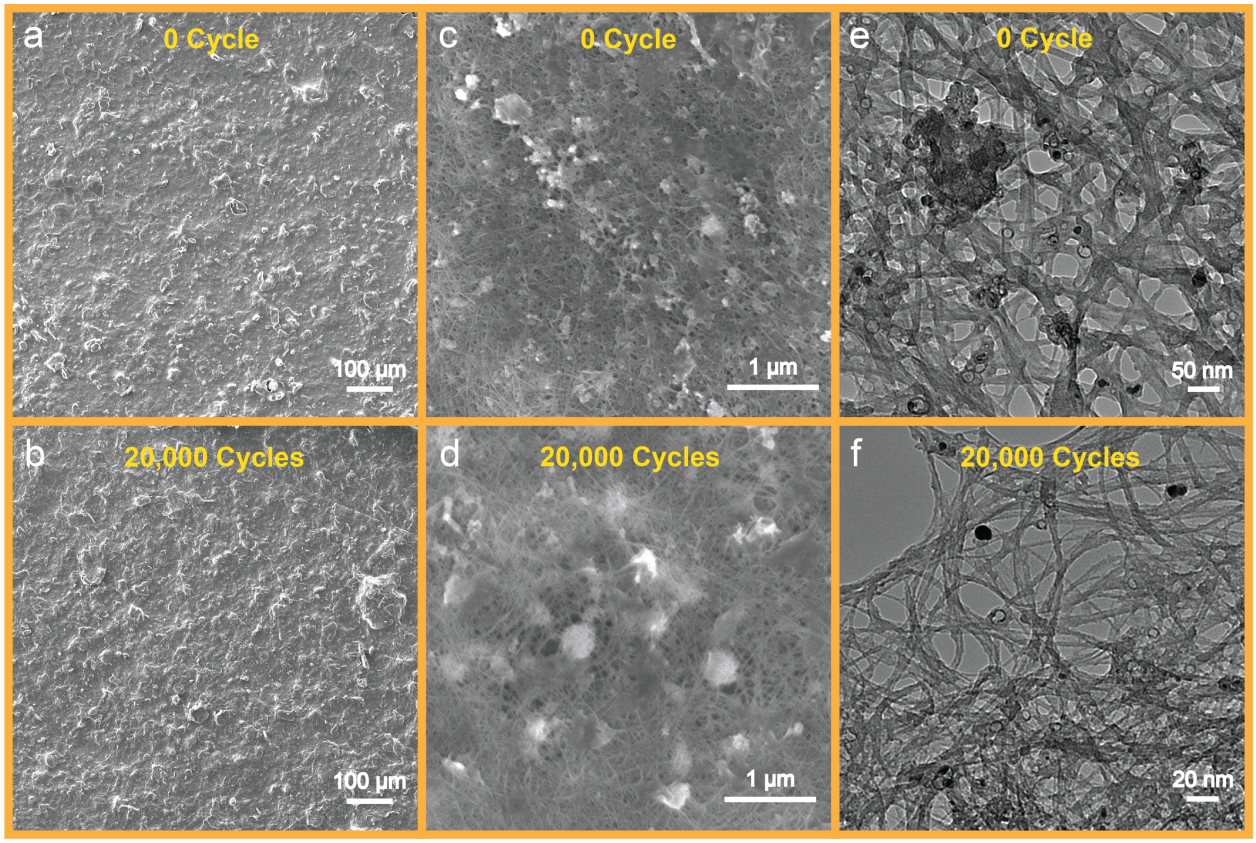

Figure 4.3. SEM images of AT/CNT at the a) pre-cycling and b) post-cycling states. SEM images of AT/CNT at higher magnification at the c) pre-cycling and d) post-cycling states. TEM images of AT/CNT at the e) pre-cycling and f) post-cycling states.

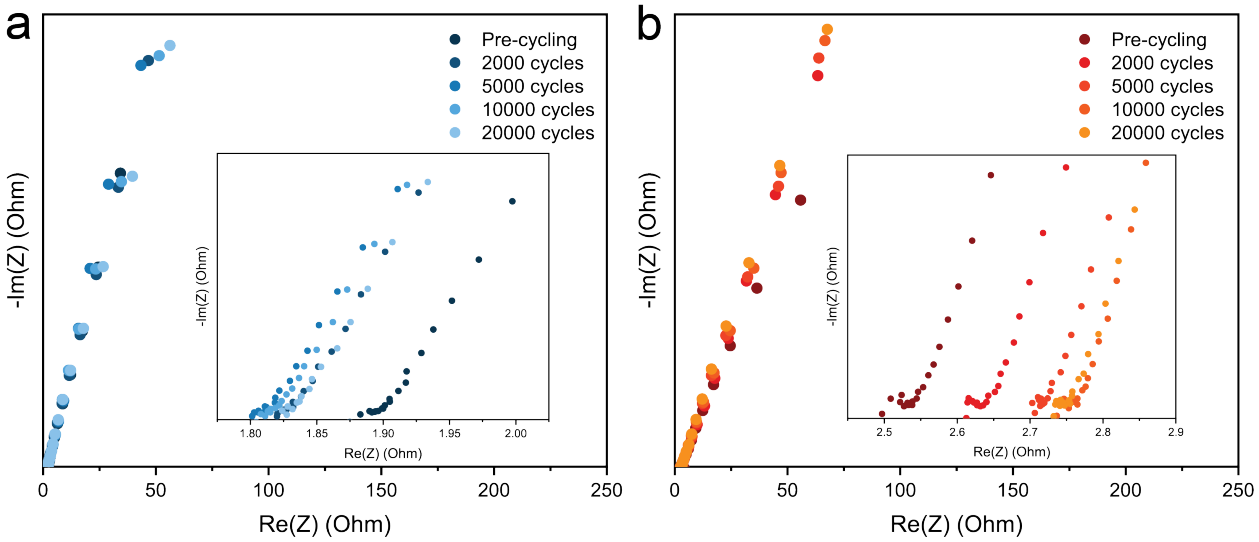

Figure 4.4. Nyquist plots of a) cc-AT/CNT and b) AT/CNT with the insets showing a zoomed-in view of the high-frequency regions.

4.6 Supporting Information

4.6.1 Experimental

Materials: Carboxylic acid-functionalized single-walled carbon nanotubes (P3 SWNT) were purchased from Carbon Solutions, Inc. (CSI). Graphite paper used as current collectors were purchased from Digi-Key Electronics (manufactured by Panasonic Electronic Components, part number: P13689-ND). All reagents were used without further purification. Sulfuric acid (H_2SO_4), hydrochloric acid (HCl), and ethanol were purchased from Fisher Scientific. P-phenylenediamine was purchased from Sigma-Aldrich. Ammonium persulfate (98+%) was purchased from Acros. Ammonium hydroxide (28–30%) was purchased from VWR.

Synthesis of Amine/Amine End-capped Aniline Trimer (NH_2/NH_2 AT): Amine/amine end-capped aniline trimer (NH_2/NH_2 AT) was prepared by a modified reported method.[44] In brief, 0.86 g of p-phenylenediamine was dissolved in a solution of 100 mL of 1.0 M HCl and 40 mL of ethanol, with the assistance of gentle ultrasonication. The solution in a round bottom flask was then chilled in a salty ice bath. Later on, 1.8 g of ammonium persulfate was added in quickly, and the solution was stirred for around 2.5 min. Once the color of the solution started appearing gray, 1.5 mL of aniline was added in and kept stirring for 40 min. The resulting solution was vacuum filtered and washed with deionized water. After treating with 1.0 M ammonium hydroxide solution for 2 hours, the solution was again vacuum filtered and washed with deionized water until the filtrate became pH neutral. A blue powder with approximately 30% yield was collected after air drying for a few days.

4.6.2 Materials Characterizations

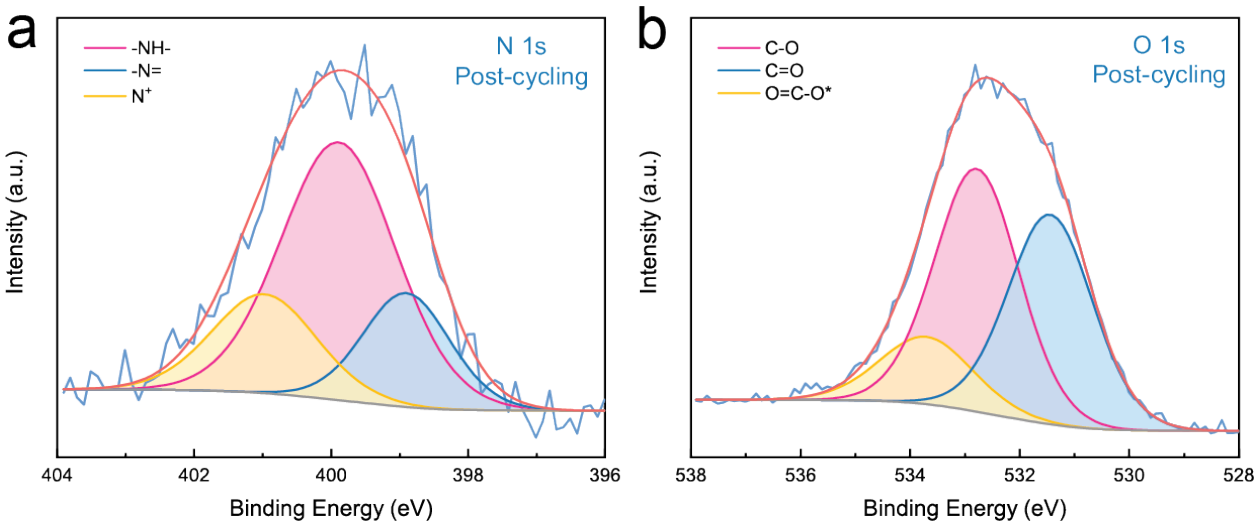

Figure S4.1. a) N 1s and b) O 1s core level XPS spectrum of an AT/CNT electrode after 20,000 charge/discharge cycles.

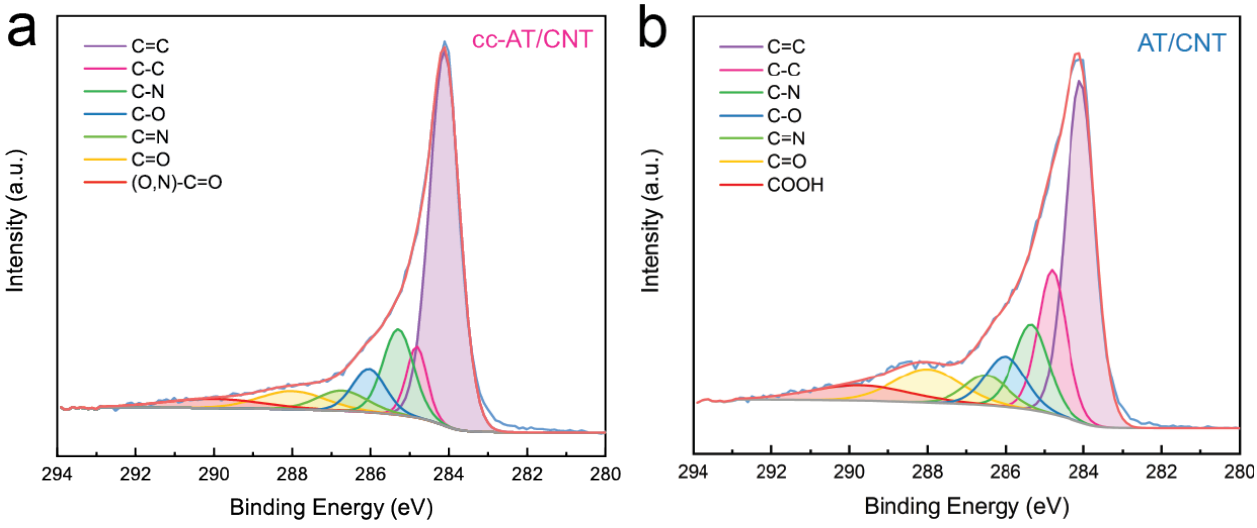

Figure S4.2. C 1s core level XPS spectrum of a) cc-AT/CNT (after laser irradiation) and b) AT/CNT (before laser irradiation) electrodes after being charged/discharged for 20,000 cycles.

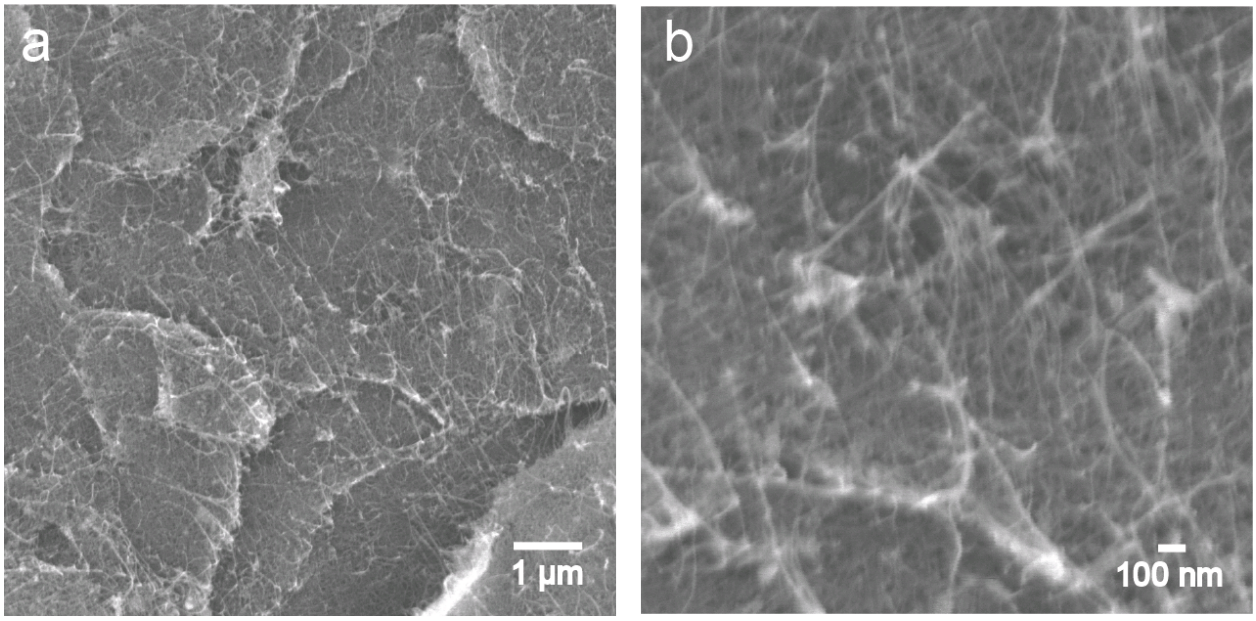

Figure S4.3. SEM images of a cc-AT/CNT (after laser irradiation) electrode at the pre-cycling state.

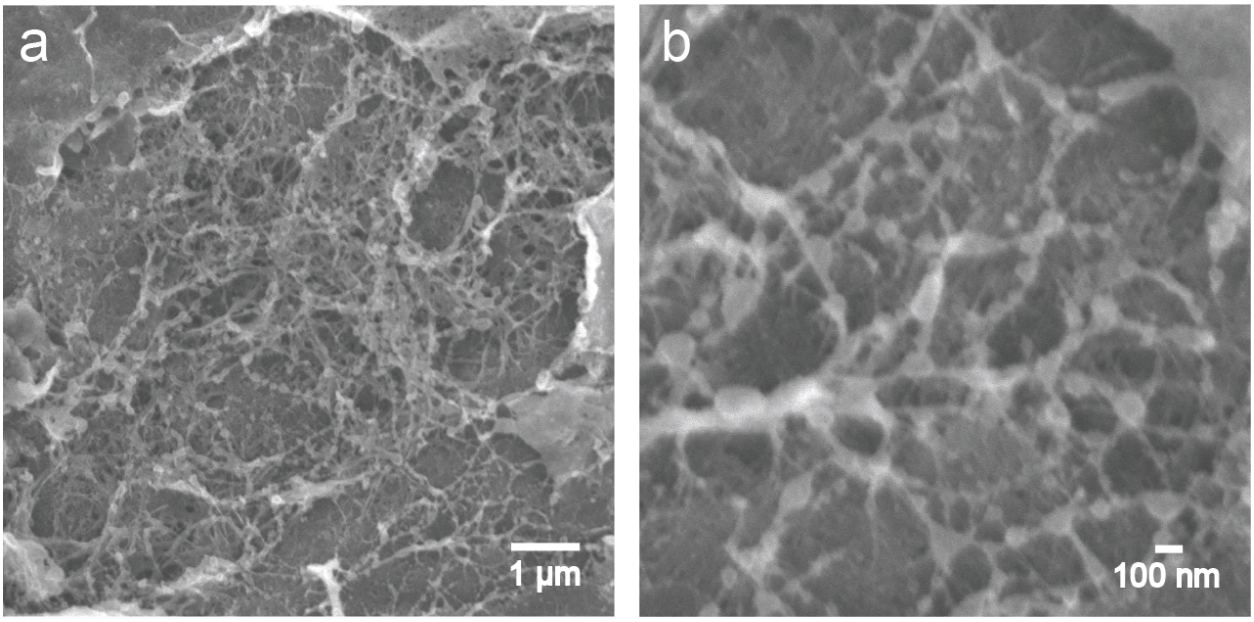

Figure S4.4. SEM images of a cc-AT/CNT (after laser irradiation) electrode at the post-cycling state (after 20,000 charge/discharge cycles).

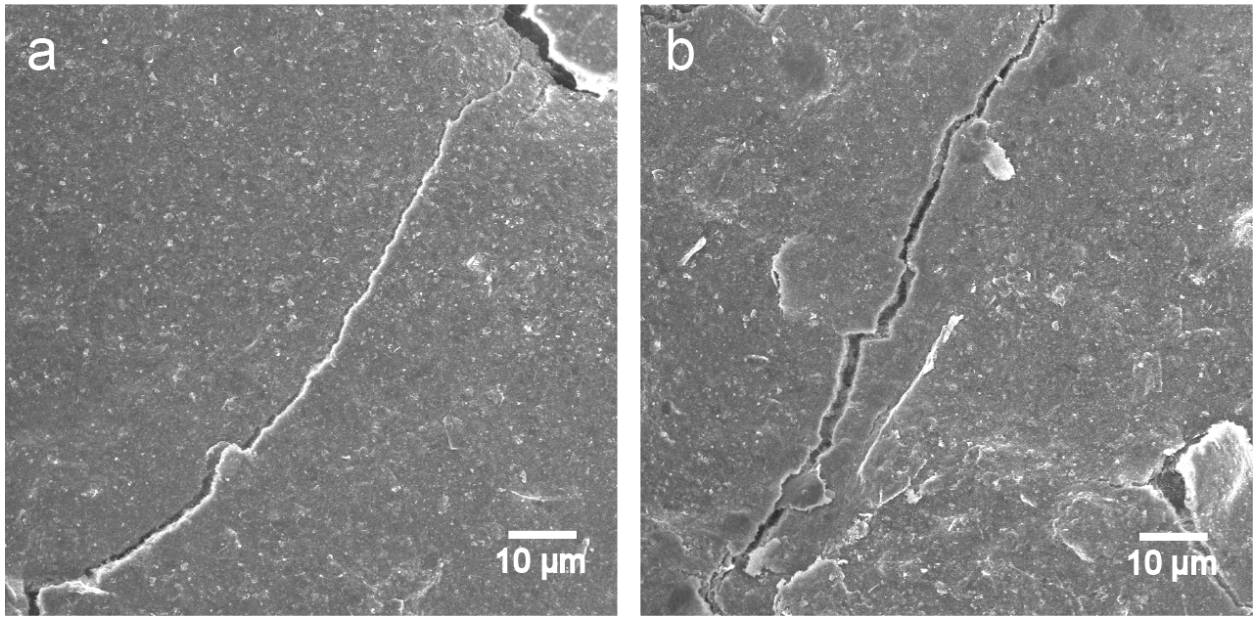

Figure S4.5. SEM images of a cc-AT/CNT (after laser irradiation) electrode at the post-cycling state (after 20,000 charge/discharge cycles).

4.6.3 Electrochemical Characterizations

As shown in **Figure S4.6a**, the measured Nyquist plot can be fit based on an equivalent Randles circuit, where R_s is the internal resistance, R_{ct} is the charge-transfer resistance, C_{dl} is the double-layer capacitance, C_l is the low-frequency mass capacitance, W_o is the Warburg element, and R_{leak} is the low-frequency leakage resistance. The sum of R_s and R_{ct} yields the equivalent series resistance (ESR).[39] The curve-fit Nyquist plots of cc-AT/CNT before cycling (**Figure S4.6b**) and after 20,000 cycles (**Figure S4.6d**) illustrate that little change in internal resistance, charge transfer resistance, and ESR occurred after the long-term cycling process. In contrast, for AT/CNT, the ESR increased from 2.53 Ω before cycling (**Figure S4.6c**) to 2.75 Ω after 20,000 cycles (**Figure S4.6e**). Combined with other characterization results, the increase in ESR indicates that the volumetric changes and the structural changes due to the detachment of aniline trimers from the CNT conductive matrix led to the electronic/ionic resistance increase in AT/CNT over a continuous cycling process.

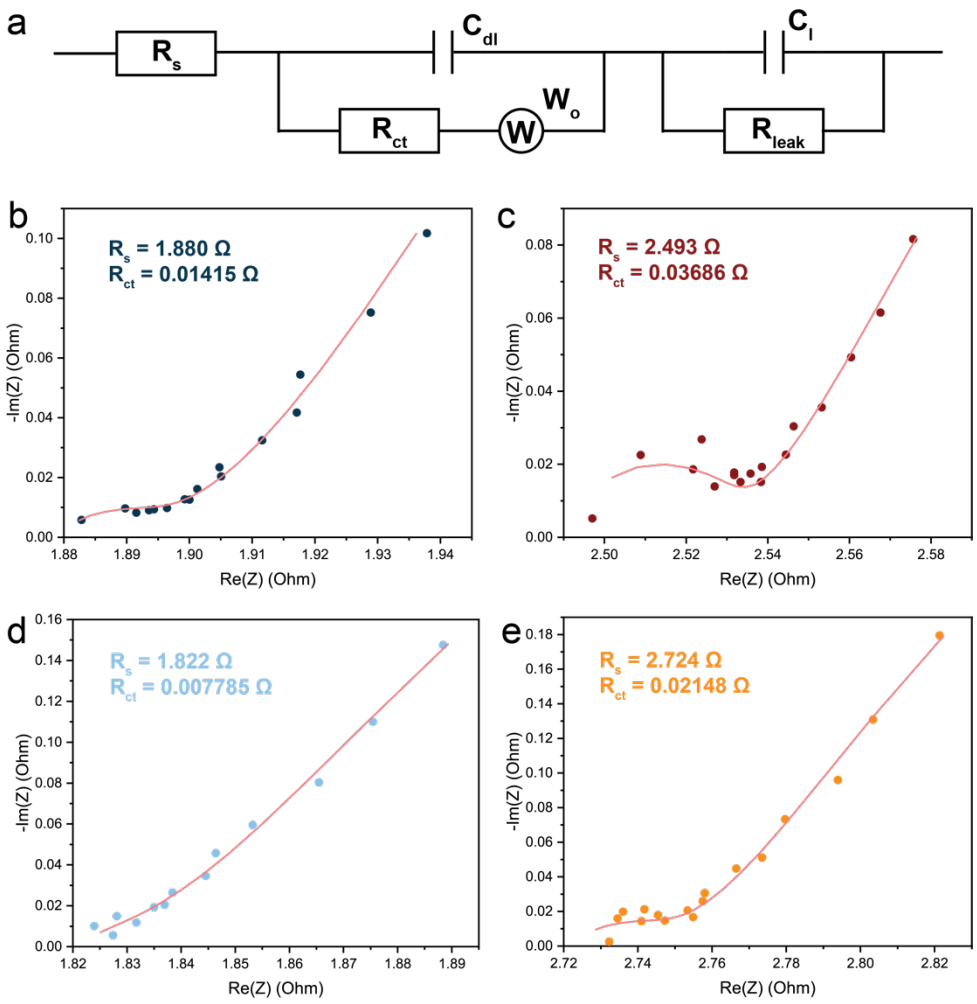

Figure S4.6. a) Equivalent circuit for impedance analysis. Curve-fit Nyquist plots of b) cc-AT/CNT and c) AT/CNT before cycling in the high-frequency region. Curve-fit Nyquist plots of d) cc-AT/CNT and e) AT/CNT after 20,000 charge/discharge cycles in the high-frequency region.

4.7 References

(1) Simon, P.; Gogotsi, Y. Materials for electrochemical capacitors. *Nat. Mater.* **2008**, *7*, 845–854.

(2) Liu, L.; Taberna, P.-L.; Dunn, B.; Simon, P. Future Directions for Electrochemical Capacitors. *ACS Energy Lett.* **2021**, *6*, 4311–4316.

(3) Yu, Z.; Tetard, L.; Zhai, L.; Thomas, J. Supercapacitor electrode materials: nanostructures from 0 to 3 dimensions. *Energy Environ. Sci.* **2015**, *8*, 702–730.

(4) Huang, A.; El-Kady, M. F.; Chang, X.; Anderson, M.; Lin, C.-W.; Turner, C. L.; Kaner, R. B. Facile Fabrication of Multivalent VO_x/Graphene Nanocomposite Electrodes for High-Energy-Density Symmetric Supercapacitors. *Adv. Energy Mater.* **2021**, *11*, 2100768.

(5) Jia, X.; Ge, Y.; Shao, L.; Wang, C.; Wallace, G. G. Tunable Conducting Polymers: Toward Sustainable and Versatile Batteries. *ACS Sustain. Chem. Eng.* **2019**, *7*, 14321–14340.

(6) Eftekhari, A.; Li, L.; Yang, Y. Polyaniline supercapacitors. *J. Power Sources* **2017**, *347*, 86–107.

(7) Liu, T.; Finn, L.; Yu, M.; Wang, H.; Zhai, T.; Lu, X.; Tong, Y.; Li, Y. Polyaniline and Polypyrrole Pseudocapacitor Electrodes with Excellent Cycling Stability. *Nano Lett.* **2014**, *14*, 2522–2527.

(8) Song, Y.; Liu, T.-Y.; Xu, X.-X.; Feng, D.-Y.; Li, Y.; Liu, X.-X. Pushing the Cycling Stability Limit of Polypyrrole for Supercapacitors. *Adv. Funct. Mater.* **2015**, *25*, 4626–4632.

(9) Zhao, Y.; Liu, B.; Pan, L.; Yu, G. 3D nanostructured conductive polymer hydrogels for high-performance electrochemical devices. *Energy Environ. Sci.* **2013**, *6*, 2856–2870.

(10) Heinze, J.; Frontana-Uribe, B. A.; Ludwigs, S. Electrochemistry of Conducting Polymers—Persistent Models and New Concepts. *Chem. Rev.* **2010**, *110*, 4724−4771.

(11) Otero, T. F.; Martinez, J. G. Structural Electrochemistry: Conductivities and Ionic Content from Rising Reduced Polypyrrole Films. *Adv. Funct. Mater.* **2014**, *24*, 1259–1264.

(12) Otero, T. F.; Alfaro, M.; Martinez, V.; Perez, M. A.; Martinez, J. G. Biomimetic Structural Electrochemistry from Conducting Polymers: Processes, Charges, and Energies. Coulovoltammetric Results from Films on Metals Revisited. *Adv. Funct. Mater.* **2013**, *23*, 3929–3940.

(13) Dianat, N.; Rahmanifar, M. S.; Noori, A.; El-Kady, M. F.; Chang, X.; Kaner, R. B.; Mousavi, M. F. Polyaniline-Lignin Interpenetrating Network for Supercapacitive Energy Storage. *Nano Lett.* **2021**, *21*, 9485–9493.

(14) Huang, F.; Chen, D. Towards the upper bound of electrochemical performance of ACNT@polyaniline arrays as supercapacitors. *Energy Environ. Sci.* **2012**, *5*, 5833–5841.

(15) Niu, Z.; Zhou, W.; Chen, X.; Chen, J.; Xie, S. Highly Compressible and All-Solid-State Supercapacitors Based on Nanostructured Composite Sponge. *Adv. Mater.* **2015**, *27*, 6002–6008.

(16) Simotwo, S. K.; Delre, C.; Kalra, V. Supercapacitor Electrodes Based on High-Purity Electrospun Polyaniline and Polyaniline–Carbon Nanotube Nanofibers. *ACS Appl. Mater. Interfaces* **2016**, *8*, 21261–21269.

(17) Meng, Y.; Wang, K.; Zhang, Y.; Wei, Z. Hierarchical Porous Graphene/Polyaniline Composite Film with Superior Rate Performance for Flexible Supercapacitors. *Adv. Mater.* **2013**, *25*, 6985–6990.

(18) Liu, L.; Niu, Z.; Zhang, L.; Zhou, W.; Chen, X.; Xie, S. Nanostructured Graphene Composite Papers for Highly Flexible and Foldable Supercapacitors. *Adv. Mater.* **2014**, *26*, 4855–4862.

(19) Wang, C.; Muni, M.; Strauss, V.; Borenstein, A.; Chang, X.; Huang, A.; Qu, S.; Sung, K.; Gilham, T.; Kaner, R. B. Graphene's Role in Emerging Trends of Capacitive Energy Storage. *Small* **2021**, *17*, 2006875.

(20) Yan, J.; Yang, L.; Cui, M.; Wang, X.; Chee, K. J.; Nguyen, V. C.; Kumar, V.; Sumboja, A.; Wang, M.; Lee, P. S. Aniline Tetramer-Graphene Oxide Composites for High Performance Supercapacitors. *Adv. Energy Mater.* **2014**, *4*, 1400781.

(21) Wang, H.; Yu, Z.; El-Kady, M. F.; Anderson, M.; Kowal, M. D.; Li, M.; Kaner, R. B. Graphene/oligoaniline based supercapacitors: Towards conducting polymer materials with high rate charge storage. *Energy Storage Mater.* **2019**, *19*, 137–147.

(22) Han, H.; Lee, S. W.; Moon, K. H.; Cho, S. Fabrication of Solid-State Asymmetric Supercapacitors Based on Aniline Oligomers and Graphene Electrodes with Enhanced Electrochemical Performances. *Acs Omega* **2019**, *4*, 1244–1253.

(23) Kumar, N. A.; Choi, H.-J.; Shin, Y. R.; Chang, D. W.; Dai, L.; Baek, J.-B. Polyaniline-Grafted Reduced Graphene Oxide for Efficient Electrochemical Supercapacitors. *ACS Nano* **2012**, *6*, 1715–1723.

(24) Liu, J.; An, J.; Zhou, Y.; Ma, Y.; Li, M.; Yu, M.; Li, S. Preparation of an Amide Group-Connected Graphene–Polyaniline Nanofiber Hybrid and Its Application in Supercapacitors. *ACS Appl. Mater. Interfaces* **2012**, *4*, 2870–2876.

(25) Liu, X.; Shang, P.; Zhang, Y.; Wang, X.; Fan, Z.; Wang, B.; Zheng, Y. Three-dimensional and stable polyaniline-grafted graphene hybrid materials for supercapacitor electrodes. *J. Mater. Chem. A* **2014**, *2*, 15273–15278.

(26) Ghosh, T.; Basak, U.; Bairi, P.; Ghosh, R.; Pakhira, M.; Ball, R.; Biswas, B.; Chatterjee, D. P. Hierarchical Nanocomposites by Oligomer-Initiated Controlled Polymerization of Aniline on Graphene Oxide Sheets for Energy Storage. *ACS Appl. Nano Mater.* **2020**, *3*, 1693–1705.

(27) Chang, X.; El-Kady, M. F.; Huang, A.; Lin, C.-W.; Aguilar, S.; Anderson, M.; Zhu, J. Z. J.; Kaner, R. B. 3D Graphene Network with Covalently-Grafted Aniline Tetramer for Ultralong-Life Supercapacitors. *Adv. Funct. Mater.* **2021**, *31*, 2102397.

(28) Chang, X.; Lin, C.-W.; Huang, A.; El-Kady, M. F.; Kaner, R. B. Molecular Engineering of Hierarchical Conducting Polymer Composites for Highly Stable Supercapacitors. *Nano Lett.* **2023**, *23*, 3317–3325.

(29) Zhang, P.; Zhai, X.; Huang, H.; Zhou, J.; Li, X.; He, Y.; Guo, Z. Capacitance fading mechanism and structural evolution of conductive polyaniline in electrochemical supercapacitor. *J Mater Sci Mater Electron* **2020**, *31*, 14625–14634.

(30) Deng, J. X.; Wang, T. M.; Guo, J. S.; Liu, P. Electrochemical capacity fading of polyaniline electrode in supercapacitor: An XPS analysis. *Prog. Nat. Sci.: Mater. Int.* **2017**, *27*, 257–260.

(31) Zhang, Q. E.; Zhou, A. A.; Wang, J.; Wu, J.; Bai, H. Degradation-induced capacitance: a new insight into the superior capacitive performance of polyaniline/graphene composites. *Energy Environ. Sci.* **2017**, *10*, 2372–2382.

(32) Moloudi, M.; Rahmanifar, M. S.; Noori, A.; Chang, X.; Kaner, R. B.; Mousavi, M. F. Bioinspired polydopamine supported on oxygen-functionalized carbon cloth as a high-performance 1.2 V aqueous symmetric metal-free supercapacitor. *J. Mater. Chem. A* **2021**, *9*, 7712–7725.

(33) Zou, Y.; Zhang, Z.; Zhong, W.; Yang, W. Hydrothermal direct synthesis of polyaniline, graphene/polyaniline and N-doped graphene/polyaniline hydrogels for high performance flexible supercapacitors. *J. Mater. Chem. A* **2018**, *6*, 9245–9256.

(34) Kim, K. S.; Park, S. J. Influence of amine-grafted multi-walled carbon nanotubes on physical and rheological properties of PMMA-based nanocomposites. *J. Solid State Chem.* **2011**, *184*, 3021–3027.

(35) Tang, P.; Zhang, Z.; Guo, C.; Zeng, S.; Chen, P.; Xu, Y.; Nie, W.; Zhou, Y. Layered Montmorillonite/3D Carbon Nanotube Networks for Epoxy Composites with Enhanced Mechanical Strength and Thermal Properties. *ACS Appl. Nano Mater.* **2022**, *5*, 8343–8352.

(36) Ghosh, T.; Ghosh, R.; Basak, U.; Majumdar, S.; Ball, R.; Mandal, D.; Nandi, A. K.; Chatterjee, D. P. Candle soot derived carbon nanodot/polyaniline hybrid materials through controlled grafting of polyaniline chains for supercapacitors. *J. Mater. Chem. A* **2018**, *6*, 6476–6492.

(37) Kovalenko, I.; Bucknall, D. G.; Yushin, G. Detonation Nanodiamond and Onion-Like-Carbon-Embedded Polyaniline for Supercapacitors. *Adv. Funct. Mater.* **2010**, *20*, 3979–3986.

(38) Zhang, H. R.; Wang, J. X.; Chen, Y. Y.; Wang, Z.; Wang, S. C. Long-term cycling stability of polyaniline on graphite electrodes used for supercapacitors. *Electrochim. Acta* **2013**, *105*, 69–74.

(39) Shao, Y.; El-Kady, M. F.; Sun, J.; Li, Y.; Zhang, Q.; Zhu, M.; Wang, H.; Dunn, B.; Kaner, R. B. Design and Mechanisms of Asymmetric Supercapacitors. *Chem. Rev.* **2018**, *118*, 9233–9280.

(40) Wu, J.; Zhang, Q. E.; Zhou, A. A.; Huang, Z.; Bai, H.; Li, L. Phase-Separated Polyaniline/Graphene Composite Electrodes for High-Rate Electrochemical Supercapacitors. *Adv. Mater.* **2016**, *28*, 10211–10216.

(41) Wu, J.; Zhang, Q. E.; Wang, J.; Huang, X.; Bai, H. A self-assembly route to porous polyaniline/reduced graphene oxide composite materials with molecular-level uniformity for high-performance supercapacitors. *Energy Environ. Sci.* **2018**, *11*, 1280–1286.

(42) Beidaghi, M.; Wang, C. Micro-Supercapacitors Based on Interdigital Electrodes of Reduced Graphene Oxide and Carbon Nanotube Composites with Ultrahigh Power Handling Performance. *Adv. Funct. Mater.* **2012**, *22*, 4501–4510.

(43) Noori, A.; El-Kady, M. F.; Rahmanifar, M. S.; Kaner, R. B.; Mousavi, M. F. Towards establishing standard performance metrics for batteries, supercapacitors and beyond. *Chem. Soc. Rev.* **2019**, *48*, 1272–1341.

(44) Wei, Y.; Yang, C. C.; Ding, T. Z. A one-step method to synthesize N,N'-bis(4'-aminophenyl)-1,4-quinonenediimine and its derivatives. *Tetrahedron Lett.* **1996**, *37*, 731−734.

CHAPTER 5. POLYANILINE-LIGNIN INTERPENETRATING NETWORK FOR SUPERCAPACITIVE ENERGY STORAGE

5.1 Abstract

Because of increasing interest in environmentally benign supercapacitors, earth-abundant biopolymers have found their way into value-added applications. Herein, a promising nanocomposite based on an interpenetrating network of polyaniline and sulfonated lignin (lignosulfonate, LS) is presented. On the basis of an appropriate regulation of the nucleation kinetics and growth behavior via applying a series of rationally designed potential pulse patterns, a uniform PANI-LS film is achieved. On the basis of the fast rate of H^+ insertion−deinsertion kinetics, rather than the slow SO_4^{2-} doping−dedoping process, the PANI-LS nanocomposite delivers specific capacitance of 1200 F g^{-1} at 1 A g^{-1} surpassing the best conducting polymer-lignin supercapacitors known. A symmetric PANI-LS||PANI-LS device delivers a high specific energy of 21.2 W h kg^{-1}, an outstanding specific power of 26.0 kW kg^{-1}, along with superb flexibility and excellent cycling stability. Thus, combining charge storage attributes of polyaniline and lignosulfonate enables a waste-to-wealth approach to improve the supercapacitive performance of polyaniline.

5.2 Introduction

Because of ever-growing environmental concerns, the development of highly efficient, low-cost, reliable, sustainable, and environmentally benign energy storage systems is imperative.

Although batteries are the leading energy storage technology today, the use of electrochemical capacitors with energy storage characteristics that complement those of batteries has been increasing substantially over the past decades.[1-4] To date, a wide variety of materials have been investigated for supercapacitive energy storage.[5-13] Conducting polymers provide the advantages of easy preparation with control over their size, morphology, and surface chemistry, tunable conductivity, high flexibility, and low cost relative to their existing inorganic counterparts.[14] One limitation of conducting polymers, however, is their relatively low charge capacity. A variety of approaches have been considered to boost the charge capacity of conducting polymers, such as incorporating redox-active side groups, organic/inorganic species, and redox active dopants, or synthesizing nanostructured polymers to increase the effective surface area for efficient electrode−electrolyte contact.[15-20] Furthermore, morphological and structural characteristics and electrochemical behavior of conducting polymers is strongly dependent on the type of counterions compensating the positive charge of the conjugated polymer chains during synthesis. Small anionic dopants such as chloride,[21] perchlorate,[22] p-toluene-sulfonate,[23] and dodecylbenzenesulfonate[24] are susceptible to migration out of the electrodes over time, whereas the use of large (bio)polymers as dopants leads to more stable confinement of the redox moieties within the conductive polymer matrix.[25]

Redox active biopolymers rich in quinones are sophisticated materials for energy conversion processes.[26-29] In particular, lignin, which is second only to cellulose in abundance, represents 20 to 30% of the solid weight of trees as well as other lignocellulosic biomasses and is comprised of

nontoxic and highly branched polyphenolic groups.[30, 31] Direct utilization of lignin or its derivatives such as sulfonated lignin (known as lignosulfonate, LS), as a pseudocapacitive material opens up new possibilities for the development of sustainable active materials for value-added applications, as the phenolic moieties on the lignin can be converted to redox-active quinone/hydroquinone species.[31, 32]

In this work, we report a facile, green, one-pot electrosynthesis approach for the preparation of PANI-LS nanocomposites on an electrochemically etched carbon fiber electrode, in which the quinone redox activity and PANI conductivity are elegantly combined to create an interpenetrated polymer−biopolymer active material (**Figure 5.1**). The symmetric (PANI-LS||PANI-LS) device displayed excellent energy/power performances, superb flexibility, and excellent cycling stability in a poly(vinyl alcohol) (PVA)-in-H_2SO_4 gel electrolyte. This new approach to fabricate metal-free electrode active materials from green and cost-effective sources marks an important step toward green energy technology development for a wide variety of applications.

5.3 Results and Discussion

The morphological structure and uniformity of the PANI-LS nanocomposite as well as the pure PANI film, electrodeposited on the electrochemically etched carbon fabric substrate under optimized conditions, were inspected using FE-SEM (**Figure 5.2a−d**). The fibers of pure PANI create an irregularly cross-linked 3D network. However, in the case of the PANI-LS nanocomposite LS acts as both a structure-directing agent and a polyanionic dopant, providing many active sites for the interaction of aniline monomers through which the nucleation and growth of polyaniline can be conducted along the LS chains. This leads to more continuous and thinner fibers with a significantly higher surface area that facilitates the transport of the electrolyte ions into and out of the PANI-LS nanocomposite, thus guaranteeing the high-rate capability of the

system. The corresponding EDX spectra confirm that the obtained PANI-LS nanocomposite consists of C, O, N, S, and Na as constituent elements of PANI and LS. Consistent with the FE-SEM images, the TEM images (**Figure 5.2**) show that the PANI-LS nonhollow fibers possess a more homogeneous and smoother surface than the pure PANI fibers.

In addition to FTIR, ATR-FTIR, Raman, and UV−vis-NIR spectroscopy, we used X-ray photoelectron spectroscopy (XPS) to analyze the elemental compositions of the as-prepared PANI and PANI-LS nanocomposites. From the XPS survey spectra (**Figure 5.2e**), we can observe that PANI and the PANI-LS nanocomposite electrodes are composed of N (~399.7 eV), C (~284.8 eV), O (~530.9 eV), and S (~167.9 eV). The deconvoluted core level N 1s spectrum of PANI (**Figure 5.2f**) is fit with the protonated imine, $=NH^{+}-$, (3.2%), nonprotonated amine, −NH−, (48.6%), and nonprotonated imine, =N−, (48.2%), and that of PANI-LS (**Figure 5.2g**) shows the presence of $=NH^{+}-$ (29.3%), protonated amine, $-NH^{+}-$, (16.4%), and −NH− (54.3%).[33] Considering that the percentages of the protonated amine and imine nitrogen moieties (that correspond to the oxidized state) are nearly equal to the percentage of the nonprotonated amine groups (that is in the reduced state), it can be concluded that both the as-prepared PANI and PANI-LS are in the emeraldine oxidation state. However, the percentage of the positively charged nitrogen moieties of the PANI-LS (45.7%) is significantly higher than that of the pure PANI electrode (3.2%), confirming that the integration of the LS biopolymer in the PANI matrix induces more active sites to the polymer. Such an interesting observation confirms the role of lignosulfonate chains in reducing the polymerization potential through the pseudocomplex formation, leading to an electro-synthesized polymer at a lower oxidation state. These protonated groups endow PANI with more active sites, improved wettability, and enhanced conductivity as well.[34] The core level XPS spectrum of S 2p, originating from the SO_4^{2-} ions doped into the PANI

polymer backbone, is deconvoluted to a doublet peak reflecting spin−orbit interactions including S $2p_{3/2}$ and S $2p_{1/2}$ with a relative ratio of 2:1 and 1.1 eV separation (**Figure 5.2h**). In the deconvoluted S 2p spectrum of PANI-LS, there are three doublets corresponding to SO_4^{2-}, $-RSO_3^-$, and C−S confirming the incorporation of lignosulfonate macromolecules in the polyaniline matrix (**Figure 5.2i**)

The $-RSO_3^-$ functionalities serve as the dopant as well as a proton reservoir, ensuring the high local H^+ concentration in the vicinity of the polymer backbone, facilitating the redox reactions, and thus enabling the excellent energy storage performance of the PANI-LS nanocomposite.[35]

Figure 5.3a shows the proposed charge−discharge mechanisms deduced from the above-discussed XPS and Raman spectroscopy as well as the CV studies. In **Figure 5.3b**, the first strong anodic peak at a less positive potential (0.38 V) is attributed to the redox transition of leucoemeraldine (LE) to emeraldine (EM) and the redox peak at 0.8 V, which is incomplete in the voltammogram, is related to the transformation of emeraldine to pernigraniline (PE). We selected the potential range from −0.2 to 0.8 V to avoid the full oxidization of emeraldine to pernigraniline, since pernigraniline is prone to degradation. The weak peaks at ∼0.6 V are attributed to the hydrolysis products and oxidation of the head-to-tail dimer as well as the intermediates of the hydroquinone/benzoquinone redox reaction.[36] The intensity of the first redox peak in the PANI-LS nanocomposite is more pronounced than that of pure PANI, because more protonated nitrogen species are available in the PANI-LS. Since the redox peak positions of the H_2Q/Q couples of the LS chains overlap with the peaks of over oxidation products of PANI, distinguishing the contributions of each component in the overall performance is not an easy task.

Note that the concentration of LS in the PANI-LS nanocomposite is very low compared to the concentration of aniline, thus enormous improvement in the pseudocapacitive behavior of the

PANI-LS nanocomposite can be in part attributed to the direct contribution of LS in charge storage but mainly to the advantageous structural, electrical, and morphological properties induced by LS to PANI. Interestingly, the presence of H_2Q/Q couples leads the unstable pernigraniline state to remain almost unpopulated during the charge−discharge process, as the H_2Q/Q couple regenerates the starting active material via a catalytic EC′ mechanism by electron transfer between polyaniline and the quinones as reported previously.[17, 37] This is one of the reasons behind the excellent long-term stability of the system as will be discussed later on.

In the PANI-LS nanocomposite electrode, PANI and H_2Q/Q couples contribute to the charge storage mechanism according to the following equations:[17, 37, 38]

$$PANI_{Ox} + 2H^+ + 2e^- \underset{Charge}{\overset{Discharge}{\rightleftarrows}} PANI_{Red} \quad (5.1)$$

$$PANI_{Red} + LS{-}Q \underset{Charge}{\overset{Discharge}{\rightleftarrows}} PANI_{Ox} + LS{-}H_2Q \quad (5.2)$$

$$LS{-}Q + 2H^+ + 2e^- \underset{Charge}{\overset{Discharge}{\rightleftarrows}} LS{-}H_2Q \quad (5.3)$$

and the overall reaction can be expressed as:

$$PANI_{Ox}.LS{-}Q + 4H^+ + 4e^- \underset{Charge}{\overset{Discharge}{\rightleftarrows}} PANI_{Red}.LS{-}H_2Q \quad (5.4)$$

The PANI-LS electrode preserves its shape even at a high scan rate of 100 mV s^{-1}, indicating the fast reaction kinetics and high rate capability of the system (**Figure 5.3c**). Whereas CV curves of the PANI electrode distort to a spindle-like shape and become resistive (**Figure 5.3d**), illustrating the low rate capability and slow reaction kinetics of the PANI electrode (**Figure 5.3e**).

Note that, the $-SO_3^-$ dopants on LS cannot move out of the polymer, so the charge balancing will be done by H^+ cation insertion into the polymer. Since the H^+ cations have a small size, their

transport into and out of the PANI-LS matrix takes place more efficiently than that of the larger SO_4^{2-} anions that are responsible for charge compensation during the redox reactions of the pure PANI electrode. The specific capacitance of the PANI-LS electrode is 1200 F g^{-1} at 1 A g^{-1} which is considerably higher than that of the PANI electrode (575 F g^{-1}, **Figure 5.3f**). **Figure 5.3g** displays the plot of specific capacitance versus the applied specific current for the two electrodes. As can be seen, GCD profiles also confirm the better rate capability of the PANI-LS electrode than the PANI electrode. The PANI-LS electrode retains 40% and 20% of the initial capacitance at high specific currents of 100 and 200 A g^{-1}, respectively, which are considerably higher than that of the PANI electrode for which the capacitance drops to zero when the specific current approaches 100 A g^{-1}. The high rate capability of the PANI-LS electrode originates from the more accessible surface area and shorter ion transport pathways within the nanocomposite matrix which facilitate the doping and dedoping processes during redox reactions. We also conducted EIS measurements to obtain more information about the charge storage mechanism for each electrode.

For a more realistic and practical investigation of the application of the prepared electrodes, the symmetric devices based on the PANI-LS and PANI were assembled and tested in 0.5 M H_2SO_4 as the electrolyte. **Figure 5.4a** shows the CV curves of the PANI-LS||PANI-LS and PANI||PANI devices at different increasing potential windows at a scan rate of 25 mV s^{-1}, respectively. The CVs of the PANI||PANI device show a more resistive behavior than that of the PANI-LS||PANI-LS device. A more rectangular-shaped CV curve of the PANI-LS||PANI-LS device with near-vertical current switches at the voltage extremes indicates the better capacitive performance of the PANI-LS||PANI-LS device compared to the PANI||PANI device. It clearly shows the role of LS chains in reducing the overoxidation reactions of polyaniline. Also, the PANI-LS system demonstrates better ability at retaining the shape of the CV profiles at different scan

rates, confirming the better rate capability of the newly developed device **(Figure 5.4b)**. This was further confirmed from GCD measurements in which the PANI-LS system illustrates more triangular and symmetrical GCD profiles (**Figure 5.4c**). The better performance of the PANI-LS||PANI-LS device can be attributed in part to its superior conductivity. The PANI-LS||PANI-LS device shows a specific capacitance of 227 F g^{-1}_{device} (equivalent to 906 F $g^{-1}_{electrode}$) at the specific current of 1.0 A g^{-1} which is higher than the previously reported capacitances of all conducting polymer-LS composites. The specific capacitance of the PANI||PANI device is 90 F g^{-1}_{device} (equivalent to 360 F $g^{-1}_{electrode}$) at the specific current of 1.0 A g^{-1}. The rate capability plot (**Figure 5.4d**) displays that the PANI-LS||PANI-LS device retains 64.6% of its initial capacitance by increasing the specific current to 50.0 A g^{-1}, whereas the PANI||PANI device does not tolerate a specific current of 50.0 A g^{-1} and maintains just 77.9% of its initial capacitance at a specific current of 10 A g^{-1}. We also conducted EIS studies on both devices at an open circuit potential (∼0 V) over a frequency range from 100 kHz to 10 mHz (**Figure 5.4e,f**).

Long-term cycling stability is one of the major challenges in conducting polymer-lignin based supercapacitors, as many devices based on conducting polymers retain less than 50% of their initial capacitance after only a few hundred charge−discharge cycles.[39, 40] The gradual decrease in capacitance can be attributed to the quinone redox couple in the LS molecules that undergo a nucleophilic addition reaction with water during the oxidation reactions.[40] The decrease in capacitance during cycling has also been attributed to the dissolution of LS into the electrolyte[39] as well as the higher amount of swelling and shrinking that happens for more porous structures during the redox reactions.[41] As a remedy for these drawbacks, we designed a PVA-in-H_2SO_4 gel electrolyte. *Via* this intriguing approach, the dissolution of LS into the electrolyte and the degradation of quinone groups significantly decreased so that we obtained a surprisingly large

improvement in cycling stability for the PANI-LS||PANI-LS device in the gel electrolyte. For cycling stability and also rate capability studies, we recorded consecutive charge−discharge cycles at 2.5, 5.0, 10.0, and again 2.5 A g^{-1} in the gel electrolyte for the PANI-LS||PANI-LS and PANI||PANI devices (**Figure 5.4g**). The PANI-LS||PANI-LS device retains 96% of its initial capacitance after 7500 cycles at different rates, whereas the PANI||PANI device retains 70% of its initial capacitance after 7500 cycles.

We also investigated the cycling stability of the PANI-LS||PANI-LS device at a constant current of 10.0 A g^{-1} over 15 000 charge−discharge cycles. The device delivers 87% of its initial capacitance after 15 000 cycles (**Figure 5.4h**) along with a high Coulombic efficiency of 93% after cycling.

The PANI-LS||PANI-LS device delivers a maximum specific energy of 21.2 W h kg^{-1} at a specific power of 278.5 W kg^{-1} and retains a specific energy of up to 14.5 W h kg^{-1} at a high specific power of 26.0 kW kg^{-1} (at 100.0 A g^{-1}), which is higher than almost all of the reported conducting polymer-lignin based supercapacitors (**Figure 5.5a**). In terms of the volumetric performance, the PANI-LS||PANI-LS device shows a maximum energy density of 0.88 W h L^{-1} at a power density of 11.24 W L^{-1} and retains an energy density of up to 0.54 W h L^{-1} at a high power density of 966.1 W L^{-1}.

Interestingly, from the viewpoint of flexibility as an important requirement for most state-of-the-art applications, utilization of the PVA-in-H_2SO_4 gel electrolyte is an added advantage. To investigate the flexibility of the PANI-LS||PANI-LS symmetric device in the PVA-in-H_2SO_4 gel electrolyte, we recorded CV curves of the device under different bending angles of 0, 45, 90, and 135° (**Figure 5.5b**). As can be seen, there is no considerable change in the shape of the voltammograms, demonstrating the excellent flexibility of the prepared device.

To demonstrate realistic and practical applications of the devices and also the voltage and current stability, several PANI-LS||PANI-LS devices in the PVA-in-H_2SO_4 gel electrolyte were assembled in parallel and in series. As can be seen, the integrated area of the CV curve (**Figure 5.5c**) and charge–discharge times of the GCD profiles (**Figure 5.5d**) increase linearly by increasing the number of devices connected in parallel, confirming the increase in the overall capacitance of the system. Additionally, with the devices connected in series, the operating voltage range was extended from 0.8 to 4 V when five devices were connected in series (**Figure 5.5e,f**). Finally, we connected three devices in parallel (3P) to obtain a circuit. Three, four, and five such circuits connected in series (i.e., 3P × 3S, 3P × 4S, and 3P × 5S) could power red, green, and blue LEDs, respectively (**Figure 5.5g**) showing the great potential of the PANI-LS||PANI-LS devices for practical applications.

5.4 Conclusions

In summary, we have developed a facile, one-step electrodeposition approach for the preparation of a polyaniline-lignosulfonate interconnected network as an excellent supercapacitive material. With intelligent engineering of the polyaniline-lignosulfonate nanoarchitecture *via* optimizing the electro-synthesis conditions, the ion transport pathways and the electron transfer networks improve dramatically, leading to high pseudocapacitance and excellent rate performance. The symmetric all-solid-state and flexible PANI-LS||PANI-LS device delivers a high specific energy (21.2 W h g^{-1} at 278.5 W kg^{-1}) along with an outstanding specific power (26.0 kW kg^{-1} at 14.5 W h kg^{-1}) that outperforms most polymer-based symmetric devices and displays excellent capacitance retention (87% of its initial capacitance after 15000 charge−discharge cycles at 10.0 A g^{-1}) in a poly(vinyl alcohol)-in-H_2SO_4 gel electrolyte. Excellent flexibility of the all-solid-state prototype device further reveals the potential practical applicability of this design as a

promising architecture for the development of high-performance state-of-the-art metal-free and environmentally benign supercapacitors for applications in flexible electronics.

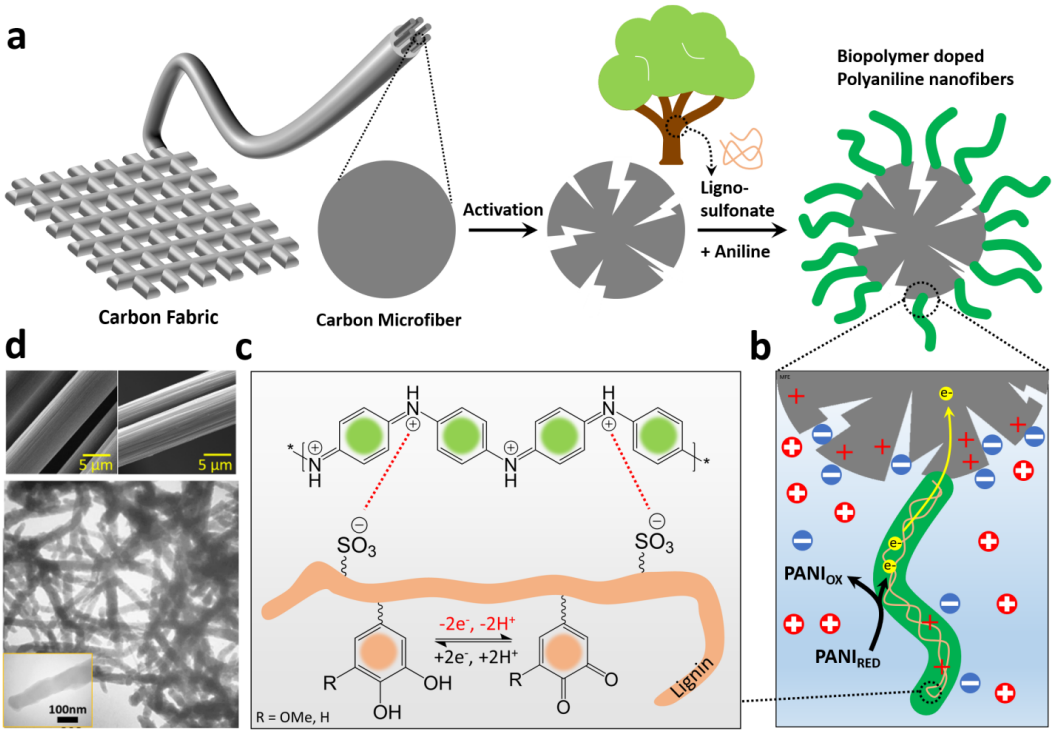

Figure 5.1. (a) The electrochemical etching of the carbon microfiber by applying a constant potential of +2.0 V for 180 s in a H_2SO_4 (0.5 M) solution followed by electropolymerization of aniline in the presence of lignosulfonate chains on an electrochemically etched carbon fiber substrate. (b) Faradaic charge transfer and electrical double layer charge accumulation at the electrode/electrolyte interface. (c) The electrochemical activity of lignosulfonate moieties as a dopant and a structure-directing agent for the PANI film and the redox activities of lignosulfonate by forming catechol moieties in the PANI-LS nanocomposite. (d) SEM images of the carbon fiber substrate before (left) and after (right) electrochemical etching along with a TEM image of the resulting PANI-LS nanocomposite.

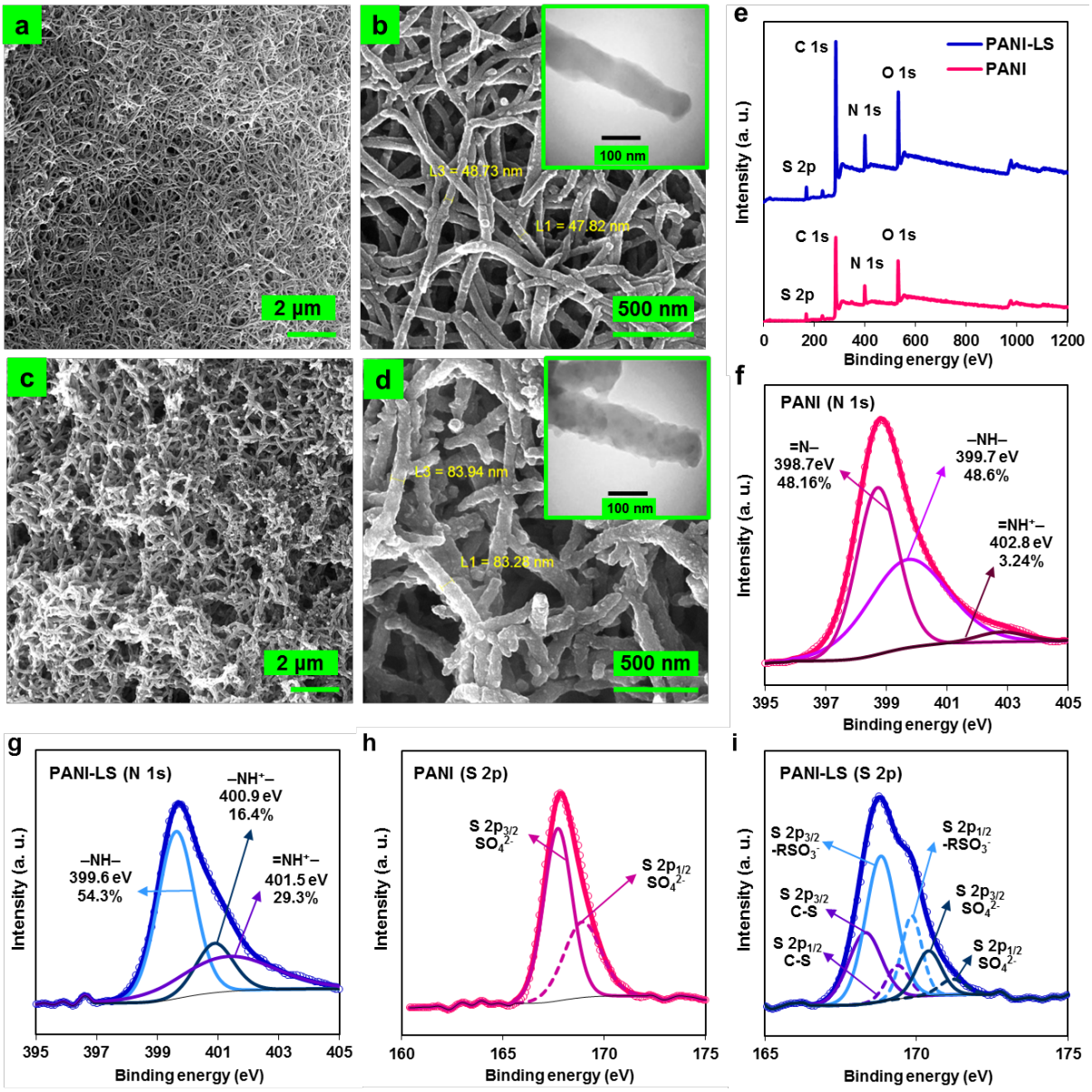

Figure 5.2. Morphological and structural characterization of PANI-LS and PANI. The FE-SEM images of (a,b) the PANI-LS nanocomposite, and (c,d) the pure PANI film at two different magnifications. The insets show the corresponding TEM images. The materials are electrosynthesized on the ECF substrate by applying pulse pattern D. (e) XPS survey spectra of PANI and PANI-LS electrodes. Deconvoluted core level XPS spectra of (f) PANI (N 1s), (g) PANI-LS (N 1s), (h) PANI (S 2p), and (i) PANI-LS (S 2p).

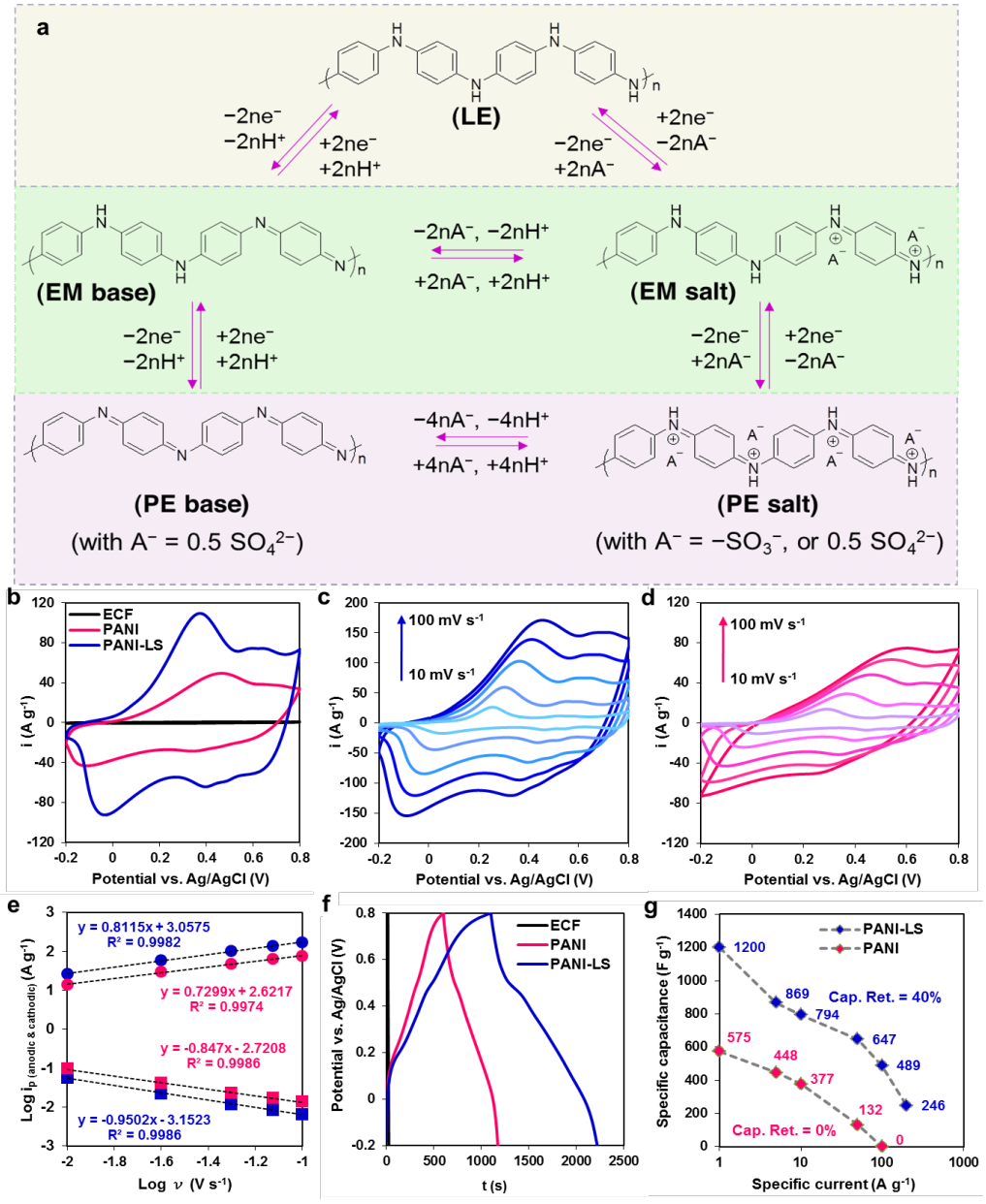

Figure 5.3. Evaluation of the electrochemical performance of the electrodes in a 3E cell setup. (a) The proposed redox mechanism of the PANI-LS and PANI electrodes. The oxidation (charging) reaction is accompanied by anion (SO_4^{2-}) insertion into the polymer and also proton (H^+) release out of the polymer into the electrolyte. (b) CV curves of ECF, PANI, and PANI-LS electrodes at a scan rate of 50 mV s^{-1} in a 0.5 M H_2SO_4 solution. CV curves of the (c) PANI-LS and (d) PANI electrodes at different scan rates from 10 to 100 mV s^{-1}. (e) The plot of log *i* versus log *v* for the

mass normalized anodic and cathodic peak currents of the (blue) PANI-LS and (pink) PANI electrodes extracted from the CV curves at different scan rates from 10 to 100 mV s^{-1}. (f) Galvanostatic charge−discharge (GCD) profiles of the ECF, PANI, and PANI-LS electrodes at 1 A g^{-1}. (g) Rate capability study; specific capacitances of the PANI-LS and PANI electrodes at various specific currents from 1 to 200 A g^{-1} in a 0.5 M H_2SO_4 solution.

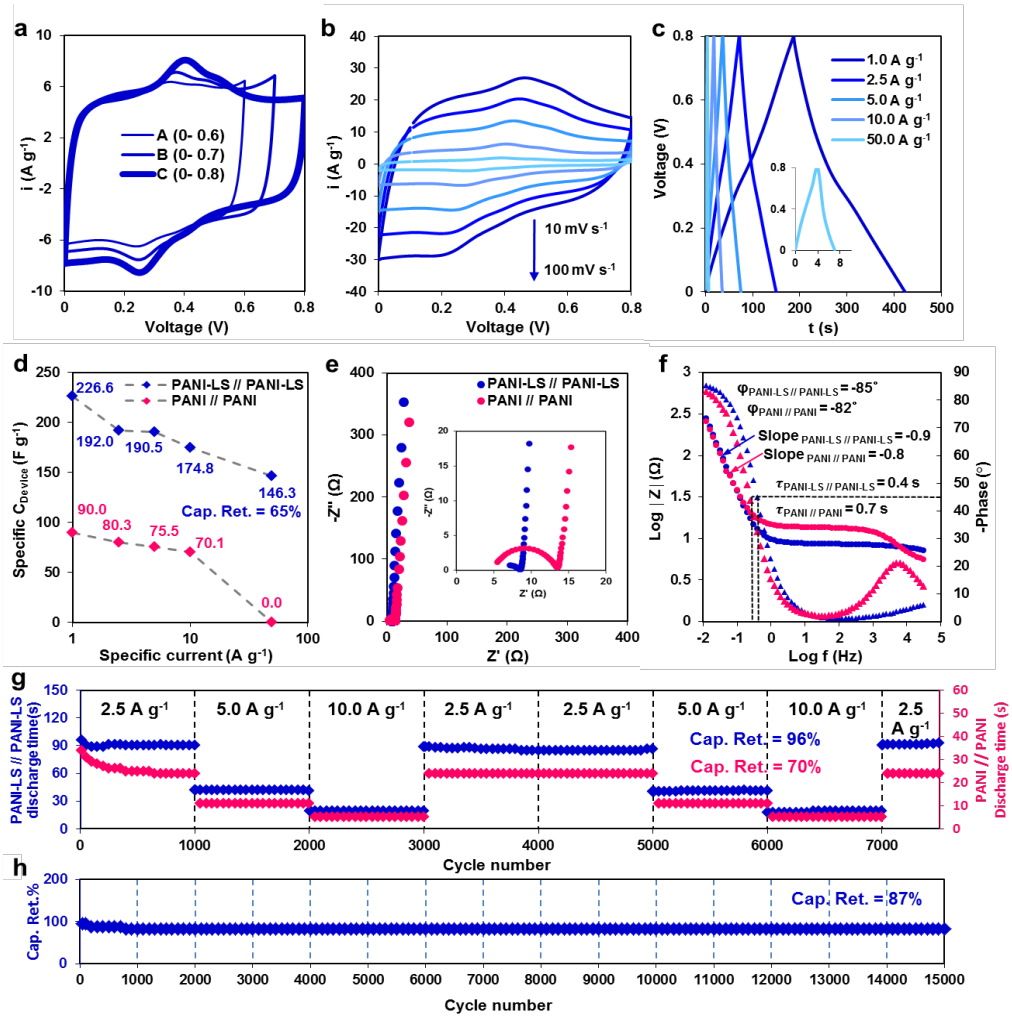

Figure 5.4. Electrochemical characterization of the PANI-LS||PANI-LS and PANI||PANI symmetric supercapacitors. (a) CV curves at different voltage windows of 0.6, 0.7, and 0.8 V

acquired at a scan rate of 25 mV s^{-1} for the PANI-LS||PANI-LS device. (b) CV curves at different scan rates from 10 to 100 mV s^{-1} for the PANI-LS||PANI-LS device. (c) GCD profiles at different specific currents from 1.0 to 50.0 A g^{-1} for the PANI-LS||PANI-LS device. (d) Emergence of the specific capacitances of the PANI-LS||PANI-LS and PANI||PANI devices as a function of current density. (e) Nyquist plots of the PANI-LS||PANI-LS and PANI||PANI devices obtained over a frequency range from 100 kHz to 10 mHz at an open circuit voltage. The inset shows a magnified high-frequency region of the plot. (f) Bode magnitude (log $|Z|$) and phase plots for the PANI-LS||PANI-LS and PANI||PANI devices. All the CV, GCD, and EIS studies were conducted in a 0.5 M H_2SO_4 electrolyte. (g) The two-round consecutive cycling stability studies at different specific currents of 2.5, 5.0, 10.0, and again 2.5 A g^{-1} of the PANI-LS||PANI-LS and PANI||PANI devices over 7500 cycles in a PVA-in-H_2SO_4 gel electrolyte. (h) Cycling stability of a PANI-LS||PANI-LS device at a constant current of 10.0 A g^{-1} over 15 000 cycles in a PVA-in-H_2SO_4 gel electrolyte.

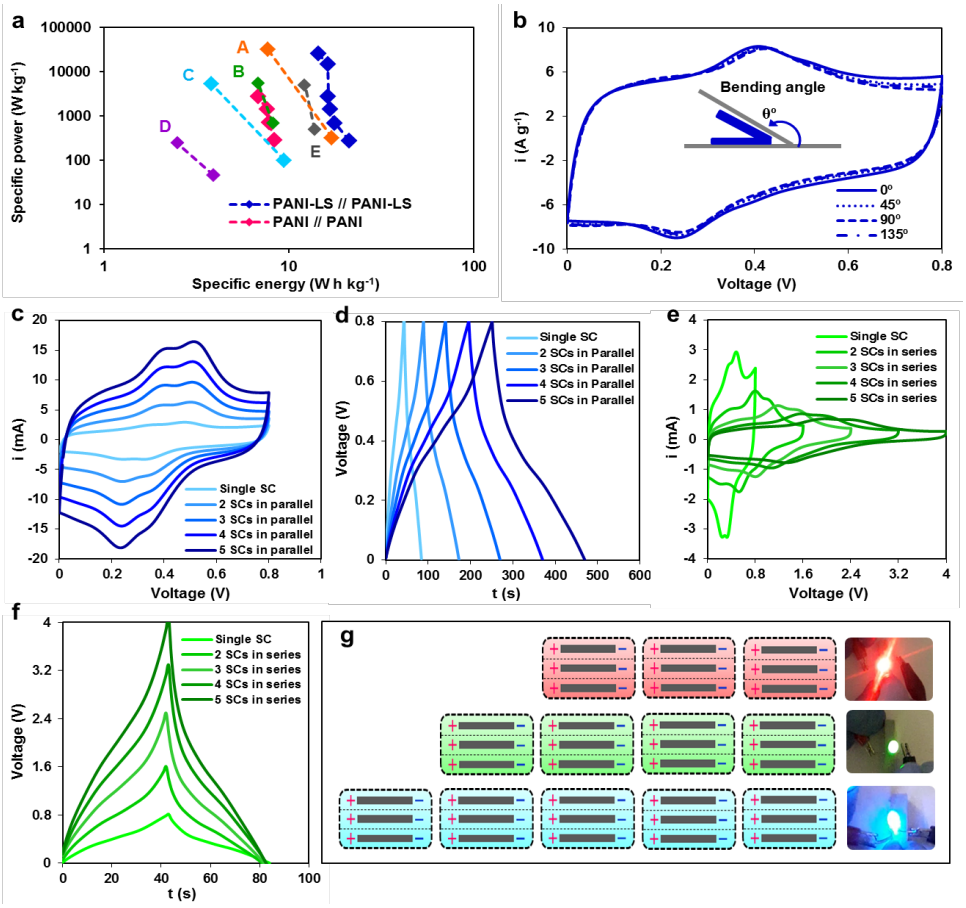

Figure 5.5. Comparative Ragone plot, flexibility behavior, and practical applications of the prototype PANI-LS||PANI-LS devices. (a) Ragone plot of the PANI-LS||PANI-LS and PANI||PANI devices and their comparison with some reported similar devices (A, FSC−Lig/SWCNT$_{HNO3}$;[42] B, PEDOT−PAAQ//PEDOT-Lignin-PAA;[43] C, ARS/PGLS−1;[44] D, LS-PPy@ CFY;[45] E, LS−GHs[46]). (b) CV curves of an all-solid-state PANI-LS||PANI-LS device under different bending angles from 0 to 135° at a scan rate of 25 mV s^{-1}. (c) CV curves and (d) GCD profiles of one to five PANI-LS||PANI-LS devices connected in parallel (P). (e) CV curves and (f) GCD profiles of one to five PANI-LS||PANI-LS devices connected in series (S). (g) Schematic illustration of three, four, and five circuits connected in series in which each circuit comprises three devices connected in parallel. These arrays, that is, 3P × 3S, 3P × 4S, and 3P × 5S, are used for lighting up red, green, and blue LEDs, respectively.

5.5 References

(1) Noori, A.; El-Kady, M. F.; Rahmanifar, M. S.; Kaner, R. B.; Mousavi, M. F. Towards establishing standard performance metrics for batteries, supercapacitors and beyond. *Chem. Soc. Rev.* **2019**, *48*, 1272−1341.

(2) Simon, P.; Gogotsi, Y. Perspectives for electrochemical capacitors and related devices. *Nat. Mater.* **2020**, *19*, 1151−1163.

(3) Pomerantseva, E.; Bonaccorso, F.; Feng, X.; Cui, Y.; Gogotsi, Y. Energy storage: The future enabled by nanomaterials. *Science* **2019**, *366*, eaan8285.

(4) Zhang, Y.; Liu, X.; Wang, S.; Li, L.; Dou, S. Bio-Nanotechnology in High-Performance Supercapacitors. *Adv. Energy Mater.* **2017**, *7*, 1700592.

(5) Zhou, Y.; Maleski, K.; Anasori, B.; Thostenson, J. O.; Pang, Y.; Feng, Y.; Zeng, K.; Parker, C. B.; Zauscher, S.; Gogotsi, Y.; Glass, J. T.; Cao, C. $Ti_3C_2T_x$ MXene-Reduced Graphene Oxide Composite Electrodes for Stretchable Supercapacitors. *ACS Nano* **2020**, *14*, 3576−3586.

(6) Shabangoli, Y.; Rahmanifar, M. S.; Noori, A.; El-Kady, M. F.; Kaner, R. B.; Mousavi, M. F. Nile Blue Functionalized Graphene Aerogel as a Pseudocapacitive Negative Electrode Material across the Full pH Range. *ACS Nano* **2019**, *13*, 12567−12576.

(7) El-Kady, M. F.; Strong, V.; Dubin, S.; Kaner, R. B. Laser scribing of high-performance and flexible graphene-based electrochemical capacitors. *Science* **2012**, *335*, 1326−1330.

(8) Shabangoli, Y.; El-Kady, M. F.; Nazari, M.; Dadashpour, E.; Noori, A.; Rahmanifar, M. S.; Lv, X.; Zhang, C.; Kaner, R. B.; Mousavi, M. F. Exploration of Advanced Electrode Materials for Approaching High- Performance Nickel-Based Superbatteries. *Small* **2020**, *16*, 2001340.

(9) Hu, M.; Zhang, H.; Hu, T.; Fan, B.; Wang, X.; Li, Z. Emerging 2D MXenes for supercapacitors: status, challenges and prospects. *Chem. Soc. Rev.* **2020**, *49*, 6666−6693.

(10) Wang, Y.; Ding, Y.; Guo, X.; Yu, G. Conductive polymers for stretchable supercapacitors. *Nano Res.* **2019**, *12*, 1978−1987.

(11) Yang, W.; Li, X.; Li, Y.; Zhu, R.; Pang, H. Applications of Metal-Organic-Framework-Derived Carbon Materials. *Adv. Mater.* **2018**, *31*, 1804740.

(12) Liu, J.; Song, X.; Zhang, T.; Liu, S.; Wen, H.; Chen, L. 2D Conductive Metal-Organic Frameworks: An Emerging Platform for Electrochemical Energy Storage. *Angew. Chem., Int. Ed.* **2021**, *60*, 5612−5624.

(13) Wang, F.; Wu, X.; Yuan, X.; Liu, Z.; Zhang, Y.; Fu, L.; Zhu, Y.; Zhou, Q.; Wu, Y.; Huang, W. Latest advances in supercapacitors: from new electrode materials to novel device designs. *Chem. Soc. Rev.* **2017**, *46*, 6816−6854.

(14) Le, T. H.; Kim, Y.; Yoon, H. Electrical and Electrochemical Properties of Conducting Polymers. *Polymers* **2017**, *9*, 150.

(15) Karazehir, T.; Sarac, B.; Gilsing, H.-D.; Eckert, J.; Sarac, A. S. Oligoether Ester-Functionalized ProDOT Copolymers on Si/Mono-layer Graphene as Capacitive Thin Film Electrodes. *J. Electrochem. Soc.* **2020**, *167*, No. 070543.

(16) Åkerlund, L.; Emanuelsson, R.; Hernández, G.; Ruipérez, F.; Casado, N.; Brandell, D.; Strømme, M.; Mecerreyes, D.; Sjödin, M. In situ Investigations of a Proton Trap Material: A PEDOT-Based Copolymer with Hydroquinone and Pyridine Side Groups Having Robust Cyclability in Organic Electrolytes and Ionic Liquids. *ACS Appl. Energy Mater.* **2019**, *2*, 4486−4495.

(17) Hashemi, M.; Rahmanifar, M. S.; El-Kady, M. F.; Noori, A.; Mousavi, M. F.; Kaner, R. B. The use of an electrocatalytic redox electrolyte for pushing the energy density boundary of a flexible polyaniline electrode to a new limit. *Nano Energy* **2018**, *44*, 489−498.

(18) Kim, J.; Kim, J. H.; Ariga, K. Redox-Active Polymers for Energy Storage Nanoarchitectonics. *Joule* **2017**, *1*, 739−768.

(19) Qu, Q.; Zhu, Y.; Gao, X.; Wu, Y. Core-Shell Structure of Polypyrrole Grown on V_2O_5 Nanoribbon as High Performance Anode Material for Supercapacitors. *Adv. Energy Mater.* **2012**, *2*, 950−955.

(20) Liu, Y.; Zhang, B.; Yang, Y.; Chang, Z.; Wen, Z.; Wu, Y. Polypyrrole-coated α-MoO_3 nanobelts with good electrochemical performance as anode materials for aqueous supercapacitors. *J. Mater. Chem. A* **2013**, *1*, 13582−13587.

(21) Zhao, Z.; Yu, T.; Miao, Y.; Zhao, X. Chloride ion-doped polyaniline/carbon nanotube nanocomposite materials as new cathodes for chloride ion battery. *Electrochim. Acta* **2018**, *270*, 30−36.

(22) Chen, G. F.; Li, X. X.; Zhang, L. Y.; Li, N.; Ma, T. Y.; Liu, Z. Q. A Porous Perchlorate-Doped Polypyrrole Nanocoating on Nickel Nanotube Arrays for Stable Wide-Potential-Window Supercapacitors. *Adv. Mater.* **2016**, *28*, 7680−7687.

(23) Liao, Q.; Hou, H.; Duan, J.; Liu, S.; Yao, Y.; Dai, Z.; Yu, C.; Li, D. Composite sodium p-toluenesulfonate/polypyrrole/TiO_2 nanotubes/Ti anode for sodium ion battery. *Int. J. Hydrogen Energy* **2017**, *42*, 12414−12419.

(24) Bilal, S.; Begum, B.; Gul, S.; Shah, A.-u.-H. A. PANI/DBSA/H_2SO_4: A promising and highly efficient electrode material for aqueous supercapacitors. *Synth. Met.* **2018**, *235*, 1−15.

(25) Leguizamon, S.; Díaz-Orellana, K. P.; Velez, J.; Thies, M. C.; Roberts, M. E. High charge-capacity polymer electrodes comprising alkali lignin from the Kraft process. *J. Mater. Chem. A* **2015**, *3*, 11330−11339.

(26) Liu, L.; Solin, N.; Inganäs, O. Bio Based Batteries. *Adv. Energy Mater.* **2021**, *11*, 2003713.

(27) Madeo, J.; Zubair, A.; Marianne, F. A review on the role of quinones in renal disorders. *SpringerPlus* **2013**, *2*, 139.

(28) Moloudi, M.; Rahmanifar, M. S.; Noori, A.; Chang, X.; Kaner, R. B.; Mousavi, M. F. Bioinspired polydopamine supported on oxygen-functionalized carbon cloth as a high-performance 1.2 V aqueous symmetric metal-free supercapacitor. *J. Mater. Chem. A* **2021**, *9*, 7712−7725.

(29) Wang, H.; Yang, Y.; Guo, L. Renewable-Biomolecule-Based Electrochemical Energy-Storage Materials. *Adv. Energy Mater.* **2017**, *7*, 1700663.

(30) Espinoza-Acosta, J. L.; Torres-Chávez, P. I.; Olmedo-Martínez, J. L.; Vega-Rios, A.; Flores-Gallardo, S.; Zaragoza-Contreras, E. A. Lignin in storage and renewable energy applications: A review. *J. Energy Chem.* **2018**, *27*, 1422−1438.

(31) Wu, X.; Jiang, J.; Wang, C.; Liu, J.; Pu, Y.; Ragauskas, A.; Li, S.; Yang, B. Lignin-derived electrochemical energy materials and systems. *Biofuels, Bioprod. Biorefin.* **2020**, *14*, 650−672.

(32) Gan, D.; Xing, W.; Jiang, L.; Fang, J.; Zhao, C.; Ren, F.; Fang, L.; Wang, K.; Lu, X. Plant-inspired adhesive and tough hydrogel based on Ag-Lignin nanoparticles-triggered dynamic redox catechol chemistry. *Nat. Commun.* **2019**, *10*, 1487.

(33) Wu, D.; Zhong, W. A new strategy for anchoring a functionalized graphene hydrogel in a carbon cloth network to support a lignosulfonate/polyaniline hydrogel as an integrated electrode for flexible high areal-capacitance supercapacitors. *J. Mater. Chem. A* **2019**, *7*, 5819−5830.

(34) Wang, S.; Huang, S.; Yao, M.; Zhang, Y.; Niu, Z. Engineering Active Sites of Polyaniline for $AlCl_2^+$ Storage in an Aluminum-Ion Battery. *Angew. Chem., Int. Ed.* **2020**, *59*, 11800−11807.

(35) Shi, H. Y.; Ye, Y. J.; Liu, K.; Song, Y.; Sun, X. A Long-Cycle-Life Self-Doped Polyaniline Cathode for Rechargeable Aqueous Zinc Batteries. *Angew. Chem., Int. Ed.* **2018**, *57*,

16359−16363.

(36) Chen, W.-C.; Wen, T.-C.; Hu, C.-C.; Gopalan, A. Identification of inductive behavior for polyaniline via electrochemical impedance spectroscopy. *Electrochim. Acta* **2002**, *47*, 1305−1315.

(37) Vonlanthen, D.; Lazarev, P.; See, K. A.; Wudl, F.; Heeger, A. J. A stable polyaniline-benzoquinone-hydroquinone supercapacitor. *Adv. Mater.* **2014**, *26*, 5095−5100.

(38) Milczarek, G.; Inganas, O. Renewable cathode materials from biopolymer/conjugated polymer interpenetrating networks. *Science* **2012**, *335*, 1468−1471.

(39) Edberg, J.; Inganäs, O.; Engquist, I.; Berggren, M. Boosting the capacity of all-organic paper supercapacitors using wood derivatives. *J. Mater. Chem. A* **2018**, *6*, 145−152.

(40) Ajjan, F. N.; Casado, N.; Rębiś, T.; Elfwing, A.; Solin, N.;́ Mecerreyes, D.; Inganäs, O. High performance PEDOT/lignin biopolymer composites for electrochemical supercapacitors. *J. Mater. Chem. A* **2016**, *4*, 1838−1847.

(41) Admassie, S.; Elfwing, A.; Jager, E. W. H.; Bao, Q.; Inganäs, O. A renewable biopolymer cathode with multivalent metal ions for enhanced charge storage. *J. Mater. Chem. A* **2014**, *2*, 1974−1979.

(42) Peng, Z.; Zou, Y.; Xu, S.; Zhong, W.; Yang, W. High-Performance Biomass-Based Flexible Solid-State Supercapacitor Constructed of Pressure-Sensitive Lignin-Based and Cellulose Hydrogels. *ACS Appl. Mater. Interfaces* **2018**, *10*, 22190−22200.

(43) Ajjan, F. N.; Vagin, M.; Rębiś,́T.; Aguirre, L. E.; Ouyang, L.; Inganäs, O. Scalable Asymmetric Supercapacitors Based on Hybrid Organic/Biopolymer Electrodes. *Adv. Sustainable Syst.* **2017**, *1*, 1700054.

(44) Wang, T.; Hu, S.; Wu, D.; Zhao, W.; Yu, W.; Wang, M.; Xu, J.; Zhang, J. Boosting the capacity of biomass-based supercapacitors using carbon materials of wood derivatives and redox

molecules from plants. *J. Mater. Chem. A* **2021**, *9*, 11839−11852.

(45) Liu, X.; Zang, L.; Liang, C.; Liu, Q.; Deng, Y.; Yang, C.; Qiu, J. Design and fabrication of high performance flexible supercapacitor with polypyrrole@carbon fiber yarn electrode and redox active dopants. *Synth. Met.* **2021**, *271*, 116654.

(46) Li, F.; Wang, X.; Sun, R. A metal-free and flexible supercapacitor based on redox-active lignosulfonate functionalized graphene hydrogels. *J. Mater. Chem. A* **2017**, *5*, 20643−20650.

CHAPTER 6. BIOINSPIRED POLYDOPAMINE SUPPORTED ON OXYGEN-FUNCTIONALIZED CARBON CLOTH AS A HIGH-PERFORMANCE 1.2 V AQUEOUS SYMMETRIC METAL-FREE SUPERCAPACITOR

6.1 Abstract

The ongoing surge in demand for sustainable energy technologies with little to no environmental impacts calls for the exploration of advanced energy storage materials. Inspiration from nature is undoubtedly a promising approach to comply with environmental legislations. Herein, we describe a facile and green electrosynthesis approach to fabricate a polydopamine (PDA) nanofilm supported on oxygen-functionalized carbon cloth (FCC). The surface functionalization of carbon cloth facilitates the PDA nanofilm adhesion and endows the as-prepared PDA-FCC electrode with excellent flexibility, good electrical conductance (22.6 mS), and outstanding wettability to the aqueous electrolyte. Owing to these merits, the PDA-FCC electrode delivers a favorable capacitance of 626 F g^{-1} at 1.0 A g^{-1} (617 mF cm^{-2} at 2.2 mA cm^{-2}, and 1296 mF cm^{-3} at 5.3 mA cm^{-3}), in which the catechol, amine, and imine moieties of PDA are responsible for its excellent pseudocapacitive behavior. The symmetric all-solid-state flexible

PDA-FCC||PDA-FCC device covers almost the entire thermodynamic stability window of aqueous electrolytes (1.2 V), delivers a high specific energy of 11.7 Wh kg^{-1}, superb specific power of up to 6.4 kW kg^{-1}, and excellent flexibility along with outstanding cycling stability (81% retention of the initial capacitance after 10,000 cycles). These performance characteristics are in part due to the binder-free PDA biopolymer film that adopts the inherent texture of the carbon cloth, enabling the pores to play the role of temporary ion-buffering reservoirs that facilitate effective mass transport. This new approach to fabricate electrodes from green sources is considered an important step toward environmentally-benign energy storage technologies.

6.2 Introduction

The growing global demand for energy to meet the requirements of modern societies is exerting ever-increasing pressure on the environment. One of the most appealing approaches to alleviate these concerns is to develop energy storage technologies that, aside from providing high energy/high power, are more affordable, reliable, sustainable, and environmentally friendly than the existing energy storage systems.[1-3] Progress so far has not, however, been satisfactory to match these expectations. On the other hand, energy access matters more than ever during the COVID-19 pandemic, as energy is key to healthcare services. COVID-19 will deliberately influence the generation, transmission, and delivery of sustainable energy, as flows of finance and technology rely on a highly interconnected global energy system that hardly seems practicable.[4] Thus, the future of renewable energy sources for electrification of communities, especially islands and remote off-grid areas, looks very bright. In these cases, electrochemical energy storage systems coupled with renewable power generation can help significantly to smooth the load profile and balance the mismatch between supply and demand.[5] Electrochemical capacitors are among the most prominent of these energy storage technologies.

The choice of supercapacitive electrode active materials has been limited mostly to carbon-based materials for electrical double layer capacitors (EDLC),[6-14] as well as transition metal redox species,[15-21] conducting polymers[22-29] and very recently metal-organic frameworks (MOFs),[30-33] layered double hydroxides (LDHs),[34-37] and MXenes[10, 29, 38-40] as redox capacitor materials. To further enhance the supercapacitive performance of the systems beyond EDLCs, our research group and others have developed strategies to fabricate organic redox species-conjugated carbonaceous materials *via* an intriguing supramolecular non-covalent surface functionalization approach.[41-42] This offers the added benefits of being environmentally benign, cost-effective, remarkably easy to prepare, and metal-free.

Nature is a rich resource that provides a vast wealth of inspirations for scientific discoveries.[43] Bioinspired all-carbon-based materials are a new emerging class of advanced materials for electrochemical energy storage applications in order to protect sustainable living on our planet.[44] For instance, inspired by mosses grown on rocks in nature, Zhang *et al.* anchored porous carbon nanosheets on bulk carbon backbones and achieved a specific capacitance of 205 F g^{-1} at 0.2 A g^{-1}.[45] In another study, Lian *et al.* dissolved konjac glucomannan, as a natural water-soluble polymer, into an L-cysteine solution and carbonized the mixture in ammonia to prepare a microporous nitrogen-containing carbon that delivered a specific capacitance of 351.7 F g^{-1} at 1.0 A g^{-1}.[46] Inspired by the interfacial interaction design of natural nacre, Wu *et al.* reported a strategy to assemble halloysite-polyaniline-graphene oxide nanocomposite films *via* noncovalent (π-π conjugation, H-bonding, and electrostatic) interactions, which displayed a specific capacitance of 291.2 F g^{-1} at 0.5 A g^{-1}.[47] In another case, Huang *et al*. applied two-level interlocking structures between the electrode active materials and the current collector. They inspired the first interlocking structure by a gecko's feet and the second one by a tree's roots in rock cracks. They developed a

flexible micro-supercapacitor with an areal capacitance of 76.6 mF cm^{-2} at 6.25 mA cm^{-2}.[48] Peng *et al.* used Moringa oleifera leaves (heated in an oven at different temperatures from 700 to 900 °C) as the precursor to prepare highly crumpled porous carbons, and achieved a maximum specific capacitance of 260 F g^{-1} at 1.0 A g^{-1}.[49] In another study, Geng *et al*. inspired by the prey-trapping of Venus flytraps fabricated a hierarchical graphene cage that captures lignin to prevent its dissolution, while serving as a three-dimensional electron transport pathway. The designed material displayed a specific capacitance of 211 F g^{-1} at 1.0 A g^{-1}.[50] Aside from these few examples of all-carbon supercapacitors, there are a vast variety of bioinspired supercapacitor chemistries and designs with a wide range of behaviors.[51-53] Invertebrate mussels can strongly adhere to diverse surfaces with high binding strength. It has been reported that 3,4-dihydroxy-L-phenylalanine (DOPA) and lysine-enriched proteins play the major role at the plaque-substrate interface, thus are the key basis of this extraordinary adhesion to virtually all types of surfaces.[54] Hypothesizing that the co-existence of catechol (DOPA) and amine (lysine) functionalities play the central role for adhesion of the mussels to different materials, Messersmith and co-workers identified that dopamine, with a molecular structure containing both catechol and amine moieties, can mimic mussel's adhesion properties.[55-56] Since its advent as a smart coating material in 2007, and because of its outstanding features including adhesive capability, componential tunability, structural complexity, and self-healing ability, polydopamine (PDA) has widely been implemented in research and for practical uses, including batteries and supercapacitors.[57-60]

In a bioinspired approach of designing all-carbon electrode active materials for supercapacitive energy storage, herein, we deposited polydopamine onto an oxygen-functionalized carbon cloth (FCC) substrate *via* two very fast, facile, and one-pot electrodeposition methods for the first time. We utilized both constant and pulsed potential techniques and investigated the influence of the

electrosynthesis parameters on the characteristics of the PDA film. Polydopamine displays many striking properties as a pseudocapacitive material that lies in its chemical structure that contains catechol, amine, and imine functionalities. *Via* this intriguing surface functionalization approach, we fabricated a binder-free and flexible PDA-FCC electrode that exhibits a high specific capacitance of 626 F g^{-1} at a discharge specific current of 1.0 A g^{-1}. The all-solid-state flexible symmetric PDA-FCC||PDA-FCC supercapacitor displays an extended operating potential window of 1.2 V in a polyvinyl alcohol (PVA)-in-H_2SO_4 gel electrolyte, and exhibits a high specific energy of 11.7 Wh kg^{-1} and an excellent specific power of 6.4 kW kg^{-1} along with 81% capacitance retention after 10,000 charge-discharge cycles. This work provides a promising design direction toward the development of more sustainable energy storage devices.

6.3 Experimental Section

Materials

Carbon cloth (CC, AvCarb G100, thickness: 0.3 mm) was purchased from FUELCELL store, Texas, USA. The dopamine hydrochloride salt was obtained from Merck, Germany. All other analytical-grade chemicals were purchased from Sigma-Aldrich (USA) or Merck (Germany), and used without further purification.

Apparatus

The morphological and structural characterizations of the electrode active materials were carried out by field-emission scanning electron microscopy (FE-SEM, Philips). Elemental analysis of the samples was obtained using an energy dispersive X-ray spectrometer (EDS, as an attachment to an SEM instrument). The crystallographic characteristics of the FCC and PDA electrodes were recorded using a powder X-ray diffractometer (XRD, Philips X'pert diffractometer with CuK_α

radiation (λ = 1.5406 Å) generated at 40 kV and 30 mA with a step size of 0.04° s^{-1}). Raman spectra were collected using an Almega Thermo Nicolet Dispersive Raman Spectrometer. Fourier transform infrared (FT-IR) spectra were obtained from a NICOLET FT-IR 100 spectrometer using KBr pellets. Surface elemental composition and the chemical states of different elements were obtained using X-ray photoelectron spectroscopy (XPS, a Kratos Axis Ultra DLD spectrometer with a monochromatic Al K_α X-ray source (λ = 1486.6 eV)). Specific surface area, pore volume, and pore width of the nanostructures were analyzed using BET and BJH procedures by an ASAP 2020 (Micromeritics, USA) instrument.

All electrochemical experiments were performed using a BioLogic SP-300 potentiostat/galvanostat (BioLogic, France) controlled *via* EC-Lab v11.01 software. In all the three-electrode studies, we used a double junction Ag/AgCl in 3.0 M KCl reference electrode and a platinum plate counter electrode, in an aqueous 1.0 M H_2SO_4 solution electrolyte. The cycling stability tests of the PDA-FCC||PDA-FCC symmetric device were recorded using a Solartron 1470A multichannel battery test unit (Solartron Analytical, UK) equipped with Cell Test software (v. 3.5.0). Electrochemical impedance spectroscopy (EIS) measurements were carried out by sweeping the ripple frequency from 100 kHz to 10 mHz and the experimental data were fit using Z-fit in EC-Lab software.

Procedure

Carbon Cloth Functionalization: Functionalization of the pristine carbon cloth (CC) proceeded according to the methods reported previously with a slight modification.[61-64] For chemical functionalization of the carbon cloth substrate, we first cleaned the pieces (1.0 cm × 1.0 cm) by sonication in a 1:1 acetone-ethanol mixture for 30 min. Then, we dipped the pieces of CC in a concentrated HNO_3:H_2SO_4 (1:2, v/v) solution (10 mL) for 5 min. After that, $KMnO_4$ (1.0 g), as an

oxidizing agent, was immediately added into the solution and stirred at 35 °C for 1 h. Next, the solution was diluted by adding 100 mL of distilled water and kept stirring for 3 h. In the next step, H_2O_2 solution (30%), that reacts with $KMnO_4$ to produce MnO_2 and O_2, was added until the gas evolution stopped. Finally, the functionalized carbon cloth (FCC) pieces were thoroughly rinsed with distilled water, followed by drying in an oven at 60 °C for 3 h. Chemical functionalization of the carbon cloth in a mixed acid solution containing an oxidizing agent introduces oxygen-containing surface functional groups as outlined in **Scheme 6.1a,b**.

Deposition of Polydopamine onto Functionalized Carbon Cloth: The synthesis solution is a phosphate buffer solution (PBS, 0.1 M, pH 7.4) containing dopamine (2.0 mg mL^{-1}). We electrodeposited polydopamine onto the FCC *via* two different methods; constant potential (CP) and pulse potential techniques. The constant potential method involves applying a nucleation potential of 0.6 V (vs. Ag/AgCl) for a short time (20 s) followed by a growth potential of 0.5 V for 600 s. The growth time is optimized so that the deposited PDA was ~1.0 mg cm^{-2}. *Via* the pulse electrodeposition method (**Scheme 6.1c,d**), the potential of the working electrode is stepped from a rest potential to 0.6 V for 0.5 s, where the nucleation takes place. After 0.5 s rest, the potential is stepped to 0.5 V for the optimized time of 0.5 s, a potential where nucleation rate is slow, instead, the previously formed nuclei grow. This electrodeposition method allows fine control over the particle size and morphology of the electro-synthesized PDA film. The number of consecutive nucleation and growth pulses are controlled so that the electrodeposited PDA film is ~1.0 mg cm^{-2}. After electrodeposition, the obtained PDA-FCC electrode was washed with distilled water and dried at 60 °C for 3 h. Electrosynthesis of the polydopamine film that likely involves oxidation of dopamine to dopamine–quinone, its intramolecular cyclization and formation of

leucodopaminechrome, oxidation of leucodopaminechrome to dopaminechrome, formation of 5,6-dihydroxyindole and its oxidation to 5,6-indolequinone are outlined in **Scheme 6.1e**.[65]

6.4 Results and Discussion

Design Considerations

The capacitive behavior of the carbon-based materials can be divided into two subclasses: (i) electrical double layer capacitors (EDLCs), and (ii) pseudocapacitors.[66] Apart from a high specific surface area and the extensively developed porosity, where the ions are adsorbed to form an electrical double layer, surface functionalization of the carbonaceous materials, to incorporate Faradaic redox reaction sites, is an efficient approach for tailoring their energy storage performance.[67] Surface modification *via* molecular design is a promising approach to confer new functionalities into existing materials, a feature that is particularly important in the field of energy storage. On account of its similar molecular structure with DOPA and tyrosine amino acid in mussel adhesive proteins, PDA can strongly adhere to a variety of substrates.[54, 56-57] In addition, PDA exhibits a promising prospect for energy storage as a nitrogen-containing carbon matrix. The presence of catechol and amine functional groups that act as active sites for Faradaic redox reactions along with excellent biocompatibility, easy preparation, controllable thickness, self-healability,[68-69] and an outstanding wettability endow PDA with extraordinary energy storage performance. Functionalized carbon cloth (FCC) was chosen as a substrate owing to its low cost, chemical stability, high electrical conductivity, and mechanical flexibility. This new type of energy storage material is well suited for high power metal-free green energy storage applications.

Physicochemical Characterizations

We investigated the surface morphology of the pristine CC as well as the FCC and PDA-FCC electrodes using a field-emission scanning electron microscope (FE-SEM). FE-SEM image of the pristine CC is composed of interlaced carbon fibers with a smooth surface (**Figure 6.1a**). After functionalization, the interlaced structure of the carbon fibers has not been destroyed, instead, numerous grooves and wrinkles are formed on the FCC surface which impart a relatively coarse surface for better polydopamine hosting (**Figure 6.1b**). The FE-SEM images of the PDA-FCC electrode, synthesized *via* a constant potential method, show a complete and uniform PDA film electrodeposited onto FCC surface (**Figure 6.1c**). The FE-SEM image also reveals a rather uniform size distribution (~20 nm) with a granular morphology of the polydopamine film. Whereas, the PDA-FCC electrode, synthesized *via* a pulse deposition method, shows a nanowall network that is well-oriented with the c-axis, and perpendicular to the FCC substrate surface (**Figure 6.1d,e**). We analyzed the elements in FCC and PDA-FCC using energy dispersive X-ray spectroscopy (EDS). The EDS spectrum of FCC displays the peak of oxygen (besides the peak of carbon) that can be attributed to the oxygen-bearing functional groups induced *via* acidic $KMnO_4$ treatment. The spectrum of PDA-FCC shows an additional strong elemental peak for nitrogen, demonstrating that the FCC is covered entirely by polydopamine. EDS spectral mapping of the PDA-FCC sample shows a homogeneous distribution of N, C, and O elements, demonstrating the atomic-scale and uniform coverage of the polydopamine film on the substrate (**Figure 6.1f**). We also characterized the pristine as well as the modified carbon cloths using Fourier transform infrared (FT-IR) spectroscopy. The FT-IR spectrum of the FCC displays some prominent bands that were not very noticeable in the spectrum of the pristine CC (**Figure 6.2a**). A broad band at ~3400 cm^{-1} in the spectrum of FCC is attributed to the stretching vibration of the hydroxyl groups. The band at 1727 cm^{-1} is ascribed to the presence of carboxylic acid and carbonyl functional moieties on the FCC

surface. The peak at 1630 cm^{-1} is associated with the skeletal vibrations of the aromatic rings, and a broad band over 1000–1400 cm^{-1} is attributed to the C–OH and C–O stretching modes. Thus, FT-IR spectroscopy provides strong evidence for successful functionalization of the carbon cloth.[70] In the FT-IR spectrum of the pulse-deposited PDA-FCC, the bands appearing at 3200, 1500, and 1398 cm^{-1} originate from N–H stretching, N–H bending, and C–N stretching vibrations, respectively. The characteristic band of C–N at 1398 cm^{-1} along with the decrease in the intensity of the band at 3400 cm^{-1} is known as demonstrative evidence of covalent conjugation of PDA onto FCC *via* amide bond formation.[71-72]

Raman spectroscopy is often used to characterize carbon-based materials. Raman spectra of the CC, FCC, and pulse-deposited PDA-FCC samples clearly present two well-known bands, the G-band which originates from the sp^2 hybridized carbon and the D-band that arises from the disordered sp^3 hybridized carbon (**Figure 6.2b**). The intensity ratio of the D to G bands (I_D/I_G) can help to estimate structural disorder of the carbon-based materials where a higher ratio indicates more defects on the sample. The value of I_D/I_G for the FCC is higher than that of the pristine CC due to the oxygen-containing functional groups that induce more structural defects.[73] After electro-polymerization of PDA onto the FCC, the I_D/I_G value decreases which can be ascribed to the formation of covalent bonds between functional groups of the FCC and the catechol or amine moieties of PDA that partially compensates for the structural disorder.[71, 74] The slight shift of the D and G bands for the PDA-FCC sample can be ascribed to the conjugation of PDA to the functional groups of the FCC.

We conducted X-ray photoelectron spectroscopy (XPS) to provide further insights into the surface elemental composition of the FCC and PDA-FCC samples (**Figure 6.2c−e**). In addition to the characteristic peak of carbon (C 1s), the survey XPS spectrum of FCC shows the characteristic

peaks of oxygen (O 1s) as well, originating from the successful incorporation of the oxygen-bearing functionalities into the FCC. The survey XPS spectrum of the PDA-FCC clearly indicates the coexistence of carbon (C 1s), oxygen (O 1s), and nitrogen (N 1s) in the sample (the peak at ~496 eV can be attributed to adsorbed sodium ions, Na KLL auger peak). The results of the XPS study are consistent with the outputs of the Raman, XRD, and FT-IR analyses, confirming proper electrodeposition of PDA on the FCC samples. The curve-fitted core level XPS spectrum of the C 1s of FCC shows five different characteristic peaks. The peaks located at 284.8 and 285.1 eV come from the C=C and C–C bonds in the aromatic rings, and the peaks centered at 285.8, 286.9, and 288.7 eV correspond to the C–O (epoxy and alkoxy), C=O, and O–C=O groups, respectively.[63, 71, 75] The small shift observed in the curve-fit core level XPS spectrum of the C 1s of FCC after electro-polymerization of PDA onto the FCC can be ascribed to covalent conjugation of the FCC functional groups to the catechol or amine moieties of PDA. **Figure 6.2d−e** display the curve-fit core level XPS spectra of the C 1s and N 1s of the pulse-deposited PDA-FCC. The deconvoluted core-level XPS spectrum of C 1s of PDA-FCC consists of six peaks that are attributed to: aromatic carbon (C=C, 284.0 eV), aliphatic carbon (C−C, 285.0 eV), carbon-nitrogen and epoxy (C–N, C−O–C, 286.1 eV), hydroxyl (C−OH, 287.4 eV), carbonyl (C=O, 289.0 eV), and carboxyl (HO–C=O, 292.5eV) groups. The peak located at 286.1 eV, which is absent in the deconvoluted core-level C 1s spectrum of the FCC, is attributed to the C–N bond and confirms the successful polymerization of PDA onto the FCC. The C–N=C, C–NH, and C–NH_2 broad peaks appearing at the binding energies of 397.8, 399.0, and 400.0 eV in the core level N 1s spectrum correspond to the amino nitrogen atoms and heterocyclic nitrogen atoms, respectively. The presence of the primary amine is ascribed to the noncovalent self-assembly of dopamine. The presence of the secondary amine indicates the formation of the heterocyclic ring of indolic moieties in the structure

of the polydopamine heteropolymer. [60, 76-77] We also compared the chemical state and surface composition of the nitrogen-containing functional groups (including imine (−N=), pyrrolic (−NH−), and amine ($-NH_2$) functionalities) of the PDA-FCC electrodes prepared *via* pulse- and CP-deposition methods. As can be seen, the pyrrolic N moieties are quite prevalent in the pulse-deposited PDA-FCC structure, whereas the imine functionalities dominate in the structure of the CP-deposited PDA-FCC.

We also used X-ray diffraction (XRD) to investigate the effect of the chemical treatment on CC. All of the samples show two broad diffraction peaks at 2θ values of 25.5°and 43° which can be attributed to the (002) and (101) planes of the amorphous graphitic CC structure.[64] The lower intensity of the XRD bands of the FCC, compared to that of the CC, demonstrates a lower degree of graphitization of the FCC, due to the presence of some functional groups in its structure.

To investigate the surface area and pore-size distribution that significantly affects specific capacitance and the rate performances of the nanoporous materials,[78-79] N_2 adsorption-desorption measurements of FCC and PDA-FCC electrodes were conducted by Brunauer-Emmett-Teller (BET) and Barrett-Joyner-Halenda (BJH) methods, respectively. As shown in **Figure 6.2f**, according to N_2 adsorption-desorption isotherms, all the samples display type IV isotherms with H1-type hysteresis loops, which indicate the formation of mesoporous structures. Wide pore-size distribution of pulse-deposited PDA-FCC compared to FCC can be extremely beneficial to amplify the kinetics of the reactions to attain enhanced supercapacitive performances. The wide range of mesopores guarantees abundant electroactive sites for Faradaic reactions, meanwhile providing low-resistance ion transport pathways in the PDA-FCC film.[80-81] The lower surface area of PDA-FCC (8.5 $m^2\ g^{-1}$) is due to the occupation of some of the pores with electrodeposited PDA.

Electrochemical Studies in a 3E Cell Setup

We employed a three-electrode cell setup to study the supercapacitive performance of the CC, FCC, and PDA-FCC electrodes using cyclic voltammetry (CV), galvanostatic charge-discharge (GCD), and electrochemical impedance spectroscopy (EIS) measurements in a 1.0 M H_2SO_4 solution as the electrolyte. Through these studies, we optimized the PDA-FCC electrode for the best supercapacitive performance, investigated the electrochemical performance of the materials, and deconvoluted the contribution from the capacitor-like and battery-like behavior in the total charge. The morphology and thickness of the polydopamine film for supercapacitive energy storage were tailored by the applied deposition technique. Note that for energy storage applications, electrodes are typically prepared by casting the slurry, comprised of the chemically synthesized active material, a conductive additive, and a binder, onto a substrate. The conductive additives and binders, which are required to preserve a firm structure and to provide continuous electron transfer pathways, do not contribute significantly to the energy storage process, and hence, reduce capacitance/energy/power of the system. In contrast, electrodeposition of the active material onto the substrate provides a strongly adhering deposit, the thickness and morphology of which can be easily tuned by manipulating the applied potential or current.

Figure 6.3a shows the CV curves of the acidic $KMnO_4$ treated FCC electrode as well as the PDA-FCC electrodes prepared *via* a constant potential method and a pulse potential technique (denoted as CP and pulse, respectively) at a scan rate of 20 mV s^{-1}. CV curves of the pristine CC and the $KMnO_4$-free mixed acid (concentrated (1:2, v/v) HNO_3:H_2SO_4) treated FCC are presented. The negligible integrated area of the CC electrode indicates that the pristine substrate has almost no contribution to the capacitive performance of the system. The CV curve of the FCC shows a pseudo-rectangular shape from −0.2 to 1.0 V. The well-defined redox peaks in the CV curve of the FCC can be ascribed to the functional groups (–C=O, –C–OH, and –COOH) introduced onto

the FCC surface *via* an acidic $KMnO_4$ treatment. These oxygen-containing functional groups not only allow proper chemical conjugation of the polydopamine, but also the remnant functionalities induce a net pseudocapacitance to the system. Compared with the FCC electrode, the CP-deposited PDA-FCC electrode displays a CV curve with a noticeably enhanced area (almost three times as large as the area under the CV curves of the FCC electrode). The two couples of reversible and stable redox peaks in the CV curves of the PDA-FCC are assigned to the oxidation of dopamine to dopamine quinone, which undergoes an intra-molecular cyclization reaction to yield leucodopaminechrome, and subsequent oxidation of leucodopaminechrome to dopaminechrome (**Scheme 6.1e**).[74] Note that, despite the fact that polydopamine can be prepared *via* a facile electrodeposition process, the molecular mechanism behind its polymerization has long been the topic of scientific debate due to the complexity of the redox processes as well as the diversity of the reactive intermediates that are formed during dopamine polymerization.[54, 65] It has recently been proposed that both covalent and noncovalent interactions are involved in the polymerization process, and the dopamine species are held together *via* a combination of H-bonding, π-π stacking, and charge transfer interactions.[74] Thus, it is likely that a complex series of reactions take place on the PDA-FCC electrode and the mechanism presented in **Scheme 6.1e** is simply the most widely proposed mechanism.

The CP-deposited PDA-FCC electrode exhibits a significantly extended potential window that spans from −0.35 to 0.95 V (0.1 V wider that the FCC electrode) along with a predominant pseudocapacitive nature. The PDA-FCC electrode prepared *via* a pulse deposition method exhibits an even larger CV integrated area (~3 times as large as the FCC electrode) along with a much wider operating potential window that spans from −0.35 to 1.05 V (0.2 V wider that the FCC electrode). The wider operating potential window of the pulse-deposited PDA-FCC electrodes

indicates that electro-polymerization of dopamine onto the FCC stabilizes the active material, which is of paramount importance for supercapacitors. Expansion of the operating potential window of the PDA-FCC electrodes, which is a straightforward approach towards enhancing the energy storage performance of supercapacitors, can likely be explained by the hydrogen-bonding capability of the polydopamine moieties and hence the kinetic barriers along the H_2 and O_2 evolution reaction pathways. Stadler and co-workers have (experimentally and theoretically) shown that among the different intermediate oxidation products of dopamine formed during polymerization, just keto-indoleamine hydrogen bonds possess a low hydrogen binding energy (ΔG_H^*) whereas the other intermediate oxidation products are so far from the summit of the so-called Volcano plot.[82] The better energy storage performance of the pulse-deposited PDA film demonstrates that size and morphology play a vital role in defining the energy storage performance of the materials. The obtained values of the areal capacitances (at a scan rate of 20 mV s^{-1}) are 165.0, 470.8, and 535.7 mF cm^{-2} for the FCC, PDA-FCC CP, and PDA-FCC-Pulse, respectively (please see the Supporting Information for the calculation formulas). The enhanced supercapacitive performance of the pulse-deposited PDA-FCC electrode can be ascribed to the high surface area, better wettability of the aqueous electrolyte to the polydopamine film, and higher conductivity of the PDA-FCC electrodes (discussed later on) compared with the FCC.

Typical CV curves of the PDA-FCC electrode at different scan rates ranging from 1 to 200 mV s^{-1} for the CP-deposited and 1 to 300 mV s^{-1} for the pulse-deposited PDA-FCC electrodes are illustrated, respectively. As can be seen, the CV curves of the PDA-FCC electrode imply excellent capacitive behavior with almost-vertical current switches at potential extremes. This demonstrates a fast charge transport within the PDA-FCC, thanks to the efficient electronic coupling between the polydopamine film and the FCC substrate. Even at a high scan rate of 300 mV s^{-1}, the pulse-

deposited PDA-FCC electrode exhibits a couple of broad redox peaks superimposed on a rectangular profile, demonstrating the excellent reversibility of the Faradaic processes and improved pseudocapacitive performance of the PDA-FCC electrode.

We further conducted GCD measurements at various specific currents ranging from 1.0 to 120.0 A g^{-1}, in an extended potential window (1.3 V), to evaluate the capacitive performance of the pulse-deposited PDA-FCC electrode (**Figure 6.3b,c**). GCD profiles of the CP deposited PDA-FCC electrode are presented. GCD profiles display a very low iR drop at the initial stage of the discharge step across all current regimes (**Figure 6.3b**, inset). GCD profiles also display an intermediate region (from 0.3 to 0.6 V) with a mild slope that is assigned to the reversible Faradaic charge-discharge processes taking place on the PDA-FCC electrode (that is in accordance with the CV curves). The CP deposited PDA-FCC electrode exhibits a high specific capacitance of 546 F g^{-1} at a discharge rate of 1.0 A g^{-1} (277 F g^{-1} at 1.0 A g^{-1} based on the total mass of the electrode, i.e. PDA plus FCC) and retains capacitance of 140 F g^{-1} at a high discharge rate of 100.0 A g^{-1} (**Figure 6.3d**). However, the pulse-deposited PDA-FCC electrode displays an excellent capacitance of 626 F g^{-1} at a discharge rate of 1.0 A g^{-1} (367 F g^{-1} at 1.0 A g^{-1} based on the total mass of the electrode) and retains capacitances of 170 and 134 F g^{-1} at high discharge rates of 100.0 and 120.0 A g^{-1}, respectively. This demonstrates outstanding supercapacitive performance and excellent high-rate capability of the PDA-FCC electrodes, especially the pulse-deposited one (**Figure 6.3d**). The high-rate capability and low *iR* drops at all discharge rates can be attributed to the efficient interaction of PDA with the FCC. This sustainable behavior in a wide current range originates from the cumulative energy storage performance of the PDA and FCC in the PDA-FCC electrode that benefits from the improved wettability and increased conductivity of the porous PDA-FCC, in which the surface of the electrode active material is easily accessible to the

electrolyte ions. The low cost, ease of synthesis, and excellent pseudocapacitive performance of the resulting PDA-FCC electrode is superior to most of the previously reported metal-free supercapacitive materials and comparable to the other pseudocapacitive materials reported in the literature.

We conducted EIS studies to obtain further insight into the electrochemical kinetics of the PDA-FCC electrode, which confirmed the trend of CV and GCD studies. **Figure 6.3e** displays the Nyquist plots of the PDA-FCC electrode (over the frequency range from 100 kHz to 10 mHz) at five different potentials as well as the open circuit potential (OCP). A representative voltammogram of the PDA-FCC electrode with the assigned potentials is presented. An expanded view of the high-frequency region is presented as an inset to **Figure 6.3e**, and the equivalent circuit fit to the experimental data is displayed. The extracted parameters corresponding to the equivalent circuit model are presented. The Z_{re}-intercepts of the Nyquist plots after extrapolation of the trend in the high frequencies (which represents the equivalent series resistance, ESR), show very low values with only a slight variation at different electrode potentials (ESR values are in the range from 0.85–0.91 Ω). The low ESR values, which comprise the ionic resistance of the electrolyte and the electronic resistance of the electrode, clearly suggest a high conductivity for the PDA-FCC electrode. Two depressed overlapping semicircles at high and middle-frequency domains, and a near-vertical line at the low-frequency region, can also be seen in the Nyquist plot of the PDA-FCC electrode. The diameter of the high-frequency semicircle (R1) is potential-dependent and slightly decreases upon increasing the applied potential; thus, the value of R1 is attributed to charge transfer resistance.[83-84] The diameter of the semicircle in the middle-frequency region is potential-independent, and thus can be ascribed to the diffusion resistance of the electrolyte within the voids in between the fiber bundles of the FCC.[85-89] The amounts of the Warburg impedance of the PDA-

FCC electrode at the pre-peak (0.4 V), peak (0.5 V) and post-peak (0.6 V) potentials are 0.12, 0.79 and 0.15 Ω $s^{-1/2}$, respectively. The significantly higher value of the Warburg impedance at peak potential clearly indicates a large contribution from diffusion-controlled redox processes in energy storage performance of the PDA-FCC at the peak potential compared to the other applied potentials. As can be seen in the Bode phase plot, the phase angle of the PDA-FCC electrode at low frequencies is −75.4°, which is far from the −90° for ideal capacitors. In addition, a slope of ~−0.78 in the low-frequency region of the Bode magnitude plot shows a significant deviation from the −1.0 expected for ideal capacitors. These characteristics imply a combination of capacitive and battery-like behavior of the electrode active material, although the capacitive behavior dominates the mechanism. The RC time constant was calculated as 0.69 s from the Bode phase plot at a phase angle of about −45° (exactly −44.89°) indicating an enhanced ion transport rate in the PDA-FCC electrode.

Based on the power law dependence of the current (i) on the sweep rate (ν) using the equation $i = a\nu^b$, which enables fast determination of the electrode kinetics, a *b*-value of 0.72 was obtained, demonstrating a behavior in the transition area from a battery-like (b = 0.5) to a supercapacitor-like (b = 1.0) response.[66,90] A critical issue in the study of energy storage materials is the deconvolution of the contribution from capacitive and battery-like processes in the total charge of the electrical energy storage system. **Figure 6.3f** shows that the potential profile for the capacitive current (the shaded region) accounts for 73% of the total charge at a sweep rate of 3 mV s^{-1}, demonstrating the fast kinetics and high-rate capability of the system.

Fabrication of a Symmetric PDA-FCC||PDA-FCC Device

To assess the suitability of the PDA-FCC electrode as a promising active material for energy storage applications, we fabricated a solid-state symmetric PDA-FCC||PDA-FCC device by PDA-

FCC as both the negative and positive electrode. We also fabricated a symmetric FCC||FCC device to form a basis for comparison of our newly developed device. We used a polyvinyl alcohol (PVA)-in-H_2SO_4 (1.0 M) gel electrolyte and stainless steel (SS) grid current collector in both devices. **Figure 6.4a** displays CV curves of the FCC||FCC device, as well as the two PDA-FCC||PDA-FCC devices, the active materials of which are prepared *via* constant potential and pulse deposition techniques, at a scan rate of 50 mV s^{-1}. As can be seen, the FCC||FCC device shows a tilted CV profile with a significant distortion from a rectangular shape at the starting and switching voltages, whereas, the PDA-FCC||PDA-FCC supercapacitors display voltammograms with almost-vertical current switches at voltage extremes. However, the pulse-deposited PDA-FCC||PDA-FCC supercapacitor exhibits a significantly higher enclosed area and a wider voltage window than the CP-deposited PDA-FCC||PDA-FCC and FCC||FCC supercapacitors, demonstrating its superior energy storage performance. The obtained values of areal capacitance at a scan rate of 50 mV s^{-1} are 129.3, 74.8, and 43.4 mF cm^{-2} for the pulse-deposited PDA-FCC||PDA-FCC, CP-deposited PDA-FCC||PDA-FCC and FCC||FCC devices, respectively (**Figure 6.4a**). The enhanced pseudocapacitive performance of the PDA-FCC||PDA-FCC devices can be attributed to the rich redox functional groups of the polydopamine and the improved wettability as well as the enhanced conductivity of the PDA-FCC electrode material.

Figure 6.4b displays CV curves of the symmetric pulse-deposited PDA-FCC||PDA-FCC device at different voltage ranges from 0.9 to 1.25 V in a PVA-in-H_2SO_4 (1.0 M) gel electrolyte. The device can endure a voltage window of 1.3 V based on the CV curve of the PDA-FCC electrode in a three-electrode cell setup (in a 1.0 M H_2SO_4 electrolyte). However, to sustain a long-term stability for the all-solid-state symmetric device, we slightly shrunk the operating voltage window to suppress potential cycling-induced structural pulverization or

overoxidation/overreduction of the polydopamine film and recorded CV curves of the device in the voltages range of 1.2 V.

Figure 6.4c shows CV curves of the pulse-deposited PDA-FCC||PDA-FCC device at different scan rates from 5 to 600 mV s^{-1}, and those of the CP-deposited PDA-FCC||PDA-FCC device (in the range from 5 to 400 mV s^{-1}) and FCC||FCC device (in the range from 10 to 400 mV s^{-1}) are presented, respectively. As can be seen, the CV curves of the pulse-deposited PDA-FCC||PDA-FCC supercapacitors retain their pseudo-rectangular shape even at a high scan rate of 600 mV s^{-1}; whereas the CV curves of the FCC||FCC supercapacitor significantly deviates from a rectangular shape and becomes very resistive when the scan rate exceeds 300 mV s^{-1}. This simplifies a better rate capability and a faster charge-discharge kinetics for the PDA-FCC||PDA-FCC device.

GCD profiles of the pulse-deposited PDA-FCC||PDA-FCC device at various specific current values from 1.0 to 18.0 A g^{-1}, areal current densities from 2.0 to 20.0 mA cm^{-2}, and volumetric current densities from 5.0 to 60.0 mA cm^{-3} are provided in **Figure 6.4d−f**, respectively. A negligible *iR* drop at the start of all discharge profiles indicates a fast charge and ion transport in the device. GCD profiles of the CP-deposited PDA-FCC||PDA-FCC device are presented.

Figure 6.4g−i shows rate capability studies of the CP- and pulse-deposited PDA-FCC||PDA-FCC devices. As depicted in **Figure 6.4**, the pulse deposited PDA-FCC||PDA-FCC device displays an excellent specific capacitance of 61 F g^{-1} at 1.0 A g^{-1} (24 F g^{-1} at 0.5 A g^{-1} based on the total mass of the electrode, **Figure 6.4g**), areal capacitance of 195 mF cm^{-2} at 1.6 mA cm^{-2} (**Figure 6.4h**), and volumetric capacitance of 325 mF cm^{-3} at 5.3 mA cm^{-3} (**Figure 6.4i**) and retains specific capacitance of 24 F g^{-1} at 18.0 A g^{-1}, areal capacitance of 77 mF cm^{-2} at 28.8 mA cm^{-2}, and volumetric capacitance of 128 mF cm^{-3} at 96.0 mA cm^{-3} (40 % capacitance retention),

further revealing the excellent rate capability of the pulse-deposited PDA-FCC||PDA-FCC device in comparison with other polymer-based symmetric devices.

The long-term cycling stability of a device is an essential requirement to meet practical applicability. We investigated the cycling stability of a pulse-deposited PDA-FCC||PDA-FCC device by recording 10,000 GCD cycles at different specific currents from 5.0 to 18.0 and then back to 5 A g^{-1} (1,000 cycles at each rate). The device lost almost 10% of its initial capacitance over the first 1,000 cycles at a specific current of 5.0 A g^{-1} and the capacitance decreased very slowly thereafter so that the device retained about 80% of the initial specific capacitance after 10,000 cycles at different rates (**Figure 6.5a**), implying good durability and electrochemical performance for the symmetric PDA-FCC||PDA-FCC device. The improved cycling stability demonstrates strong interactions between catechol and amine moieties of the PDA with oxygen-containing functional groups of the FCC. Note that by extending the operating voltage window of the symmetric PDA-FCC||PDA-FCC device to 1.3 V, the device retains 65% of the initial capacitance after 10,000 cycles (via the same steps displayed in **Figure 6.5a**). Chemical degradation, which is mainly the consequence of over-oxidation or over-reduction of the electrode active materials, is a possible degradation pathway for the PDA-FCC during the long-term GCD cycling. The CP and pulse-deposited PDA-FCC||PDA-FCC devices retain 74% and 75% of their initial capacitance by recording 10,000 consecutive GCD cycles at a specific current of 5.0 A g^{-1}.

Mechanical deformation of the as-fabricated device was evaluated under various bending states. As shown in **Figure 6.5b**, the CV curves of the device display a negligible change at different bending angles (from 30° to 120° corresponding to radii of curvature from 4.7 to 2.5 mm, respectively), indicating the robustness and mechanical flexibility of the device. The satisfactory

performance under mechanical bending is due to the strong immobilization of polydopamine on the flexible FCC substrate.

For conductivity measurements, we plotted the I-E graph for the FCC and PDA-FCC in the solid state that shows conductance values of 12.3 and 22.6 mS for the FCC and PDA-FCC, respectively (**Figure 6.5c**). The enhanced conductivity of the PDA-FCC electrode can be attributed to the diminution of the HOMO-LUMO gap from 4.14 eV to 3.18 eV after the polymerization of dopamine molecules into polydopamine.[91]

Specific energy and specific power of the prepared PDA-FCC||PDA-FCC device, as two of the fundamental parameters for the characterization of energy storage devices, are presented in a Ragone plot (**Figure 6.5d**). The device provides a specific energy of up to 11.7 Wh kg^{-1} at a specific power of 385.3 W kg^{-1} and a volumetric energy density of up to 38.1 mW h L^{-1} at a volumetric power density of 2,131.0 mW L^{-1} and can still maintain a specific energy of 4.7 Wh kg^{-1} at a high specific power of 6,400.0 W kg^{-1} and a volumetric energy density of 28.9 mWh L^{-1} at a volumetric power density of 22,000.0 mW L^{-1}. These values reveal the excellent energy/power performance of the as-fabricated PDA-FCC||PDA-FCC device, which are higher than or comparable to those of the previously reported metal-free symmetric devices.[26, 60, 92]

In order to evaluate the potential of the symmetric PDA-FCC||PDA-FCC device for practical applications in real energy-storage systems, we connected two as-fabricated devices in series and fully charged the assembly at 2.2 V. The assembled devices light a red LED (1.8 V, 20 mA) for more than 6 min and can turn on a mini-motor (1.0 V, 30 mW) for several seconds. The excellent practical applicability of the symmetric PDA-FCC||PDA-FCC device suggests its potential, as a flexible solid-state metal-free supercapacitor, for state-of-the-art applications.

According to the EIS measurements of the symmetric PDA-FCC||PDA-FCC device at an open-circuit voltage over the frequency range from 100 kHz to 10 mHz, a Nyquist plot of the device consists of a semicircle at high frequency followed by a near-vertical line at low frequency, with an ESR of 2.1 Ω and a small R_{ct} of 0.7 Ω, indicating the good conductivity and fast reaction kinetics of the electrode materials.

6.5 Conclusions

In summary, we have employed two novel, facile, and convenient one-pot electro-synthetic procedures (constant potential and pulsed potential deposition techniques) for the electro-deposition of polydopamine on a flexible functionalized carbon cloth (FCC) substrate to prepare a pseudocapacitive electrode material that does not need any post-preparation process. Excellent pseudocapacitive behavior of the pulse-deposited PDA-FCC electrode along with its wide operating potential window can be ascribed to the effective conjugation between catechol and amine moieties of PDA and the oxygen-bearing functional groups of the FCC. Promising and desirable electrochemical characteristics of the PDA-FCC electrode that outperform most polymer-based active materials reveal the suitability of our designed electrode for more sustainable development. The symmetric solid-state PDA-FCC||PDA-FCC device (prepared *via* the pulse deposition approach) delivers a high specific energy of 11.7 Wh kg^{-1}, an excellent specific power of 6.4 kW kg^{-1}, along with outstanding cycling stability over 10,000 consecutive GCD cycles, and excellent flexibility, demonstrating that our device design is a promising approach for the development of high-performance metal-free green supercapacitors.

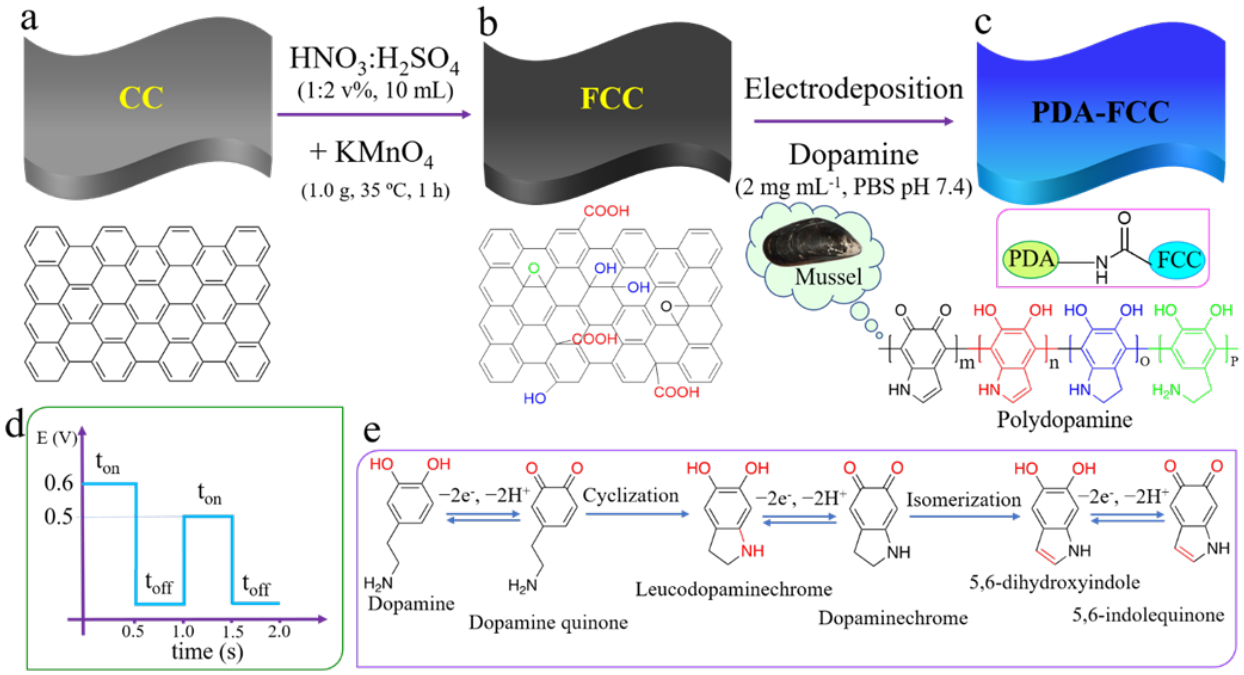

Scheme 6.1. Schematic illustration of the fabrication process of the PDA-FCC electrode. (a) pristine carbon cloth. (b) Preparation of the functionalized carbon cloth *via* a chemical treatment process using a $KMnO_4$ incorporated mixed HNO_3:H_2SO_4 (1:2, v/v) acidic solution. (c) Electrodeposition of the Mussel-inspired polydopamine film onto the functionalized carbon cloth (FCC) substrate. Covalent conjugation of PDA onto the FCC *via* amide bond formation, as one of the possible conjugation mechanisms, as well as the possible structure of the Mussel-inspired polydopamine film are also presented. (d) A typical pulsed potential waveform for the electrodeposition of dopamine onto functionalized carbon cloth substrate. (e) The possible electrochemical oxidation mechanism of dopamine and formation of the polydopamine film via the formation of dopamine quinone, leucodopaminechrome, dopaminechrome, 5,6-dihydroxyindole, and 5,6-indolequinone intermediates.[2]

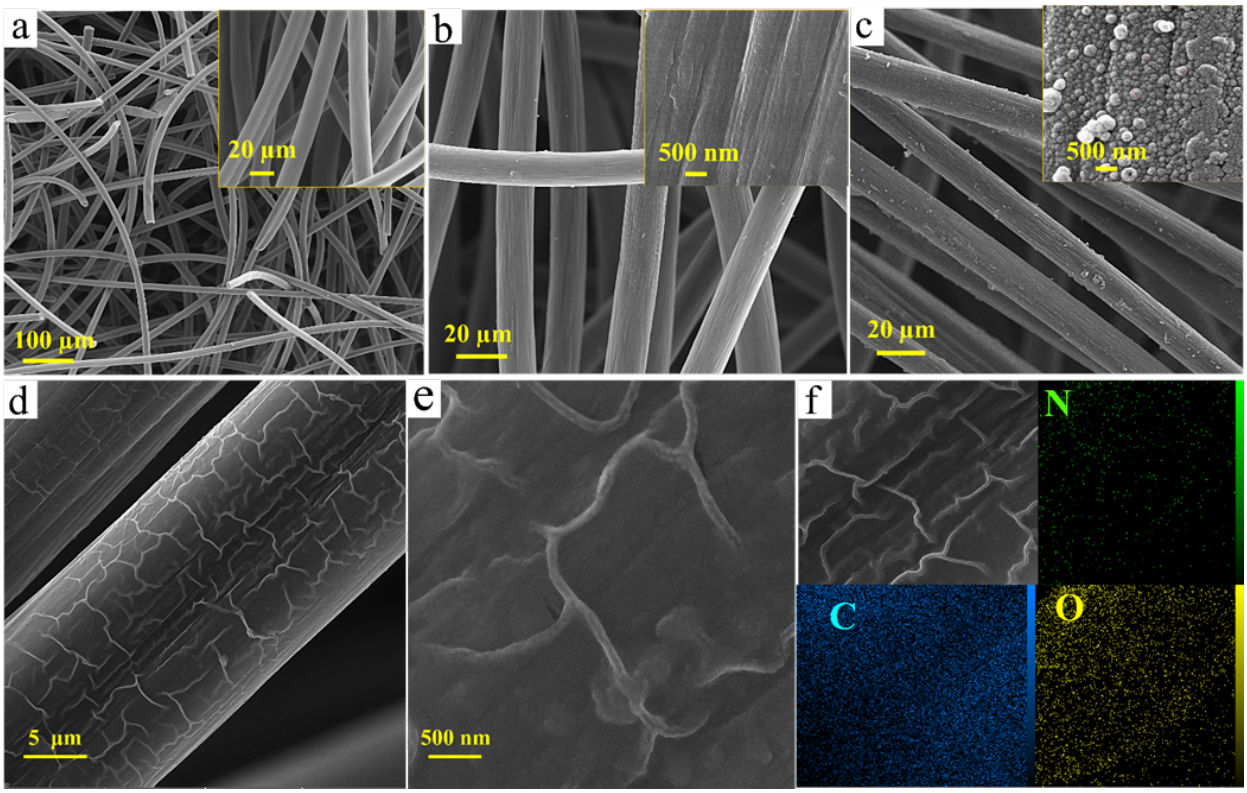

Figure 6.1. Morphological characterizations of the CC, FCC, and PDA-FCC. FE-SEM images of the (a) carbon cloth (CC), (b) functionalized carbon cloth (FCC), (c) constant potential deposited PDA-FCC, and (d, e) pulse deposited PDA-FCC electrodes. The insets show the images with a higher magnification. (f) Energy dispersive X-ray (EDS) elemental mapping of nitrogen, carbon, and oxygen of the PDA-FCC sample.

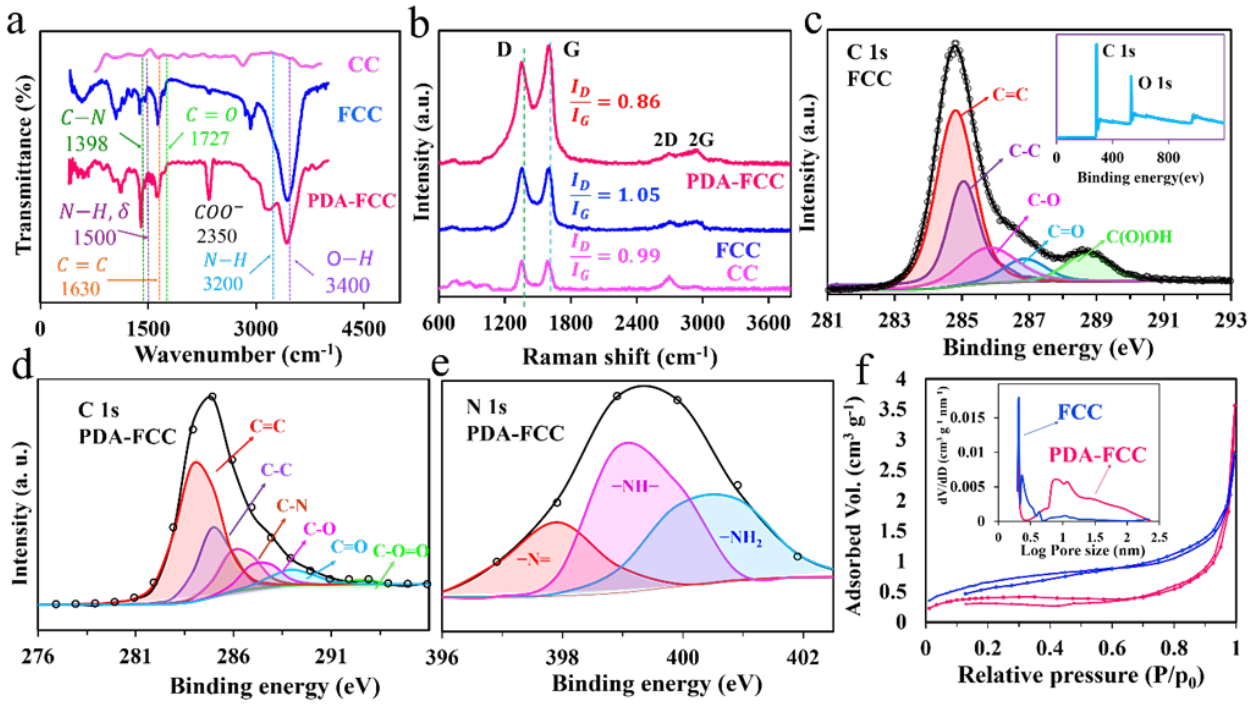

Figure 6.2. Structural characterizations of the CC, FCC, and pulse-deposited PDA-FCC. (a) FT-IR spectra, and (b) Raman spectra of the CC, FCC, and PDA-FCC electrodes. (c) Deconvoluted core level XPS spectrum of the FCC, C 1s. The inset shows the survey XPS spectrum of the FCC sample. Deconvoluted core level XPS spectra of the PDA-FCC electrode; (d) C 1s, and (e) N 1s. (f) Nitrogen adsorption-desorption isotherms of FCC (blue) and PDA-FCC (red) electrodes. The inset shows BJH pore size distributions of the FCC and PDA-FCC samples.

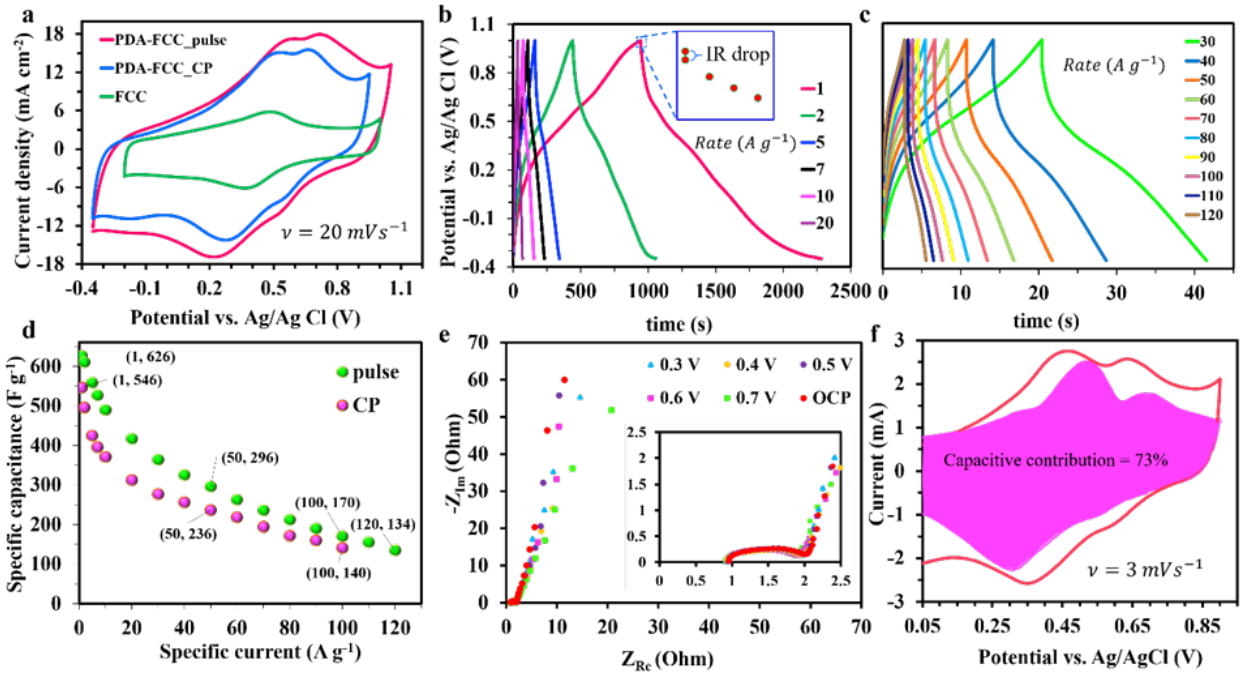

Figure 6.3. Investigation of the electrochemical performances of the prepared electrodes in a three-electrode cell setup. (a) CV curves of the FCC as well as the constant potential and pulse deposited PDA-FCC electrodes at a scan rate of 20 mV s^{-1} in an aqueous 1.0 M H_2SO_4 electrolyte. (b, c) GCD profiles of the pulse deposited PDA-FCC electrode at different specific currents ranging from 1 to 120 A g^{-1}. The inset of panel b shows the magnified view of the initial stage of the discharge step, IR drop. (d) Rate capability study; specific capacitances of the constant potential and pulse deposited PDA-FCC electrodes at different specific current values. (e) A series of Nyquist plots measured at various potentials of the CV curve (0.3, 0.4, 0.5, 0.6, 0.7 V and open circuit potential (OCP) over a frequency range from 100 kHz to 10 mHz. The inset shows a magnified high-frequency region. (f) Decoupling the contribution of capacitive and battery-like charge storage processes for a PDA-FCC electrode at a scan rate of 3.0 mV s^{-1}.

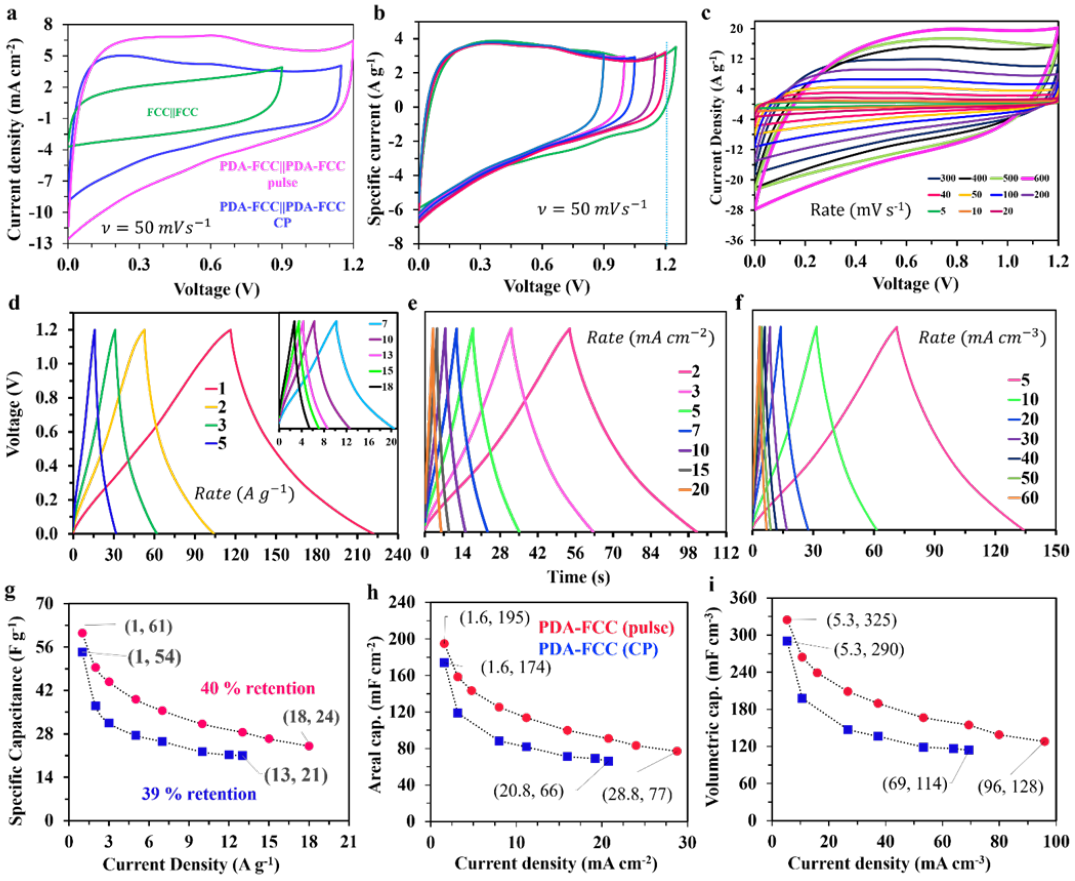

Figure 6.4. Electrochemical studies of the symmetric PDA-FCC||PDA-FCC and FCC||FCC devices in a PVA-in-H_2SO_4 gel electrolyte. (a) CV curves of the FCC||FCC device as well as the PDA-FCC||PDA-FCC devices, the materials of which were prepared *via* either a constant potential or a pulsed waveform ($\nu = 50$ mV s^{-1}). (b) CV curves of the pulse deposited PDA-FCC||PDA-FCC device at different voltage windows ($\nu = 50$ mV s^{-1}). (c) CV curves of the pulse deposited PDA-FCC||PDA-FCC device at various scan rates from 5 to 600 mV s^{-1}. (d-f) GCD profiles of the pulse-deposited PDA-FCC||PDA-FCC device at different specific current values from 1.0–18.0 A g^{-1} (d), areal current densities from 2.0 to 20.0 mA cm^{-2} (e), and volumetric current densities from 5 to 60 mA cm^{-3} (f). (g-i) Rate capability studies of the constant potential (blue squares) and pulse-deposited (red circles) PDA-FCC||PDA-FCC devices at different specific currents (g), areal current densities (h), and volumetric current densities (i).

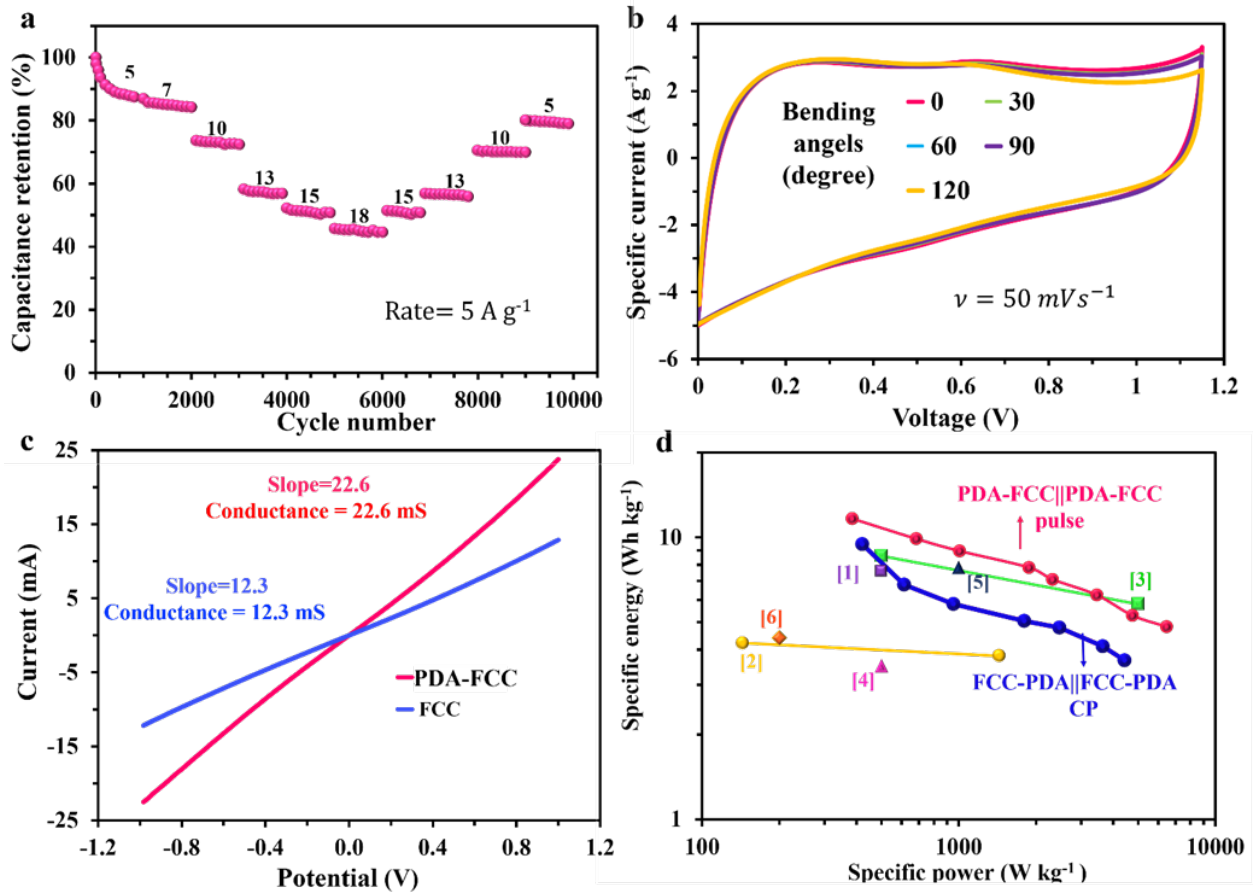

Figure 6.5. Evaluation of cycling stability, and flexibility of the PDA-FCC||PDA-FCC device along with a Ragone plot. (a) Cycle life performance of the PDA-FCC||PDA-FCC device at different specific current values from 5.0 to 18.0 A g^{-1} in a PVA-in-H_2SO_4 gel electrolyte. (b) CV curves (υ = 50 mV s^{-1}) of the PDA-FCC||PDA-FCC device (1.0 cm × 1.0 cm) at different bending angles from 0° to 120°. The bending radii of curvature at bending angles of 30, 60, 90, and 120º are 4.7, 4.3, 3.5, and 2.5 mm, respectively. (c) Solid state conductivity studies of the materials. I–V plots of the FCC and PDA-FCC electrodes in an electrolyte-free medium. (d) Ragone plot of PDA-FCC||PDA-FCC device and its comparison with some reported similar devices. [1] C-PDA/PMA,[67] [2] rGO/CNTNH2/PDA,[92] [3] PpPD/graphene,[93] [4] C-PDA,[60] [5] SPAN-FC[94] and [6] CFC/PEDOT[26].

6.6 References

(1) Liu, W.-J.; Jiang, H.; Yu, H.-Q. Emerging applications of biochar-based materials for energy storage and conversion. *Energy Environ. Sci.* **2019**, *12*, 1751−1779.

(2) Liu, T.; Zhang, L.; Cheng, B.; Yu, J. Hollow carbon spheres and their hybrid nanomaterials in electrochemical energy storage. *Adv. Energy Mater.* **2019**, *9*, 1803900.

(3) Jin, H.; Li, J.; Yuan, Y.; Wang, J.; Lu, J.; Wang, S., Recent Progress in Biomass-Derived Electrode Materials for High Volumetric Performance Supercapacitors. *Adv. Energy Mater.* **2018**, *8*, 1801007.

(4) Broto, V. C.; Kirshner, J. Energy access is needed to maintain health during pandemics. *Nat. Energy* **2020**, *5*, 419−421.

(5) Hollas, A.; Wei, X.; Murugesan, V.; Nie, Z.; Li, B.; Reed, D.; Liu, J.; Sprenkle, V.; Wang, W. A biomimetic high-capacity phenazine-based anolyte for aqueous organic redox flow batteries. *Nat. Energy* **2018**, *3*, 508−514.

(6) L Wang, L. J.; El-Kady, M. F.; Dubin, S.; Hwang, J. Y.; Shao, Y.; Marsh, K.; McVerry, B.; Kowal, M. D.; Mousavi, M. F.; Kaner, R. B. Flash Converted Graphene for Ultra-High Power Supercapacitors. *Adv. Energy Mater.* **2015**, *5*, 1500786.

(7) Shao, H.; Wu, Y.-C.; Lin, Z.; Taberna, P.-L.; Simon, P. Nanoporous carbon for electrochemical capacitive energy storage. *Chem. Soc. Rev.* **2020**, *49*, 3005−3039.

(8) Lukatskaya, M. R.; Kota, S.; Lin, Z.; Zhao, M.-Q.; Shpigel, N.; Levi, M. D.; Halim, J.; Taberna, P.-L.; Barsoum, M. W.; Simon, P. Ultra-high-rate pseudocapacitive energy storage in two-dimensional transition metal carbides. *Nat. Energy* **2017**, *2*, 17105.

(9) Shao, Y.; El-Kady, M. F.; Wang, L. J.; Zhang, Q.; Li, Y.; Wang, H.; Mousavi, M. F.; Kaner, R. B. Graphene-based materials for flexible supercapacitors. *Chem. Soc. Rev.* **2015**, *44*, 3639−3665.

(10) Ghidiu, M.; Lukatskaya, M. R.; Zhao, M.-Q.; Gogotsi, Y.; Barsoum, M. W. Conductive two-dimensional titanium carbide 'clay' with high volumetric capacitance. *Nature* **2014**, *516*, 78−81.

(11) Ji, H.; Zhao, X.; Qiao, Z.; Jung, J.; Zhu, Y.; Lu, Y.; Zhang, L. L.; MacDonald, A. H.; Ruoff, R. S. Capacitance of carbon-based electrical double-layer capacitors. *Nat. Commun.* **2014**, *5*, 1−7.

(12) El-Kady, M. F.; Strong, V.; Dubin, S.; Kaner, R. B. Laser scribing of high-performance and flexible graphene-based electrochemical capacitors. *Science* **2012**, *335*, 1326−1330.

(13) Hou, R.; Liu, B.; Sun, Y.; Liu, L.; Meng, J.; Levi, M. D.; Ji, H.; Yan, X. Recent advances in dual-carbon based electrochemical energy storage devices. *Nano Energy* **2020**, *72*, 104728.

(14) Wang, C.; Strauss, V.; Kaner, R. B. Carbon nanodots for capacitor electrodes. *Trends Chem.* **2019**, *1*, 858−868.

(15) Rahmanifar, M. S.; Hemmati, M.; Noori, A.; El-Kady, M. F.; Mousavi, M. F.; Kaner, R. B. Asymmetric supercapacitors: An alternative to activated carbon negative electrodes based on earth abundant elements. *Mater. Today Energy* **2019**, *12*, 26−36.

(16) Yun, Q.; Li, L.; Hu, Z.; Lu, Q.; Chen, B.; Zhang, H. Layered Transition Metal Dichalcogenide-Based Nanomaterials for Electrochemical Energy Storage. *Adv. Mater.* **2020**, *32*, 1903826.

(17) Pendashteh, A.; Rahmanifar, M. S.; Kaner, R. B.; Mousavi, M. F. Facile synthesis of nanostructured $CuCo_2O_4$ as a novel electrode material for high-rate supercapacitors. *Chem. Commun.* **2014**, *50*, 1972−1975.

(18) Lin, L.; Lei, W.; Zhang, S.; Liu, Y.; Wallace, G. G.; Chen, J. Two-dimensional transition metal dichalcogenides in supercapacitors and secondary batteries. *Energy Storage Mater.* **2019**, *19*, 408−423.

(19) Ma, J.; Guo, X.; Yan, Y.; Xue, H.; Pang, H. FeOx-Based Materials for Electrochemical Energy Storage. *Adv. Sci.* **2018**, *5*, 1700986.

(20) Pendashteh, A.; Mousavi, M. F.; Rahmanifar, M. S. Fabrication of anchored copper oxide nanoparticles on graphene oxide nanosheets via an electrostatic coprecipitation and its application as supercapacitor. *Electrochim. Acta* **2013**, *88*, 347−357.

(21) Geng, P.; Zheng, S.; Tang, H.; Zhu, R.; Zhang, L.; Cao, S.; Xue, H.; Pang, H. Transition metal sulfides based on graphene for electrochemical energy storage. *Adv. Energy Mater.* **2018**, *8*, 1703259.

(22) Hashemi, M.; Rahmanifar, M. S.; El-Kady, M. F.; Noori, A.; Mousavi, M. F.; Kaner, R. B. The use of an electrocatalytic redox electrolyte for pushing the energy density boundary of a flexible polyaniline electrode to a new limit. *Nano Energy* **2018**, *44*, 489−498.

(23) Zhao, C.; Jia, X.; Shu, K.; Yu, C.; Wallace, G. G.; Wang, C. Conducting polymer composites for unconventional solid-state supercapacitors. *J. Mater. Chem. A* **2020**, *8*, 4677−4699.

(24) Wang, Z.; Zhu, M.; Pei, Z.; Xue, Q.; Li, H.; Huang, Y.; Zhi, C. Polymers for supercapacitors: Boosting the development of the flexible and wearable energy storage. *Mater. Sci. Eng., R* **2020**, *139*, 100520.

(25) Mousavi, M. F.; Hashemi, M.; Rahmanifar, M. S.; Noori, A. Synergistic effect between redox additive electrolyte and PANI-rGO nanocomposite electrode for high energy and high power supercapacitor. *Electrochim. Acta* **2017**, *228*, 290−298.

(26) Rajesh, M.; Raj, C. J.; Manikandan, R.; Kim, B. C.; Park, S. Y.; Yu, K. H. A high performance PEDOT/PEDOT symmetric supercapacitor by facile in-situ hydrothermal polymerization of PEDOT nanostructures on flexible carbon fibre cloth electrodes. *Today Energy* **2017**, *6*, 96−104.

(27) Li, Z.; Ma, G.; Ge, R.; Qin, F.; Dong, X.; Meng, W.; Liu, T.; Tong, J.; Jiang, F.; Zhou, Y. Free-standing conducting polymer films for high-performance energy devices. *Angew. Chem. Int. Ed.* **2016**, *55*, 979−982.

(28) Ghenaatian, H.; Mousavi, M.; Rahmanifar, M. High performance battery–supercapacitor hybrid energy storage system based on self-doped polyaniline nanofibers. *Synth. Met.* **2011**, *161*, 2017−2023.

(29) Boota, M.; Anasori, B.; Voigt, C.; Zhao, M. Q.; Barsoum, M. W.; Gogotsi, Y. Pseudocapacitive electrodes produced by oxidant-free polymerization of pyrrole between the layers of 2D titanium carbide (MXene). *Adv. Mater.* **2016**, *28*, 1517−1522.

(30) Hou, C. C.; Xu, Q. Metal–organic frameworks for energy. *Adv. Energy Mater.* **2019**, *9*, 1801307.

(31) Rahmanifar, M. S.; Hesari, H.; Noori, A.; Masoomi, M. Y.; Morsali, A.; Mousavi, M. F. A dual Ni/Co-MOF-reduced graphene oxide nanocomposite as a high performance supercapacitor electrode material. *Electrochim. Acta* **2018**, *275*, 76−86.

(32) Bi, S.; Banda, H.; Chen, M.; Niu, L.; Chen, M.; Wu, T.; Wang, J.; Wang, R.; Feng, J.; Chen, T. Molecular understanding of charge storage and charging dynamics in supercapacitors with MOF electrodes and ionic liquid electrolytes. *Nat. Mater.* **2020**, *19*, 552−558.

(33) Sheberla, D.; Bachman, J. C.; Elias, J. S.; Sun, C.-J.; Shao-Horn, Y.; Dincă, M. Conductive MOF electrodes for stable supercapacitors with high areal capacitance. *Nat. Mater.* **2017**, *16*, 220.

(34) Shabangoli, Y.; El-Kady, M. F.; Nazari, M.; Dadashpour, E.; Noori, A.; Rahmanifar, M. S.; Lv, X.; Zhang, C.; Kaner, R. B.; Mousavi, M. F. Exploration of Advanced Electrode Materials for Approaching High-Performance Nickel-Based Superbatteries. *Small*, **2020**, *16*, 2001340.

(35) Yan, A.-L.; Wang, X.-C.; Cheng, J.-P. Research progress of NiMn layered double hydroxides for supercapacitors: a review. *Nanomaterials* **2018**, *8*, 747.

(36) Nam, H. J.; Park, E. B.; Jung, D.-Y. Bioinspired polydopamine-layered double hydroxide nanocomposites: controlled synthesis and multifunctional performance. *RSC Adv.* **2016**, *6*, 24952−24958.

(37) Shabangoli, Y.; Rahmanifar, M. S.; El-Kady, M. F.; Noori, A.; Mousavi, M. F.; Kaner, R. B. An integrated electrochemical device based on earth-abundant metals for both energy storage and conversion. *Energy Storage Mater.* **2018**, *11*, 282−293.

(38) Lin, Z.; Shao, H.; Xu, K.; Taberna, P.-L.; Simon, P. MXenes as High-Rate Electrodes for Energy Storage. *Trends Chem.* **2020**, *2*, 654−664.

(39) Pang, J.; Mendes, R. G.; Bachmatiuk, A.; Zhao, L.; Ta, H. Q.; Gemming, T.; Liu, H.; Liu, Z.; Rummeli, M. H. Applications of 2D MXenes in energy conversion and storage systems. *Chem. Soc. Rev.* **2019**, *48*, 72−133.

(40) Yang, J.; Bao, W.; Jaumaux, P.; Zhang, S.; Wang, C.; Wang, G. MXene-Based Composites: Synthesis and Applications in Rechargeable Batteries and Supercapacitors. *Adv. Mater. Interfaces* **2019**, *6*, 1802004.

(41) Shabangoli, Y.; Rahmanifar, M. S.; Noori, A.; El-Kady, M. F.; Kaner, R. B.; Mousavi, M. F. Nile Blue Functionalized Graphene Aerogel as a Pseudocapacitive Negative Electrode Material across the Full pH Range. *ACS Nano*, **2019**, *13*, 12567−12576.

(42) Shabangoli, Y.; Rahmanifar, M. S.; El-Kady, M. F.; Noori, A.; Mousavi, M. F.; Kaner, R. B. Thionine functionalized 3D graphene aerogel: combining simplicity and efficiency in fabrication of a metal-free redox supercapacitor. *Adv. Energy Mater.* **2018**, *8*, 1802869.

(43) Gong, S.; Ni, H.; Jiang, L.; Cheng, Q. Learning from nature: constructing high performance graphene-based nanocomposites. *Mater. Today* **2017**, *20*, 210−219.

(44) Gong, C.; Sun, S.; Zhang, Y.; Sun, L.; Su, Z.; Wu, A.; Wei, G. Hierarchical nanomaterials via biomolecular self-assembly and bioinspiration for energy and environmental applications. *Nanoscale* **2019**, *11*, 4147−4182.

(45) Zhang, H.; He, X.; Wei, F.; Dong, S.; Xiao, N.; Qiu, J. Moss-Covered Rock-like Hybrid Porous Carbons with Enhanced Electrochemical Properties. *ACS Sustainable Chem. Eng.* **2020**, *8*, 3065−3071.

(46) Lian, J.; Pang, D.; Yang, C.; Xiong, L.; Cheng, R.; Yang, S.; Lei, J.; Chen, T.; Yang, F.; Zhu, W. Konjac glucomannan-derived nitrogen-containing layered microporous carbon for high-performance supercapacitors. *New J. Chem.* **2020**, *44*, 1400−1406.

(47) Wu, C.; Zhou, T.; Du, Y.; Dou, S.; Zhang, H.; Jiang, L.; Cheng, Q. Strong bioinspired HPA-rGO nanocomposite films via interfacial interactions for flexible supercapacitors. *Nano Energy* **2019**, *58*, 517−527.

(48) Huang, C.; Kang, L.; Zhang, N.; Wan, S.; Zhou, X.; Zhang, J. Bioinspired Interfacial Strengthening Flexible Supercapacitors via Hierarchically Topological Interlocking Strategy. *ACS Appl. Mater. Interfaces* **2019**, *11*, 38303−38312.

(49) Peng, L.; Cai, Y.; Luo, Y.; Yuan, G.; Huang, J.; Hu, C.; Dong, H.; Xiao, Y.; Liang, Y.; Liu, Y. Bioinspired highly crumpled porous carbons with multidirectional porosity for high rate

performance electrochemical supercapacitors. *ACS Sustainable Chem. Eng.* **2018**, *6*, 12716−12726.

(50) Geng, X.; Zhang, Y.; Jiao, L.; Yang, L.; Hamel, J.; Giummarella, N.; Henriksson, G.; Zhang, L.; Zhu, H. Bioinspired ultrastable lignin cathode via graphene reconfiguration for energy storage. *ACS Sustainable Chem. Eng.*, **2017**, *5*, 3553−3561.

(51) Li, B.; Xing, R.; Mohite, S. V.; Latthe, S. S.; Fujishima, A.; Liu, S.; Zhou, Y. CoS_2 nanodots anchored into heteroatom-doped carbon layer via a biomimetic strategy: Boosting the oxygen evolution and supercapacitor performance. *J. Power Sources* **2019**, *436*, 226862.

(52) Wu, Q. N.; Wen, J. H.; Wen, M.; Wu, Q. S.; Fu, Y. Q. Bioinspired sea-sponge nanostructure design of Ni/$Ni(HCO_3)_2$-on-C for a supercapacitor with a superior anti-fading capacity. *J. Mater. Chem. A* **2018**, *6*, 15781−15788.

(53) Song, K.; Wang, X.; Wang, J.; Zhang, B.; Zuo, C. Bioinspired Reduced Graphene Oxide/Polyacrylonitrile-Based Carbon Fibers/$CoFe_2O_4$ Nanocomposite for Flexible Supercapacitors with High Strength and Capacitance. *ChemElectroChem* **2018**, *5*, 1297−1305.

(54) Liu, Y.; Ai, K.; Lu, L. Polydopamine and its derivative materials: synthesis and promising applications in energy, environmental, and biomedical fields. *Chem. Rev.* **2014**, *114*, 5057−5115.

(55) Lee, H.; Lee, B. P.; Messersmith, P. B. A reversible wet/dry adhesive inspired by mussels and geckos. *Nature* **2007**, *448*, 338−341.

(56) Lee, H.; Dellatore, S. M.; Miller, W. M.; Messersmith, P. B. Mussel-inspired surface chemistry for multifunctional coatings. *Science* **2007**, *318*, 426−430.

(57) Huang, Q.; Chen, J.; Liu, M.; Huang, H.; Zhang, X.; Wei, Y. Polydopamine-based functional materials and their applications in energy, environmental, and catalytic fields: State-of-the-art review. *Chem. Eng. J.* **2020**, *387*, 124019.

(58) El Yakhlifi, S.; Ball, V. Polydopamine as a stable and functional nanomaterial. *Colloids and Surfaces B: Biointerfaces Colloids Surf., B* **2020**, *186*, 110719.

(59) Qu, K.; Wang, Y.; Vasileff, A.; Jiao, Y.; Chen, H.; Zheng, Y. Polydopamine-inspired nanomaterials for energy conversion and storage. *J. Mater. Chem. A* **2018**, *6*, 21827−21846.

(60) Zhang, Z. J.; Deng, G. L.; Huang, X.; Wang, X.; Xue, J. M.; Chen, X. Y. Highly boosting the supercapacitor performance by polydopamine-induced surface modification of carbon materials and use of hydroquinone as an electrolyte additive. *Electrochim. Acta* **2020**, *339*, 135940.

(61) Miao, Z.; Huang, Y.; Xin, J.; Su, X.; Sang, Y.; Liu, H.; Wang, J.-J. High Performance Symmetric Supercapacitor Constructed Using Carbon Cloth Boosted by Engineering Oxygen-containing Functional Groups. *ACS Appl. Mater. Interfaces* **2019**, *11*, 18044−18050.

(62) Tabti, Z.; Ruiz-Rosas, R.; Quijada, C. s.; Cazorla-Amorós, D.; Morallon, E. Tailoring the surface chemistry of activated carbon cloth by electrochemical methods. *ACS Appl. Mater. Interfaces* **2014**, *6*, 11682−11691.

(63) Wang, G.; Wang, H.; Lu, X.; Ling, Y.; Yu, M.; Zhai, T.; Tong, Y.; Li, Y. Solid-state supercapacitor based on activated carbon cloths exhibits excellent rate capability. *Adv. Mater.* **2014**, *26*, 2676−2682.

(64) Jiang, S.; Shi, T.; Zhan, X.; Long, H.; Xi, S.; Hu, H.; Tang, Z. High-performance all-solid-state flexible supercapacitors based on two-step activated carbon cloth. *J. Power Sources* **2014**, *272*, 16−23.

(65) Ding, Y.; Floren, M.; Tan, W. Mussel-inspired polydopamine for bio-surface functionalization. *Biosurf. Biotribol.* **2016**, *2*, 121−136.

(66) Noori, A.; El-Kady, M. F.; Rahmanifar, M. S.; Kaner, R. B.; Mousavi, M. F. Towards establishing standard performance metrics for batteries, supercapacitors and beyond. *Chem. Soc. Rev.* **2019**, *48*, 1272−1341.

(67) Chen, X.; Song, Q. Z.; He, W. X.; Liu, P. P.; Xiao, Y. H.; Liang, J. Y. Dual surface modification of carbon materials by polydopamine and phosphomolybdic acid for supercapacitor application. *Dalton Transact.* **2019**, *48*, 17321−17330.

(68) Holten-Andersen, N.; Harrington, M. J.; Birkedal, H.; Lee, B. P.; Messersmith, P. B.; Lee, K. Y. C.; Waite, J. H. pH-induced metal-ligand cross-links inspired by mussel yield self-healing polymer networks with near-covalent elastic moduli. *Proc. Natl. Acad. Sci.* **2011**, *108*, 2651−2655.

(69) Liu, Y.; Liu, Z.; Liu, Y.; Hu, H.; Li, Y.; Yan, P.; Yu, B.; Zhou, F. One-step modification of fabrics with bioinspired polydopamine@octadecylamine nanocapsules for robust and healable self-cleaning performance. *Small* **2015**, *11*, 426−431.

(70) Kordek, K.; Jiang, L.; Fan, K.; Zhu, Z.; Xu, L.; Al-Mamun, M.; Dou, Y.; Chen, S.; Liu, P.; Yin, H. Two-Step Activated Carbon Cloth with Oxygen-Rich Functional Groups as a High-Performance Additive-Free Air Electrode for Flexible Zinc–Air Batteries. *Adv. Energy Mater.* **2018**, *9*, 1802936.

(71) Lee, W.; Lee, J. U.; Jung, B. M.; Byun, J.-H.; Yi, J.-W.; Lee, S.-B.; Kim, B.-S. Simultaneous enhancement of mechanical, electrical and thermal properties of graphene oxide paper by embedding dopamine. *Carbon* **2013**, *65*, 296−304.

(72) Tan, J.; Zhang, Z.; He, Y.; Yue, Q.; Xie, Z.; Ji, H.; Sun, Y.; Shi, W.; Ge, D. Electrochemical synthesis of conductive, superhydrophobic and adhesive polypyrrole-polydopamine nanowires. *Synth. Met.* **2017**, *234*, 86−94.

(73) Vecera, P.; Chacón-Torres, J. C.; Pichler, T.; Reich, S.; Soni, H. R.; Görling, A.; Edelthalhammer, K.; Peterlik, H.; Hauke, F.; Hirsch, A. Precise determination of graphene functionalization by in situ Raman spectroscopy. *Nat. Commun.*, **2017**, *8*, 1−9.

(74) Cortés, M. T.; Vargas, C.; Blanco, D. A.; Quinchanegua, I. D.; Cortés, C.; Jaramillo, A. M. Bioinspired Polydopamine Synthesis and Its Electrochemical Characterization. *J. Chem. Educ.* **2019**, *96*, 1250–1255.

(75) Liu, T.; Lee, B.; Kim, B. G.; Lee, M. J.; Park, J.; Lee, S. W. In situ polymerization of dopamine on graphene framework for charge storage applications. *Small* **2018**, *14*, 1801236.

(76) Xiong, T.; Lee, W. S. V.; Chen, L.; Tan, T. L.; Huang, X.; Xue, J. Indole-based conjugated macromolecules as a redox-mediated electrolyte for an ultrahigh power supercapacitor. *Energy Environ. Sci.* **2017**, *10*, 2441−2449.

(77) Zangmeister, R. A.; Morris, T. A.; Tarlov, M. J. Characterization of polydopamine thin films deposited at short times by autoxidation of dopamine. *Langmuir* **2013**, *29*, 8619−8628.

(78) Wang, Y.; Chen, B.; Zhang, Y.; Fu, L.; Zhu, Y.; Zhang, L.; Wu, Y. ZIF-8@MWCNT-derived carbon composite as electrode of high performance for supercapacitor. *Electrochim. Acta* **2016**, *213*, 260−269.

(79) Qie, L.; Chen, W.; Xu, H.; Xiong, X.; Jiang, Y.; Zou, F.; Hu, X.; Xin, Y.; Zhang, Z.; Huang, Y. Synthesis of functionalized 3D hierarchical porous carbon for high-performance supercapacitors. *Energy Environ. Sci.* **2013**, *6*, 2497−2504.

(80) Smolin, Y. Y.; Van Aken, K. L.; Boota, M.; Soroush, M.; Gogotsi, Y.; Lau, K. K. Engineering ultrathin polyaniline in micro/mesoporous carbon supercapacitor electrodes using oxidative chemical vapor deposition. *Adv. Mater. Interfaces* **2017**, *4*, 1601201.

(81) He, W.; Wang, C.; Zhuge, F.; Deng, X.; Xu, X.; Zhai, T. Flexible and high energy density asymmetrical supercapacitors based on core/shell conducting polymer nanowires/manganese dioxide nanoflakes. *Nano Energy* **2017**, *35*, 242−250.

(82) Coskun, H.; Aljabour, A.; de Luna, P.; Sun, H.; Nishiumi, N.; Yoshida, T.; Koller, G.; Ramsey, M. G.; Greunz, T.; Stifter, D.; Strobel, M.; Hild, S.; Hassel, A. W.; Sariciftci, N. S.; Sargent, E. H.; Stadler, P. Metal-Free Hydrogen-Bonded Polymers Mimic Noble Metal Electrocatalysts. *Adv. Mater.* **2020**, *32*, 1902177.

(83) Galal, A.; Atta, N. F.; Ali, S. M. Optimization of the synthesis conditions for $LaNiO_3$ catalyst by microwave assisted citrate method for hydrogen production. *Appl. Catal., A* **2011**, *409*, 202−208.

(84) Qu, D.; Wang, G.; Kafle, J.; Harris, J.; Crain, L.; Jin, Z.; Zheng, D. Electrochemical Impedance and its Applications in Energy-Storage Systems. *Small Methods* **2018**, *2*, 1700342.

(85) Mei, B.-A.; Munteshari, O.; Lau, J.; Dunn, B.; Pilon, L. Physical interpretations of Nyquist plots for EDLC electrodes and devices. *J. Phys. Chem. C* **2018**, *122*, 194−206.

(86) Mei, B.-A.; Lau, J.; Lin, T.; Tolbert, S. H.; Dunn, B. S.; Pilon, L. Physical interpretations of electrochemical impedance spectroscopy of redox active electrodes for electrical energy storage. *J. Phys. Chem. C* **2018**, *122*, 24499−24511.

(87) Thangappan, R.; Kalaiselvam, S.; Elayaperumal, A.; Jayavel, R.; Arivanandhan, M.; Karthikeyan, R.; Hayakawa, Y. Graphene decorated with MoS_2 nanosheets: a synergetic energy storage composite electrode for supercapacitor applications. *Dalton Transact.* **2016**, *45*, 2637−2646.

(88) Lasia, A. Modeling of impedance of porous electrodes. *Modeling and Numerical Simulations*, Springer **2008**, *43*, 67−137.

(89) Wang, C.; Appleby, A. J.; Little, F. E. Criteria for reliable electrochemical impedance measurements on Li-ion battery anodes. *J. Electrochem. Soc.* **2003**, *150*, A143−A148.

(90) Mathis, T. S.; Kurra, N.; Wang, X.; Pinto, D.; Simon, P.; Gogotsi, Y. Energy storage data reporting in perspective—guidelines for interpreting the performance of electrochemical energy storage systems. *Adv. Energy Mater.* **2019**, *9*, 1902007.

(91) Yin, B.-S.; Zhang, S.-W.; Ke, K.; Wang, Z.-B. Biology-inspired polydopamine-assisted strategy for high-performance supercapacitor. *Chem. Eng. J.* **2019**, *375*, 122056.

(92) Zeng, R.; Deng, H.; Xiao, Y.; Huang, J.; Yuan, K.; Chen, Y. Cross-linked graphene/carbon nanotube networks with polydopamine "glue" for flexible supercapacitors. *Compos. Commun.* **2018**, *10*, 73−80.

(93) Ramaprabhu, S. Poly(p-phenylenediamine)/graphene nanocomposites for supercapacitor applications. *J. Mater. Chem.* **2012**, *22*, 18775−18783.

(94) Bian, L.-J.; Luan, F.; Liu, S.-S.; Liu, X.-X. Self-doped polyaniline on functionalized carbon cloth as electroactive materials for supercapacitor. *Electrochim. Acta* **2012**, *64*, 17−22.

CHAPTER 7. CONCLUSIONS AND A LOOK FORWARD

7.1 Conclusions

The primary goal of this thesis has been the development of advanced electrochemical energy storage devices that are sustainable and reliable, with high energy/power densities, fast charging/discharging rate, and long cycle life and calendar life. Pursuing this goal, this research has explored diverse electrode materials design approaches and fabrication techniques to improve the performance of state-of-the-art commercial supercapacitors and to meet the higher demands of future systems. Physicochemical and electrochemical characterizations have been systematically conducted to investigate the correlations between structures and properties and to gain insights into the underlying mechanisms and chemistry.

From the perspective of materials design, polyaniline and other conducting polymers are promising pseudocapacitive electrode materials due to their adjustable conductivity, high theoretical capacitance, affordable cost, and environmental friendliness. However, their long-term use has been hindered by their instability, which leads to a sharp loss of capacitance over time. To surmount this challenge, we have explored a facile way to covalently attach aniline tetramers, which are the basic building blocks of polyaniline, to 3D graphene networks using a one-step perfluorophenylazide coupling reaction. This molecular-level design creates a hybrid electrode material with excellent cycling stability (85% capacitance retention after 30,000 cycles). A redox-active electrolyte based on the hydroquinone/quinone redox couple has been further introduced to the energy storage system to achieve higher capacitance and energy density. The fabricated

symmetric quasi-solid-state devices deliver not only high specific capacitance but also ultralong cycle life beyond 100,000 cycles with 82% capacitance retention.

From a manufacturing perspective, the conventional synthesis of conducting polymer hybrid materials is typically time- and/or energy-consuming, where multiple synthetic steps and/or high-temperature treatments are typically needed. Therefore, we further seek to develop a scalable, effortless, and cost-efficient approach toward the fabrication of conducting polymer-based electrodes to reduce the time/energy consumption. Specifically, a facile and potentially scalable laser scribing technique is employed to enable the formation of amide covalent linkages to bind short-chain aniline trimers and carbon nanotubes through molecular engineering. This technique produces a durable conducting polymer-based hybrid electrode material with superior cycling stability and rate capability without the need for binders or conductive additives. Compared to conventional synthetic methods, the laser scribing technique operating under ambient conditions can be accomplished within seconds and the as-prepared electrodes can achieve comparable electrochemical performance.

From the perspective of mechanism comprehension, although extensive efforts have been made to address the instability issue of conducting polymers, there is a lack of research on the causes of cycling stability degradation and the mechanisms responsible for capacitance fading in conducting polymer or oligomer materials. To better understand how aniline oligomer-based materials experience capacitance degradation over extended cycling periods, two composite electrodes were studied as model systems. These electrodes, composed of aniline trimers and carbon nanotubes, were subjected to thorough physicochemical and electrochemical analyses both before and after the cycling process. The covalent bonding between aniline trimers and carbon nanotubes greatly contributes to enhanced cycling stability by preventing the detachment of aniline

trimers and maintaining the electrode microstructure during long-term cycling. At the same time, the greater porosity has a positive impact on electron/ion transfer and the adaptation to volumetric changes, leading to higher conductivity and extended cycle life. This study provides insights into the structural design features of conducting polymer hybrid materials toward long-term cycling energy storage devices.

From the perspective of sustainability, as environmental worries persist, it is imperative to develop energy storage systems that are efficient, affordable, reliable, sustainable, and environmentally friendly. Lignin, a redox-active biopolymer found abundantly in trees and other lignocellulosic biomasses, offers exciting possibilities as a pseudocapacitive material. Its direct utilization, along with its derivatives, provides novel avenues for developing sustainable active materials with added value for various applications. A nanocomposite based on an interpenetrating network of polyaniline and sulfonated lignin is demonstrated, which exhibits a specific capacitance of 1200 F g^{-1} at 1 A g^{-1}, surpassing the best-known conducting polymer-lignin supercapacitors. The fabricated symmetric devices can deliver both high specific energy (21.2 W h kg^{-1}) and outstanding specific power (26.0 kW kg^{-1}), along with superb flexibility and excellent cycling stability.

Another approach to developing sustainable energy storage systems involves the fabrication of a bioinspired polydopamine nanofilm supported on oxygen-functionalized carbon cloth through a facile and green electrosynthesis process. The pseudocapacitive behavior of polydopamine arises from its chemical composition, which includes catechol, amine, and imine groups. By creating a binder-free and flexible electrode, a high specific capacitance (626 F g^{-1} at 1.0 A g^{-1}) is achieved. Furthermore, the symmetric all-solid-state flexible device covers a wide range within the thermodynamic stability window of aqueous electrolytes (1.2 V), with high specific energy

(11.7 Wh kg^{-1}), impressive specific power (up to 6.4 kW kg^{-1}), excellent flexibility, and exceptional cycling stability.

Overall, the work presented in this dissertation has improved the energy storage performance of conducting polymer-based supercapacitors from several perspectives and contributed to the next generation of sustainable and eco-friendly energy storage systems. With the aim to enhance the performance of commercial energy storage devices and fulfill the increasing requirements of future systems, continuous efforts are still highly needed.

7.2 A Look Forward

Long cycle life and high energy/power density are imperative to electrochemical energy storage systems. To improve the energy storage capacity and cycling stability of conducting polymer-based supercapacitors, the following directions should be taken into account.

In this study, we meticulously designed binary hybrid materials combining conducting polymers (or oligomers) with carbon materials or other organic materials through molecular engineering. Binary or ternary nanostructured composites based on oligomeric forms of conducting polymers can be constructed with pseudocapacitive materials such as metal oxides (e.g. V_2O_5 and Co_3O_4) and metal sulfides (e.g. MoS_2 and $NiCo_2S_4$), that might replace carbon materials as excellent candidates for creating composites for high-performance conducting polymer-based supercapacitors. Furthermore, novel 2D materials including MXenes,[1] black phosphorus,[2] metal-organic frameworks (MOFs),[3] and covalent organic frameworks (COFs)[4] have been explored for energy storage systems in recent years. Coupling these potential materials with conducting polymers (or oligomers) presents a significant prospect for generating optimized hybrid electrode materials. By rationally designing integrated architectures for these composite materials, the

structural features and electrochemical activity of each component can be fully manifested with excellent synergistic effects for improving the electrochemical performance of composite electrode materials.

In addition to developing high-performance active electrode materials, the introduction of a redox-active electrolyte into a supercapacitor system can be another auspicious strategy.[5, 6] By adding a redox additive into an inert electrolyte, extra capacity will be contributed by high-speed solution-phase Faradaic reactions and maintain the high rate capability and cycling stability. Various redox couples have been investigated in supercapacitors, including VO_2^+/VO^{2+}, $Fe[(CN)_6]^{4-}/Fe[(CN)_6]^{3-}$, halides, methylene blue, viologen, and quinones.[5] A 50% increase in the specific capacitance of an aniline tetramer hybrid electrode material has been achieved in this study by introducing a small amount of the hydroquinone/quinone redox couple in the aqueous electrolyte.[7] To achieve a substantial enhancement in the energy density of a conducting polymer-based supercapacitor, it is a promising approach to develop aqueous/organic electrolytes and ionic liquids with redox-active species, which provide broader operating potential windows, higher electrochemical stability, and better ionic conductivity. Pairing these redox-active electrolytes with appropriate conducting polymer hybrid materials holds potential for boosting the energy density of conducting polymer-based energy storage systems while maintaining excellent cycling stability.

The inherent nature of conducting polymers provides them with significant structural versatility and remarkable flexibility. Their electrochromic properties present a distinct advantage for potential applications in intelligent supercapacitors. Given the substantial interest in conducting polymer composites over the past decade and the ongoing research advancements, it is anticipated that conducting polymers will play a pivotal role in future energy storage applications that emphasize flexibility, intelligence, sustainability, and cost-effectiveness.

7.3 References

(1) Lukatskaya, M. R.; Mashtalir, O.; Ren, C. E.; Dall'Agnese, Y.; Rozier, P.; Taberna, P. L.; Naguib, M.; Simon, P.; Barsoum, M. W.; Gogotsi, Y. Cation intercalation and high volumetric capacitance of two-dimensional titanium carbide. *Science* **2013**, *341*, 1502–1505.

(2) Hao, C.; Yang, B.; Wen, F.; Xiang, J.; Li, L.; Wang, W.; Zeng, Z.; Xu, B.; Zhao, Z.; Liu, Z.; et al. Flexible All-Solid-State Supercapacitors based on Liquid-Exfoliated Black-Phosphorus Nanoflakes. *Adv. Mater.* **2016**, *28*, 3194–3201.

(3) Gittins, J. W.; Balhatchet, C. J.; Fairclough, S. M.; Forse, A. C. Enhancing the energy storage performances of metal–organic frameworks by controlling microstructure. *Chem. Sci.* **2022**, *13*, 9210–9219.

(4) Deblase, C. R.; Silberstein, K. E.; Truong, T.-T.; Abruña, H. D.; Dichtel, W. R. β-Ketoenamine-Linked Covalent Organic Frameworks Capable of Pseudocapacitive Energy Storage. *J. Am. Chem. Soc.* **2013**, *135*, 16821–16824.

(5) Chun, S.-E.; Evanko, B.; Wang, X.; Vonlanthen, D.; Ji, X.; Stucky, G. D.; Boettcher, S. W. Design of aqueous redox-enhanced electrochemical capacitors with high specific energies and slow self-discharge. *Nat. Commun.* **2015**, *6*, 7818.

(6) Shao, Y.; El-Kady, M. F.; Sun, J.; Li, Y.; Zhang, Q.; Zhu, M.; Wang, H.; Dunn, B.; Kaner, R. B. Design and Mechanisms of Asymmetric Supercapacitors. *Chem. Rev.* **2018**, *118*, 9233–9280.

(7) Chang, X.; El-Kady, M. F.; Huang, A.; Lin, C.-W.; Aguilar, S.; Anderson, M.; Zhu, J. Z. J.; Kaner, R. B. 3D Graphene Network with Covalently-Grafted Aniline Tetramer for Ultralong-Life Supercapacitors. *Adv. Funct. Mater.* **2021**, *31*, 2102397.